Design and Simulation of an Optimized Small Wind Turbine

Submitted in fulfilment of the requirements of the degree of Master of Engineering: Mechanical Engineering in the Faculty of Engineering and the Built Environment at the Durban University of Technology

Norberto Fernando Soares Sanjimba

2021

Supervisor: Prof. P. Tabakov

Declaration

I, Norberto Fernando Soares Sanjimba, declare that:

1. This dissertation has not been submitted for any examination at any other university.
2. The research work presented in this dissertation besides where otherwise indicated, is my original research work.
3. This dissertation does not contain graphics, text, or tables that are copied from the internet, unless specifically acknowledged, and the source being indicated in the dissertation and in the bibliography.

Student: Norberto Fernando Soares Sanjimba

Signature: Date: June 13, 2021

As the student's supervisor I agree to the submission of this thesis.

Supervisor: Prof. P. Tabakov

Signature: Date: June 13, 2021

ACKNOWLEDGEMENT

First and foremost, I would like to thank the Lord God Almighty for the gift of life, for guarding and giving me strength throughout this research. Without Him, this work would not have been possible, as the Bible says: "for in Him we live and move and have our being..." - Acts 17:28.

Secondly, I would like to acknowledge the guidance, advice, and support of my supervisor, Prof. P. Tabakov. Whenever consulted, Prof. Tabakov was always available and willing to impart knowledge and give guidance to propel the research, he always pointed to the right tools to use to solve the problems encountered during the research. I was privileged to work with him and learned a lot from his experience and wisdom.

Last but not least, I would like to thank my relatives (parents and siblings) for their unconditional love and support. They believed in me in every moment and supported me in whatever way possible. I also would like to thank in a special way my two beloved Ms. Ayanda Mabhoza and Mr. Leeward Mabheka Dube for their unceasing support.

Abstract

The volatility of fossil fuel's price, pollution, and emission associated with converting fossil fuel into a useful type of energy led man to search for more sustainable energy sources that are pollution-free and renewable. Today, renewable energy technologies, such as solar and large wind turbines, are developed to a stage of maturity, having the cost of producing electricity dropping significantly in the last decade, therefore making these technologies competitive with the traditional counterpart.

The cost of producing electricity through small wind turbines is still high compared to large wind turbines or photovoltaic technology. For small wind turbines to successfully compete with other technologies and contribute to the diversification of off-grid technology, further research is needed to reduce the levelised cost of energy (LCOE). Therefore, this study aims to reduce the levelised cost of energy (LCOE) of small wind turbines. To achieve the objective, a 10 kW wind turbine operating at a site of an average wind speed of 7.5 m/s was designed, optimized, and simulated.

With low LCOE in mind, the turbine components were designed as simple as possible to reduce manufacturing costs. The blades are made of uniform cross-sectional area, which made possible to use aluminum as the blade material, and the blade cross-sectional area is made out of a high lift airfoil. The hub is made of aluminum and modelled and designed as a disc with holes to bolt the blades and attach the main shaft. The mainframe is treated as a thick plate with a proper arrangement to connect the generator, the main and yaw bearings, the tail support, and any other ancillaries needed. An octal tapered tower with a height of 20 m made of steel was designed and optimized for low weight. The electrical power is to be produced by a direct drive variable speed permanent magnet synchronous generator. The control system is designed in such a way that allows the turbine to operate in maximum power efficiency for any speed below the rated speed, and to increase reliability, a sensorless control system is suggested.

The research started with a broad review of the relevant literature on wind turbines in general and small wind turbines. The turbine blades design began by analysing the aerodynamic performance of the blade. To accomplish that, XFoil was used to generate the aerodynamic parameters of the airfoil, the Blade Element Momentum (BEM) method was used to estimate the blades' aerodynamic performance, and Qblade was employed to compare the results, and Computational Fluid Dynamics (CFD) was used to verify the results. The preliminary design was done using standard IEC 61400-2 to obtain the load cases, and general engineering formulas, CFD and Finite Element Analysis (FEA) was used to analyse the load in the components according to IEC 61400-2, FAST-V7 was used to simulate the turbine's overall performance, standard formulas were used to evaluate the economic performance of the design, MatLab was used to perform all needed calculations. In this study, it is evident that using standard IEC 61400-2 to estimate the load, gyroscopic load components dominate the design, and the control system must be used to limit those loads. The designed turbine has relatively high efficiency and low LCOE.

Nomenclature

Symbol	Description	Unit
α	Angle of attack	[deg]
α_{stall}	Angle of attack when stall start to occur	[deg]
$\bar{c}$	Airfoil average chord length	[m]
$\bar{u}, \bar{v}, \bar{w}$	Average velocities in x,y,z direction respectively	[m/s]
γ_f	Partial safety factor loads	[−]
γ_m	Partial safety factor for materials	[−]
λ	Tip speed ratio	[−]
λ_r	Local speed ratio	[−]
μ	Viscosity	[Ns/m^2]
μ_t	Turbulent viscosity	[m^2/s]
Ω	Rotor angular speed	[rad/s]
ω	Induced angular speed to the wind	[rad/s]
ω_n	Rotational speed of the rotor	[rad/s]
ω_{yaw}	Yaw rate	[rad/s]
ρ	Density, here assumed 1.225	[kg/m^3]
σ_d	Design stress	[MPa]
σ	Normal stress	[MPa]
$\sigma^{'}$	Solidity	[−]
τ	Shear stress	[MPa]
$\theta_{P,0}$	Blade pitch angle	[deg]

θ_T	Section twist angle	[deg]
φ	Angle of relative wind	[m/s]
A	Cross section area	[m^2]
a	Axial induction factor	[–]
$a^{'}$	Tangential induction factor	[–]
A_{proj}	Projected area	[m^2]
AR	Aspect ratio	[–]
B	Number of blades	[–]
b	Blade span	[m]
c	Airfoil chord length	[m]
C_d	Drag coefficient	[–]
C_f	Force coefficient	[–]
C_l	Lift coefficient	[–]
C_P	Power coefficient	[–]
C_T	Thrust coefficient	[–]
C_{d-max}	Maximum drag that can be obtained from the airfoil	[–]
$C_{d-stall}$	Drag coefficient at the stall angle	[–]
$C_{l-stall}$	Lift coefficient at the stall angle	[–]
D	Diameter	[m]
e_r	Distance from the CoG of the rotor to the rotation axis force	[m]
F	Force or tip speed loss coefficient, depend on the context	[N]
F_h	Speed loss at the root of the blade	[–]
f_k	Characteristic value for material strength	[–]

F_t	Speed loss at the tip of the blade	[–]
$F_{x-shaft}$	Axial shaft force	[N]
F_{zB}	Force on the blade at the blade root in spanwise direction	[N]
G	Ratio between rated torque and generator short circuit torque	[–]
g	Acceleration due to gravity	[m/s^2]
I_B	Mass moment of inertia of the blade about the blade root flap axis	[kgm^2]
L_{rb}	Distance between the rotor center and the first bearing	[m]
L_{rt}	Distance between the rotor center and the yaw axis	[m]
m_B	Blade mass	[kg]
m_r	Mass of the blade plus the mass of the hub	[kg]
M_{brake}	Torque on the low speed shaft caused by the brake	[Nm]
M_{shaft}	Combined bending moment for the shaft at the first bearing	[Nm]
$M_{x-shaft}$	Torsion moment on the rotor shaft at the first bearing	[Nm]
M_{xB}, M_{yB}	Blade root bending moment	[Nm]
n	Rotor speed	[rad/s]
$N(.)$	Number of cycle to failure as a function of the stress	[–]
n_i	Counted number of fatigue cycles in load bin i	[–]
P	Electrical power	[W]
p_i	Average wind pressure at section i	[Pa]
Q	Rotor torque	[Nm]
R	Rotor radius	[Nm]
r	Local radius	[m]

R_{cog}	Radial distance between the CoG of a blade and the rotor center	[m]
s_i	Stress level associated with the counted number of cycles	[MPa]
T_d	Design life	[yrs]
U	Wind free stream velocity	[m/s]
U_i	Wind velocity at section i	[m/s]
U_{rel}	Relative wind velocity	[–]
V	Wind speed	[m/s]
V_{ave}	Annual average wind speed at hub height	[m/s]
V_{des}	Design wind speed	[m/s]
$Ve1$	For 1 year	[m/s]
V_{e50}	For 50 years	[m/s]
V_{eN}	Extreme wind speed, with recurring time interval of N years.	[m/s]
V_{eN}	Largest gust magnitude with an expected recurrence period N years	[m/s]
V_{hub}	Wind speed at hub height averaged over 10 minutes	[m/s]
V_{in}	Cut-in wind speed	[m/s]
V_{out}	Cut-out wind speed	[m/s]
V_{ref}	Reference wind speed averaged over 10 minutes	[m/s]
W	Section modulus used in the stress calculations	[m^3]
x, y, z	Coordinate system used for the wind field description.	[m]
dF_D	Elemental drag force	[N]
dF_L	Elemental lift force	[N]
dF_N	Elemental normal force	[N]

dF_T	Elemental tangential force	[N]

List of Figures

List of Tables

Contents

Chapter 1

Introduction

This chapter introduces the topic of the research. Section 1.1 gives a little background of the reasons behind the interest to study this topic. Section 1.2 discusses the area that the research will be focused on. The research aim and objectives are explained in Section 1.3. The research methodology is given in Section 1.4. The value of the research is given in Section 1.5. Section 1.6 outlines the structure of the research.

1.1 Background

Energy is vitally important in the development of a country. Globally the need for energy is ever increasing. Fossil fuels have been the most used form of energy for transportation and electricity generation. However, fossil fuels are non-renewable energy; they are very volatile in price; they contribute heavily to environmental pollution and greenhouse gas emission. These facts have led man to seek alternative energy sources that are sustainable, pollution-free, and renewable energy. Thus, hydropower, wind, solar, geothermal, tide, ocean energy, and biofuel have been studied and developed into mature technology, and nowadays, they are used as alternative sources of energy. In terms of capacity, with 564GW installed globally in 2018, wind energy is the second renewable energy most used to generate electricity, after hydropower [1]. According to the World Wind Energy Association (WWEA), about 95000GW wind power is available worldwide [2]. It is estimated that 1787GW of wind turbines will be installed by 2030 and 5044GW by 2050 [1].

Eleven out of fifty people in the world do not have the privilege of having electricity. Most of those people live in region far or difficult to access and therefore connect to regional or national grids. Most of these people are found in sub-Saharan Africa and South Asia [3]. Disperse populations have the needed energy for their activities using a diesel generator, liquefied petroleum gas (LPG), disposable batteries, paraffin (or kerosene), and biomass technology. Diesel generators, with capacities varying from 5kW to few MW, have been the traditional solution to remote electrification. However, the high cost of fuel and transportation to the remote areas, the need for regular, skilled maintenance of equipment, and the environmental consideration constitute the main drawbacks of this technology [4].

The photovoltaic system is easy to install and operate, and they do not have any moving parts; therefore, it requires little maintenance. The cost of installing a PV system has dropped considerably in the past years; hence this system has been the technology of choice for electrification of remote areas. Electricity Home System (EHS) is used as an alternative to electrify isolated household or small businesses. These systems provide a readily available, relatively low cost, and low maintenance solution [5]. Pico PV system (PPS), solar home systems (SHS), small hydro plants (SHP), or wind home systems (WHS) are used as EHS [5]. In these systems, the power generation is installed near the loads, and there are no transmission and distribution costs.

South Africa's energy depends heavily on coal due to the country abundance of coal supply. In March 2018, Eskom had a production capacity of 48GW, broken down intro: about 83% coal, 6% pumped storage, 5% gas, 4% nuclear, 2% hydro and 0.2% wind energy [6]. The dependency of coal makes the country ranked as one of the highest GHG emitters in the world, with about 400MtCO2 per year [7]. South African government has committed to reducing carbon emissions. In 2009, in Copenhagen, the president committed to reducing carbon emissions by 34% by 2020 and further reducing by 42% by 2025 [8]. In 2015, in the Paris agreement, the government signed the agreement for decarbonization and zero greenhouse gases emission by 2050 [9]. In 2019, the South African parliament signed the Carbon Tax Act, 2019, where the tax is fixed to R120 per ton of carbon dioxide produced [10]. The government has also made policies to promote renewable energy integration into the national electricity generation capacity, enhancing energy diversification and mitigating GHGs emissions. Three key policy support the implementation of renewable energy in South Africa, namely, the White Paper on Energy Policy (1998), the Renewable Energy White Paper (2003), and the National Climate Change Response Policy White Paper (2011) [8]. The South African government's effort to reduce carbon emission has resulted in 1860MW of renewable energy been added to the national energy capacity in 2015, which constituted about 4% of the total capacity from zero percent [9].

The South African electrification program has been a success. In 2002, about 77.1% of houses in South Africa had electricity. By 2013, the numbers of the electrified house had increased to 85.4% [11]. The increase of electrification in South Africa is in line with the National Development Plan (NDP). Accord to this plan, the country is to have 90% of the houses connected to the national grid line by 2030, and the remainder is to be electrified by off-grid technology [12]. To achieve a universal distribution of electricity, the South African government has been giving free essential energy (FEE) to needy families through Eskom and local municipalities. If the low-income family house is located in areas accessible to the national gridline, 50kWh per month is provided to the family. However, suppose the low-income family house is situated in areas inaccessible to the gridline or where extension of it is not economically feasible. In that case, the houses are proved with off-grid electrification, which consists of 50 Watt Solar Home Systems (SHS), which is used for lighting, communication, and small entertainment system [13].

1.2 Research Focus

The electricity provided by the government to low-income families in off-grid areas has not been sufficient to fulfill the basic needs. Because the 50 Watt SHS installed can barely produce 0.3 to 0.4 kWh on a good sunny day [13]. On average, the houses electrified by SHS get about 7.5 kWh per month, which is significantly less than the FBE that the low-income family gets in the grid-connected locations, 50 kWh per month [14]. To solve this difference, Jamal [13] suggested that different off-grid technologies should be used according to the region's weather conditions [13]. For example, in Cape regions (Eastern, Western and Northern Cape), where the wind is usually quite strong, a hybrid system made of wind turbine and photovoltaic (PV) system should be used. Whereas in other regions with low to moderate wind, a hybrid system of a PV system and diesel generator or standalone PV system is suggested [13]. Monyei [14] suggested that a hybrid system of PV-DG would solve the current injustice in the FEE provision to the low-income family in off-grid regions [14].

Small wind turbines (turbines with a capacity lower than 50kW) can be used as a standalone system to electrify remote regions. Normally they are used in small farms, small businesses, schools, remote telecommunication stations, and small remote villages. Today, the large wind turbines technology has been developed to a stage of maturity. They can compete with conventional ways of producing electricity in terms of cost. The price of producing electricity using small wind turbine technology is still high. "In 2017, the average cost reached 11953 $/kW for SWTs up to 20 kW and 7389 $/kW for those between 21 and 100 kW" [15, p.13]. The South African government has promoted large wind turbines, and policy has been put into place to favor large wind turbines installation. This fact culminated in installing 1468 MW in 2017 [9]. The Integrated resource plan 2010-2030 projected 8.4 GW of wind energy to be installed by 2030 with the bulk of it being from large wind turbine technology and a small portion of it being reserved for off-grid technology [16]. Small wind technology in South Africa is still in its infant development stage. For this technology to contribute significantly to the total projected wind energy capacity, further research is needed.

The PV system is a robust off-grid technology competitor of small wind turbines due to its low overall costs. The Levelized cost of energy (LCOE) of a small wind turbine is too high compared to the photovoltaic (PV) system. If SWTs are to compete with PV technologies, further advances have to be made to reduce costs. Improvement in small wind overall technology and manufacturing, maintenance techniques, and installation procedures would make small wind turbines more economically appealing to investors. Many studies have been done and literature written about large wind turbines; therefore, its technology is well established. Even though large and small wind turbines have many similarities; thus, some aspects of large wind turbines can be applied in small counterparts, they have some critical differences that need to be considered. Therefore, small wind technology needs to be studied in a matter that encompassed its peculiarity and not as a down-scale of large wind turbines. Hence, there is a need to do further studies addressing the particular aspects of small wind turbines.

Although small wind turbine is not as attractive as PV technology, it should be promoted through government tax incentives, firm policies, financial support, developing costumers awareness. Chargas stated: "If a technology is still in its initial stages of development, with high costs and low market participation, it needs a strong legal framework to regulate it and lower risks for investors" [15, p.19]. Developing small wind technology should be viewed and an opportunity to diversify off-grid technology through sustainable energy and clean energy to contribute to the decentralization of energy generation and complement other technology.

1.3 Overall Research Aim and Individual Research Objectives

This research aims to design a 10 kW wind turbine that operates at a region with an average wind speed of 7.5 m/s, and the overall cost of it must be below R40000/kW of electrical power generated. The components of the small turbine are to be optimized for cost reduction. With this in mind, the question that this research is the following: What are the procedures to design a 10 kW wind turbine operating at a main annual wind speed of 7.5 m/s that will yield an overall cost of R40000kW of electrical power generated?

The following research objectives are to be accomplished to answer the above question:

1. Review the available literature on the wind turbine and optimization techniques.
2. Identification of the small wind turbine components that need to be design and those which are to be selected.
3. Design and select the components or system preliminarily.
4. Do the detailed design of the components or system
5. Analyze the economic aspects of the design by comparing it with a diesel generator.
6. Conclusion and Recommendation.

The first objective is needed to have updated information about the state of the art of wind turbines in general and the specific detailed technology and trend of small wind turbines. The second objectives clarify what components of the turbine need to be designed to achieve global optimization of the turbine design. The third objective gives a theoretical background that serves as the backbone of the components or system to be designed. The fourth objective serves to analyze whether the components will carry the load during standard operations. Objective number five gives the design's economic aspect and compares the revenue obtained from saving diesel if the designed turbine is installed instead, finally from the reviewed literature. The analyses were done it is needed to conclude and recommend, when applicable.

1.4 Research Methodology

Due to the nature of the research, quantitative research methodology, and indirect data collection was used. The study started with an extensive review of the available literature to clarify and put into perspective the state of the art of wind turbines in general and small wind turbines in particular. Thus, the university library and the web were used to collect the necessary information. The information was gathered from books, journal articles, technical reports, catalogs, engineering standard codes, companies' websites, product user guides, etc.

The online airfoil database was used to select the blade's airfoil, and XFoil was used to determine the two-dimensional blade's aerodynamic properties, which is usually used in the Blade Element Momentum (BEM) method to estimate the aerodynamic parameters. MatLab was used to solve the created blade model. Qblade is a free software used to evaluate wind turbine blades' aerodynamic performance based on the BEM method. Qblade was used in the study to verify the model formulated in MatLab. The turbine's blade was modeled in SolidWorks and imported to Ansys Fluent for CFD analysis. It was used to prove the BEM model because it considers the influence of the blade's 3D aspect in the aerodynamic parameters and considers the turbulence effect.

The detailed design was done by constructing the CAD model in SolidWorks first, and then the model was then exported to SolidWorks FlowSimulation to get the components' aerodynamic loads. The aerodynamic loads were then transferred to SolidWorks Simulation to estimate the stresses on the turbine components. Due to computational power, the parts were analyzed separately. FAST was used to simulate the turbine because it is available to the public free of charge. It is generally accepted to generate the aeroelastic model for turbine certification. Solidworks was used to get the turbine's physical properties and XFoil to generate the needed aerodynamic parameters. The components' cost was estimated according to the current market's available price and the manufacturing process involved to create the final product. The prices of the components'material and their manufacturing processes were obtained from the web.

1.5 Value of the Research

This research project will:

- Present a step by step procedure to design a 10 kW wind turbine
- Present a holistic optimization of small wind turbine
- Reduce cost of small wind turbines
- Attract potential investors

1.6 Outline Structure

This dissertation is divided into various sections. Chapter one gives an introduction of the project, discuss the relevance of it by the proffered background of the need to reduce the cost of a small wind turbine. It also describes the research focus, the aim and objectives of the project, and the research outcomes.

Chapter two review the literature around the topic of the wind turbine in general and small wing turbine in particular, and the specific aspects of remote wind turbine technology that need give incites in the design improvement.

Chapter three discuss the critical theory in the design of the blades of horizontal axis wind turbine with emphasis on the Blade Element Momentum (BEM) method, then the chapter proceeds by analyzing the blade performance preliminarily using the BEM method and verifying the blade aerodynamic performance by CFD analysis.

Chapter four presents the preliminary design of the main turbine components as well as their optimization where applicable. The chapter starts with the initial structural design of the blades then proceeds with the creation of the tower, nacelle, and mainframe. Then the furling mechanism design follows, and the chapter ends with the theory of the control model for a small wind turbine.

Chapter five starts by designing the turbine's brakes, followed by the fitting of the critical components. It then proceeds by analyzing the static stresses of the main features by simulation software and, according to IEC61400-2. The last sections of the chapter discuss the material and the manufacturing methods of the SWT'S main components. The final chapter deals with the economic aspects of the small wind turbine.

Chapter six discusses the cost and benefits of the research project where quantity like simple payback period, net present value, and livelised cost of energy are determined, Chapter six also gives a sensitivity studies of the designed turbine economical feasibility. The final chapter gives the conclusions and recommendations to improve the current study.

Chapter 2

Literature Review

In this chapter, the theory, a brief historic background as well as the current state of the art of wind turbine are given. Section 2.1 gives the basic concept of wind turbines, classification of wind turbines, as well as the turbine layout. In Section 2.2, a brief historical background of wind turbines is presented. Section 2.3 gives the theoretic background of the various aspects to be considered in designing the turbine blades; the section discusses the aerodynamics of the blades, the blades' structure models, the analysis model of the blades' cross-sectional area, the turbine blades' material normally used, and the blades' manufacturing processes. The types of towers normally used in small wind turbines are discussed in Section 2.4. Section 2.5 presents the concepts of the turbine hub pertaining to small wind turbines. The turbine nacelle is briefly discussed in Section 2.6. Section 2.7 gives a brief overview of the various components that compose the drive train system. In Section 2.8 the fastening and joining are briefly discussed. Section 2.9 explains the use of wire rope in wind turbines. Section 2.10 describes the type of generator used in wind turbines. A brief discussion of the control system specific to wind turbines is given in Section 2.11. Section 2.12 discusses issues pertaining to small wind turbines only.

2.1 Basic Concept

A wind turbine is a machine that converts the kinetic energy of the air into mechanical and electrical energy. The air's kinetic energy is caught by the turbine blades, which in turn convert it into mechanical or electrical energy, depending on the end-use [17].

Wind turbines are classified according to how they produce the forces that generate torque needed to produce the required power. When the force is generated due to lift force, they are called lift-type turbines. If the drag force is used as the mechanism to generate the force, the turbine is called drag-type turbines. Wind turbines are also classified according to the axis of rotation. When the axis of the rotation is horizontal, they are called horizontal axis wind turbines (HAWT); if the axis of rotation is vertical, they are called vertical axis wind turbines (VAWT).

The vast majority of modern wind turbines are designed using the lift force concept. The

drag type turbine presents two fundamental problems: (1) they are inherently inefficient, and (2) it is difficult to protect them from extreme wind conditions [18]. The HAWT is vastly used commercially because of its good efficiency and relatively low cost per kWh produced. In the 1970s and 1980s, both the United States and Canada conducted extensive studies in VAWT, particularly the Darrieus turbine. It was found that they do not match their horizontal contour part in terms of energy cost and have major reliability problems [18].

There are many ways the HAWTs can be classified, depending on the aspect of interest one wishes to consider. If the wind orientation is the element of interest HWAT are classified as upwind (when the incoming wind flows through the blades first before reaching the tower) and downwind (when the incoming wind flows through the tower first before getting to the blades). The number of the turbine's blade used by a HAWT gives them the name of one, two, three or more bladed turbine. The way the hub is designed makes the turbine to be classified as a rigid or teetering turbine. The type of control used to regulate the load and power makes the turbine to be called pitched or stalled turbine. How the turbine is aligned to the wind is called active yaw or passive yaw turbine [18].

The main components of a HAWT are the rotor, hub, drive train, nacelle, tower, foundation, machine control, and balance of the electrical system. Figure 2.1 shows the schematic representation of a HAWT.

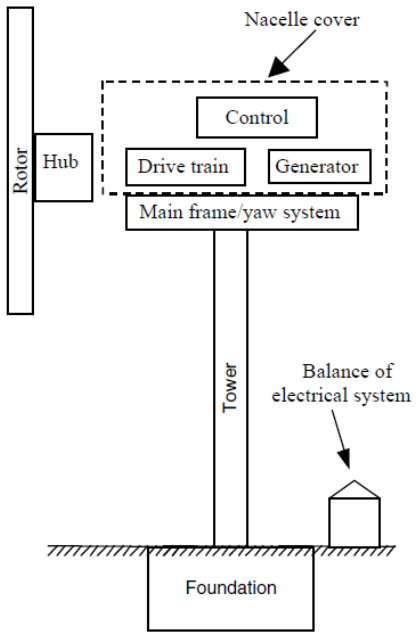

Figure 2.1: Wind turbine main components [18]

2.2 Historic Background

The need to turn wind energy into useful work can be dated back to ancient times when the wind was used as the primary energy source to propel ships and boats. At a later period, men used the wind to drive water pumps and grain mill. The earliest documented windmill design can be dated back to 200 B.C. During this period, the Persians utilized windmills sole for grinding grains. The windmills were designed to be driven by drag forces, and they had vertical orientation. Woods or bundles of reeds were the preferable materials to use for the sails. The sails were connected to horizontal struts used as the main shaft, and a vertical shaft was attached to the grinding stone. The sails' size was determined by the type of materials used for its fabrication; usually, 5 m long and was mounted in a 9 m tall tower [17].

In Europe, windmills appeared around the 10th or 11th century [19]. The European windmills were designed to be driven by lift forces, and their axis of rotation was horizontal. They were used in almost all activities that required mechanical power that included grinding grain, water pumping, sawing wood, and powering tools [18]. The tail of the machine was manually adjusted to align the rotor with the inflowing wind. When the wind speed was high, the machine had to be turned away from the wind or the canvas had to be removed from the rotor to protect the windmill. [17].

Just before the Industrial Revolution, wind energy was the primary source of power. During the Industrial Revolution, due to the fact that wind energy is non-dispatchable and non-transportable, they started losing ground to thermal energy.

In 1890, the first machine designed solely to generate electricity using wind energy was constructed in Denmark. This machine gave origin to the modern wind turbine. This machine was used to provide electricity in rural locations. During this time, in Cleveland (Ohio), a 17 m rotor wind turbine electric generator was built. The turbine produced a rated power of 12 kW and operated for 20 years [17].

The oil crisis of 1972 ignited the new era of the excitement of developing wind turbine for electricity production. Initially, the wind turbine was small, in order of a few hundred kilo Watts up until 1992, but the size and the capacity of the turbine increased as advances in technology were made. By the end of the year 2002, we had a growth of 1000% in turbine size [20]. At present, the largest turbine is 164-meter in blades diameter and 10 MW rated power [1].

2.3 Turbine Blade

2.3.1 Blade Aerodynamic Model

The process of developing the aeroelastic model of a wind turbine usually makes use of one of the four models available, namely: the Blade Element Momentum (BEM), Computational Fluid Dynamics (CFD) model, vortex model, and actuator type model [21].

The BEM

The BEM theory treats the blades as elements that do not interact with each other aerodynamically, this is called blade element theory. Each of them has their aerodynamics properties (airfoils). Combining the blade element theory with momentum theory gives the blade element momentum (BEM) which allows the calculation of the aerodynamics performance parameters of the turbine blades [22, 21].

The original BEM theory has several limitations that are overcome by using empirical correction taken from wind turbine experiences or helicopter applications [21].

The following are the main limitations of the BEM theory:

- **Tip loss**– the difference of pressure between the lower and upper surface resulting in the air flowing around the blade's tip, which causes the lift to be reduced, and consequently, power is lost [18]. The Prandtl correction model is usually used to account for tip loss. Xu [23] corrected the Prandtl model, which allowed them to obtain results that agree with experimental data [24, 23, 21].

- **Turbulent wake state** – The BEM is invalid when the axial induction factor (see the definition of axial induction factor in Section 3.1.1) becomes greater than 0.4. Several correction models ware developed [21]. Such as the Glauert model [25], Buhl model [26], Burton model [27], AeroDyn model [28], Spera model [29], and GH-Bladed model [30].

- **Dynamic Inflow** – It is how the flow field responds to any wind turbulence and/or changes in the rotor operating conditions. if the inflow varies before the system reaches equilibrium a new position, there is a time delay which depends on the wind speed and the rotor diameter [21]. To account for this limitation Øye model [31], the Pitt-Peters model [32], or Henriksen model [33], is used.

- **Dynamic stall** – is considered to be the rapid aerodynamic changes that cause stall delay or occur suddenly. Various models have been developed to account for the dynamic stall. Here is a list of them: Beddoes-Leishman model [34], Snel model [35], ONERA model [33], Boeing-Vertol model [36], Øye model [31], and Risø model [37]. Even though all the models show a close correlation with the experimental data, none of them offers an outstanding result in all aspect than the others [21].

- **Stall delay** – Stall delay happens due to blade rotation. For stall delay models, see [38, 21, 39]

- **Radial flow** – Radial flow is the flow through the axis of the blade, see [40] for corrections model.

- **Skewed wake** – Skewed wake occurs when the incoming wind forms an angle with a rotation rotor axis. For the correction model, see [41].

In the current study, for simplicity and ease for computation only the first two correction models will be considered in the preliminary design, in later chapters, CFD studies will be done to refine the model. BEM needs very little computation time compared to other models. If reliable aerodynamic data for airfoil is available, BEM provides accurate results [21].

Vortex Model

Vortex wake methods determine the arrangement of vorticity in the wake region to calculate the resultant velocity field [18]. The vortex model calculates the wake by utilizing either the free-wake method or the pre-described wake method. The pre-described wake method describes the wake coming from the blades by semi-empirical formulation and assumes that it behaves as a rigid body [21]. The Free-wake model is used to model unsteady flow. For more information on free-wake applied in wind turbines, see [42, 43, 44, 45].

The vortex model has little application in wind turbine modelling because it demands higher computational capacity than the BEM model, and it often diverges due to the complexity of the developing wake. [21].

Actuator Type Model

The actuator type model is probably the first model utilized to study rotor performance. It treats the turbine blade as a disc, line, or surface with diffused loads on the disc, line, or surface [21]. Generally, the actuator disc model is numerically coupled with Navier-Stokes or Euler equation [21]. For more information in the actuator type model see [46, 47, 48].

When the actuator disc is combined with Navier-Stokes equations, it needs more computational sources than the BEM model because Navier-Stokes equations need to be solved. The actuator type model assumes that the blades' loads are calculated from the blade element theory and tables of airfoil aerodynamic parameters. However, this method does not offer any advantage of accurately forecasting the aerodynamic loads than the BEM model [21].

Computational Fluid Dynamics Model

Computational Fluid Dynamics (CFD) has been substantially used in the wind turbine industry for it offers accurate results, and it gives good flow visualization. CFD consists of solving the governing equations numerically by using mathematics techniques. The governing equations for the wind turbine are Navier-Stokes equations coupled with energy and continuity equations.

The flow in the wind turbine is considered to be incompressible. To model a wind turbine using CFD, a 3D CAD model must be created, using one of the many available CAD modeling software. The CAD model is discretized (meshed) to solve the governing equations at a set of predefined points using a mathematical algorithm that changes the governing equations from a differential form into algebraic equations. When the results are calculated,

any flow parameter values are found throughout the flow domain by interpolating the results from the predefined points. After running the calculations, the results are post-processed to analyze parameters or visualize the flow.

Typically, meshing is classified into three categories: Structured, unstructured, and a combination of them also called hybrid. structured mesh offers the advantage of high resolution, low memory required, and, quickness of convergence. The unstructured mesh usually generates more cell numbers than the structured mesh. This fact increases the computational time needed to converge to a solution when the unstructured mesh is used in CFD. The hybrid meshing, sometimes called adaptive mesh, combines the two meshes types. This mesh gives the flexibility of using unstructured mesh in portion with complex shape and structured mesh whenever it is appropriate. This mesh has been vastly used in the wind turbine CFD modelling [21].

The discretization of the governing equations used in CFD is done using one of the three methods are commonly used: finite volume method (FVM), finite-element method (FEM), and finite-difference method (FDM). Most CFD model uses FVM because it has the advantage of using less space; therefore, it requires less memory and less processing time. FEM can also be used in CFD modeling, but it is frequently used in structural analysis. FEM is much more stable than FVM, but it takes more time to compute the results, as it requires more computational space memory than FVM. FDM is more straightforward to implement than all three methods mentioned, but it is only used in simple applications [49, 21].

It is necessary to develop turbulence models to use the Navier-Stokes equation to solve wind turbine problems. Models such as ω - k SST model ϵ - k model [50, 21], and Spalart-Allmaras model [51, 21] based on Reynold Averaged Navier-Stokes turbulence model has been adopted for wind turbine applications [21]. when modelling two-dimensional airfoils and three-dimensional blades in CFD the omega-k SST model is preferred among the other methods [21]. For more information see [52, 53, 54].

2.3.2 Blade Structure Model

To fully develop an elastoplastic model for a wind turbine blade, the structural blade's response needs to be known. There are two models used to describe the blade's structural response: the three-dimensional finite element method (3D FEM) model, and the one-dimensional equivalent beam model [21].

The 3D FEM model, when used with the commercial FEA, is very laborious and time-consuming. However, it gives accurate results when coupled with CFD; therefore, it has been used to generate the aeroelastic model for wind turbine blades [21].

A typical wind turbine blade has one dimension, which is much larger than the other two; therefore, it can be modeled as a one-directional beam with a span along the longest dimension and a cross-sectional area perpendicular to it. Therefore, beam model theory can be used to analyze wind blade structure response. There are two categories of beam theory:

linear and nonlinear. The Euler-Bernoulli beam model and the Timoshenko beam model are the two dominant model used in beam theory. When these models are applied to wind turbine blades, they show very close results. Euler-Bernoulli model is more comfortable to implement; therefore, it is more frequently employed in the wind turbine blades' structural modeling. When a nonlinear wind turbine blade model is needed, The Nonlinear Aeroelastic Model for Wind Turbine Blades (NAM_WTB) is used, for it shows an excellent approximation with experimental results.

Modal approach, multi-body dynamics (MBD), and one-dimensional finite element method (FEM) are used to discretize wind turbine blades. Recent developers have used the one-dimensional FEM to generate their aeroelastic wind turbine blades models [21]. See also [55].

2.3.3 Blade Cross-sectional Analysis Model

The cross-sectional properties of wind turbine blades can be obtained using one of the three models: classical lamination theory (CLT)-based model, two-dimensional FEM-based model, and 3D FEM-based model. Each of the models has its limitations [21].

Classical lamination theory (CLT) is efficient and reasonably accurate. It has been widely used to analyze the structural response of composite material. Among the three models used to determine the cross-section of the blade, CLT is more efficient. However, it does not consider the shear deformation when calculating the cross-sectional properties, making it unsuitable to use in short and thick blades [21].

The two-dimensional FEM-based model converts the 3D blade model into a two-dimensional model by using a pre-processor. The two-dimensional FEM-based model requires less computational power than the 3D FEM-based model. However, the fact that they need a pre-processor made them less efficient.

The 3D model-based model is the most complex among the three. It offers accurate stress analysis and displacement; however, they do not undeviatingly generate the cross-sectional property of wind turbine blades [21].

The most widely used aeroelastic models within the wind turbine industry and organization are STALLVIB, ADAMS/WT FAST, FLEX5, GAST, GH-Bladed, HAWC2, and PHATAS [21].

2.3.4 Wind Turbine Blade Material

In early stages of the evolution of wind turbines, the blades were made from wood, sometimes folded with a cloth. Later on (around the 1950s or so), metals (especially steel) were adopted as turbine blades' material. Since the 1970s until today, most horizontal axis wind turbine blades have been made from composite materials. Fiberglass in a polyester resin is the most commonly used blade material, but vinyl ester and wood epoxy laminates have also

been use [18].

When looking for materials to design a wind turbine's blades, it is desired that the material should have high stiffness, high strength to weight ratio, and long life cycles. Additionally, the material should also be widely available and inexpensive, and the manufacturing processes involved should be relatively cheap. Wood, metals, plastics, and composite materials have been used in the wind turbine blade design.

Wood

Wood is very compelling to be used as wind turbine blade material because they are environmentally friendly. They have a relatively high strength to weight ratio. If they are adequately aligned, they also have good fatigue strength. However, wood is not abundantly available with a homogeneous quality, and they are susceptible to moisture. The process of turning wood into a complex blade shape can be costly. Therefore, in wind turbine design, wood is only used for small applications where the blade diameter does not exceed 2.5 m [18, 56].

Metals

Steel is vastly used in many engineering applications. In the past, it was used as a wind turbine blade material to replace wood. Steel has a high density. This fact was used to stabilize the turbine's output power because as the weight of the blade increases, so does the mass moment of inertia; steel is also relatively cheaper. However, due to their low strength to weight ratio, poor machinability, and low fatigue strength, steel is no longer used as wind turbine blade material [18].

Aluminum is the most abundant metal in the Earth. It is much lighter than steel, and it also has greater strength to weight ratio than steel, and it is relatively cheap. However, aluminum has a lower fatigue strength than steel. Currently, in wind turbine design, aluminum is used in the testing situation, and in small wind turbines were the cross-sectional area of the blade is uniform [18].

Composite Materials

Composite materials are the most widely used materials for wind turbine blades. They have good fatigue strength, high strength, and high stiffness to weight ratio, good corrosion, and environmental degradation resistance. They are also easy to form into complex shapes using various processes. The composite material is obtained by mixing two different materials (mostly fibers) held together by a binder matrix. The material used for composites are fiberglass, carbon fibers, and wood. They are bound by polyester, epoxy, or vinyl ester. The most used composite material for wind turbine blades is fiberglass reinforced plastic.

Fiberglass

In wind turbine applications, E-glass and S-glass are the most widely used type of fibreglass. The tensile strength of the S-glass is 25-30% higher than the E-glass, but E-glass is about twice cheaper than S-glass. Tows, also so known as unidirectional bundles of fibres, are used when high strength is required [18].

Binder

Epoxies have the advantage of been having good chemical resistance, low shrinkage upon curing, and excellent adhesion. They are also more vigorous. However, they are about 1.5 times more expensive than polyesters, and polyester has a better cure time than them. Vinyl esters are similar to epoxies-based resin, but they are cheaper and have a better cure time. They are also environmentally more stable [18].

Carbon Fiber

Carbon fiber is stronger than fiberglass, but they are substantially more expensive than fiberglass (approximately eight times more)[18]. In wind turbine blade design, carbon fiber is not used to replace fiberglass; instead, they are used with fiberglass to strengthen the materials in the blade's specific location where it is needed [18].

Laminated Wood

Wood has an excellent strength to weight ratio and has good fatigue strength. In some applications, wood is preferred rather than synthetic fibers for composite material. Douglas Fir is the most common wood used in wind turbine applications. [18]. Wood-epoxy laminates have good fatigue characteristics. Turbine blades made of wood epoxy have never failed in service due to fatigue. [18].

2.3.5 Blade Manufacturing Process

Many processes can be used to manufacture wind turbine blades. The process to be used depend on blade's material, size, and shape; the economic constraints also play an essential role.

Wood Technology

When timber is the material of choice for the turbine's blade, the process used is computer numerically controlled (CNC) router, copying machine, or hand carving. Although CNC can be very accurate and durable routers, they are expensive to be used as a turbine blade manufacturing process, even if the blades are small. Copying machines are more inexpensive compared to CNCs but to adapt a commercial unit designed explicitly for gun stocks and other related items to blade manufacturing was found inappropriate especially for blades that have a tip chord of about 5 cm. Hand carving offers a cheaper solution but generates blades with poor performance [56].

Hand-lay-up

Hand-lay-up is a process whereby fibers or other reinforce clothes are lay on the mold by hand and infused with resin. The resin is pressured into the fibre by squeegees or rollers. This process is simple, but it is labor-intensive. The quality of the product depends on the worker; therefore, it is difficult to obtain good product quality consistently. Another drawback of this process is that it releases fume into the room; therefore the workers are susceptible to inhaling it [18].

Pre-preg

In the pre-preg process, the impregnated fiberglass is placed on the mold, and then heat is applied to allow the resin to flow and harden the material. The heating process is carried out in an autoclave or a low-temperature oven. With this method, it is possible to achieve resin to fiber consistency, and good results can be easily attained. However, the cost of the material can be higher [18].

Resin infusion

In resign infusion, the dry reinforcing material is laid into the mold, and then resin is forced into the material by a carefully arranged mechanism. In one type of infusion process, namely vacuum-assisted resin transfer molding (VARTM), the air is removed from one side of the mold by a vacuum pump. A vacuum bag is placed over the mold to create a vacuum. The vacuum bag allows the resin to flow from an external reservoir to the mold. The external reservoir is opened to the atmosphere. Compared to the hand-lay-up process, resin infusion has a superior final quality product, and it does not release fume in the room [18].

Pultrusion

Pultrusion is a manufacturing process in which the material is forced through a die to form an object of a predefined cross-sectional area. Pultrusion is very appealing if mass production of uniform cross-sectional area is required [18].

Filament Winding

Filament winding consists of winding the fiberglass around a mandrel while the resin is placed simultaneously. This method is used in the aerospace industry and is also popular in wind turbines. Filament winding cannot be applied to the concave surface [57, 56].

2.4 Tower

In a wind turbine system, the tower is the component that allows the nacelle and rotor to be mounted in the desired height and carries all the component loads to the foundation. For a turbine to operate appropriately, the tower should be structurally strong and relatively stiff, and vibration should also be considered. The main towers used in modern turbines are lattice towers, tubular steel towers, and guyed towers [18].

For the same height, Lattice towers consume less material than a tubular tower (about half of the material). Therefore, they need a lighter foundation [18]. Lattice towers have many problems; the major ones are aesthetics, intense avian activities, and not maintenance-friendly.

The tubular tower allows optimum bending resistance in all directions due to their circular cross-section. These towers have pleasing aesthetics; they provide protected climbing are for maintenance, and they significantly reduce avian activities [17].

Tower with guyed steel poles can be used to support a small wind turbine. In this system, the load is shared by the tower and the guy wires, which makes it possible to design a much lighter tower than it would have been needed otherwise, therefore, less expensive. Usually, the tower is supported by four cables equally spaced and inclined at 45°, support the tower [18].

Tower height usually is not less than 20 m. For large wind turbines they should around 1 to 1.5 times the rotor diameter [17].

Throughout its life span, the wind turbine tower experiences two significant types of wind load: steady and dynamic. When designing a wind turbine tower, at least two load conditions must be considered: at stationary the survival wind speed and the operation at the rated power. For survival wind speed, International Electrotechnical Commission (IEC) standards recommend that the 50-year extreme wind speed be used [18].

The rotor can induce vibration to the tower. Therefore, the tower's stiffness must be careful analysis as it determines the dynamic system response to the rotor excitation. The tower's natural frequency should not coincide with the rotor frequency or the blade-passing frequency [18].

The structural analysis of a wind turbine tower can be done using the classical theory of beams or the Finite Element Method (FEM). Wind turbine towers are generally made out of steel coated for corrosion resistance. Sometimes concrete is used as well.

2.5 Hub

In a wind turbine, the hub has the function of connecting the blades to the main shaft. They carry and transmit all the loads induced by the blades. Hubs usually are made out of steel, either cast or welded. There are three types of hubs: rigid hubs, teetering hubs, and hubs for hinged blades [18].

When no other relative movement between the hub and the main shaft is allowed except the blade's pitching, the hub is said to be rigid. Rigid blades are used when the turbine has three or more blades. There is a relative motion between the parts connecting the blades

and those connecting to the main shaft in Teetering hubs. In this mechanism, the blades move flapwise, alternatively. The two and one bladed wind turbine usually use teetering hubs. Presently no commercial wind turbine uses a teetering hub [18].

2.6 Nacelle

The nacelle is where all turbine components reside. It grants protection to the components which are sensitive to environmental conditions. It is where the generator, gearbox, drive train, control systems are mounted. The nacelle is composed of two components: the mainframe and the nacelle cover.

The mainframe serves as a rigidity provider to allow the components to be aligned and not have relative motion between one another during operations; it also provides a point of attachment of the yaw bearing. The mainframe transmits loads from the rotor, generator, gearbox, tail to the tower. There are two types of frames: a separate mainframe and a gearbox mainframe. The separate mainframe is rigid steel casting or weldment provided with holes and other attachments in a proper location to allow the components to be attached to it. The gearbox mainframe is made strong to carry all the necessary load, and they are also provided with holes and other attachment places to assemble other components on it [21].

The nacelle cover protects the turbine components and the control system from rain, moisture, ice, snow, sunlight, salt, and solid particles (grains found in the air). When needed, the nacelle cover can be equipped with materials that help to reduce noise. The nacelle is designed in a way that allows air to circulate through the components. This design approach facilitates the cooling of the components where needed. Fiberglass usually is used as the material for nacelle cover due to its high strength-to-weight ratio. On small and medium-sized turbines, the nacelle house is usually designed so that the components can be readily accessed when it is opened [18].

2.7 Drive Train

The main machine components used in a wind turbine are shaft, bearings, coupling, brakes, gearboxes, clutches, dumper, springs, fastening and joining, and wire rope. These elements are commercially available, and they have been designed according to engineering standards available.

There are many works of literature available that deal with the design of those elements. Any machine design textbook gives a lot of information about the design of machine elements. Each element components, as applied to the design of wind turbines, are briefly discussed below

2.7.1 Main Shaft

In a wind turbine, the main shaft is used to transmit rotational power from the generator's blades. The main shaft is subjected to a torsional load as well as a bending moment. The loads usually are time-varying, which makes it necessary to design the shaft for the fatigue aspect. The shaft should not operate close to its natural resonant frequencies at critical speeds to avoid high vibrations. The main shaft carries the rotor blade loads, and they are supported by bearings, which takes the load from the shaft to the mainframe. In a small wind turbine, the shaft is attached to the hub by using keys. Other methods used to attach the shaft in the hub is called Ringfeder Shrink Disc and a permanent flange attached to one end of the shaft, and the flange is connected to the hub by bolts [18].

The conditions under which the main shaft operates determine the type of material to be used. Hot-rolled plain carbon steel is typically used when the operating conditions are less severe. If the application requires greater strength, usually, the carbon content in steel is increased to strengthen it. For severe operating conditions, alloy steel is used. Usually, the shaft is heat-treated to increase its yield strength and hardness after being machined [18].

2.7.2 Bearing

Bearings are used to allow relative motion, usually rotational motion, between surfaces. In a wind turbine, bearings are used in the main shaft, in gearboxes, in the yaw mechanism, in the pitch control, generator, and some teetering systems. Ball bearings are the most used ones in wind turbine design. They are generally made out of steel. In wind turbine gearboxes, roller bearings are also used. In designing the bearing, the critical parameters to consider are the load that they will be subjected to, and the number of cycles they are expected to have [18].

2.7.3 Coupling

Couplings are mechanical elements that connect two shafts to transmit torque. In a wind turbine, the coupling is used to connect the gearbox or the main shaft to the generator. They consist of two pieces connected by bolts (reliable coupling); usually the pieces are prevented from rotating against the shafts by using a key [18].

2.7.4 Gear

In wind turbines, gears are elements used to transmit energy from the rotor to the generator at a different rotational speed from that of the rotor. The gear used in wind turbines is made out of steel with high strength and surface hardness obtained through heat treatment. Wind turbines need to use a gearbox because the blades of a wind turbine rotate at a slow speed as compared to most of the electrical generator (60 or 50 Hz). The load conditions encountered in wind turbines are very different from other applications, making the gears used in wind turbines different from other applications. Under-designed gearboxes are reported to be the

cause of many wind turbine operational problems. The gearbox is one of the most massive and most expensive components in wind turbine design [18].

2.7.5 Clutches

Clutches are components used to transmit torque to a portion of a system when engaged and to isolate the portion of the system from torque when disengaged. In wind turbine, clutches are used in clutch-type brakes and in pitch linkage. Clutches are engaged by springs, and disengaged by a mechanical or electromechanical system [57].

2.7.6 Brakes

Aerodynamic and mechanical brakes are the two types of brakes usually used in a wind turbine. The aerodynamic brakes are controlled surfaces, mounted in the blade, that regulate stall. The aerodynamic brakes, can spoilers, tip brakes, or flaps. The aerodynamic brakes are controlled by electromagnets that allow the surfaces to go in and out of the blade when needed. The mechanical brakes are used to stop the turbine, for service purposes, such as parking brakes and as a backup system for aerodynamic brakes. They are also used as part of the yaw and/or pitch control systems. Disc and clutch brakes are the two most utilized mechanical brakes in wind turbines. A hydraulic system controls disc brakes, whereas spring and pneumatic or hydraulic systems control clutch brakes.

In the wind turbine, brakes can be installed anywhere along the drive train. When the brakes are installed on the low rotation side, the brakes will have to generate higher torque than it would have generated if installed in the high rotation side. Therefore the brake system will have to be design heavier and consume more power. On the other hand, if the brakes are installed on the high rotation side, it will cause wear on the gearbox, and in case of gearbox failure, the brake might not be able to stop the rotor.

2.7.7 Springs

In a wind turbine, springs are used in passively actuated safety systems such as brakes, blade pitch linkage, aerodynamic surface, teeter damper, and rubber damper [57]. Springs are usually designed for tension, compression, or torsion applications. The most widely used springs are made of steel wires shaped into a spiral coil [57].

2.7.8 Dampers

Wind turbines use dampers to mitigate the adverse effects of dynamic loads. There are three main types of devices used as a damper in wind turbines: fluid couplings, linear viscous fluid and hydraulic pumping circuits. Fluid couplings are used to reduce torque fluctuations. one- or two-bladed rotors uses linear viscous fluid dampers as a teetering damper. Hydraulic pumping circuits are applied when the damping of yaw motion is needed [18].

2.8 Fastening and Joining

Fasteners are used to join parts together in such a way that they can be easily undone whenever it is necessary. The primary fasteners used are bolts and screws. The main issue to be accounted for in designing the fastener is fatigue, which can be reduced if the bolts are pre-stressed. In a wind turbine, bolts and screws tend to be loosened due to vibrations and shocks that the turbines are subjected to. One of the following methods is used to solve this problem: washers, locknuts, lock wire, and chemical locking agents. In wind turbines design, parts are also joined in a way that is not easily disassembled, such as welding, riveting, soldering, or bonding with adhesives [18].

2.9 Wire Rope

In a wind turbine, meteorological masts or guyed wind turbine towers usually use wire rope to put the tower in equilibrium. The wire ropes are also used when the turbine is being erected. The primary factor to consider when designing a wire rope is the tensile strength. Fatigue also plays a substantial role. When hoisting is being carried out, sheaves or pulleys often prevent the wire rope from changing direction abruptly. The sheave has to have a diameter that is at least 20 to 40 times greater than the wire rope's diameter [57].

2.10 Generator

The most commonly used generator in wind turbines are synchronous, induction (asynchronous) generators, DC generators, and permanent magnet synchronous generator (PMSG) for small applications. In some applications, direct-drive generators are also considered [18].

In a wind turbine, synchronous generators are occasionally used on large grid-connected turbines or power electronic converters in variable-speed wind turbines.

Some stand-alone wind turbines use permanent magnet synchronous generators. The output power is usually converted into DC before it is delivered to the intended use [18].

Most of the time, wind turbines use an induction generator. They have the advantage of been simple, robust, inexpensive, and can easily be connected and disconnected to the grid [18]. DC generators were the commonly used generators in smaller, battery-charging wind turbines. However, due to high cost and maintenance, DC generators are seldom used today in wind turbine applications [18].

In small wind turbine applications with power up to at least 10kW, permanent magnet generators are preferred. Permanent magnet generators are also used in large wind turbine applications. The generator is designed to have a stationary armature where the power is taken from. Consequently, the use of commutators, brushes, or slip rings are not required. Because the machine's construction is so simple, the permanent magnet generator is quite rugged [18].

Permanent magnet generators are also known as permanent magnet synchronous generator (PMSG). Their operating principle is similar to the synchronous generator, with the main difference being the magnet field production. The synchronous generator uses an electromagnet while PGSM uses a permanent magnet. Direct drive generators are a unique design of a synchronous generator. These generators are designed to have enough number of poles that allow the wind turbine rotor to be connected directly to the generator without requiring a gearbox. However, the high number of poles forces the generator diameter to be relatively large [18].

2.11 Turbine Control System

A control system is needed in wind turbine applications to maximize power production, ensure the turbine's safe operation, minimize operation costs, and reduce induced loads. The control of a wind turbine consists of orienting the turbine to the wind, protected the turbine against over-speed, and monitoring the quality of the electricity produced to the end-user. There are two control levels to be considered in wind turbines: supervisory control level and dynamics control level.

The turbine operation, as well as the sequence of control action, are monitored and managed by the supervisory control. The response of the turbine to environmental changes that can affect its performance or integrity is managed by dynamic control [18].

The task of the supervisory control includes: monitoring for safe operation, gathering information and reporting them, monitoring for operation, managing turbine operation and actuating safety and emergency systems [18].

In wind turbines that use constant speed generator, the torque can only be controlled by changing the aerodynamics torque. For variable speed generator turbines, the torque control can be done by changing the generator torque and/or changing the aerodynamic torque.

The aerodynamics torque is controlled through pitch control, changing the blade surface using ailerons, flaps, spoilers, and pitchable tips. More information about the wind turbine's control system is found in references [18, 58].

2.12 Small Wind Turbine

Since the 1970s, small wind turbines have improved considerably. However, reliability and turbine noise is still a concern in this technology. Therefore, further studies are needed to make the operation of small wind turbine reliable and to reduce the noise into acceptable levels [18].

Several small wind turbines (SWTs) are not economically feasible, and government incentives play a vital role in the profitability of SWTs. Sleiti and Mehrabian [59] proposed a

model based on turbine *Air* X but changing the rotor design, yaw system, nacelle, generator, and the tower. It was found that this model would save approximately $137 per year for an average household. For small wind turbines, design, simplicity, and reliability, rather than cutting edge technology, are more cost-effective [60]. Simic [61] reported a turbine that cost as low as 1000 $/kW.

de Freitas et al. [62] demonstrated that to optimize a turbine aerodynamically blades, the drag to lift ratio has to be as low as possible. Shen [63] considered the optimization of small wind turbine blades with 3D blade geometries for multiple objectives.

The most widely used airfoils for small wind turbines are: FX 63-137, S822, S834, SD2030, SG6043, and SH3055; the corresponding thin versions airfoils have a greater lift to drag ratio and reduce noise [64].

Bassyouni et al. [65] provided a method to select materials for the design of wind turbine blades. The blade's mechanical properties made of fiberglass can be predicted through a numerical model [66].

Pourrajabian et al. [67] created a model to show that to reduce the starting time at low speed and yet maintain the efficiency, the moment of inertia should be decreased by making the blade hollow [67].

Most small wind turbines are installed on steel monopole towers, often difficult to transport to a remote location. Adhikari et al. [68] demonstrated that bamboo is a feasible material for a 12 m 500 W turbine. Clifton and Wood [69] reported that a monopole tower's manufacturing cost could be 30-40% of the installation cost. They presented numerical optimization procedures for self-support octal monopole tower. Wood [70] studied the height that maximizes the ratio of average power output to the turbine's total capital cost.

The control of a small wind turbine consists of: orienting the turbine into the direction of the wind, protect the turbine against over-speed; control the power from generator to the intended application [71]. Small wind turbines mostly use furling for power and over-speed control. Audierne et al. [72] presented a consistent model of gravity-controlled furling systems' dynamics based on Lagrangian formalism [72, 18].

Small wind turbine frequently uses permanent magnets to produce the generator's excitation field. Latoufis et al. [73] described the basic theoretical concepts and construction methods of coreless axial flux permanent magnet generators for low-cost rural electrification [73]. For more information on the control and electrical part of wind turbines, see [74, 75, 76, 58].

Chapter 3

Blade Aerodynamic Design

In Chapter 3 the aerodynamic design of the turbine blade is presented. Three methods are used to aerodynamically design the blades. The blade element momentum method is discussed first in Section 3.3 and the blade is designed preliminarily based on the BEM method in Section 3.2 and Qblade is used to verify the results. Section 3.3 the Computational Fluid Dynamics analysis is done and the results are compared to those from BEM calculations and Qblade. Section 3.4 presents the conclusion of the blades' aerodynamic design.

3.1 Aerodynamic Theory of HAWT Blade

The power that a wind turbine extracts from wind depends on the rotor blades' interaction with the inflow wind. The stochastic wind speed can be converted into a mean speed which allows determining aerodynamic forces; consequently, the mean power and aerodynamic load of the wind turbine can also be known. The fatigue loads are caused by irregular aerodynamic forces induced by wind shear, rotation of the blades, misalignment between the rotor axis and inflow wind, and randomly fluctuating loads induced by dynamic effects and turbulence [18]. The steady-state operation of the wind turbine helps to understand all the factors mentioned above. In this chapter, the steady-state aerodynamic performance of a wind turbine blade will be discussed.

3.1.1 One-dimensional Momentum Theory

One-dimensional momentum theory assumes a control volume formed by stream tubes whose boundaries are the stream tube cross-sections and the stream tube's surface. It assumes that the only flow occurs in the axial direction, which is across the stream tube's ends. This theory assumes:

- homogeneous, incompressible, steady-state fluid flow
- no drag force due to friction;
- constant thrust throughout the rotor area or the disc;
- an infinite number of blades;

- no wake induced by the rotor;
- the upstream and downstream pressure far from the rotor is precisely equal to the ambient pressure.

Using the conservation of the linear moment and the control volume of Figure 3.1, the force that the wind applies to the actuator disk can be determined as follow:

$$T = \dot{m}\,(U_1 - U_2) \tag{3.1}$$

$$\dot{m} = \rho A U_2 \tag{3.2}$$

Combining Eqs. (3.1) and (3.2) gives

$$T = \rho A U_2\,(U_1 - U_2) \tag{3.3}$$

In Figure 3.1, if Bernoulli's equation is applied from 1 to 2 we have,

$$p_1 + \rho U_1^2/2 = p_2 + \rho U_2^2/2 \tag{3.4}$$

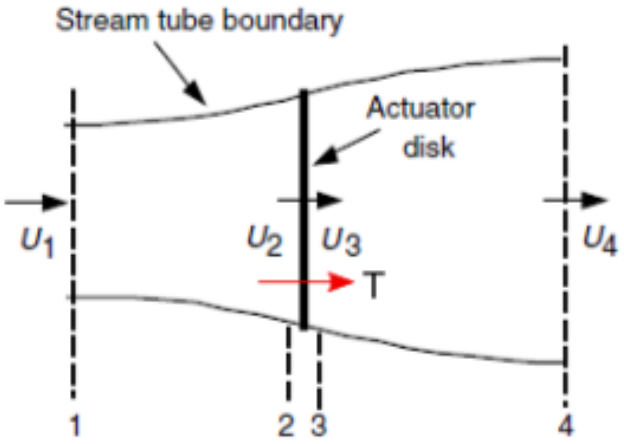

Figure 3.1: Actuator disc model [18]

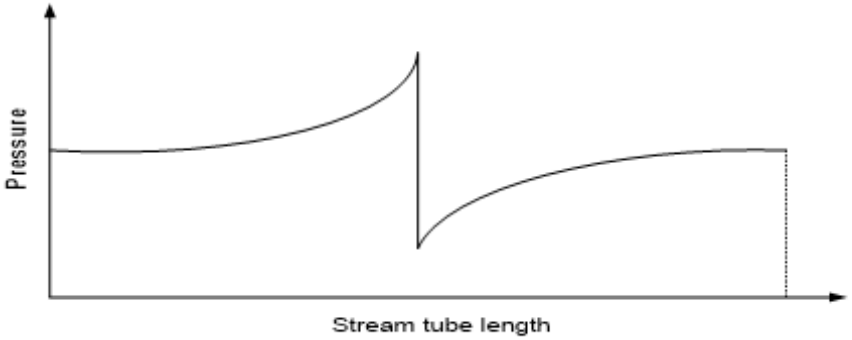

Figure 3.2: Pressure distribution

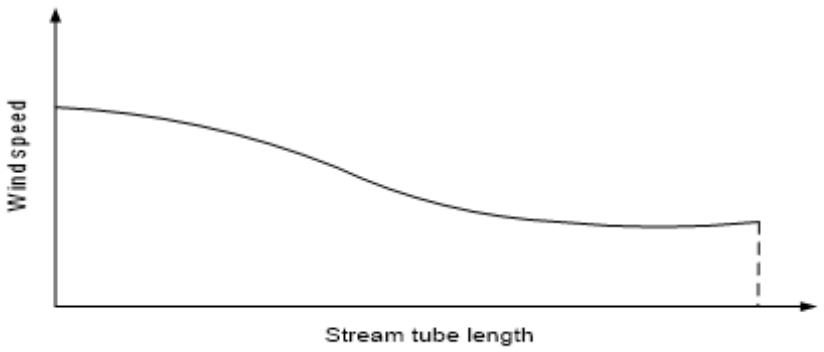

Figure 3.3: Velocity distribution

Applying Bernoulli's equation from 3 to 4 the gives,

$$p_3 + \rho U_3^2/2 = p_4 + \rho U_4^2/2 \tag{3.5}$$

But

$$U_2 = U_3 \tag{3.6}$$
$$p_1 = p_4 \tag{3.7}$$

Combining Eqs. (3.4) through (3.7) we have,

$$p_2 - p_3 = \rho U_1^2/2 - \rho U_4^2/2 \tag{3.8}$$

The thrust can also be found by the pressure gradient across the actuator disk as follow:

$$T = (p_2 - p_3)A \tag{3.9}$$

Substituting Eq. (3.8) into (3.9) gives,

$$T = (U_1^2/2 - U_4^2/2)\rho A \tag{3.10}$$

Combining Eq. (3.3) with (3.10) gives:

$$U_2 = \frac{U_1 + U_4}{2} \tag{3.11}$$

The presence of the actuator disc in the stream tube induces a velocity variation that interacts with the free-stream velocity. To account for this effect, we introduce a term called axial induction factor defined as the ratio of the difference of the free-stream speed and the speed in the rotor speed to the free-stream speed; that is [27].

$$a = \frac{U_1 + U_4}{U_1} \tag{3.12}$$

Therefore,

$$U_2 = U_1(1 - a) \tag{3.13}$$

and

$$U_4 = U_1(1 - 2a) \tag{3.14}$$

The power output can be found using the following formula:

$$P = TU_2 \tag{3.15}$$

Substituting Eqs. (3.10), (3.13) and (3.14) into (3.15) we have,

$$P = 0.5\rho AU^3 4a(1 - a)^2 \tag{3.16}$$

Where: U replaces U_1.

Usually, the power output is characterized by a non-dimensional quantity called power coefficient C_P, defined as the ratio of the rotor's power output to the power of the wind that passes through the area equal to the actuator disc removed from the stream tube.

$$C_P = \frac{P}{0.5\rho U^3 A} \tag{3.17}$$

Substituting Eq. (3.16) into (3.17) we get,

$$C_P = 4a(1 - a)^2 \tag{3.18}$$

The thrust is also represented by a non-dimensional quantity called thrust coefficient C_T. It is defined as a ratio of the actuator disc thrust to the thrust that would have been obtained if the free speed was brought to rest with no losses of energy. Therefore,

$$C_T = \frac{T}{\rho AU^2} \tag{3.19}$$

But,

$$T = 0.5\rho AU^2 4a(1 - a) \tag{3.20}$$

Consequently,

$$C_T = 4a(1 - a) \tag{3.21}$$

If Eq. (3.18) is differentiated with respect to a and equated to zero; we get the maximum value of the power coefficient. This value is, $a = 1/3$; which yields, $CP = 16/27$. This value is known as Betz Limit and is the maximum efficiency that a wind turbine can attain. In reality, three factors make it impossible to attain the Betz Limit, these factors are

- the losses of speed due to the formation of the wake region behind the rotor;
- a finite number of blades and their correspondent tip losses;
- losses associated with the aerodynamic drag [18].

3.1.2 Wind Turbine Model with Wake Rotation

Wind turbine blades are designed so that when the air flows through the rotor it generates a torque, and this torque generates electrical power through an electrical generator. The rotor also generates a torque into the inflowing air of equal magnitude and in the opposite direction. This torque causes the air to gain angular momentum. It signifies that in the wake region, the air particles velocity has two components one in the tangential and the other in the axial direction [27]. See Figure 3.4.

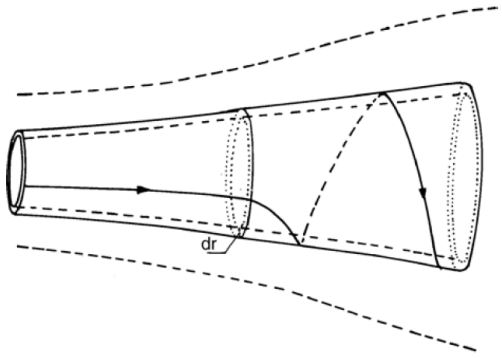

Figure 3.4: Stream tube model for wake region [18]

The flow entering the actuator disc does not have any rotation [27]. The flow coming from the disc has some rotation, and this rotation is constant throughout the wake region. The air gains the rotational velocity entirely because of the presence of the disc in the stream tube [27].

The rotational kinetic energy in the wake region constitute a loss of energy; that is, the rotor extracts less energy than it would have if the rotation were not present [27]. This is because some energy is needed to generate the whirl velocity.

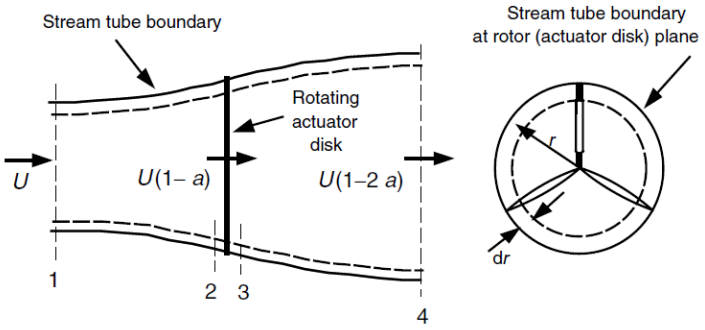

Figure 3.5: Geometry for rotor analysis [18]

Let ω be the induced air angular velocity and Ω the rotor angular velocity. The increase of the angular velocity of the air relative to the blade is given ω, that is, it goes from Ω to $\omega+\Omega$.

Considering a strip of the actuator disc of radius r and thickness dr gives an infinitely small area of,

$$dA = 2\pi r dr \tag{3.22}$$

Let's choose a control volume attached to the blade which also rotates with it, the energy equation before and after the blades can be used to calculate the pressure difference across the blades [18], as shown below.

$$p_2 - p_3 = \rho(\Omega + \omega/2)\omega r^2 \tag{3.23}$$

The thrust on the annular element is:

$$dT = (p_2 - p_3)dA = \rho(\Omega + \omega/2)(2\pi r dr)\omega r^2 \tag{3.24}$$

The angular induction factor is defined as:

$$a^{'} = \frac{\omega}{2\Omega} \tag{3.25}$$

Therefore,

$$dT = 4a^{'}(1 + a^{'})\rho\Omega^2 r^2 \pi r dr \tag{3.26}$$

From Eq. (3.10) we can write:

$$dT = 4a(1 - a)\rho U^2 \pi r dr \tag{3.27}$$

Combining Eqs. (3.26) with (3.27) gives,

$$\frac{a(1-a)}{a^{'}(1+a^{'})} = \frac{\Omega^2 r^2}{U^2} \tag{3.28}$$

The ratio of the element's tangential velocity to it axial velocity is defined as local speed ratio, expressed by,

$$\lambda_r = \frac{\Omega r}{U} \tag{3.29}$$

When the blade element is located at the tip, the local speed ratio is called tip speed ratio.

$$\lambda = \frac{\Omega R}{U} \tag{3.30}$$

Applying the conservation of angular momentum in the control volume of Figure 3.5, we have,

$$dQ = 4a^{'}(1 - a)\rho U \pi r^3 \Omega dr \tag{3.31}$$

3.1.3 Blade Element Mometum (BEM)

The Blade element theory evaluates the influence of the blade geometry on the forces at a section of the blade [18]. Combining the momentum theory with the blade element theory we have the blade element momentum (BEM) sometimes also called as the strip theory. The blade element theory assumes that

- The blade elements do not iterate aerodynamically between each other; that is, the radial component of the velocity is zero in all blade elements;
- The airfoil shape of the blade is the only property responsible for generating the lift and drag forces. [18].

From Figure 3.6 the following expressions can be obtained:

$$\theta_T = \theta_P - \theta_{P,0} \tag{3.32}$$

$$\varphi = \theta_P + \alpha \tag{3.33}$$

$$\tan\varphi = \frac{(1-a)U}{(1+a')\Omega r} = \frac{(1-a)}{(1+a')\lambda_r} \tag{3.34}$$

$$U_{rel} = \frac{U(1-a)}{\sin\varphi} \tag{3.35}$$

$$dF_L = 0.5\rho C_l U_{rel}^2 c dr \tag{3.36}$$

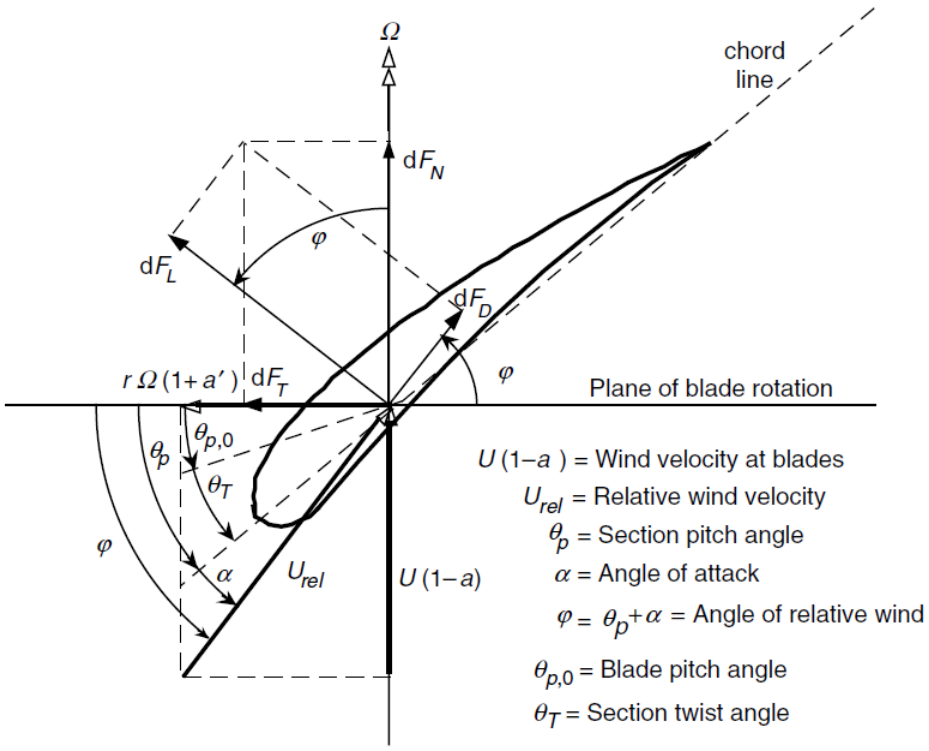

Figure 3.6: Blade geometry for analysis of a horizontal axis wind turbine [18]

$$dF_D = 0.5\rho C_d U_{rel}^2 c dr \tag{3.37}$$
$$dF_N = dF_L \cos\varphi + dF_D \sin\varphi \tag{3.38}$$
$$dF_T = dF_L \sin\varphi - dF_D \cos\varphi \tag{3.39}$$

Let the number of blades be B. The total normal and tangential force at the section of radius r becomes:

$$dF_N = 0.5(C_l \cos\varphi + C_d \sin\varphi)\rho c {U_{rel}}^2 dr \tag{3.40}$$
$$dF_T = 0.5(C_l \sin\varphi - C_d \cos\varphi)\rho c {U_{rel}}^2 dr \tag{3.41}$$
$$dQ = dF_T Br \tag{3.42}$$
$$dQ = 0.5(C_l \sin\varphi - C_d \cos\varphi)\rho c {U_{rel}}^2 Br dr \tag{3.43}$$

But, the thrust is equal to the normal force. Expressing the relative velocity as a function of the free-stream wind, and after combining Eqs. (3.35) and (3.40) we have,

$$dF_N = (C_l \cos\varphi + C_d \sin\varphi)\pi\sigma' \rho \frac{U^2(1-a)^2}{\sin^2\varphi} r dr \tag{3.44}$$

Where σ' is called solidity and is defined as,

$$\sigma' = \frac{Bc}{2\pi} \tag{3.45}$$

Combining Eqs. (3.35), (3.43) and (3.45) we get,

$$dQ = (C_l \sin\varphi - C_d \cos\varphi)\pi\sigma' \rho \frac{U^2(1-a)^2}{\sin^2\varphi} r^2 dr \tag{3.46}$$

In the calculation of induction factors, a and a', it is a common practice to consider C_d to be equal to zero [18].

Combining Eq (3.31) with (3.46), and assuming $C_d = 0$, we obtain,

$$\frac{a'}{1-a} = \frac{\sigma' C_l}{4\lambda_r \sin\varphi} \tag{3.47}$$

Combing Eqs. (3.27), (3.35) and (3.40), and after some algebraic simplifications we get,

$$\frac{a}{1-a} = \frac{\sigma' C_l \cos\varphi}{4\sin^2\varphi} \tag{3.48}$$

Relating a', a, φ and λ_r in Eq. (3.34) with (3.47) and (3.48) the following expression is obtained:

$$C_l = 4\sin\varphi \frac{\cos\varphi - \lambda_r \sin\varphi}{\sigma'(\sin\varphi + \lambda_r \cos\varphi)} \tag{3.49}$$
$$\frac{a'}{1+a'} = \frac{\sigma' C_l}{4\cos\varphi} \tag{3.50}$$

From Figure 3.6 the following is obtaining:

$$\frac{a^{'}}{a} = \frac{\lambda_r}{\tan\varphi} \tag{3.51}$$

$$a = \frac{1}{1+\frac{4\sin^2\varphi}{\sigma^{'}C_l\cos\varsigma}} \tag{3.52}$$

$$a^{'} = \frac{1}{\frac{4\cos\varphi}{\sigma^{'}C_l}-1} \tag{3.53}$$

Power Coefficient

The power coefficient C_P can be calculated by the following equations [77]:

$$C_P = \frac{8}{\lambda^2}\int_{\lambda_h}^{\lambda} {\lambda_r}^3 a^{'}(1-a)\left[1-\frac{C_d}{C_l}\cot\varphi\right]d\lambda_r \tag{3.54}$$

Where λ_h is the local speed at the hub. De Vries [24] proposed an equivalent equation to determine the power coefficient.

$$C_P = \frac{8}{\lambda^2}\int_{\lambda_h}^{\lambda} \sin^2\varphi(\cos\varphi-\lambda_r\sin\varphi)(\sin\varphi+\lambda_r\cos\varphi)\left[1-\frac{C_d}{C_l}\cot\varphi\right]{\lambda_r}^2 d\lambda_r \tag{3.55}$$

Tip Loss

The pressure on the pressure side of a blade is greater than that on the suction side. Therefore, the air flows around the tip from the low to the high-pressure side. This phenomenon causes a reduction of lift, which in turn reduces the extracted power near the tip [18]. Prandtl's developed a method to consider the tip loss [24], expressing it in the following equation:

$$F_{tip} = \frac{2}{\pi}\cos\left(e^{-\frac{B(R-r)}{2r\sin\varphi}}\right) \tag{3.56}$$

The hub loss is given by the following expression:

$$F_{hub} = \frac{2}{\pi}\cos\left(^{-\frac{B(r-R_h)}{2r\sin\varphi}}\right) \tag{3.57}$$

The total loss is given by,

$$F = F_{hub}\times F_{tip} \tag{3.58}$$

The tip loss correction factor should be included in the momentum equations. Therefore, Eqs. (3.27) and (3.31) become,

$$dT = 4a(1-a)\rho F U^2 \pi r dr \tag{3.59}$$
$$dQ = 4a'(1-a)\rho F U \pi r^3 \Omega dr \tag{3.60}$$

The rest of the equations are modified as following:

$$\frac{a'}{1-a} = \frac{\sigma' C_l}{4\lambda_r F \sin\varphi} \tag{3.61}$$
$$\frac{a}{1-a} = \frac{\sigma' C_l \cos\varphi}{4F\sin^2\varphi} \tag{3.62}$$
$$C_l = 4F\sin\varphi \frac{\cos\varphi - \lambda_r \sin\varphi}{\sigma'(\sin\varphi + \lambda_r \cos\varphi)} \tag{3.63}$$
$$\frac{a'}{1+a'} = \frac{\sigma' C_l}{4F\cos\varphi} \tag{3.64}$$
$$a = \frac{1}{1 + \dfrac{4F\sin^2\varphi}{\sigma' C_l \cos\varphi}} \tag{3.65}$$
$$a' = \frac{1}{\dfrac{4F\cos\varphi}{\sigma' C_l} - 1} \tag{3.66}$$
$$U_{rel} = \frac{U(1-a)}{\sin\varphi} = \frac{U}{\sin\varphi + \dfrac{\sigma' C_l}{4F}\cot\varphi} \tag{3.67}$$
$$C_P = \frac{8}{\lambda^2}\int_{\lambda_h}^{\lambda} F {\lambda_r}^3 a'(1-a)\left[1 - \frac{C_d}{C_l}\cot\varphi\right] d\lambda_r \tag{3.68}$$
$$C_P = \frac{8}{\lambda^2}\int_{\lambda_h}^{\lambda} F\sin^2\varphi(\cos\varphi - \lambda_r\sin\varphi)(\sin\varphi + \lambda_r\cos\varphi)\left[1 - \frac{C_d}{C_l}\cot\varphi\right] {\lambda_r}^2 d\lambda_r \tag{3.69}$$

Glauert Correction for High Values of a

When the axial induction factor becomes greater than 0.5, the momentum theory no longer applies because it would cause the far wake velocity to be negative. When the value of a is greater than 0.5, an empirical relationship between a and C_P is used. Glauert formulated this empirical relationship.

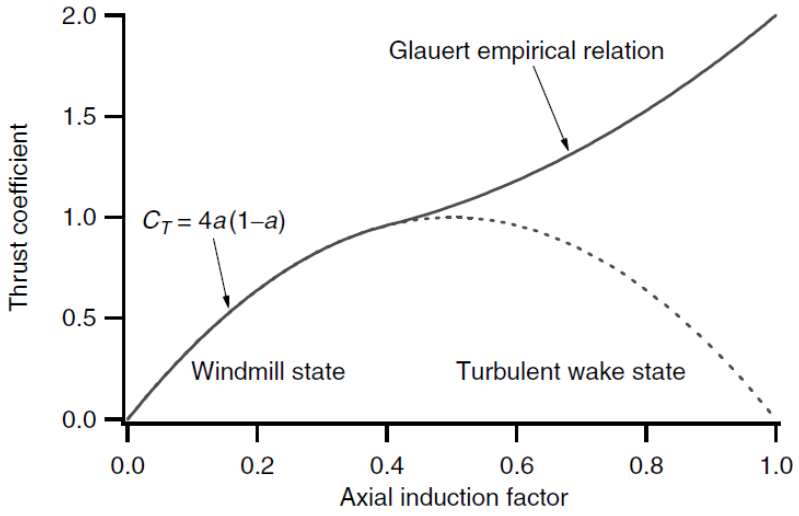

Figure 3.7: Fits to measured wind turbine thrust coefficients [18]

The region where the axial induction factor is less than 0.5 is said that the wind turbine is operating at windmill state; when the axial induction factor is greater than 0.5, the wind turbine is said to be operating at turbulent wake state.

If $a > 0.4$ or $C_T > 0.96$; a and C_T are related as follow:

$$a = (1/F)\left[0.143 + \sqrt{0.0203 - 0.6427(0.889 - C_T)}\right] \tag{3.70}$$

$$C_T = \frac{\sigma'(1-a)^2(C_l \cos\varphi + C_d \sin\varphi)}{\sin^2\varphi} \tag{3.71}$$

Wilson-Walker method

Spera [78] found an expression of thrust coefficient C_T base on the axial induction factor a.

Where a_c is about 0.2 and F is the Prandtl's loss factor.

If $a > a_c = 0.2$; then a should be calculated using the following formula:

$$a = 0.5\left[2 + K(1-2a_c) - \sqrt{(K(1-2a_c)+2)^2 + 4K(a_c{}^2 - 1)}\right] \tag{3.72}$$

where:

$$K = \frac{4F\sin^2\varphi}{\sigma' C_n} \tag{3.73}$$

Buhl Method

Buhl Jr. [26] developed a relationship for C_T and a.

$$C_T = 8/9 + (4F - 40/9)a + (50/9 - 4F)a^2 \tag{3.74}$$

$$a = \frac{18\sigma' C_n + 36F^2 \sin^2\varphi - 40F\sin^2\varphi}{2(9\sigma' C_n - 50F\sin^2\varphi + 36F^2\sin^2\varphi)} \pm \frac{6\sqrt{18F\sigma C_n \sin^2\varphi + 36F^4\sin^4\varphi - 48F^3\sin^4\varphi}}{2(9\sigma' C_n - 50F\sin^2\varphi + 36F^2\sin^2\varphi)} \tag{3.75}$$

These equations are valid when $a > 0.4$.

Blade Shape for Optimum Rotor with Wake Rotation

$$\frac{\partial}{\partial\varphi}\left[\sin^2\varphi(\cos\varphi - \lambda_r\sin\varphi)(\sin\varphi + \lambda_r\cos\varphi)\right] = 0 \tag{3.76}$$

This give us,

$$\lambda_r = \frac{\sin\varphi(2\cos\varphi - 1)}{(1-\cos\varphi)(2\cos\varphi + 1)} \tag{3.77}$$

Consequently, after some algebraic simplifications

$$\varphi = \frac{2}{3}\arctan\left(\frac{1}{\lambda_r}\right) \tag{3.78}$$

$$C = \frac{8\pi r}{BC_{l,des}}(1-\cos\varphi) \tag{3.79}$$

The tangential induction factor is given by:

$$a' = \frac{1-3a}{4a-1} \tag{3.80}$$

$$a = \frac{1}{1 + \dfrac{4\sin^2\varphi}{\sigma' C_l \cos\varphi}} \tag{3.81}$$

Airfoil for Small Wind Turbine Blades

As stated in chapter 2, the most widely used airfoils for small wind turbines are FX 63-137, S822, S834, SD2030, SG6043, and SH3055. In this research, the SG6043 airfoil is used because it has a very high lift to drag ratio, consequently would yield a high power coefficient.

It is critical to choose the Reynolds number that the blade will operate. As a rule of thumb, the Reynolds number range from $75000R$ to $150000R$ [56]. Since R is chosen to be 3.5 m; therefore, Re ranges from about 250 000 to 500 000. In this study Re is chosen to be 500 000.

The figure bellow shows the aerodynamic properties of the airfoil SG6043. The values were obtained from the XFOIL software program.

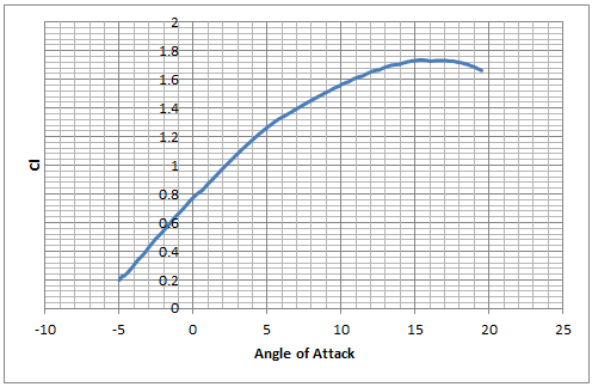

Figure 3.8: SG6043 lift coefficient vs angle of attack at Re=500000

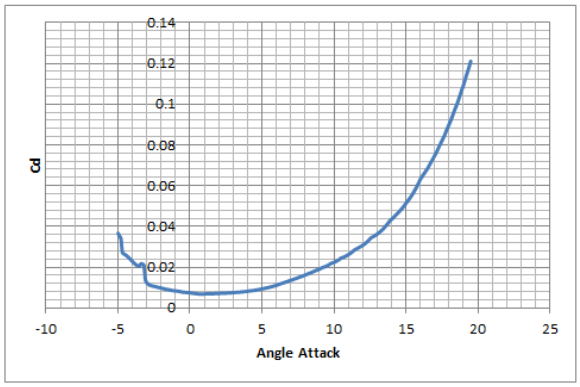

Figure 3.9: SG6043 drag coefficient vs angle of attack at Re=500000

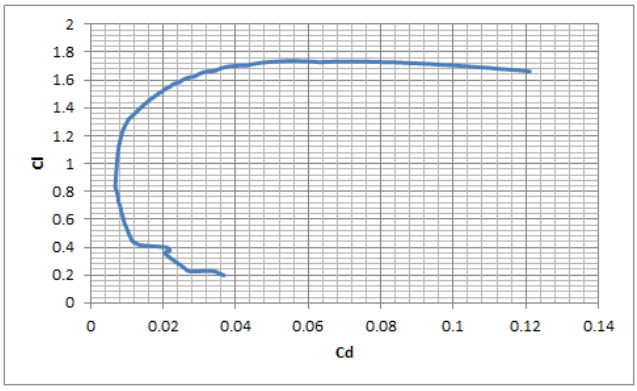

Figure 3.10: SG6043 lift vs drag at Re=500000

Lift and drag coefficient after stall

The airfoil aerodynamic data should be available for an angle of attack ranging from 0° to 360°, to apply the BEM to calculate the rotor blade's preliminary aerodynamic performance. Since XFoil only converges when the angle of attack is small, when there is no stall, alternative methods are used to estimate the aerodynamic properties of airfoils after stall. Two

approaches will be discussed here, the flat plate and Viterna method.

In the flat plate method, the airfoil is considered to behave like a plate when it starts to stall. The lift and drag coefficient are calculated using the following formulae:

$$C_l = 2\sin\alpha\cos\alpha \tag{3.82}$$
$$C_d = 2\sin^2\alpha \tag{3.83}$$

In the Viterna approach, the lift and drag are found using the following formulae:

$$C_l = A_1\sin 2\alpha + A_2\frac{\cos^2\alpha}{\sin\alpha} \tag{3.84}$$
$$C_d = B_1\sin^2\alpha + B_2\cos\alpha \tag{3.85}$$

Where:

$$B_1 = 1.11 + 0.018AR \tag{3.86}$$
$$B_2 = \frac{C_{d-stall} - C_{d-max}\sin^2\alpha_{stall}}{\cos\alpha_{stall}} \tag{3.87}$$
$$A_1 = \frac{B_1}{2} \tag{3.88}$$
$$A_2 = (C_{l-stall} - 0.5C_{d-max}\sin 2\alpha_{stall})\frac{\sin\alpha_{stall}}{\cos^2\alpha_{stall}} \tag{3.89}$$
$$AR = \frac{Span^2}{Area} = \frac{b^2}{b\bar{c}} = \frac{b}{\bar{c}} \tag{3.90}$$

Where b is the blade span, and $\bar{c}$ is the mean chord. In the present research, the Viterna method will be used. Therefore, for angle of attack ranging from $-5°$ to $19.5°$ the XFoil table is used to obtain the aerodynamic properties; For other angles the Viterna method will give the airfoil's approximated aerodynamic properties after stall.

3.2 Blade Aerodynamic Preliminary Design

Aluminum will be used rather than fiberglass composite material, because aluminum is cheaper compared to fiberglasses, and extrusion process can be used to manufacture the blade, which is also cheaper as compared to one of the processes employed in the manufacturing of composite materials blades.

For aluminum blades to be manufactured successfully, it has to have a uniform cross-section. The blade will not be twisted. The untwisted blades will be less efficient and use more material than the traditional blade design procedures.

The BEM theory was used as a preliminary analysis to evaluate the uniform untwisted blade's aerodynamic performance.

3.2.1 Blade Aerodynamic Pre-analysis

After tries and errors, it was found that the blade would be more efficient if it is given a pitch angle of 7.5°.

The following is the algorithm used to analyze the preliminary blade aerodynamic performance:

1. Obtain the airfoil aerodynamics parameters (angle of attack, lift coefficient, and drag coefficient) from XFoil software
2. From the data obtained from XFoil, derive the post-tall region using the Viterna model. This study's angle of attack was as follows: $-5°$ to 19.5° for the attached flow regime, and the rest of the angles for the post-stall region.
3. For a specific tip speed ratio, calculate the lift coefficient for each blade element using Eqs. (3.29), (3.33), (3.45), (3.56)-(3.58), and (3.63), for all of the angle of attacks
4. Plot the graphs of lift coefficients found from the above methods (XFoil plus Viterna model and the one found from Eq. (3.63)) versus angle of attack, and obtain the interception points for each blade element. The interception points obtained are found appendix A
5. Calculate the flow parameters from Eqs. (3.65),(3.66), (3.70), and (3.71), for each blade element.
6. Calculate the power coefficient from Eq. (3.55)
7. Repeat steps 3-6 for a different value of tip speed ratio. The tip speed ratio used in the current study varied from 1 to 11 in an incremental step of 0.5
8. Plot the value of power coefficient versus tip speed ratio

The Matlab code for the above algorithm is given in Appendix A.1.

Table 3.1: Data from figure 3.11

λ	1	1.5	2	2.5	3	3.5	4	4.5	5	5.5	6
C_p	0.019	0.052	0.112	0.188	0.26	0.323	0.382	0.427	0.461	0.466	0.498
λ	6.5	7	7.5	8	8.5	9	9.5	10	10.5	11	
C_p	0.501	0.496	0.47	0.446	0.398	0.34	0.267	0.18	0.079	-0.052	

From the calculated values, the maximum power coefficient of 0.501 occurs when the tip speed ratio is 6.5. This is an approximation value because the values of the interception points are not exact; they were approximated.

The power coefficient versus tip speed ratio (TSR) graph is shown in the Figure 3.11:

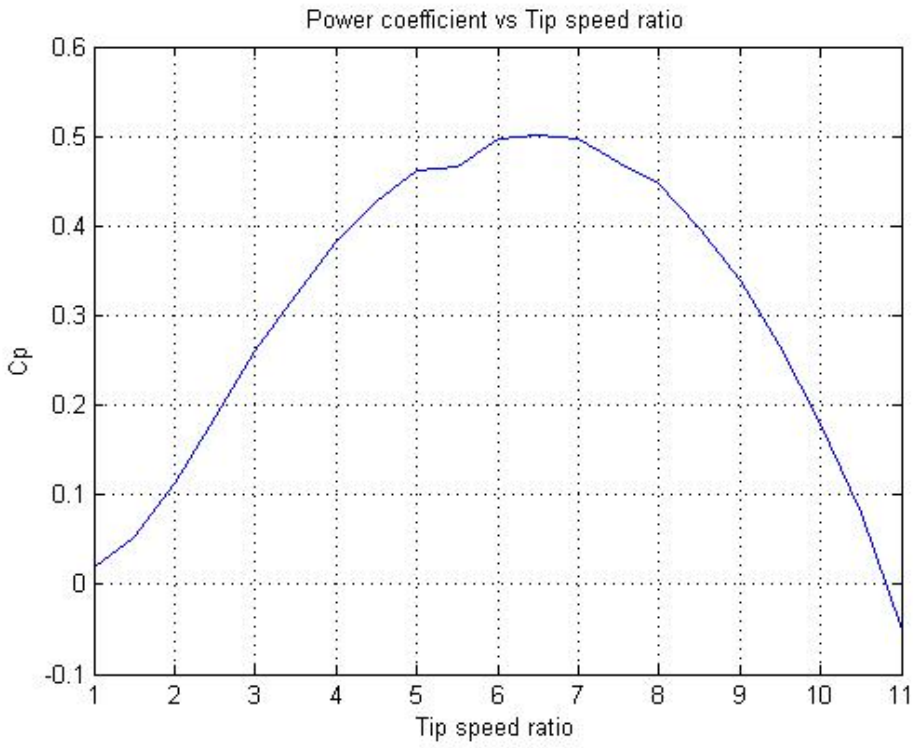

Figure 3.11: Power coefficient versus tip speed ratio

Table 3.1 shows values from Figure 3.11.

3.2.2 Blade design from Qblade

The obtained power coefficients were compared with Qblade software.

The following are the steps to set up the study in Qblade:

1. Open the Qblade.
2. Select the Airfoil Design icon.
3. Go to Foil menu and select import Foil
4. Choose the file that contain the airfoil coordinates in .dat format then click open.
5. Go to XFoil Direct Analysis icon and click in New Polar.
6. In the dialog box enter the Reynolds Numbers, Mach Number and the turbulence parameter NCrit. Leave the other options to default, and then click ok. In the current analysis Re was set to 500 000, Mach to 0, and NCrit to 9.
7. Choose the range of the angle of attack and the increment then click on Analyze.
8. Set Polar Extrapolation to 360 icon. Choose Viterna then click Extrapolate.

9. Set the extrapolation parameters accordingly, then click Save.
10. Go to 360 polar menu the click Generate a Circular Foil option then click Ok.
11. Select HAWT Rotorblade Design icon, then click New.
12. Enter the hub radius, the chords of each elements, and its pitch angle. In the current study the chord and the pitch angle of each element (21 in this study) was set to 0.25 and 7.5 respectively, then click Save.
13. Go to Blade BEM Simulation icon and click Define Simulation.
14. In the dialogue box enter the simulation parameters accordingly and click Create, and then Start Simulation.

Figure 3.12: Power coefficient from QBlade vs tip speed ratio

Table 3.2 shows the result was obtained from Qblade:

Table 3.2: Qblade power coefficient vs tip speed ratio

C_P	1	1.5	2	2.5	3	3.5	4	4.5	5	5.5	6
λ	0.021	0.053	0.11	0.18	0.247	0.31	0.363	0.405	0.438	0.459	0.469
C_P	6.5	7	7.5	8	8.5	9	9.5	10	10.5	11	
λ	0.47	0.461	0.438	0.408	0.361	0.302	0.233	0.15	0.061	-0.054	

As shown in Figure 3.13, the values obtained from calculations compared to those obtained from QBlade show an excellent approximation. The maximum C_P value found from Qblade

is 0.47, which also occurs at a tip speed ratio of 6.5. In the tip speed ratio ranging from five to seven, the calculation shows considerably higher C_P values. The maximum error between the calculated C_P values and those obtained from Qblade is about 6%, a reasonable approximation.

Figure 3.13: Power coefficient from QBlade vs tip speed ratio

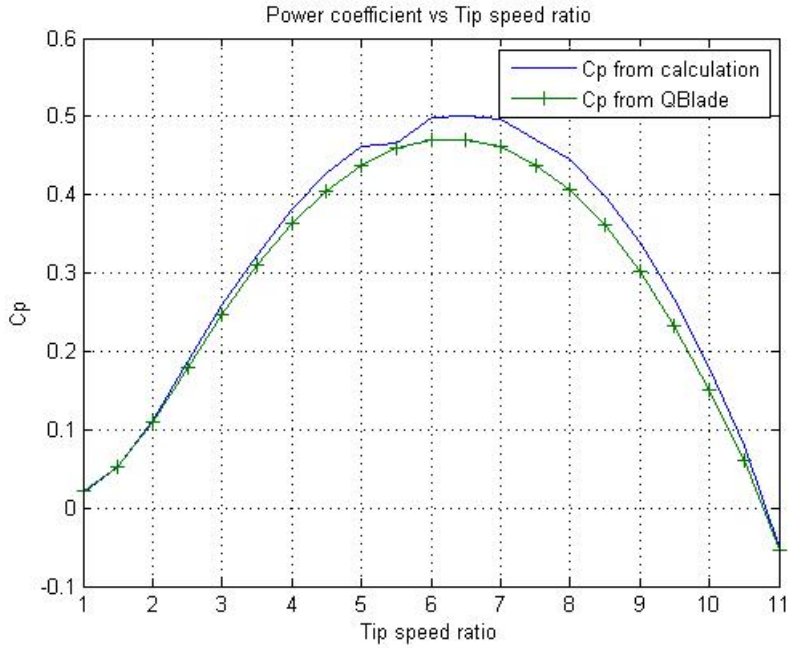

Figure 3.14: Comparison of power coefficient obtained from calculations and Qblade

3.3 Rotor Blade CFD Analysis

The power coefficients obtained from the calculation and Qblade showed acceptable values, which made it justifiable to proceed with further studies in the aerodynamic performance of a uniform blade designed using the airfoil SG6043. In this section, the CFD study of the blade was performed.

3.3.1 Governing Equations

The governing equations that the CFD software package should solve are as follow:

- Continuity equation

$$\frac{\partial}{\partial x}(\rho\bar{u}) + \frac{\partial}{\partial y}(\rho\bar{v}) + \frac{\partial}{\partial z}(\rho\bar{w}) = 0 \tag{3.91}$$

- Momentum equations

$$\begin{aligned}
\frac{\partial}{\partial x}(\rho\bar{u}\bar{u}) + \frac{\partial}{\partial y}(\rho\bar{u}\bar{v}) + \frac{\partial}{\partial z}(\rho\bar{u}\bar{w}) &= -\frac{\partial P}{\partial x} + (\mu_t + \mu)\left(\frac{\partial^2\bar{u}}{\partial x^2} + \frac{\partial^2\bar{u}}{\partial y^2} + \frac{\partial^2\bar{u}}{\partial z^2}\right) \\
\frac{\partial}{\partial x}(\rho\overline{u\bar{v}}) + \frac{\partial}{\partial y}(\rho\overline{\bar{v}\bar{v}}) + \frac{\partial}{\partial z}(\rho\bar{v}\bar{w}) &= -\frac{\partial P}{\partial y} + (\mu_t + \mu)\left(\frac{\partial^2\bar{v}}{\partial x^2} + \frac{\partial^2\bar{v}}{\partial y^2} + \frac{\partial^2\bar{v}}{\partial z^2}\right) \\
\frac{\partial}{\partial x}(\rho\overline{u\bar{w}}) + \frac{\partial}{\partial y}(\rho\overline{\bar{v}\bar{w}}) + \frac{\partial}{\partial z}(\rho\bar{w}\bar{w}) &= -\frac{\partial P}{\partial z} + (\mu_t + \mu)\left(\frac{\partial^2\bar{w}}{\partial x^2} + \frac{\partial^2\bar{w}}{\partial y^2} + \frac{\partial^2\bar{w}}{\partial z^2}\right)
\end{aligned} \tag{3.92}$$

Turbulence models have to be used to find the turbulence viscosity. In the current study, the k-omega, shear stress transport (SST) model was used. For more details on the k-omega SST model, see [79].

Ansys Fluent was used to solve the above system of differential equations, which uses an algorithm based on Finite Volume Method FVM. For more information about FVM, see [80].

3.3.2 Computational Fluid Domain

For computational efficiency purposes, only one-third of the computational domain was considered. The domain was made to be a one-third tapered cylinder, with an arc of 6.7 m in the inlet and 13, 3 m outlet. The cylinder is 15 m long, and the blade is located 5 m away from the inlet surface. The blade has a radius of 3.5 m, with its root 0.15 m away from the axis of rotation. The domain is shown in Figure 3.14. The blade has a cross-sectional area made from airfoil SG6043 with 0.25 m chord length then extruded 3.5 m in Solidworks, see Figure 3.16. It was then exported to DesignModeler, rotated 7.5°, counterclockwise direction, and then extracted from the flow domain, as shown in Figures 3.17 and 3.18.

3.3.3 Meshing

To have acceptable results, a proper fine meshing of the flow domain is essential. In the present study, we will be focus on torque; therefore, the meshing must be refined in the region near the blades. The regions away from the blade must have coarser cells because if the entire domain were refined, it would generate a very high number of nodes and cells, which would require higher computational resources. The simulation results would take very long to be generated.

Most of the features in the general meshing were left to default to mesh the domain. The Size Function was set to Proximity and Curvature. The Element Size around the blade was set to 8.5 mm. For inflation around the blade, five layers with a growth rate of 1.2 were chosen. To refine the element in the vicinity of the blade, a sphere of influence center in the middle of the blade, with a radius of 1.7 m and an element size of 0.055 m, was used.

The result of the meshing gave 463365 nodes and 2191755 elements. More meshing details are given in Appendix A.2.2.

3.3.4 General Settings

In the general setting section, **Pressure-based**, **Absolute** and **Steady** options were selected. In the **Cell Zone** the fluid was set to air with a constant density of 1.225 kg/m^3 and a viscosity of 1.7894×10^{-5} kg/ms. The **Frame Motion** option was activated and 19.5 rad/s was given to the **Rotational Velocity**. The boundary conditions were set as follow: inlet 10.5 m/s, inlet_top 10.5 m/s, outlet 0 kPa gauge pressure and the two inclined planes were set to interfaces. The $k-\omega$ SST model and Coupled Pseudo-transient were chosen. All the residuals were set to 10^-6. More details about the settings are given in Appendix A.2.3.

3.3.5 Numerical Results

In the CFD considered here a constant velocity of -10.5 m/s in the z direction and a 19.5 rad/s counterclockwise rotational speed was considered. After 1420 iteration the torque coefficient did not show any change as illustrated in the Figure 3.22.

Settings

The residuals quantities were as following (see figure 3.23):

- Continuity: 1.2717×10^{-5}.
- x-component of the velocity: 4.1962×10^{-7}.
- y-component of the velocity: 6.1558×10^{-7}.
- z-component of the velocity: 6.6671×10^{-7}.

- k variable: 1.4771×10^{-6}.
- ω variable: 1.8351×10^{-7}.

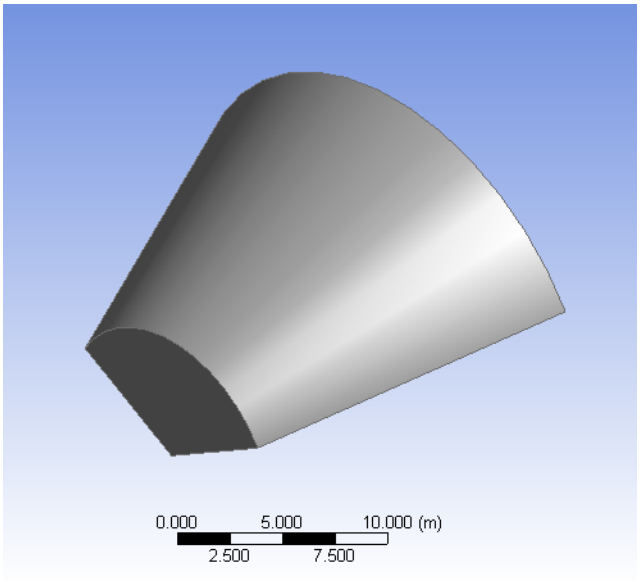

Figure 3.15: Flow domain

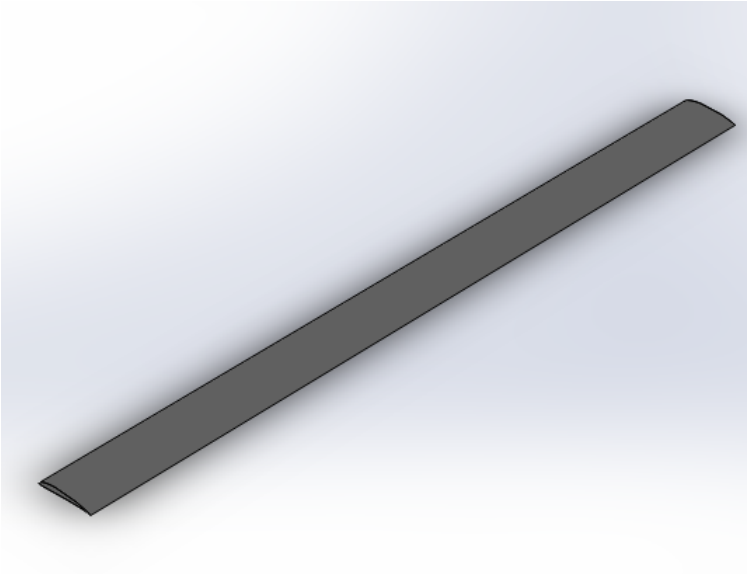

Figure 3.16: Uniform blade

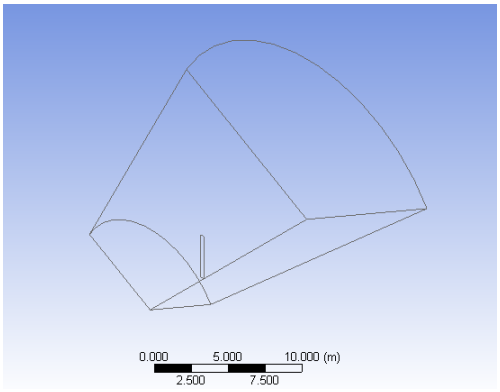

Figure 3.17: Flow domain with the blade subtracted in it

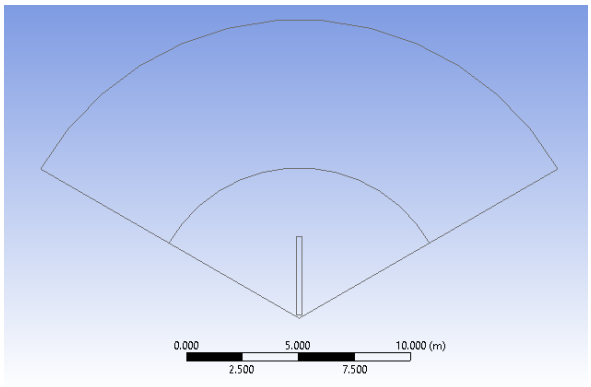

Figure 3.18: Flow domain front view

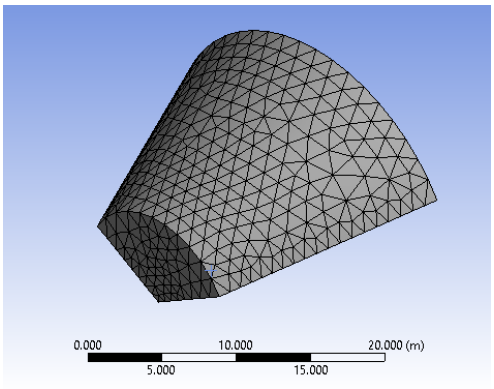

Figure 3.19: General meshing

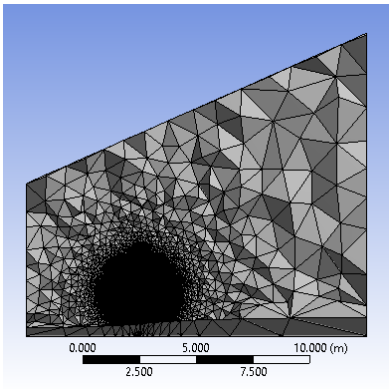

Figure 3.20: Detailed meshing

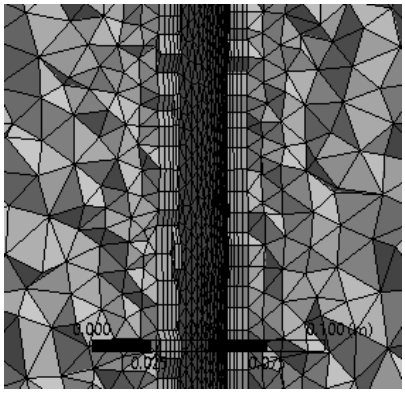

Figure 3.21: Meshing around the blade

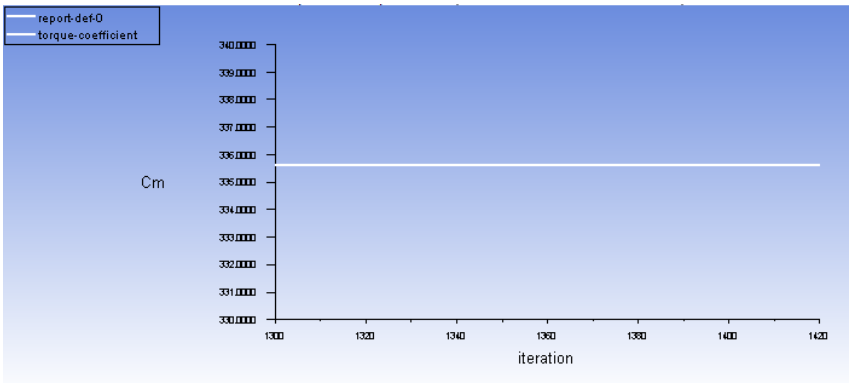

Figure 3.22: Torque coefficient after 1420 iteration

The torque obtained is 205.57 Nm. But,

$$\dot{W} = T\Omega \tag{3.93}$$

Therefore, the power obtained per each blade is,

$$\dot{W} = 205.57 \times 19.5 = 4008.645 \text{ W}$$

Since the turbine has three blade the total power is,

$$\dot{W}_T = 3 \times \dot{W} = 3 \times 4008.645 = 12026 \text{ W}$$

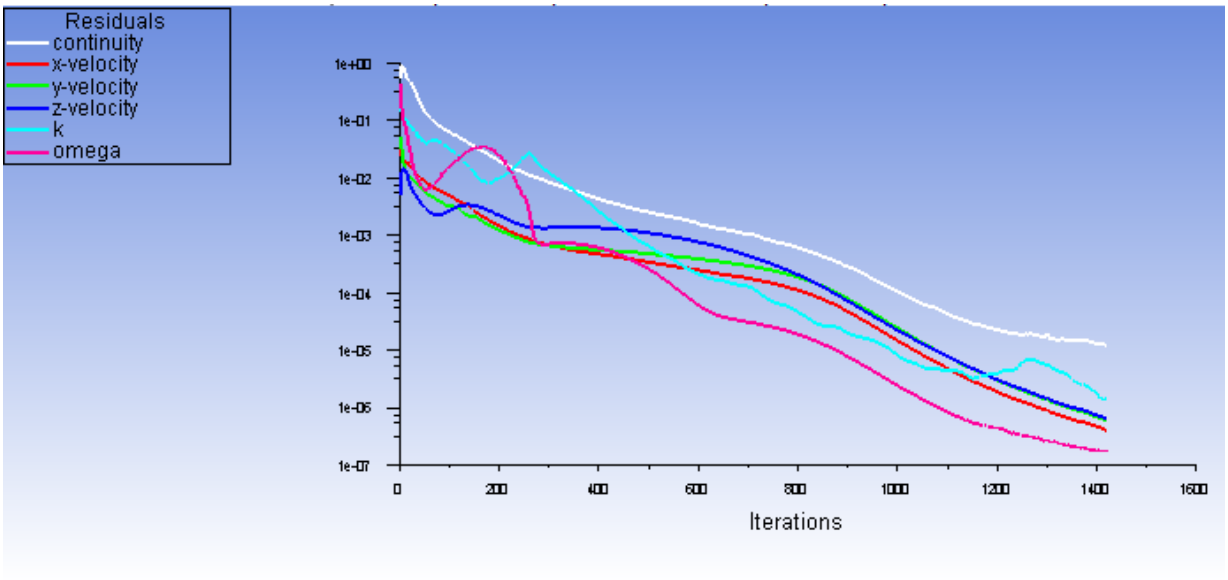

Figure 3.23: Residuals quantities

The power coefficient by definition can be expressed by the following formula,

$$C_P = \frac{\dot{W}_T}{0.5\pi\rho R^2 V^3} \tag{3.94}$$

Therefore,

$$C_P = \frac{12026}{0.5\pi \times 1.225 \times 3.5^2 \times 10.5^3} = 0.44$$

This power coefficient corresponds to a tip speed ratio of:

$$\lambda = \frac{3.5 \times 19.5}{10.5} = 6.5$$

3.3.6 Flow Field

The following figures illustrate the flow field of the domain being studied. It can be seen from Figure 3.24 that the maximum speed occurs at the tip of the blade, which agrees with what is expected. Figure 3.25 shows how the pressure is distributed throughout the blade. The pressure on the pressure side of the blade is greater than the suction side, as expected. Figure 3.27 shows the velocity contour from a plane normal to y-axis and offset 3 m from xz-plane. It can be seen that the velocity field accelerates on the suction side of the blade which means the pressure would be lower in this region, as seen in Figure 3.28. This pressure difference creates a lift force on the blade; consequently, torque is generated.

To have the tip speed ratio varying from 1 to 11, the rotation speed had to be varied. With everything else being equal, the numerical results obtained are presented in Table 3.3. Figure 3.29 shows the graph of the date from Table 3.3.

Figure 3.30 shows the comparison of the power coefficients C_{ps}, obtained from the three approaches. It can be seen that the results obtained from CFD show less power coefficient, having a maximum Cp of 0.458 at a tip speed ratio of 7.5. The graph obtained from CFD differs from the other two previous graphs quite considerably for low tip speed ratio (from 1 to 7), but it shows a close approximation from tip speed ratio ranging from 8 to 11. It is suggested that the mesh should be refined further to increase the accuracy of the CFD, but that would require more powerful computational resources and time. In the present study, a computer with 8 GB of RAM and an $i7$ processor is used. It took a considerable amount of time to obtain the results. Therefore for further mesh refinement, a more powerful computer is needed.

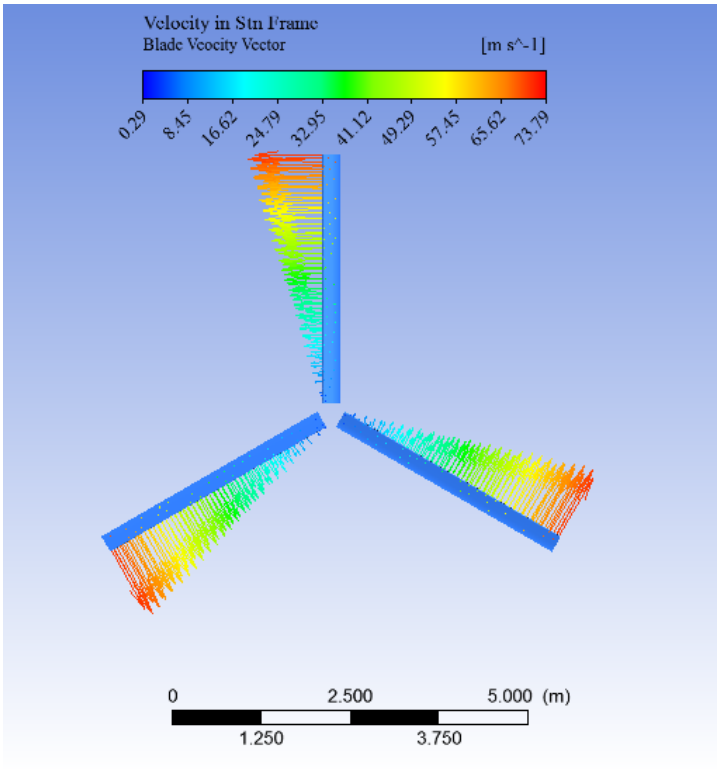

Figure 3.24: Blades velocity

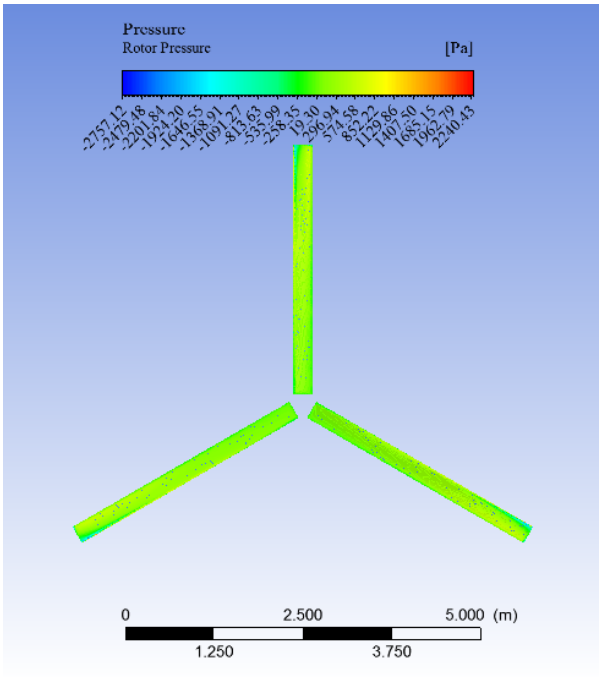

Figure 3.25: Pressure distribution on the blade surface

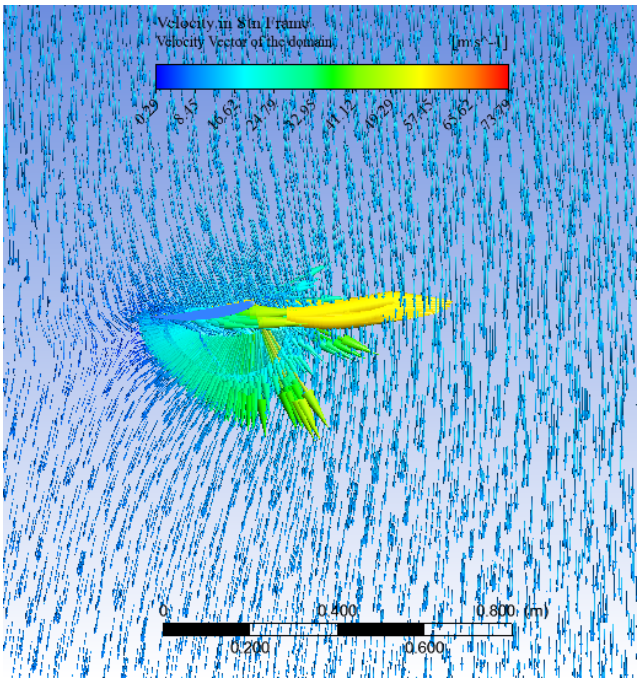

Figure 3.26: Velocity field around the blade

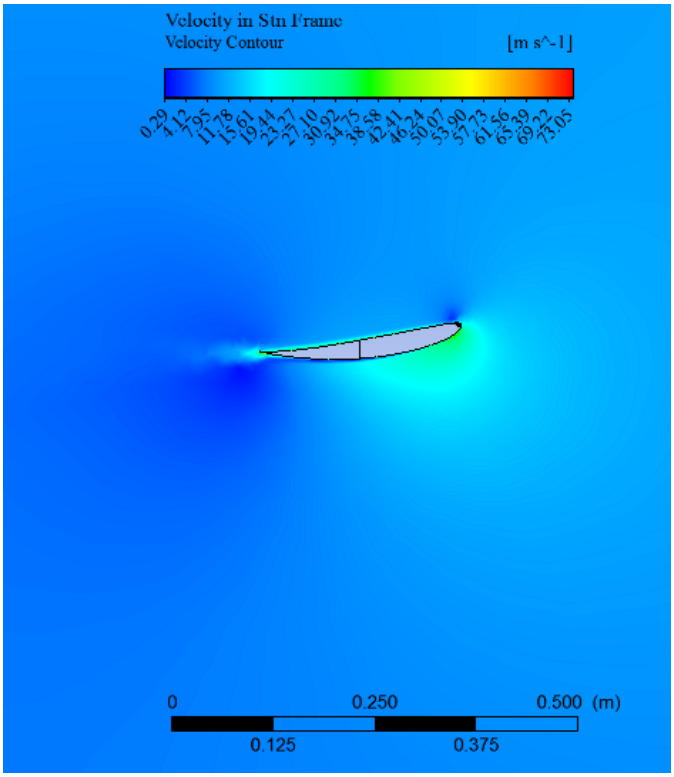

Figure 3.27: Vecticity contour

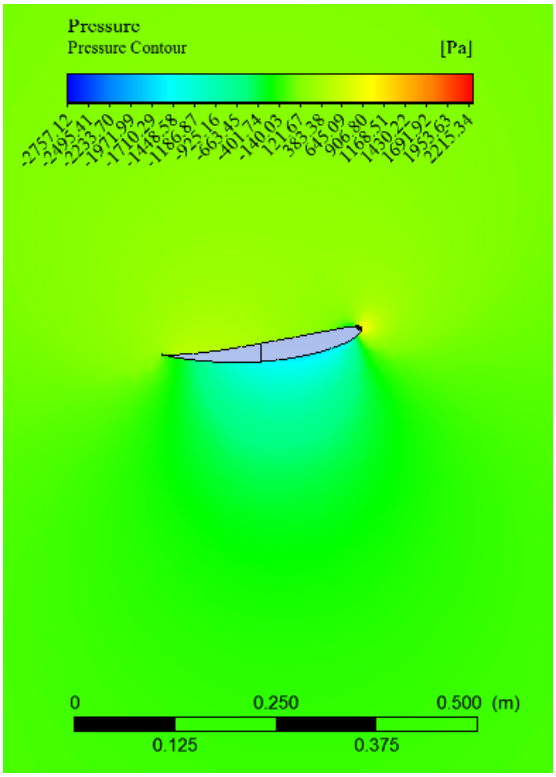

Figure 3.28: Pressure Contour

Table 3.3: Power Coefficient obtained from Ansys Fluent

ω	$\dot{W}$	C_P	ω	$\dot{W}$	C_P
3	328.5	0.012039	19.5	12027.6	0.440776
4.5	602.1	0.022065	21	12429.9	0.45552
6	1146.6	0.04202	22.5	12507.8	0.458374
7.5	1815.75	0.066542	24	11966.4	0.438534
9	2786.4	0.102113	25.5	11031.3	0.404265
10.5	4057.2	0.148685	27	9590.4	0.35146
12	5529.6	0.202644	28.5	7583.85	0.277926
13.5	7204.95	0.26404	30	5040	0.184701
15	8851.5	0.324382	31.5	2022.3	0.074111
16.5	10291	0.377135	33	-1603.8	-0.05877
18	11334.6	0.41538			

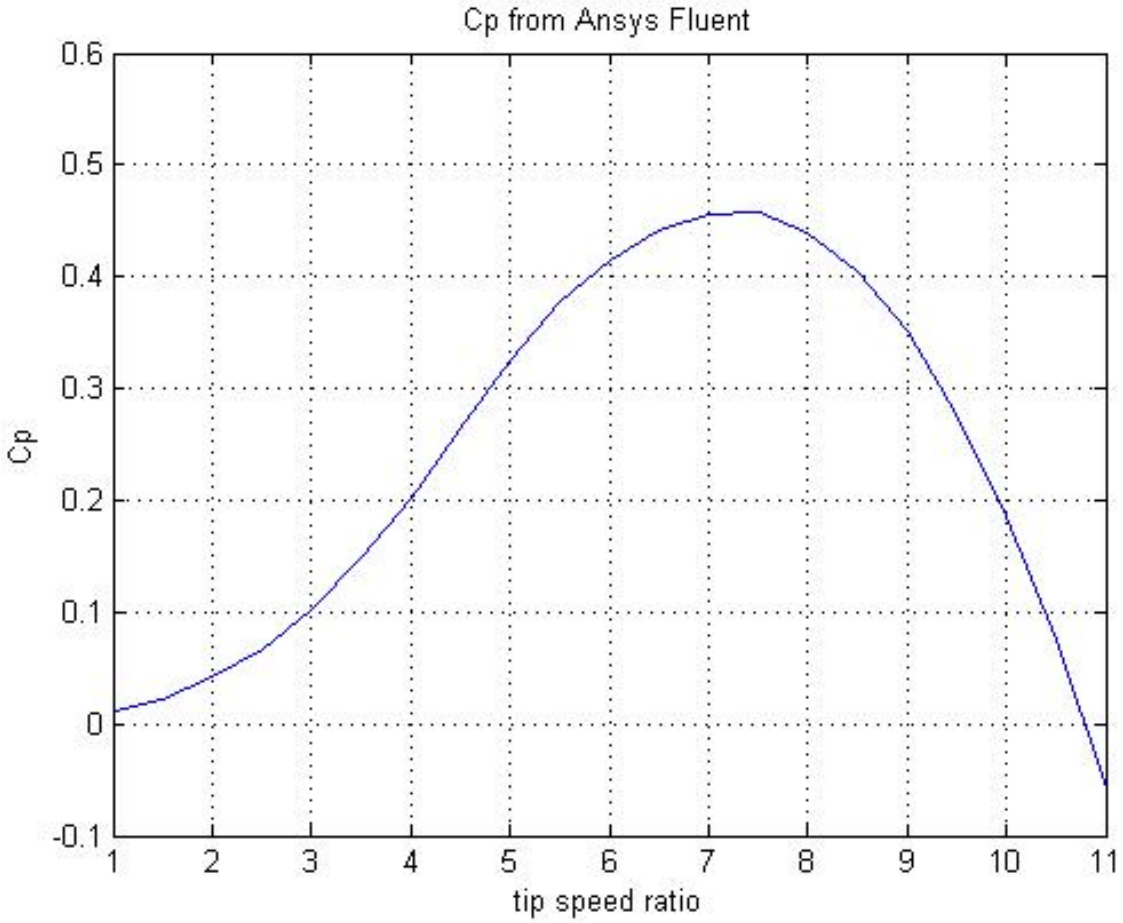

Figure 3.29: Cp obtained from Ansys Fluent

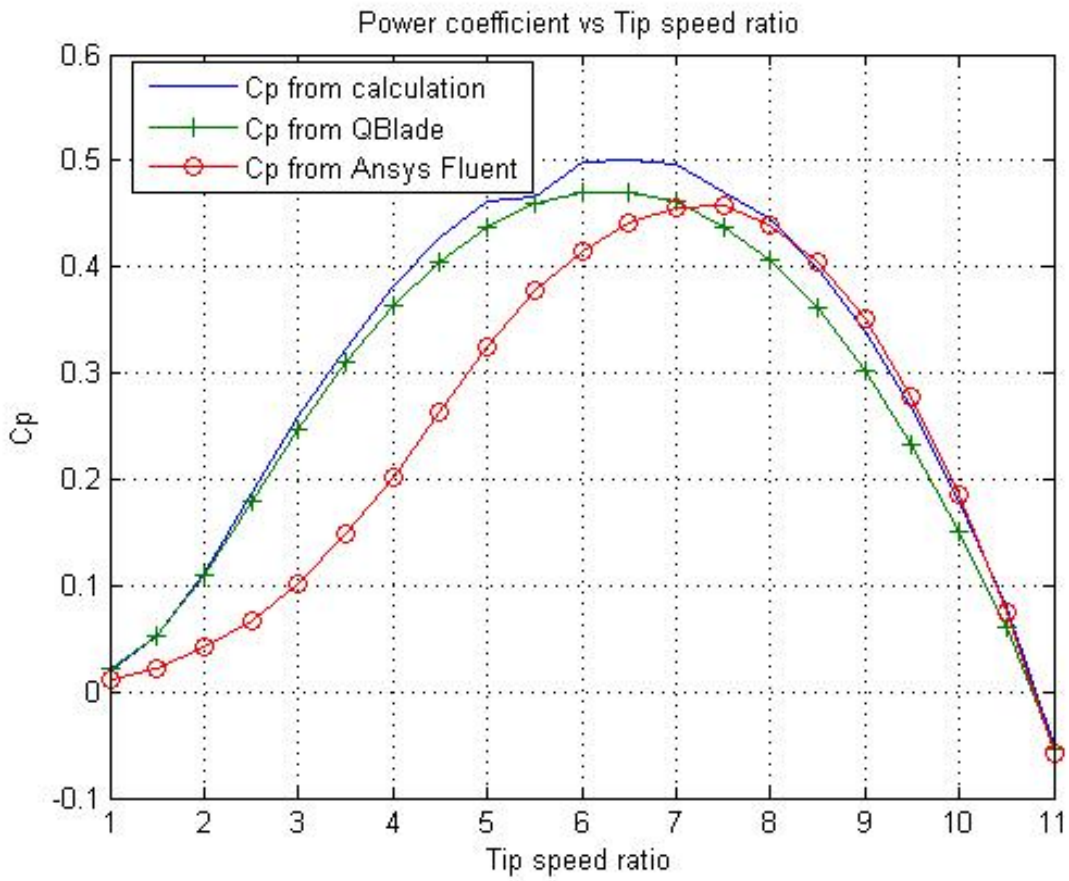

Figure 3.30: C_P comparison from three different procedures

3.4 Conclusion

The three methods used to evaluate the blade aerodynamic performance yielded good results for the power coefficient for a tip speed ratio ranging from five to nine, with the maximum power coefficient C_P being greater than 0.45 in all the three approaches used. Considering the fact that the blade was not optimized to yield the maximum C_p possible when using the airfoil SG6043, a power coefficient greater than 0.45 is a good result, as the maximum power that an ideal horizontal wind turbine can have (Betz limit) is 0.59, 0.45 is about 76% of Betz limit. The blade aerodynamic analysis carried out in this chapter showed promising results in terms of aerodynamic efficiency, which allows us to conclude that this design model is worth to be considered for further studies. In the next chapter, the blade will be analyzed structurally.

Chapter 4

Preliminary Structure Design

In this chapter, the structural design of the turbine components will be evaluated preliminarily. For this purpose, the engineering standards IEC 61400-2, EN 61400-2, or BS 61400-2 will be used.

IEC 61400-2 gives three ways to determine the design loads for wind turbine:

- Simplified load equations;
- Aeroelastic modeling and;
- Mechanical loads testing.

For the simplified load model to be used, IEC 61400-2 demands that all of the following turbine requirements be met:

- The turbine must be a horizontal axis;
- Its rotor must have two or more blades;
- The blades must be a cantilever blades; and
- The hub must be rigid (the blade must be attached to the hub rigidly)

Since all of the above design criteria are met in the current research project, the simplified load equation modeling will be used for the preliminary design. Most of the content of this section is based on Reference [81].

The chapter starts by defining the coordinate system used in the analysis in Section 4.1. Section 4.2 explains the simplified model of standard IEC 61400-2. The theory of blades' stresses calculation is presented in Section 4.3. In Section 4.4, the blade structure calculations and optimization is done. Section 4.5 gives the preliminary design of the main shaft. The tower preliminary design and optimization is given in Section 4.6. In Section 4.7, the nacelle model is presented and analysed. Section 4.8 discusses the mainframe preliminary design. The furling theoretical model, the tail preliminary design, and the furling analysis are given in Section 4.9. Section 4.10 presents the generator used in the small wind turbine design as well as the theory of its control system. Finally, Section 4.11 discusses the design of the turbine brake system.

4.1 Coordinate Systems

The coordinate systems are shown in Figure 4.1.

Tower

The x axis is positive when pointing down, z axis is positive when pointing up, y points towards the direction completes the right-hand coordinate system. The tower is assumed to be fixed.

Shaft

The $x - shaft$ axis is positive when the positive moment coincides with the rotation of the blades. The y and z axes are unused. The shaft axis system is assumed to be attached to the nacelle.

Blade

The $x - blade$ axis is positive when the positive moment coincides with the rotation of the blades.
The $y - blade$ axis considered positive if the positive moment bends the blade tip downwind.
The $z - blade$ axis completes the right-hand coordinate system.

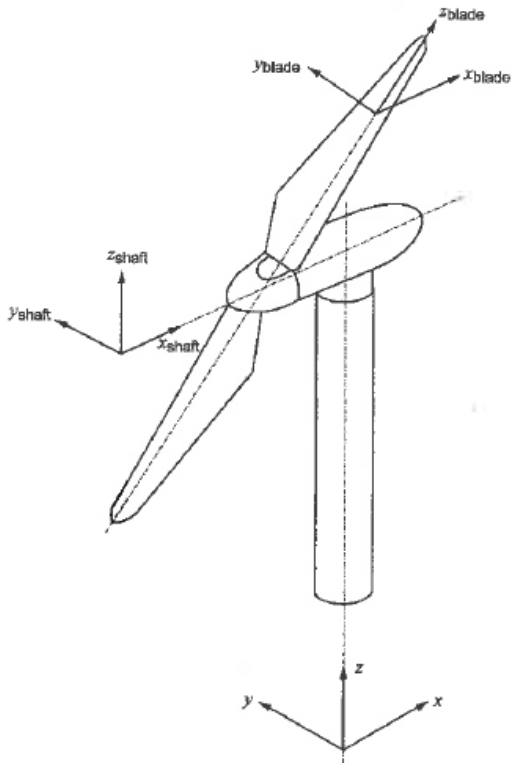

Figure 4.1: Coordinate system for simplified model [81]

4.2 IEC 61400-2 Simplified Model

There are ten load cases that the standard IEC61400-2 establishes for the simplified load models, as summarized in Table 4.1. In the following paragraphs, the description of each load case is given.

4.2.1 Load Case A: Normal Operation

The load case A represents a fatigue load. In this load case, the blade and shaft are assumed to have a constant range of fatigue load. The formulae for blades fatigue load are given below. The load ranges are considered to vary from peak-to-peak.

$$\Delta F_{zB} = 2m_B R_{cog} {\omega^2}_{n,des} \tag{4.1}$$

$$\Delta M_{xB} = \frac{Q_{des}}{B} + 2m_B R_{cog} g \tag{4.2}$$

$$\Delta M_{yB} = \frac{\lambda_{des} Q_{des}}{B} \tag{4.3}$$

$$P = \eta \omega Q_{des} \tag{4.4}$$

$$\eta = \begin{cases} 0.6 + 0.005P & for\ P < 20\ kW \\ 0.7 & for\ P > 20\ kW \end{cases} \tag{4.5}$$

as provided by [82].

The fatigue is the result of the sum of centrifugal load (ΔF_{zB}), and bending moments (ΔM_{xB} and ΔM_{yB}).

For shaft loads,

$$\Delta F_{x-shaft} = \frac{3}{2}\frac{\lambda_{des} Q_{des}}{B} \tag{4.6}$$

$$\Delta M_{xB} = Q_{des} + 2m_r e_r g \tag{4.7}$$

$$\Delta M_{shaft} = 2m_r L_{rb} g + R\frac{\Delta F_{x-shaft}}{6} \tag{4.8}$$

Where $e_r = 0.005R$.

The rotor shaft's fatigue load shall be considered at the first bearing (closest to the rotor). The stress range for fatigue analysis is calculated by finding the combination of the thrust ($\Delta F_{x-shaft}$), bending moment (ΔM_{shaft}), and the torsion moment (ΔM_{xB}).

4.2.2 Load Case B

In this load case, the gyroscopic forces and moments are considered by assuming that the nacelle rotates at the maximum yawing speed $\omega_{yaw,max}$, when the rotor is running at the design rotational speed n_{des}.

The maximum yaw rate in a passive yaw system is calculated by

$$\omega_{yaw,max} = 3 - 0.01\left(\pi R^2 - 2\right) \tag{4.9}$$

The bending moment on the blades and shaft is given by,

$$M_{yB} = m_B R_{cog} L_{rt} \omega^2{}_{yaw} + 2 I_B \omega_{yaw} \omega_n + \frac{R}{9} \Delta F_{x-shaft} \tag{4.10}$$

$$M_{shaft} = m_r g L_{rb} + B I_B \omega_{yaw} \omega_n + \frac{R}{6} \Delta F_{x-shaft} \tag{4.11}$$

Table 4.1: IEC61400-2 Load conditions [81]

Design situation	**Load Case**		**Wind inflow**	**Type of analysis**	**Remarks**
Power	A	Normal operation		F	
production	B	Yawing	$V_{hub} = V_{des}$	U	
	C	Yaw error	$V_{hub} = V_{des}$	U	
	D	Maximum thrust	$V_{hub} = 2.5 V_{ave}$	U	Rotor spinning but could be furling or fluttering
Power production	E	Maximum rotational speed		U	
plus occurrence of fault	F	Short at load connection	$V_{hub} = V_{des}$	U	Maximum short-circuit generator torque
Shutdown	G	Shutdown (braking)	$V_{hub} = V_{des}$	U	
Parked (idling or standstill)	H	Parked wind loading	$V_{hub} = V_{e50}$	U	
Parked and fault conditions	I	Parked wind loading,maximum exposure	$V_{hub} = V_{ref}$	U	Turbine is loaded most unfavourable exposure
Transport, assembly, maintenance and repair	J	To be stated by manufacturer		U	

4.2.3 Load Case C: Yaw Error

In load case C, the yaw error is assumed to be 30°.

The flapwise bending moment induced by the yaw error is calculated by

$$M_{yB} = \frac{1}{8}\rho A_{proj,B} C_{l,max} R^3 {\omega^2}_{n,des} \left[1 + \frac{4}{3\lambda_{des}} + \left(\frac{1}{\lambda_{des}}\right)^2\right] \tag{4.12}$$

In case $C_{l,max}$ is not known, a value of 2 is used.

4.2.4 Load Case D: Maximum Thrust

The thrust acting on the rotor is parallel to the rotor shaft and has maximum value calculated by the following formula:

$$F_{x-shaft} = 3.125\rho\pi C_T R^2 V_{ave}^2 \tag{4.13}$$

Where C_T is the thrust coefficient, equal to 0.5.

4.2.5 Load Case E: Maximum Rotational Speed

The centrifugal forces and rotor unbalance induce forces in the blades and bending moment in the shaft, respectively, calculated by the equations below.

$$F_{zB} = m_B R_{cog} {\omega^2}_{n,max} \tag{4.14}$$

$$M_{shaft} = m_r e_r L_{rb} {\omega^2}_{n,max} + m_r g L_{rb} \tag{4.15}$$

4.2.6 Load Case F: Short at Load Connection

In the case of a short circuit in the generator, a high torque is generated on the rotor shaft due to the generator's short circuit torque. This torque is calculated as follow:

$$M_{x-shaft} = GQ_{des} \tag{4.16}$$

$$M_{xB} = \frac{M_{x-shaft}}{B} \tag{4.17}$$

In the absence of any accurate value, G is taken to be equal to 2.

4.2.7 Load Case G: Shutdown (Braking)

Load case G is assumed that the brakes are applied while the generator is still delivering the design torque. The formulae give the torque generated by applying the brakes (mechanical or electrical).

$$M_{x-shaft} = M_{brake} + Q_{des} \tag{4.18}$$

$$M_{xB} = \frac{M_{x-shaft}}{B} + m_B R_{cog} g \tag{4.19}$$

In the current design, M_{brake} is assumed to be thrice Q_{des}.

4.2.8 Load Case H: Parked Wind Loading

In load case H, the turbine is considered to be parked in a normal way. In this case, the loads are found by the following formulae:

$$M_{yB} = 0.25\rho C_d A_{proj,B} {V^2}_{e50} R \tag{4.20}$$

Where C_d is taken to be 1.5, and

$$V_{e50} = 1.4 V_{ref} \tag{4.21}$$

The thrust load is calculated by the formula,

$$F_{x-shaft} = 0.5\rho B C_d A_{proj,B} {V^2}_{e50} \tag{4.22}$$

4.2.9 Load Case I: Parked Wind Loading, Maximum Exposure

If the yaw mechanism fails, the turbine is subjected to wind from all directions. To take into account this fact when designing blades, nacelle, tower, and tail, the forces must be considered to be induced when the component is in its worse position; that is, the position that yield the greatest force. This force is given by

$$F = 0.5\rho C_f A_{proj,B} {V^2}_{ref} \tag{4.23}$$

Where C_f is the force coefficient that may result from lift or drag.

4.2.10 Load Case J: Transportation, Assembly, Maintenance and Repair

These loads are due to transportation, assembly, maintenance, and repair of the system. Therefore it will not be considered.

4.3 Stress Calculation

4.3.1 Axial Loads

For the turbine blade:

$$\sigma_{zB} = \frac{F_{zB}}{A_B} \tag{4.24}$$

For rotor shaft:

$$\sigma_{x-shaft} = \frac{F_{x-shaft}}{A_{shaft}} \tag{4.25}$$

4.3.2 Bending

$$\sigma_{MB} = \frac{\sqrt{M^2{}_{xB} + M^2{}_{yB}}}{W_B} \tag{4.26}$$

For turbine blade with rectangular root:

$$\sigma_{MB} = \frac{M_{xB}}{W_{xB}} + \frac{M_{yB}}{W_{yB}} \tag{4.27}$$

For the rotor shaft:

$$\sigma_{M-shaft} = \frac{M_{shaft}}{W_{shaft}} \tag{4.28}$$

4.3.3 Shear

The shear stress acting on the blades can be ignored. Therefore only shear stress in the rotor shaft is calculated.

Rotor shear stress:

$$\tau_{M-shaft} = \frac{M_{x-shaft}}{2W_{Shaft}} \tag{4.29}$$

4.3.4 Stress Combination

The following formulae are used to obtain the total stresses acting in the elements:

For turbine blade

$$\sigma_{eqB} = \sigma_{zB} + \sigma_{MB} \tag{4.30}$$

For rotor shaft

$$\sigma_{eq} = \sqrt{\left(\sigma_{x-shaft} + \sigma_{M-shaft}\right)^2 + 3\tau^2{}_{M-shaft}} \tag{4.31}$$

4.3.5 Limit State Analysis

Ultimate Strength Analysis

The design stress can be obtained from the ultimate strength by the following expression:

$$\sigma_d \leq \frac{f_k}{\gamma_m \gamma_f} \tag{4.32}$$

According to the IEC61400-2 standard, γ_m and γ_f must be equal to 3.

Fatigue Failure

According to Miner's rule, the accumulated damage throughout a turbine's lifetime must be less than or equal to one.

$$Damage = \sum_{i=0}^{n} \frac{n_i}{N\left(\gamma_m \gamma_f s_i\right)} \tag{4.33}$$

$$n_i = \frac{B n_{des} T_d}{60} \tag{4.34}$$

Where T_d is the turbine's design life in seconds; in the present study, according to the current standard γ_m must be equal to 3 (it is assumed that the materials used were tested according to the engineering standards for testing materials), and γ_f is equal to 1.0.

4.4 Blade Structure Preliminary Design

The preliminary blade geometric proprieties were obtained from CAD software (SolidWorks) and XFoil. The data obtained is as follows:

$m_B = 34.4$ kg
$R_{Cog} = 1.6315$ m
$L_{rb} = 0.075$ m
$L_{rt} = 5$ cm
$Q_{des} = 506$ Nm
$I_B = 124.58$ kgm^2
$\lambda_{des} = 6.5$
$R = 3.5$ m
$A_B = 108$ cm^2
$W_{yB} = 81.80$ cm^3
$W_{xB} = 2384.56$ cm^3

4.4.1 Blade Preliminary Loads

Load Case A

$\eta = 0.6 + 0.005 \cdot 10 = 0.65$
$Q_{des} = \dfrac{10000}{19.5 \cdot 0.65} = 789$ Nm
$\Delta F_{zB} = 2 \times 34.4 \times 1.6315 \times 19.5^2 = 42.682$ kN

$$\Delta M_{xB} = \frac{789}{3} + 2 \times 34.4 \times 1.6315 \times 9.81 = 1.364 \text{ kNm}$$

$$\Delta M_{yB} = \frac{6 \times 789}{3} = 1.578 \text{ kNm}$$

$$\Delta F_{x-shaft} = \frac{3}{2} \times \frac{6 \times 789}{3} = 2.367 \text{ kN}$$

Load Case B

$\omega_{yaw,max} = 3 - 0.01\left(\pi \times 3.5^2 - 2\right) = 2.635$ rad/s

$$M_{yB} = 34.4 \times 1.6315 \times 0.05 \times 2.635^2 + 2 \times 124.58 \times 2.635 \times 19.5 + \frac{3.5}{9} \times 2367 = 13.742 \text{ kNm}$$

Load Case C

$$M_{yB} = \frac{1}{8} \times 1.225 \times 0.22 \times 3.5 \times 2 \times 3.5^3 \times 19.5^2 \times \left[1 + \frac{4}{3 \times 6.5} + \left(\frac{1}{6.5}\right)^2\right] = 4.724 \text{ kNm}$$

Load Case D

$F_{x-shaft} = 0.5 \times 3.125 \times 1.225 \times 7.5^2 \times \pi \times 3.5^2 = 4143.47$ Nm

Load Case E

$F_{zB} = 34.4 \times 1.6315 \times 30^2 = 50.511$ kN

Load Case F

$$M_{xB} = \frac{2 \times 789}{3} = 526 \text{ Nm}$$

Load Case G

$$M_{xB} = \frac{3 \times 789}{3} + 34.4 \times 1.6315 \times 9.81 = 1.340 \text{ kNm}$$

Load Case H

$M_{yB} = 0.25 \times 1.225 \times 1.5 \times 0.22 \times 3.5 \times 52.5^2 \times 3.5 = 3.412$ kNm

The thrust is given by

$$\begin{aligned} F_{x-shaft} &= B \times C_d \frac{1}{2} \rho V_{e50} A_{proj,B} \\ F_{x-shaft} &= 3 \times 1.5 \times \frac{1}{2} \times 1.225 \times 52.5^2 \times 3.5 \times 0.22 = 5.850 \text{ kN} \end{aligned}$$

According to IEC for wind class C, $V_{e50} = 52.5$ m/s.

Load Case I

$F = 0.5 \times 1.225 \times 1.5 \times 0.22 \times 3.5 \times 37.5^2 = 995$ N

4.4.2 Preliminary Blade Stresses

Load Case A According to IEC 61400-2, only load case A is considered in the fatigue analysis.
The stresses due to load case A are as follow:

Axial stress

$$\sigma_{zB} = \frac{F_{zB}}{A_B} = \frac{42682}{108 \times 10^{-4}} \approx 3.606 \text{ MPa}$$

Bending stress

$$\sigma_{MB} = \frac{M_{xB}}{W_{xB}} + \frac{M_{yB}}{W_{yB}} = \frac{1364}{2384.56 \times 10^{-6}} + \frac{1578}{81.80 \times 10^{-6}} \approx 19.863 \text{ MPa}$$

$$\sigma_{eq} = \sigma_{zB} + \sigma_{MB} = 3.606 + 19.863 = 23.469 \text{ MPa}$$

According to [70], the maximum equivalent stress under which the material will not fail due to fatigue can be found by the formula,

$$\sigma_{eq,max} = \frac{\sigma_y}{2}\left(\sqrt{\left(\frac{\sigma_y}{\sigma_l}\right)^2 + 4} - \frac{\sigma_y}{\sigma_l}\right) \tag{4.35}$$

Where σ_y is the yield stress of the blade material, and σ_l is the endurance limit.

Aluminium 7075 has a fatigue limit of 159 MPa at 5×10^8 cycles when the stress applied for fatigue is completely reversed. And it has yield and tensile strength of 503 and 572 MPa, respectively. Therefore,

$$\sigma_{eq,max} = \frac{503}{2}\left(\sqrt{\left(\frac{503}{159}\right)^2 + 4} - \frac{503}{159}\right) = 145.666 \text{ MPa}$$

Dividing the obtained equivalent fatigue load by a factor of 1.25 as recommended by IEC 61400-2, we have,

$$\sigma_{des} = \frac{145.666}{1.25} = 116.533 \text{ MPa}$$

.
The fatigue design stress is greater than the induced fatigue stress; therefore, the blade will not fail due to fatigue.

Load Case B

$$\sigma_{MB} = \frac{M_{yB}}{W_{yB}} = \frac{13742}{81.80 \times 10^{-6}} = 167.995 \text{ MPa}$$

Load Case C

$$\sigma_{MB} = \frac{M_{yB}}{W_{yB}} = \frac{4724}{81.8 \times 10^{-6}} = 57.751 \text{ MPa}$$

Load Case E

$$\sigma_{eq} = \frac{F_{zB}}{A_B} = \frac{50510}{108 \times 10^{-4}} = 4.677 \text{ MPa}$$

Load Case F

$$\sigma_{MB} = \frac{M_{xB}}{W_{xB}} = \frac{526}{2384.56 \times 10^{-6}} = 0.221 \text{ MPa}$$

Load Case G

$$\sigma_{MB} = \frac{M_{xB}}{W_{xB}} = \frac{1340}{2384.56 \times 10^{-6}} = 0.562 \text{ MPa}$$

Load Case H

$$\sigma_{MB} = \frac{M_{yB}}{W_{yB}} = \frac{3412}{81.80 \times 10^{-6}} = 41.712 \text{ MPa}$$

4.4.3 Effect of Changing Blade's Dimensions on the Power Coefficient

The blade has to be optimized to operate efficiently at lowest possible weight. To proceed with blade optimization, the effect of changing the blade's dimension on the power coefficient needs to be analyzed. To accomplish this task QBlade was used. The setting for this analysis are very similar to that used in the aerodynamic study in the previous chapter. Firstly, the blade length is fixed to 3.5 m and the chord length is varied from 20 to 27.5 cm with a step of 2.5, and then the chord is fixed to 25 cm while varying the blade's length from 3 to 4 m with a step of 0.5 m. Figures 4.2 and 4.3 shows that the blade's maximum power coefficient is not affected by increasing the chord length or blade radius they change only increases the area under the power coefficient with respect to tip speed ratio; that is, the turbine will have greater average power coefficient as the chord length or blade radius is increased. Since the turbine is designed to operate at maximum power coefficient it can be concluded that the change in the blade dimension will not affect the design.

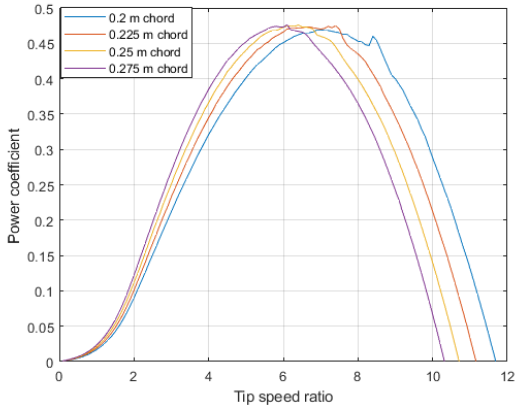

Figure 4.2: Variation of the power coefficient with chord length

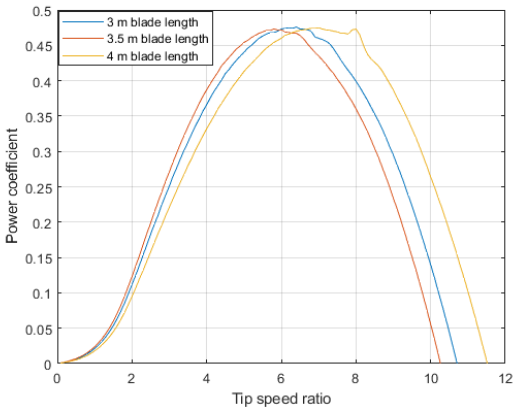

Figure 4.3: Variation of the power coefficient with blade length

4.4.4 Blade Optimization

The blade of the turbine is optimized to carry the critical loads with as minimum material as possible. For this purpose, the load cases that resulted in the high bending moment is considered. In this case, only load case study H of IEC 61400-2 is considered, since load case B and C give high-stress values that the blade has to be controlled to avoid high gyroscopic load, that is, brakes have to be applied to reduce the rotor rotational speed before it is allowed to yaw.

Problem Description

The blade of the wind turbine under study is to be designed to deliver 10 kW of electrical power when the wind is blowing at a speed of 10.5 m/s. The blade is to carry a load as specified in the code standard IEC 61400 part 2, with an appropriate factor of safety without failing. The radius of the blade should be in the range of 1 to 10 m, and the chord ranges from 1 to 50 cm. The aim is to design the blade for minimum weight.

Definition of the Design Variables

The blade is assumed to be made of a uniform cross-sectional area. Therefore, only two variables are needed to express the blade optimization studies, namely, the chord length and the blade radius.

x_1– Airfoil chord length (meters);
x_2– Blade radius (meters).

Data and Information Collection

The geometrical proprieties of the blade cross-section were derived from SolidWorks. The values obtained which are relevant for this study are as follow:

$$A_B \approx kx_1^2 \text{ (cm}^2\text{)}; \tag{4.36}$$
$$W_{yB} \approx 8.486546 \times 10^{-4} x_1^3 \text{ (cm}^3\text{)}; \tag{4.37}$$
$$k \approx 6.87 \times 10^{-2}. \tag{4.38}$$

The power produced by the turbine can be estimated by the formula,

$$P = 0.5\rho\eta\pi Cp(x_2 - x_3)^2 U^3 \tag{4.39}$$

The formula given for load case H can be expressed in two parts one for the root section and another for the section of the blade where the root is connected to the body. The formulae are given below.

$$M_{yB} = \frac{1}{4}\rho C_d U_{e50}^2 x_1 x_2^2 \tag{4.40}$$

Other useful formulae are

$$\sigma = \frac{M_{yB}}{W_y}; \tag{4.41}$$
$$1 \leq x_3 \leq 5; \tag{4.42}$$
$$0.1 \leq x_1 \leq 0.5; \tag{4.43}$$
$$\sigma_{des} = \frac{\sigma_u}{3.3}. \tag{4.44}$$

Optimization Criteria

The goal is to minimize the weight of the blade. Since the density is constant, the objective function for this particular problem is the volume of the blade, and it is given by,

$$f(x_1, x_2, x_3) = kx_1^2(x_2 - x_3) \tag{4.45}$$

Formulation of the Constrains

The first two constrains are due to the fact that the blade should be able to withstand load case H, that means

$$\sigma_{des} \geq \frac{1}{4}\rho C_d U_{e50}^2 x_1 x_2^2 \times \frac{10^4}{8.486546 x_1^3} \tag{4.46}$$

The geometric constrains are as follow:

$$1 \leq x_3 \leq 5; \tag{4.47}$$
$$0.1 \leq x_1 \leq 0.5; \tag{4.48}$$
$$x_4 \geq x_1 + 0.02; \tag{4.49}$$
$$x_5 \geq 0.1x_1 + 0.015. \tag{4.50}$$

The final constraint come from the need for the blade to produce at least 10 kW of electrical power, therefore,

$$P = 0.5\rho\eta\pi Cp(x_3 - x_2)^2 U^3 \geq 10^4 \tag{4.51}$$

MatLab Solution for the Blade Optimization Problem

The solution for the blade optimization problem above discussed was obtained using the optimization tools available in MatLab. The procedures to obtain it is described below.

The nature of the current problem clearly shows that we are dealing with a non-linear constrained problem. Therefore, the solver **fmincon** is used. First, a function called *nlcons*, in *.m* file format, is created containing the constraint functions, reformulated to the standard form for minima optimization problems. This file also contain the gradients of the constraint functions.

Next, another *.m* file was created having all the parameters needed for $fmincon$ solver to solve the problem, namely: $@(x)\ 6.87 \times 10^{-2} * x(1) * x(2)^2$ was the objective function; $x0 =$ [0.1 1 0.5] for the initial conditions; $lb =$ [0.1 1 0.5] for the lower boundary; $ub =$ [0.5 5 0.75] for the upper boundary; $A =$ [ ] and $b =$ [ ] for linear inequality constraint; $Aeq =$ [ ] and $beq =$ [ ] for linear equality constant; $nonlincon = @nlcons$ for inequality constraint; the options was set to $options =$ optimoptions(@fmincon,'MaxFunctionEvaluations',1e6, 'MaxIterations',$1e6$,'StepTolerance',$1e-6$,'OptimalityTolerance',$1e-9$). The rest remained as default. At this starting point the solver did not converged to a solution point. Therefore the *GlobalSearch* solver needed to be used.

Step two of the last paragraph was repeated, but this time it was done in the MatLab Command Window to solve the problem using the *GlobalSearch* solver. Next *GlobalSearch* was assigned to gs; that is $gs = GlobalSearch$. Finally it was run as follow: $[x, f, exitflag, output, solution] = run(gs, P1)$. The file used to solve this problem is found in Appendix A.3. Below is the result obtained.

exitflag =
1

output = struct with fields:
funcCount: 11864
localSolverTotal: 24
localSolverSuccess: 24
localSolverIncomplete: 0
localSolverNoSolution: 0
message: 'GlobalSearch stopped because it analyzed all the trial points. All 24 local solver runs converged with a positive local solver exit flag.'

solution =
1×4 GlobalOptimSolution array with properties:

X Fval Exitflag Output X0
The result for the global optimization was as follow

$$\begin{aligned} x_1 &= 0.2875 \\ x_2 &= 3.4259 \\ x_3 &= 0.500 \\ f &= 0.0122 \end{aligned}$$

4.5 Rotor Shaft Preliminary Design

Just as in the case of the blades' design, the preliminary shaft design will also be considered using IEC 61400-2 standard. The load cases presented in Secs. 4.2 and 4.3 will be considered, where it is applicable. The following data were obtained using CAD 3D modeller (SolidWorks). The initial values to calculate the shaft loads are given below.

$$\begin{aligned} I_B &= 124.58 \text{ kgm}^2 \\ L_{rB} &= 0.075 \text{ m} \\ m_r &= 119.26 \text{ kg} \\ \omega_{yaw} &= 2.672 \text{ rad/s} \\ \Delta F &= 675 \text{ N} \\ e_r &= 0.005R = 0.005 \times 3.5 = 17.5 \text{ mm} \\ d_{shaft} &= 80 \text{ mm} \end{aligned}$$

4.5.1 Preliminary Shaft Fatigue Analysis

According to IEC 61400-2 only load case A is considered in the fatigue analysis.

Load Case A

$$\Delta F_{x-shaft} = \frac{3}{2} \cdot \frac{6.5 \cdot 789}{3.5} = 2.198 \text{ kN}$$

$$\Delta M_{x-shaft} = 789 + 2 \cdot 9.81 \cdot 119.26 \cdot 0.005 \cdot 3.5 = 830 \text{ Nm}$$

$$M_{shaft} = 2 \times 119.26 \times 9.81 \times 0.075 + \frac{3.5}{6} \times 2198 = 1.458 \text{ kNm}$$

4.5.2 Preliminary Shaft Ultimate Stress Analysis

Load Case B

$$M_{yB} = 3 \cdot 124.58 \cdot 2.635 \cdot 19.5 + 119.26 \cdot 9.81 \cdot 0.075 + \frac{3.5}{6} \cdot 2198 = 20.5 \text{ kNm}$$

Load Case D

$$F_{x-shaft} = 0.5 \cdot 3.125 \cdot 1.225 \cdot 7.5^2 \cdot \pi \cdot 3.5^2 = 4.14 \text{ kN}$$

Load Case E

$M_{shaft} = 119.26 \cdot 0.075\,(\cdot 9.81 + 0.005 \cdot 3.5 \cdot 30^2) = 228.6$ Nm

Load Case F

$M_{x-shaft} = 2 \cdot 789 = 1578$ Nm

Load Case G

$M_{x-shaft} = 3 \cdot 789 = 2367$ Nm

Load Case H

$F_{x-shaft} = 3 \cdot 1.5 \cdot \frac{1}{2} \cdot 1.225 \cdot 52.5^2 \cdot 0.22 \cdot 3.5 = 5.85$ kN

Shaft Dimensions Load Case B gives the highest moment. Therefore, it is used to calculate the shaft dimensions.

$$W_{shaft} = \frac{M_{shaft}}{\sigma_{eq}} = \frac{20495 \times 3.3}{572} = 118.24 \text{ cm}^3$$

For the solid shaft, the diameter is given by

$$D_{shaft} = \sqrt[3]{\frac{32 \cdot W_{shaft}}{\pi}} \tag{4.52}$$

Therefore, the diameter of the shaft will be

$$D_{shaft} = \sqrt[3]{\frac{32 \cdot 118.24}{\pi}} = 10.64 \text{ cm}$$

Since the shaft is to be threaded, its diameter has to have a standard dimension. The next more significant standard dimension available is 12 cm.

$$\begin{aligned} A_{shaft} &= \frac{\pi \cdot 12^2}{4} = 113.1 \text{ cm}^2 \\ I_y &= \frac{\pi \cdot 12^4}{64} = 1018 \text{ cm}^4 \\ W_y &= \frac{2 \times 1018}{12} = 169.65 \text{ cm}^3 \end{aligned}$$

4.5.3 Shaft Stresses

Load Case A

$$\sigma_{x-shaft} = \frac{2.198}{113.1} = 194.34\ kPa$$

$$\sigma_{M-shaft} = \frac{1458}{169.65} = 8.594\ MPa.$$

$$\tau_{M-shaft} = \frac{830}{169.65} = 4.892\ MPa$$

The equivalent stress is

$$\sigma_{eq} = \sqrt{(0.19434 + 8.594)^2 + 3 \times 4.892^2} = 12.208\ MPa.$$

Assuming full characterization of the material, a factor of safety of 1.25 can be used as suggested by standard IEC 61400-2. Therefore

$$\sigma_{eq} = 12.208 \cdot 1.25 = 15.260\ MPa$$

A factor of safety of 1.25 is used as suggested by standard IEC 61400-2. Therefore, Let us check the shaft material fatigue strength and compare it with the obtained value to see if the shaft will fail due to fatigue. According to Eq. (9.59b) of reference [82] the maximum equivalent stress that the material can safely carry is given by,

$$\sigma_{eq,max} = \frac{\sigma_y}{2}\left(\sqrt{\left(\frac{\sigma_y}{\sigma_l}\right)^2 + 4} - \frac{\sigma_y}{\sigma_l}\right) \tag{4.53}$$

Where σ_y = yield strength; σ_l =endurance limit.

Let ASTM-A574 be assigned to be the shaft material. Therefore, we have $\sigma_y = 700$ MPa and $\sigma_l = 200$ MPa.

Hence,

$$\sigma_{eq,max} = \frac{700}{2}\left(\sqrt{\left(\frac{700}{200}\right)^2 + 4} - \frac{700}{200}\right) = 185.8951 \text{ MPa}$$

Since the maximum equivalent stress $\sigma_{eq,max}$ is about twelve times greater than the equivalent induced stress σ_{eq}, the shaft will not fail due to fatigue.

Load Case B

$$\sigma_{eq} = \frac{20.495}{169.65} = 169.59 \text{ MPa}$$

Load Case D

$$\sigma_{eq} = \frac{4140}{113.1} = 366 \text{ kPa}$$

Load Case E

$$\sigma_{eq} = \frac{228.6}{169.65} = 1.347 \text{ MPa}$$

Load Case F

$$\sigma_{eq} = \frac{\sqrt{3}M_{x-shaft}}{2W_{shaft}} = \frac{\sqrt{3} \times 1578}{2 \times 169.65} = 8.055 \text{ MPa}$$

Load Case G

$$\sigma_{eq} = \frac{\sqrt{3}M_{x-shaft}}{2W_{shaft}} = \frac{\sqrt{3} \times 2367}{2 \times 98.1748} = 12.083 \text{ MPa}$$

Load Case H

$$\sigma_{eq} = \frac{5.85}{113.1} = 517.241 \text{ kPa}$$

4.6 Tower Preliminary Design

The towers usually used in small wind turbines are tubular steel towers, lattice towers, and guyed towers. Guyed and lattice towers have been predominant, but recently tubular towers have been taking over because they do not need guy-wires. Table 4.2 below illustrates the advantages and disadvantages of each tower.

A tapered tubular tower with an octal cross-section will be designed to withstand the wind and the turbine loads in the current section. This section aims to estimate the buckling capacity, stresses, defection, fatigue, natural frequency, and tower mass. Later on, the tower will be optimized to reduce its weight and cost.

The simple load model from IEC-61400-2 will be used to design the tower preliminarily. Considering load cases A, B, and H. Since load case H represents a situation when the tower has to withstand an extreme wind load, it will result in the highest stress that the turbine can expect, as compared to other loads. Therefore, load case H will be used to design the turbine.

4.6.1 Tower Model

The tower will be subjected to the wind's drag forces due to the blades and the tower from load case H. The rotor is considered to be parked. The blade forces in load case H was already calculated in Sec. 4.4. For simplicity of analysis, the wind speed will be assumed to be constant.

Table 4.2: Type of towers for small wind turbines

Type	**Advantages**	**Disadvantages**
Guyed	Cheap, lightweight, good ground for lightning, adjustable tower stiffness through the wires tension.	Susceptible to vandalism, not used in urban areas.
Lattice	Low transportation cost, assembled on site.	Low lifetime due to corrosion.
Tubular	Good aesthetics.	Heaviest among other types, high manufacturing and transportation costs.

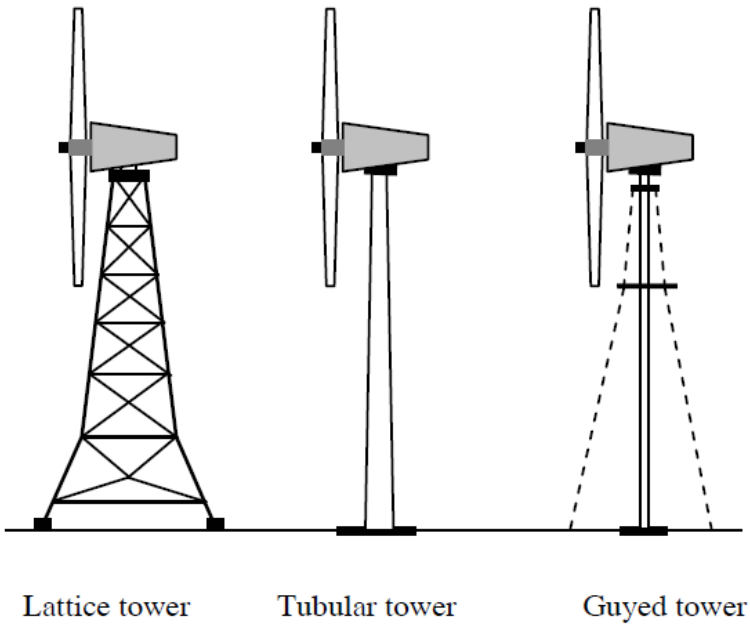

Figure 4.4: Tapes of tower for SWT [17]

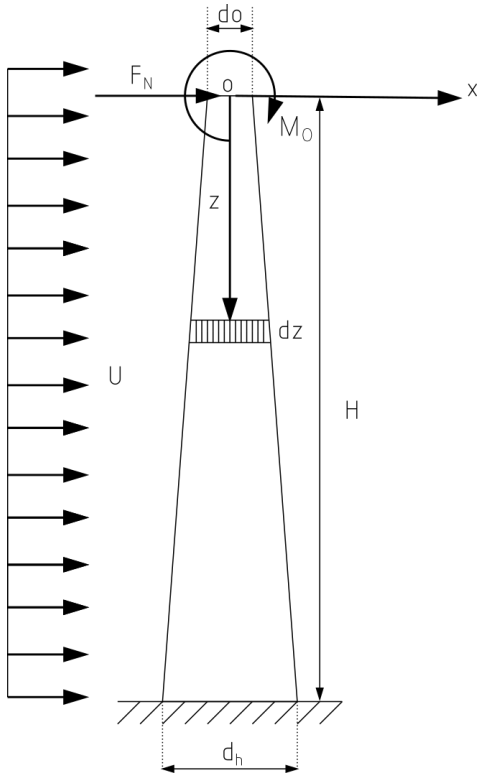

Figure 4.5: Tapered tower model

The drag force in each section of the tower is given by,

$$dF_D = 0.5\rho C_D U^2 D(z) dz \tag{4.54}$$

If we assume that the tower diameter varies linearly with height, we can write

$$D = \frac{d_h - d_o}{H} z + d_o \tag{4.55}$$

From Eqs. (4.55) and (4.54), and using Figure 4.5, we can obtain the equation of moment as follow:

$$M = M_0 + F_N z + 0.5\rho C_D U^2 \left(\frac{d_0}{2} z^2 + \frac{d_1}{6} z3 \right) \tag{4.56}$$

Where,

$$d_1 = \frac{d_h - d_o}{H} \tag{4.57}$$

The bending stress at any section is given by

$$\sigma_b = \frac{M(z) D(z)}{2I(z)} \tag{4.58}$$

The second moment of area for octal cross section is given by

$$I(z) = \frac{10 + 6\sqrt{2}}{24\left(1+\sqrt{2}\right)^3}\left[D^4(z) - (D(z) - 2t)^4\right] \tag{4.59}$$

The axial stress due to the weight of the tower and turbine is

$$\sigma_a = \frac{(m_{tb} + m_{tw})\, g}{A(z)} \tag{4.60}$$

Where

$$A(z) = \frac{2}{1+\sqrt{2}}\left[D^2(z) - (D(z) - 2t)^2\right] \tag{4.61}$$

$$m_{tw} = \frac{8\rho t}{1+\sqrt{2}}\left[\frac{d_1}{2}z^2 - (d_o - t)\, z\right] \tag{4.62}$$

For buckling of tower of small wind turbine, Wood [82] used guidelines from ASCE, which correlates the experimental results of regular polygon sections to find the limiting values of $\frac{a}{t}$, where a is the side length. For octagonal cross section a is given by

$$a = \frac{D}{1+\sqrt{2}} \tag{4.63}$$

From the above-mentioned guidelines, the buckling conditions are expressed as follows:

$$\frac{a}{t}\sqrt{\sigma_y} < \begin{cases} 680 & for\ \sigma_a < 6.9\ \text{MPa} \\ 630 & otherwise \end{cases} \tag{4.64}$$

with σ_a given in MPa.

If inequality (4.65) holds, there will be no buckling [82]. If the left-hand side of inequality (4.65) is greater than the right-hand side but less than 960, the buckling will be analyzed by the following expression:

$$\sigma < \begin{cases} 1.42\sigma_y\left(1 - 4.34\times 10^{-4}\frac{a}{t}\sqrt{\sigma_y}\right) & for\ \sigma_a < 6.9\ \text{MPa} \\ 1.45\sigma_y\left(1 - 4.91\times 10^{-4}\frac{a}{t}\sqrt{\sigma_y}\right) & otherwise \end{cases} \tag{4.65}$$

The capacity factor is given by

$$CF = \frac{\sigma_{max}}{\sigma_A} \tag{4.66}$$

Where $\sigma_A = min(\sigma, \sigma_y)$. The value of capacity factor is normally less or equal to 0.6 [82].

The tower's deflection can be analyzed using beam theory, found in general Mechanics of

Materials textbooks. If the moment equation is integrated twice, we can find the deflection equation or solve the following differential equation:

$$\frac{d^2\delta}{dz^2} = \frac{M(z)}{EI(z)} \tag{4.67}$$

The value of the tower stiffness is found by dividing the maximum deflection to the thrust at the top of the tower. The natural system frequency is

$$\omega_n = \sqrt{\frac{k}{m}} \tag{4.68}$$

Where k is the stiffness and $m = m_{tower} + m_{turbine}$ or $m = 0.23m_{tower} + m_{turbine}$ [82].

4.6.2 Preliminary Tower Results

A Matlab code was created to calculate the tower parameters. The top and the base diameter, the tower thickness, and the tower height had to be set to start the calculations. The tower is set to have a height of 20 m. The values of the diameters and thickness had to be chosen to bear the loads with as minimum material and manufacturing costs as possible. For ease of manufacturing, the thickness is chosen to be constant. The base and top diameters and the thickness are to be chosen in a way that the capacity factor is to be less than 0.6.

As a help to chose D_h, D_o, and t, two graphs were plotted. Figure 4.6 represents the contour plot of the tower base area as a function of D and t, and Figure 4.7 represents the contour plot of the tower base second moment of area as a function of D and t. After some trial and error the following values were obtained: $D_h = 0.5$ m, $D_o = 0.2$ m and $t = 4.7$ mm. The material chosen for the tower is steel ASTM-A572 grade 50.

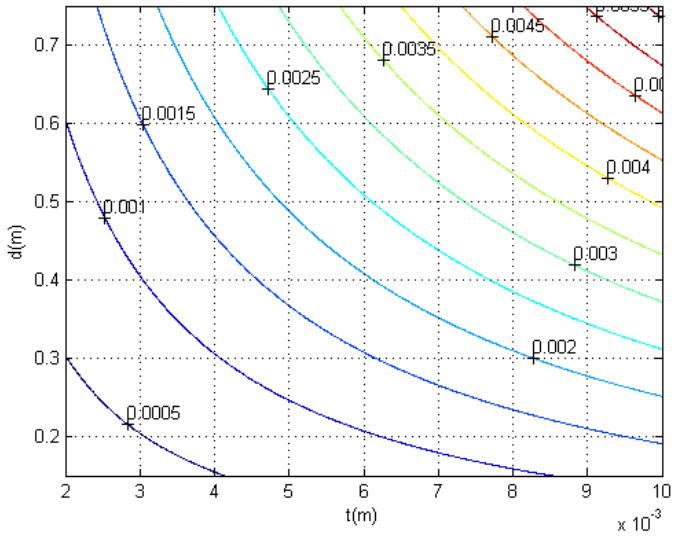

Figure 4.6: Contour plot of the tower base area

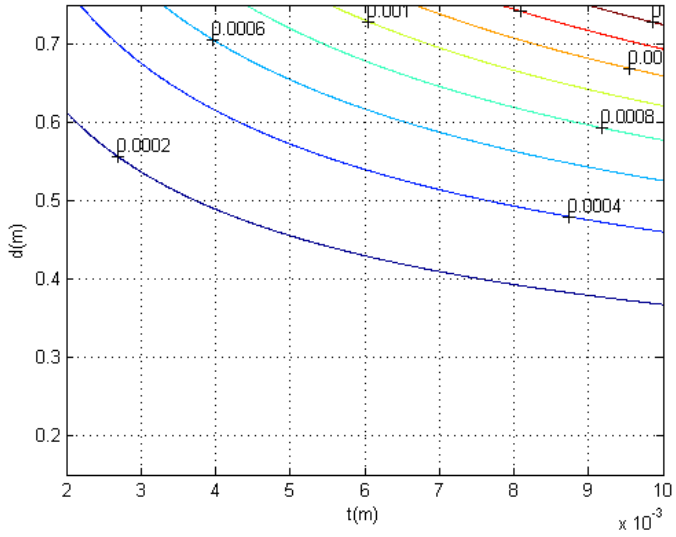

Figure 4.7: Contour plot of the tower base second moment of area

The deflection was found by solving the second-order differential equation. The equation was solved numerically by using a Matlab built-in function @ode45. Below is a snapshot of the result obtained:

Enter the value of the base diameter in meters; 0.5
Enter the value of the top diameter in meters; 0.2
Enter the value of the thickness in meters; 0.0047
Enter #1 to calculate the parameters for load case H: 1
The tower mass is 844.323 kg
The maximum buckling factor for load case H is, CF=0.585
The maximum stress factor for load case H is, CF=0.535
The maximum deflection for the load case H is 0.053 m
The maximum stress for the load case H is 184.726 Mpa
The natural frequency of turbine+tower for the load case H is 2.640 Hz
The natural frequency of turbine+0.23tower for the load case H is 3.759 Hz
Enter #2 to calculate the parameters for load case B: 2
The maximum buckling factor for load case B is, CF=0.169
The maximum stress factor for load case H is, CF=0.154
The maximum deflection for the load case H is 0.031 m
The maximum stress for the load case H is 53.296 Mpa
The natural frequency of turbine+tower for the load case H is 1.328 Hz
The natural frequency of turbine+0.23tower for the load case H is 1.891 Hz Enter #3 to calculate the parameters for load case A: 3
The maximum buckling factor for load case B is, CF=0.195
The maximum stress factor for load case H is, CF=0.179
The maximum deflection for the load case H is 0.039 m
The maximum stress for the load case H is 61.601 Mpa

The natural frequency of turbine+tower for the load case H is 1.228 Hz
The natural frequency of turbine+0.23tower for the load case H is 1.749 Hz
»

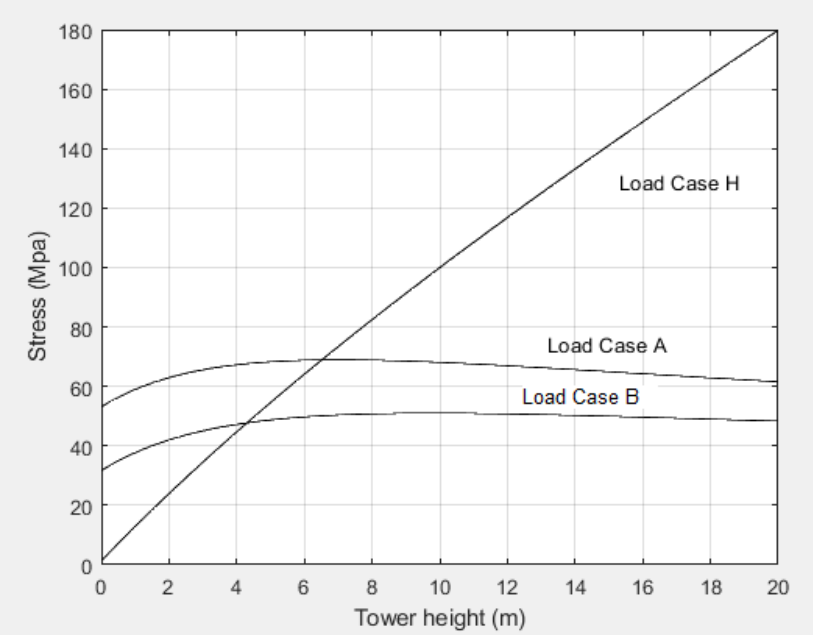

Figure 4.8: Tower stresses for load cases A, B and H

The full Matlab code is given in Appendix A.3.3.

4.7 Nacelle Preliminary Design

In this section, the nacelle model is discussed. The nacelle is the house of the turbine; therefore, it must protect the turbine components from the adverse ambient weather conditions. Here, the only condition of interest to model the nacelle is its ability to withstand extreme wind conditions.

4.7.1 Nacelle Model

Load case I can be used to estimate the load in the nacelle. If the force is assumed to act in the center of the projected area, the nacelle can be modeled as a rectangular frame, as shown in Figure 4.9.

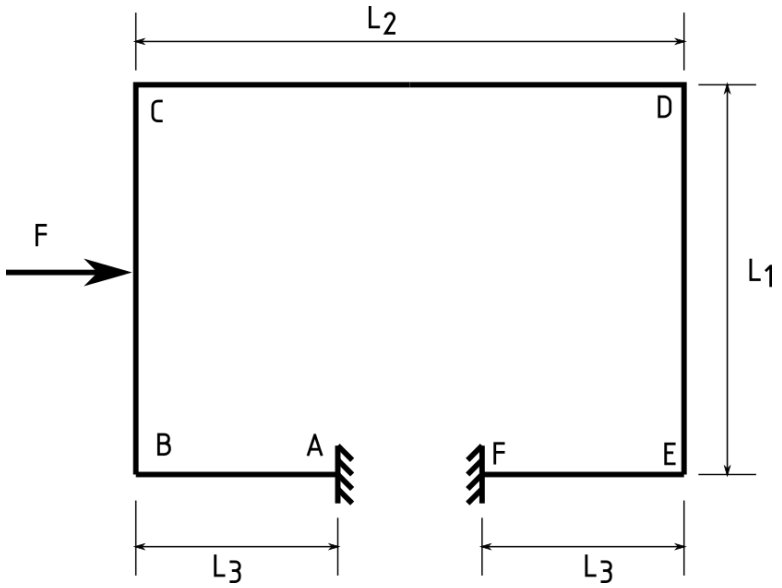

Figure 4.9: Nacelle model

The Nacelle dimensions are as follow: $L_1 = 700$ mm; $L_2 = 600$ mm; $L_3 = 225$ mm; $A_{proj} = 5950$ cm^2.

The force F is calculated by Eq. 4.23.

$$F = 0.5 \times 1.5 \times 1.225 \times 0.595 \times 37.5^2 = 768.74 \text{ N}$$

Solving the problem represented in Figure 4.10, we can find the maximum moment in the frame. The reactions forces and moments found are:

$$\begin{aligned} R_{Ax} &= 582.02 \text{ N}; \\ R_{Ay} &= 157.51 \text{ N}; \\ M_A &= 143.96 \text{ Nm}; \\ R_{Fx} &= 186.72 \text{ N}; \\ R_{Fy} &= 157.51 \text{ N}; \\ M_F &= 101.47 \text{ Nm}. \end{aligned}$$

The bending moment diagram is shown in Figure 4.11

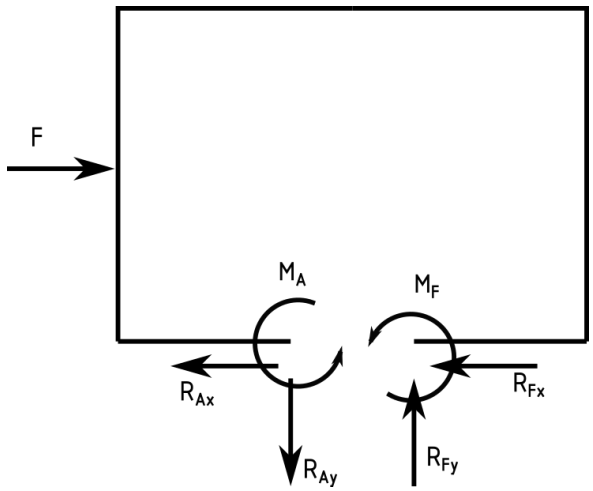

Figure 4.10: Nacelle free body diagram

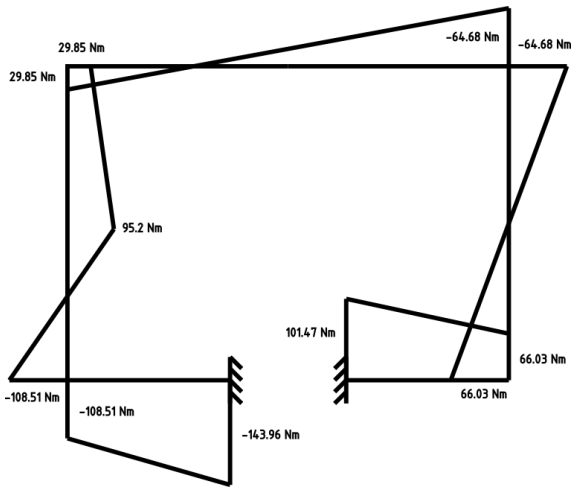

Figure 4.11: Nacelle bending moment diagram

4.7.2 Preliminary Cross Sectional Thickness of the Nacelle

Figure 4.11 clearly shows that the maximum load occurs at the support A. Therefore, it will be used to calculate the maximum stress in the nacelle. The nacelle stress element that undergoes the maximum stress is shown in Figure 4.12.

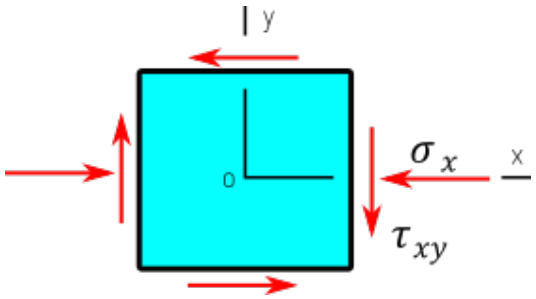

Figure 4.12: Stress element

The normal stress is given by

$$\sigma_x = \frac{6M_A}{db^2} + \frac{R_{Ax}}{db}, \tag{4.69}$$

$$\tau_{xy} = \frac{R_{Ay}}{db} \tag{4.70}$$

Where, $d = 0.85$ m.

The maximum stress is given by a modified version of Eq. 4.31, given bellow.

$$\sigma_{max} = \sqrt{{\sigma_x}^2 + 3{\tau_{xy}}^2} \tag{4.71}$$

Let us assume that the material to be used for nacelle is fiberglass vinyl ester, which has a ultimate strength of 550 MPa. Using a factor of safety of 3.3 the equivalent stress is

$$\sigma_{eq} = \frac{550}{3.3} = 166.67 \text{ MPa} \tag{4.72}$$

Letting $\sigma_{max} = \sigma_{eq}$, and substituting the values into the appropriate equations the thickness of the nacelle can be found. The result obtained is, $b = 0.00247129$ m. Therefore, the nacelle thickness should be equal or greater than 2.5 mm.

4.8 Mainframe preliminary design

Load case H is used because the blades experience the maximum load to model the turbine's mainframe. The blade and hub weight is assumed to be applied at the tip of the mainframe. The total load is assumed to be applied at the center of the mainframe. The thrust acts at the tip of the hub's nose. Therefore, when the load is transferred to the mainframe, it is assumed that besides the thrust, it also generates a moment, as the hub nose is offset from the mainframe's axis. Figure 4.13 shows the mainframe model.

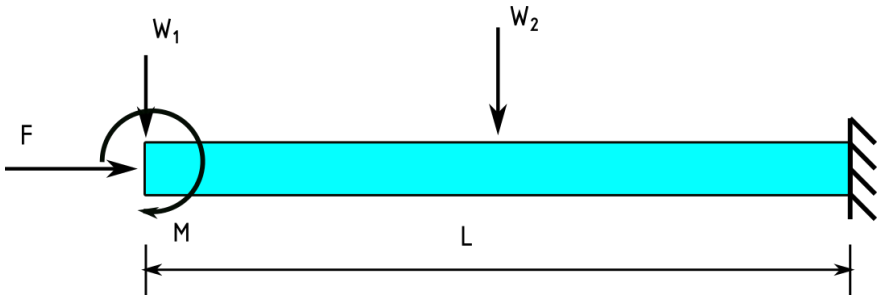

Figure 4.13: Main frame model

The hub nose and mainframe are offset by 278.5 mm, and the thrust in the shaft, obtained in load case H, is used. The mass of the turbine (except the tail and the rotor mass) $m_T = 326.72$ kg , and it was obtained from the CAD model. The mass of the rotor was already calculated previously, which was $m_r = 113.1$ kg, and $L = 850$ mm. Using these data, we have the following loads:

$$\begin{aligned} W_1 &= 1100 \text{ N} \\ W_2 &= 3205.1 \text{ N} \\ F &= 5850 \text{ N} \\ M &= 1629 \text{ Nm} \end{aligned}$$

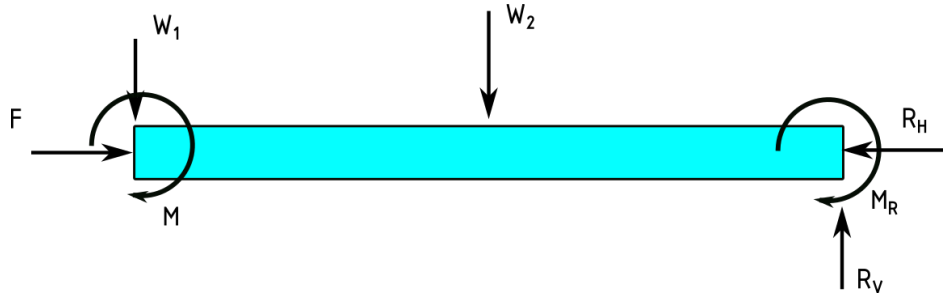

Figure 4.14: Main frame free body diagram

Figure 4.14 shows the model-free body diagram, which is a statically determined problem that can be easily solved to find the maximum shear force and bending moment. The result is presented in Figure 4.15 in the form of shear force and bending moment diagram.

Even though the maximum shear force occurs in the middle of the beam, it does not influence much in the calculation of the maximum stress because the shear stress is inversely proportional to the square of the thickness, and the bending stress is inversely proportional to the power of three of the thickness, since the magnitude of the shear stress and bending moment are not far apart from each other, therefore the bending moment has more impact in the calculation of the total stress than the shear force. Hence we can say that the maximum stress occurs at the tip of the beam.

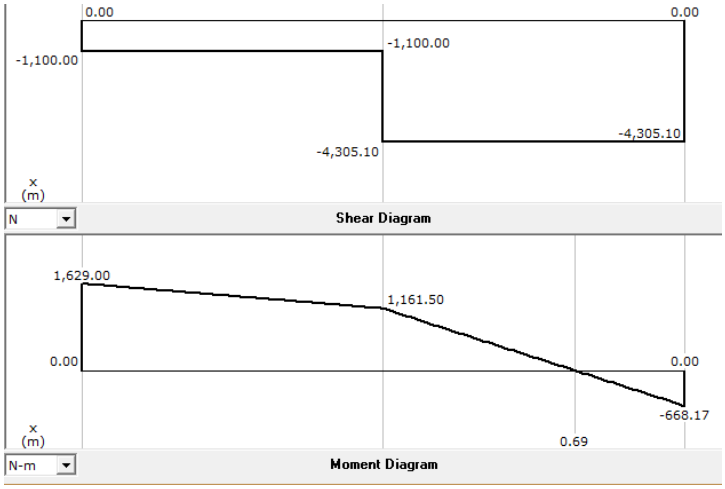

Figure 4.15: Main frame free body diagram

Let us assume that the mainframe has a rectangular cross-sectional area. Therefore the maximum stress is calculated from Eq. 4.71. Using the same procedure employed in Section 4.7.2 to calculate the thickness of the nacelle, we can find the minimum thickness required for the mainframe to withstand the loads. The value of the thickness was found to be $t = 0.01434$ m. Therefore, the value of 15 mm is used as the mainframe thickness.

4.9 Over-Speed Protection

Small wind turbine technology uses furling or pitching control method to control the turbine's produced power and to protect it against over-speed; in SWT, furling is the preferred method to accomplish those tasks. Pitching control can be done over a narrow range of wind speed, which improves the efficiency of the turbine because the power loss associated with a mean yaw angle is reduced and the yaw rate is lower than the furling method. However, the strong gyroscopic moments can upset the moment equilibrium. The pitch movement can be favored or opposed by the moment, depending on the sign of the yaw rate [83]. In the current study, furling control will be used. Therefore, pitch control will not be discussed any further.

4.9.1 Furling

The majority of small wind turbines use gravity and aerodynamic forces to protect the turbine against rotor over-speed and to control the turbine power. This passive method of controlling small wind turbine speed and power is called furling.

The mechanism used to furl small wind turbines is simple and straight forward. However, the mathematical model to describe the furling behavior is quite complex for the furling motion of the small wind turbine tail depend on many parameters such as wind speed and direction, the turbine geometry, the thrust generated by the rotor, the distance between the rotor's axis of rotation and furling axis, the geometry and dimensions of the tail (tail boom and vane).

Furling is achieved by offsetting the rotor axis of rotation from the yaw axis. This causes the rotor thrust to generate a moment in the yaw axis; consequently, it will tend to yaw the turbine. A tail fin mounted on a furling hinge generates a moment that balances the moment generated by the rotor thrust. When the wind speed increases, the thrust moment from the rotor increases, and it rotates the turbine away from the incoming wind. As the turbine turns away from the inflowing wind, the thrust generated decreases. Consequently, its moment decreases as well until it is balanced by the moment generated by the tail. The furling hinge allows the tail to be aligned with the wind speed while the rotor is yawing.

Audierne et al. [72] studied the dynamics of gravity-controlled furling systems based on the Lagrangian formalism. They used Xfoil to determine the aerodynamic forces acting on the tail vane, and BEM to calculate the aerodynamic forces on the blades. They accessed the impact of the axis tilt angles and the vane lever lengths on the wind speed values for entering and leaving the furling regime. In their study, firstly, the inflow speed was fixed, and the system was allowed to stabilize. The furling and yaw angles were recorded as a function of wind speed. Secondly, the constant wind speed signal was superimposed with a slow variation of input wind speed, and the dynamic response of the system was analyzed. The following paragraphs are a description of the coordinate system and formulae used in their study [72].

The detailed derivation of the furling behavior can be found in Audierne et al. work [72]. Here, only a brief explanation of the coordinate system used, as well as the final derived equations, are given.

Coordinate systems

Coordinate system $A(x_A, y_A, z_A)$ is a fixed coordinate system that coincides with the yaw axes. Where y_A points North and z_A points vertically downward. The x_A is obtained by applying the right-handed rule for the coordinate system. Coordinate system $B(x_B; y_B; z_B)$ is chosen to be attached to the turbine. Where y_B is parallel to the rotor axis of rotation, and $z_B = z_A$. Coordinate system $C(x_C; y_C; z_C)$ is attached to the furling axis of rotation. y_C is parallel to the tail boom when the furling angle is zero, and z_C is aligned with the furl axis pointing upwards.

The other quantities used are as follows: The distance L_1 is the distance between the furling and yaw axis. L_2 is the distance between the yaw and furl axis measured in the rotor's perpendicular direction. L_3 describes the distance between the tail's center of gravity and the furling axis. L_4 is the distance from rotor's center of mass to the yaw axis measured from a direction normal to the rotor's plane, and L_5 is the distance between the rotor's center of mass and the yaw axis measured from a axis parallel to the rotor. ΔL_3 is the distance between the center of gravity of the tail and its aerodynamic center. Finally, ΔL_4 is the distance between the rotor's aerodynamic center and its center of mass. Other symbols used are described below.

θ – yaw angle
ϕ – furling angle
ξ – wind speed angle
β – rotation around the x_B axis
γ – rotation around the y_C axis
δ – rotation around the x_C axis

Coordinator Systems Matrices

$$R_\theta = \begin{pmatrix} cos\,\theta & sin\,\theta & 0 \\ -sin\,\theta & cos\,\theta & 0 \\ 0 & 0 & 1 \end{pmatrix} \tag{4.73}$$

$$R_\beta = \begin{pmatrix} 1 & 0 & 0 \\ 0 & cos\,\beta & sin\,\beta \\ 0 & -sin\,\beta & cos\,\beta \end{pmatrix} \tag{4.74}$$

$$R_\gamma = \begin{pmatrix} cos\,\gamma & 0 & -sin\,\gamma \\ 0 & 1 & 0 \\ sin\,\gamma & 0 & cos\,\gamma \end{pmatrix} \tag{4.75}$$

$$R_\delta = \begin{pmatrix} 1 & 0 & 0 \\ 0 & cos\,\delta & sin\,\delta \\ 0 & -sin\,\delta & cos\,\delta \end{pmatrix} \tag{4.76}$$

$$R_\xi = \begin{pmatrix} cos\,\xi & sin\,\xi & 0 \\ -sin\,\xi & cos\,\xi & 0 \\ 0 & 0 & 1 \end{pmatrix} \tag{4.77}$$

$$R = R_\beta R_\gamma R_\delta \tag{4.78}$$

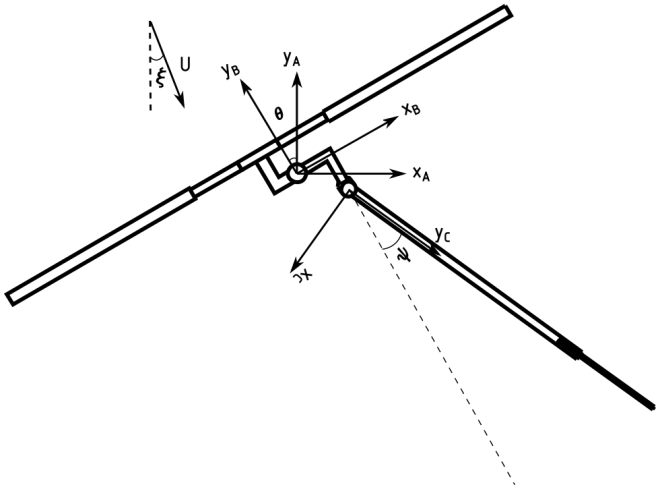

Figure 4.16: Turbine model (top view)

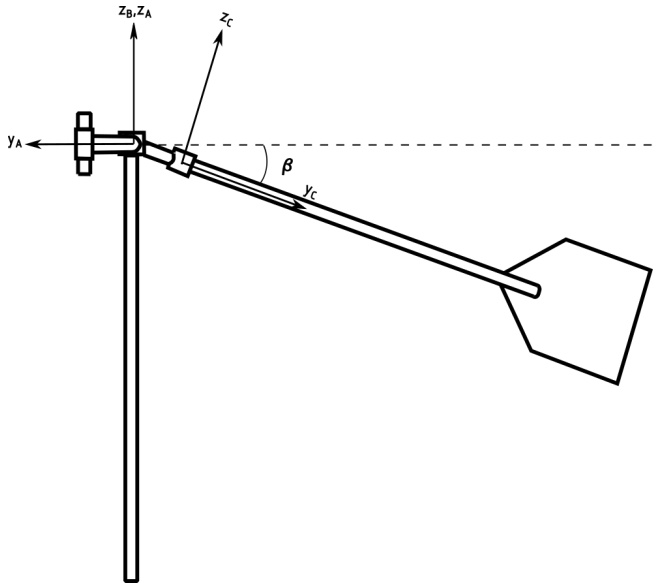

Figure 4.17: Turbine model (view normal the blade cross section)

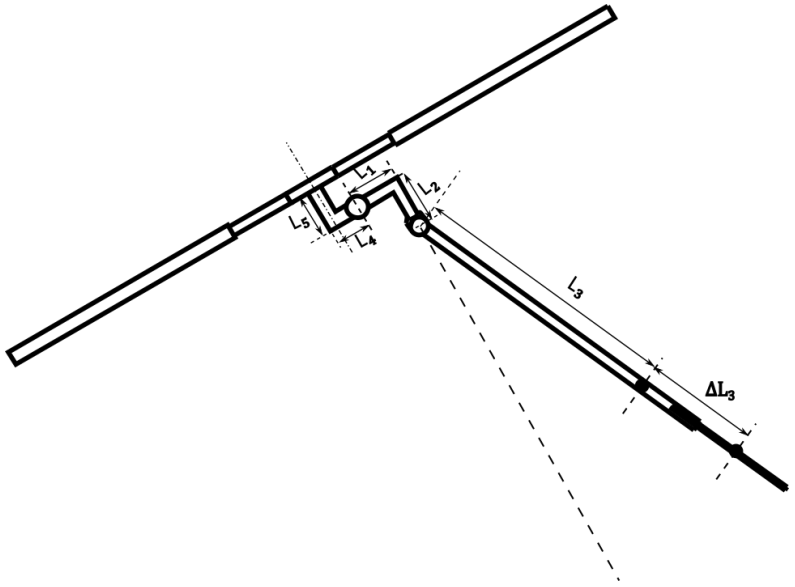

Figure 4.18: Turbine model basic dimensions (top view)

Equations of motion

Audierne in [72] derived the equation of motion of a turbine during furling from Lagrange formalism using θ to represent the angular motion of the generator around the yaw axis and ψ to describe the angular motion of the tail about the furling axis, as shown in Figure 4.16.

The equations were derived from general expression

$$Q_\theta = \frac{d}{dt}\left(\frac{\partial L}{\partial \dot{\theta}}\right) - \frac{\partial L}{\partial \theta} \tag{4.79}$$

$$Q_\psi = \frac{d}{dt}\left(\frac{\partial L}{\partial \dot{\psi}}\right) - \frac{\partial L}{\partial \psi} \tag{4.80}$$

$$L = T - V \tag{4.81}$$

Where T and V are the total kinetic and potential energy of the turbine system, respectively.

$$T = \frac{M_T}{2}\vec{\mathbf{V}}_T \cdot \vec{\mathbf{V}}_T + \frac{J_{ot}}{2}\vec{\boldsymbol{\omega}}_T \cdot \vec{\boldsymbol{\omega}}_T + \frac{J_{ot}}{2}\dot{\theta}_T^2 \tag{4.82}$$

But,

$$V_T = \frac{d\vec{\mathbf{r}}_T}{dt} \tag{4.83}$$

Where $\vec{\mathbf{r}}_T$ is expressed in the fixed reference frame. But $\vec{\mathbf{r}}_T$ can readily be expressed into coordinate seen from reference frame B as follow:

$$\mathbf{r}_T{}^{(B)} = L_1\mathbf{x}_B - L_2\cos\beta\ \mathbf{y}_B - L_2\sin\beta\ \mathbf{z}_B + L_3\sin\phi\ \mathbf{R}^{-1}\mathbf{x}_C + L_3\cos\phi\ \mathbf{R}^{-1}\mathbf{y}_C \tag{4.84}$$

Therefore $\vec{\mathbf{r}}_T^{(B)}$ needs to be defined in terms of coordinate system A through rotational transformation matrix. Thus,

$$\vec{\mathbf{r}}_T = \mathbf{R}_\theta{}^{-1}\vec{\mathbf{r}}_T^{(B)} \tag{4.85}$$

Substituting Eqs. (4.85) and (4.84) into (4.83), and after some mathematics operations, we have

$$V_T = \frac{\partial \mathbf{R}_\theta{}^{-1}}{\partial\theta}\vec{\mathbf{r}}_T^{(B)}\dot{\theta} + \mathbf{R}_\theta{}^{-1}\frac{\partial}{\partial\psi}\vec{\mathbf{r}}_T^{(B)}\dot{\psi} \tag{4.86}$$

The angular velocity of the tail as seen from reference frame A is a combination of the yaw and furling angular velocities. Therefore,

$$\vec{\boldsymbol{\omega}}_T = \dot{\psi}\,\mathbf{z}_C + \dot{\theta}\,\mathbf{z}_B \tag{4.87}$$

Substituting Eqs. (4.87) and (4.86) into (4.82) and after some manipulations we have,

$$T = \frac{1}{2}J_1\dot{\theta}^2 + \frac{1}{2}J_2\dot{\psi}^2 + J_3\dot{\theta}\dot{\psi} \tag{4.88}$$

Where

$$J_1 = M_T\left(\frac{\partial \mathbf{R}_\theta{}^{-1}}{\partial\theta}\vec{\mathbf{r}}_T^{(B)}\right)^2 + J_{ot} + J_{gy} \tag{4.89}$$

$$J_2 = M_T\left(\mathbf{R}_\theta{}^{-1}\frac{\partial}{\partial\psi}\vec{\mathbf{r}}_T^{(B)}\right)^2 + J_{ot} \tag{4.90}$$

$$J_3 = M_T\left(\left(\frac{\partial \mathbf{R}_\theta{}^{-1}}{\partial\theta}\vec{\mathbf{r}}_T^{(B)}\right)\cdot\left(\mathbf{R}_\theta{}^{-1}\frac{\partial}{\partial\psi}\vec{\mathbf{r}}_T^{(B)}\right)\right) + J_{ot}\left(\mathbf{z}_B\cdot\mathbf{z}_C\right) \tag{4.91}$$

The potential energy is given by

$$\mathbf{V} = M_T \left(\vec{\mathbf{r}}_T^{(B)} \cdot \mathbf{z}_B \right) \tag{4.92}$$

Substituting Eqs. (4.89) to (4.92) into equation (4.81) and consequently into (4.79) and (4.80) we have a set of non-linear different equation shown below.

$$\begin{pmatrix} J_1 & J_3 \\ J_3 & J_2 \end{pmatrix} \begin{pmatrix} \ddot{\theta} \\ \ddot{\psi} \end{pmatrix} = \begin{pmatrix} Q_\theta - \dfrac{\partial J_3}{\partial \psi}\dot{\psi}^2 - \dfrac{\partial J_1}{\partial \psi}\dot{\theta}\dot{\psi} \\ Q_\psi - \dfrac{\partial J_2}{2\partial \psi}\dot{\psi}^2 + \dfrac{\partial J_1}{2\partial \psi}\dot{\theta}^2 - \dfrac{\partial J_3}{\partial \theta}\dot{\theta}^2 - \dfrac{\partial V}{\partial \psi} \end{pmatrix} \tag{4.93}$$

To solve Eq. (4.93) the yaw and furling moments must be known or defined in term of the variables θ and ψ. The equations needed to find Q_θ are shown below.

$$\begin{aligned}
Q_\theta &= {M_T}^\theta + {M_R}^\theta && (4.94)\\
{M_T}^\theta &= \left({\mathbf{r}_{T,2}}^{(B)} \times {\mathbf{F}_T}^{(B)} \right) \cdot \mathbf{z}_B && (4.95)\\
{\mathbf{r}_{T,2}}^{(B)} &= {\mathbf{r}_T}^{(B)} + \mathbf{R}^{-1} \left(\Delta L_3 \sin\psi \, \mathbf{x}_C - \Delta L_3 \cos\psi \, \mathbf{y}_C \right) && (4.96)\\
{F_T}^{(B)} &= \left(F_L cos\xi + F_D sin\xi \right) \mathrm{x}_A + \left(F_L sin\xi - F_D cos\xi \right) \mathrm{y}_A && (4.97)\\
F_L &= 0.5\rho {U^2}_{tail} A_t C_L(\alpha) && (4.98)\\
F_D &= 0.5\rho {U^2}_{tail} A_t C_D(\alpha) && (4.99)\\
\alpha &= \xi - \theta - \psi && (4.100)\\
{M_R}^\theta &= \left({\mathbf{r}_{rotor}}^{(B)} \times {\mathbf{F}_r}^{(B)} \right) \cdot \mathbf{z}_B && (4.101)\\
{\mathbf{r}_{rotor}}^{(B)} &= -L_5 \mathbf{x}_B + L_4 \mathbf{y}_B && (4.102)\\
{\mathbf{F}_r}^{(A)} &= {F_r}^0(v) \cos^2(\xi - \theta) \left(\cos\theta \, \mathbf{y}_A + \sin\theta \, \mathbf{x}_A \right) && (4.103)\\
{\mathbf{F}_r}^{(B)} &= \mathbf{R}_\theta {\mathbf{F}_r}^{(A)} && (4.104)
\end{aligned}$$

The equation to find the furling moment are given by

$$\begin{aligned}
Q_\psi &= {M_T}^\psi + {M_{lim}}^\psi && (4.105)\\
{M_T}^\psi &= \left({\mathbf{r}_f}^{(B)} \times {\mathbf{F}_T}^{(B)} \right) \cdot \mathbf{z}_C && (4.106)\\
{\mathbf{r}_f}^{(B)} &= \mathbf{R}^{-1} \left(L_3 \cos\psi \, \mathbf{y}_C + L_3 \sin\psi \, \mathbf{x}_C \right) && (4.107)\\
{\mathbf{r}_{f,2}}^{(B)} &= \mathbf{R}^{-1} \left((L_3 + \Delta L) \cos\psi \, \mathbf{y}_C + (L_3 + \Delta L) \sin\psi \, \mathbf{x}_C \right) && (4.108)\\
{M_{lim}}^\phi &= \begin{cases} -K_1 (\psi - \psi_{upper}) & \psi \geq \psi_{upper} \\ 0 & \psi_{upper} \geq \psi \geq \psi_{lower} \\ -K_1 (\psi - \psi_{upper}) & \psi \leq \psi_{lower} \end{cases} && (4.109)
\end{aligned}$$

When damping effects and Coulomb friction for both rotor and tail are included in the above equations the final equations is

$$\begin{pmatrix} J_1 & J_3 \\ J_3 & J_2 \end{pmatrix} \begin{pmatrix} \ddot{\theta} \\ \ddot{\psi} \end{pmatrix} = \begin{pmatrix} Q_\theta - \dfrac{\partial J_3}{\partial \psi}\dot{\psi}^2 - \dfrac{\partial J_1}{\partial \psi}\dot{\theta}\dot{\psi} + C_1\dot{\theta} + C_0 \\ Q_\psi - \dfrac{\partial J_2}{2\partial \psi}\dot{\psi}^2 + \dfrac{\partial J_1}{2\partial \psi}\dot{\theta}^2 - \dfrac{\partial J_3}{\partial \theta}\dot{\theta}^2 - \dfrac{\partial V}{\partial \psi} + C_3\dot{\psi} + C_2 \end{pmatrix} \tag{4.110}$$

Let

$$f_1 = Q_\theta - \frac{\partial J_3}{\partial \psi}\dot{\psi}^2 - \frac{\partial J_1}{\partial \psi}\dot{\theta}\dot{\psi} + C_1\dot{\theta} + C_0 \tag{4.111}$$

$$f_2 = Q_\psi - \frac{\partial J_2}{2\partial \psi}\dot{\psi}^2 + \frac{\partial J_1}{2\partial \psi}\dot{\theta}^2 - \frac{\partial J_3}{\partial \theta}\dot{\theta}^2 - \frac{\partial V}{\partial \psi} + C_3\dot{\psi} + C_2 \tag{4.112}$$

After some algebraic simplification equation 4.110 becomes

$$\begin{pmatrix} {J_3}^2 - J_1 J_2 & 0 \\ 0 & {J_3}^2 - J_1 J_2 \end{pmatrix} \begin{pmatrix} \ddot{\theta} \\ \ddot{\psi} \end{pmatrix} = \begin{pmatrix} J_3 f_2 - J_2 f_1 \\ J_3 f_1 - J_1 f_2 \end{pmatrix} \tag{4.113}$$

Equation 4.113 is a system of second order nonlinear differential equation. Therefore it is very difficult to obtain an analytical expression that characterize the turbine system response. Numerical method will be used iteratively to solve these equations.

4.9.2 Tail Preliminary Design

At this stage, the thrust induced by the rotor when the turbine is operating at normal condition is known. Therefore, the design of the furling system is confined in answering the following questions: how far should the rotor axis be offset from the yaw axis? What dimensions should the tail vane and the boom have? What type of airfoil should the tail vane have? The preliminary design of the tail is formulated as an optimization problem which must have a minimum tail weight as the objective function, and the aerodynamic forces generated by the tail has to balance the yaw moment induced by the rotor thrust.

Equilibrium Equation

From Figure 4.19 and 4.20, and if we take the equation of moment of the external forces about the yaw and furling axes, respectively, when the turbine system is in equilibrium, we will have the following expression:

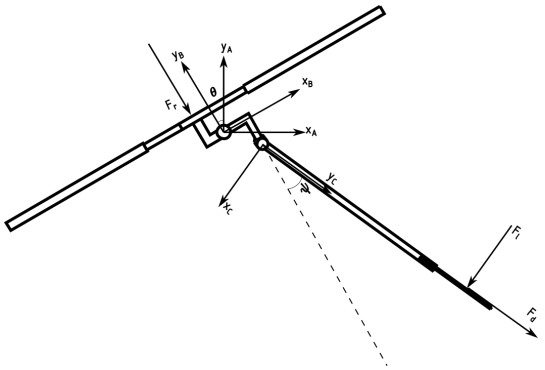

Figure 4.19: Turbine free body diagram

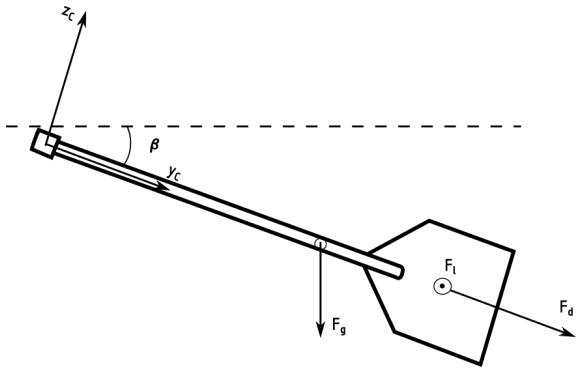

Figure 4.20: Tail free body diagram

$$\left(\mathbf{r}_{rotor}{}^{(B)} \times \mathbf{F}_r{}^{(B)}\right) \cdot \mathbf{z}_B + \left(\mathbf{r}_{T,2}{}^{(B)} \times \mathbf{F}_T{}^{(B)}\right) \cdot \mathbf{z}_B = 0 \tag{4.114}$$

$$\left(\mathbf{r}_{f,2}{}^{(B)} \times \mathbf{F}_T{}^{(B)}\right) \cdot \mathbf{z}_C + \left(\mathbf{r}_f{}^{(B)} \times \mathbf{F}_g{}^{(B)}\right) \cdot \mathbf{z}_C = 0 \tag{4.115}$$

Equation 4.115 can be solved for weight of the turbine tail as

$$Fg = \frac{\left(\mathbf{r}_{f,2}{}^{(B)} \times \mathbf{F}_T{}^{(B)}\right) \cdot \mathbf{z}_C}{(\mathbf{r}_f{}^{(B)} \times \mathbf{z}_B{}^{(B)}) \cdot \mathbf{z}_C} \tag{4.116}$$

Equilibrium Equations Solution

To solve the above equilibrium equations, parameters such as lift and drag coefficient at any angle of attack and the rotor thrust have to be specified. The thrust, as well as the lift and drag coefficients, were obtained from Qblade. In equilibrium position, the turbine is assumed to be aligned with the wind, and the tail is set to have an angle of attack of 5°. This resulted in 2500 N, 0.545, and 0.0118 for thrust lift and drag coefficient, respectively. Now the optimization problem to find the tail parameters that satisfy the equilibrium equations with as minimum mass as possible can be formulated.

Tail Problem description The aim of the tail optimization is to define the tail parameters that satisfy the equilibrium condition and minimize the mass of both boom and the vane of the tail.

Definition of the Design Variables The geometric parameters were allowed to vary in order to obtain the optimum combination of them. Thus the problem design variables were L_1, L_2, L_3, L_4, L_5,A_{tail}, ΔL_3, β, γ and δ.

Data Collection For the tail optimization problem, the following parameters were set as constant: $\rho = 1.225\ kg/m^3$, $U = 10.5\ m/s$, $g = 9.81\ m/s^2$, $F_r{}^{(B)} = 2500\ N$, $\psi = 5°$, $C_L = 0.5339$, $C_D = 0.0427$, $L_5 = 0.75\ m$, $L_6 = 0.2384\ m$.

Optimization Criteria Equation 4.116 was set as objective function. Thus

$$Objective(L_1, L_2, L_3, L_4, \Delta L_3, \beta, \gamma, \delta, A_{tail}) = \frac{\left(\mathbf{r}_{f,2}{}^{(B)} \times \mathbf{F}_T{}^{(B)}\right) \cdot \mathbf{z}_C}{\left(\mathbf{r}_f{}^{(B)} \times \mathbf{z}_B{}^{(B)}\right) \cdot \mathbf{z}_C}.$$

Formulation of the Constraint There is only one equality constraint to be satisfied, which is Eq. 4.114. Therefore,

$$h(L_1, L_2, L_3, L_4, \Delta L_3, \beta, \gamma, \delta, A_{tail}) = \left(\mathbf{r}_{rotor}{}^{(B)} \times \mathbf{F}_r{}^{(B)}\right) \cdot \mathbf{z}_B + \left(\mathbf{r}_{T,2}{}^{(B)} \times \mathbf{F}_T{}^{(B)}\right) \cdot \mathbf{z}_B.$$

Apart from the equality constraint the design variables were also limited as follow: $0.2 \leq L_1, L_2 \leq 1$; $0.5 \leq L_3 \leq 2.5$; $0.2 \leq L_4 \leq 1$; $0.01 \leq \Delta L_3 \leq 1$; $0.05 \leq A_{tail} \leq 10$; and $0 \leq \beta, \gamma, \delta \leq \frac{\pi}{6}$.

Solution A global solution was obtained using MatLab, as described in this paragraph. Firstly, a function containing the constraint equation is defined in the transcript and saved as **.m** file format. Then, in the Command Window, the optimization problem was assigned to variable P1, as can be seen in Appendix A.4.1. Subsequently, the **GlobalSearch** algorithm, which uses **fmincon** solver, was set to variable **gs**. Finally, the gs file was run. Appendix A.4.1 shows all the steps.

The solution converged into 6 global solutions with the best being the one that yields $L_1 = 0.2\ m$, $L_2 = 0.2\ m$, $L_3 = 2.5\ m$, $L_4 = 0.05\ m$, $L_5 = 0.75\ m$, $\Delta L_3 = 1\ m$, $\beta = 0°$, $\gamma = 30°$, $\delta = 0°$, and $A_{tail} = 1.424\ m^2$.

System Response

To determine the system response, all the preliminary parameters such as turbine mass moment of inertia about the yaw axis, tail shape, and optimum area, tail mass as well as mass moment of inertia about the furling axis, the tail center of gravity, and center of pressure, have to be defined accurately.

Thrust It was assumed that the wind speed at the rotor is the same as that experienced by the tail. The thrust generated by the rotor is found using the BEM theory embedded in Qblade. Thrust values corresponding to wind speed varying from 1 to 20 m/s were determined to analyze the response of the system when the wind speed varies. The thrust values obtained from Qblade are only valid when the wind velocity is aligned with the rotor axis. To account for the situation when the wind velocity is not aligned with the rotor axis, it is assumed that thrust is directly proportional to the square of the cosine of the angle between the wind velocity and the rotor axis of rotation, as shown in Eq. (4.103) [72]. Table A.3 shows the thrust values (in N) vs. wind speed (m/s) when it is aligned with the rotor axis of rotation.

Tail Shape and Area The area obtained from the last section is used here as an optimum area. The tail vane is chosen to be composed of a triangle and a rectangle. Now the task is to find the optimum dimensions of the triangle and rectangle that gives the same area and minimum perimeter. It problem can be defined as an optimization problem, as described in the following paragraph.

- **Problem Definition** The problem consists in finding the dimensions of the tail shape that minimizes the perimeter and gives an area of 1.424 m^2.
- **Definition of the design variable** x_1, x_2, and x_3 are chosen as design variables as shown in Figure 4.21.
- **Data collection** The only data needed in this problem is the tail vane area and basic formulae to calculate the area and perimeter of the tail vane.

$$\begin{aligned} A_{tail} &= 1.424\ m^2 \\ P &= 2\sqrt{x_1^2 + \frac{x_3^2}{4}} + 2x_2 + x_3 \\ A_{tail} &= x_2 \cdot x_3 + \frac{x_1 \cdot x_3}{2} \end{aligned}$$

- **Optimization criteria**

$$ObjectiveFunction = 2\sqrt{x_1^2 + \frac{x_3^2}{4}} + 2x_2 + x_3$$

- **Formulation of the constraint**

$$x_2 \cdot x_3 + \frac{x_1 \cdot x_3}{2} = 1.424$$
$$0.1 \leq x_1, x_2, x_3 \leq 10$$

- **Solution** As with other optimization problem in this project, the solution was obtained using the same procedures used in the previous optimization problems. Appendix A.4.2 shows the constraint function as well as the step by step procedure used to solve this problem. The result were as follow: $x_1 = 0.3566\ m$, $x_2 = 0.9743\ m$, $x_3 = 1.2354\ m$

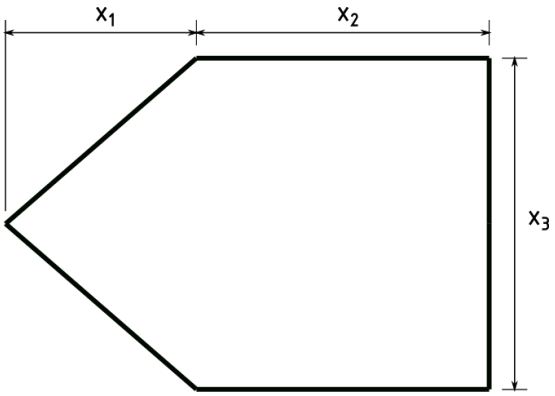

Figure 4.21: Tail vane

Tail Aerodynamic Properties The airfoil chosen for the tail vane was NACA0006, for it is used in the design of vertical airplane tails, and it offers a moderately high lift coefficient, which is suitable to use in turbine tail vane design. The drag and lift coefficient for the low angle of attack was obtained from XFOIL embedded in Qblade. For the high angle of attack, the Viterna approach was used. The angle of attack ranges from $-180°$ to $180°$. Table A.4 presents the lift and drag coefficient vs the angle of attack.

Tail Geometry The geometry of the tail was created in SolidWorks. As was mentioned in the last paragraph, NACA0006 was used as the tail vane cross-section. Therefore, a .txt file having the coordinates of NACA0006 and suitable to be used in Solidworks was imported to Solidworks and then edited to have a chord length of 1.3309 m ($x_1 + x_2$) in the middle section of the tail, and 0.9743 m (x_2) at the upper and lower section of the tail. Then loft command with a thickness of 2.5 mm was applied as seen in Figure 4.22. The tail boom was chosen to have a hollow circular cross sectional area with an external diameter of 75 mm and a inner diameter of 60 mm, the boom is 3 m long. One end of the boom is attached to the tail vane and the other end holds the furling axis as shown in Figure 4.23. A coordinate system was created to represent the furling coordinate. It was attached to center of the furling axis with the y axis pointing in the direction of the boom and the z axis parallel to the furling axis, positive when pointing up. Choosing Aluminium as the vane and boom material, using the **Evaluate** ribbon and choosing the created coordinate, the following values were obtained: center of mass $= (0; 2.75223 \text{ m}; 0)$, mass moment of inertia about furling axis $= 330 \text{ kg/m}^2$, mass of the tail $= 35$ kg.

Tail Vane Center of Pressure To determine the center of pressure following steps were followed:

1. The tail vane was exported into SolidWorks Flow Simulation. The wind velocity was set to 10.5 m/s, and it had an angle of $30°$ with the airfoil chord. The mesh was set to seven (which the finest available) so that the result obtained would be as accurate as possible. The surface of the tail vane was defined as a real wall in the boundary conditions option. The goals to monitor were the average static pressure and average speed as global goals and force z, force y, and torque y as surface goals.

2. The results obtained from Solidworks Flow Simulation were exported to Solidworks Simulation and served as the external load. The mesh was set to the finest, and the control surface was also applied on the surface of the tail vane to obtain a good quality mesh. The part of the tail where it attaches to the boom was set as fixed surface.

3. The coordinate system, which its origin coincides with the tail vane's tip, was created to evaluate the force and moment in the fixed surface. The value obtained was as are shown in Figure 4.24

4. Calculate the center of pressure by the formula

$$\vec{M} = \vec{r} \times \vec{F}$$

.

$$\{0, 0, 26.8\} = \{x, y, z\} \times \{53.9, 1, 0\}$$
$$\{x, y, z\} = \{0, 0.497217, 0\}$$
$$\Delta L_3 = 0.497217 + 3 - 2.75223 = 0.74498 \text{ m}$$

Turbine Moment of Inertia Figure 4.25 shows the turbine without the nacelle. To find the turbine mass moment of inertia, a coordinate system that is 50 mm offset from the rotor axis has the $z-$axis pointing up, and the $y-$axis parallel to the axis of rotation. The mass moment of inertia was found to be equal to $I_{turbine} = 244.7$ kgm^2. To account for other component that were not considered at this design stage, the value obtained is added by 20 percent of its initial value that is $I_{turbine} = 1.2 \times 244.7 = 294$ kgm^2

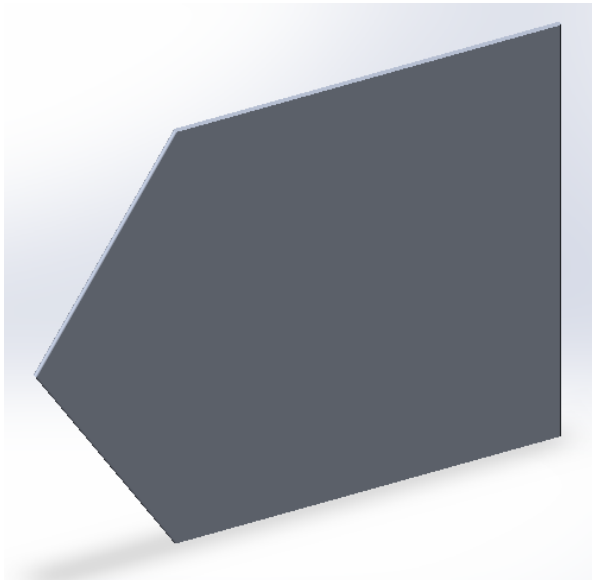

Figure 4.22: Tail vane

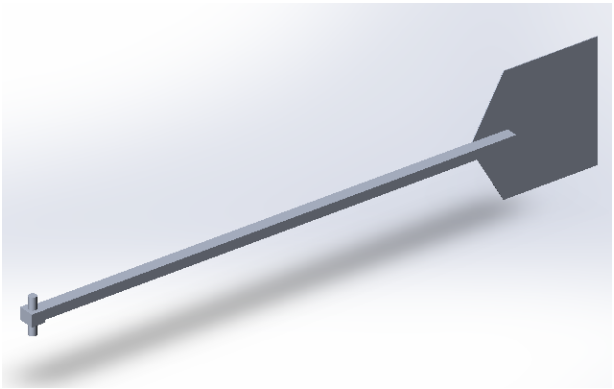

Figure 4.23: Tail

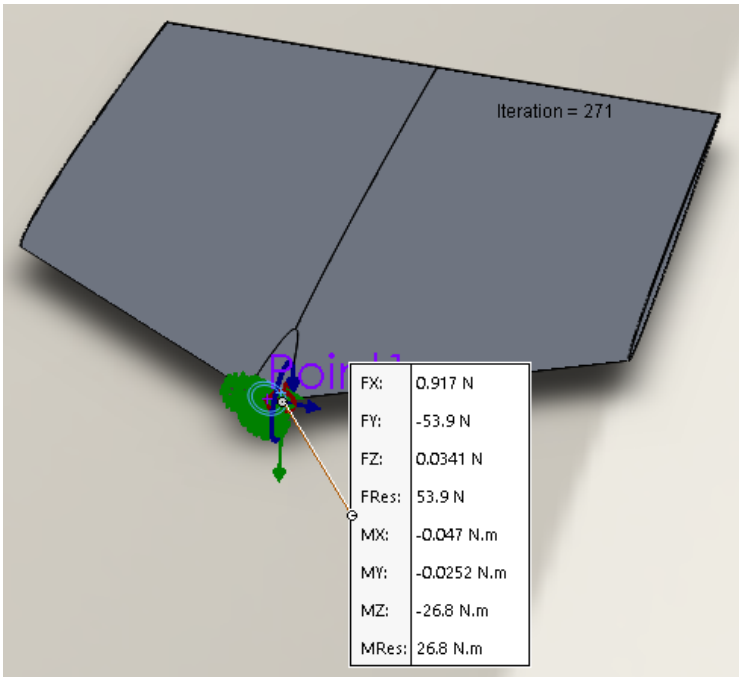

Figure 4.24: Turbine

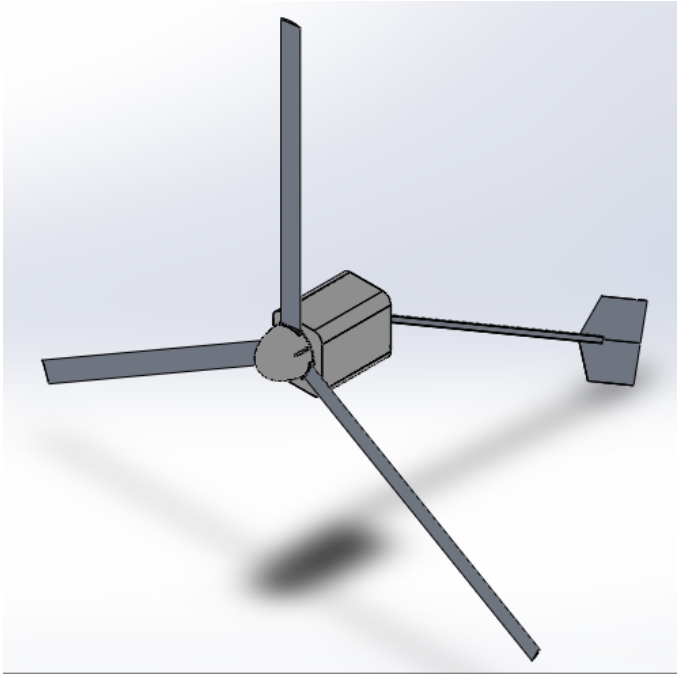

Figure 4.25: Turbine

Solution To obtain the system response the followed steps were done

1. The angle of attack of the tail is transformed into an angle raging from $-180°$ to $180°$

2. The lift and drag coefficient must be known for any given value of the angle of attack
3. The thrust generated by the rotor must be known given any value of the wind speed ranging from 1 to 20 m/s
4. The stepwise function of the limiting momentum (Eq. 4.109) is defined
5. A program that generates the analytical expression for the system of nonlinear differential equations to be solved (equation 4.113) is created
6. The created analytical expressions is transferred to the function used to solve the differential equation by using @15s solver (a build-in solver used to solve complex differential equations).

To transform any angle into an equivalent angle ranging from $-180°$ to $180°$, we divide the given angle by $360°$. The remainder is its equivalent in the range from $0°$ to $360°$. When the remainder is between $[0°, 180°]$, the equivalent angle is equal to the remainder. When the angle is in the range $[180°, 360°]$, the equivalent angle is remainder $-360°$. If the remainder is in the range $[-180°, 0°]$, the equivalent angle is the remainder. If it is in between $[-360°, -180°]$, then the equivalent angle is remainder $+360°$. Appendix A.4.3 gives the MatLab code.

To obtain the values of the drag and lift coefficient from any given angle of attack, using the data obtained from Qblade, linear interpolation is used. The angle of attack used was the one obtained from the last paragraph. The MatLab code was used to create a function that uses the attack angle as input and gives lift and drag coefficient as output. See the MatLab code in Appendix A.4.3.

The approached used to determine the thrust form any given wind speed varying from 1 to 20 m/s is the same one described in the previous paragraph. A function was created to yield thrust as output and wind speed as input. Appendix A.4.3 shows the MatLab code for this function.

The solver @15s only solve a differential equation numerically; it does not give the solution analytically. Since the system of the differential equation being solved needs to be represented in algebraic form, and the stepwise function assumes three possible expressions, depending on the value of the furling angle, it has to be expressed separately and evoked later on the appropriate program. Appendix A.4.3 shows the MatLab code for this function. if we express Eq. 4.113 by doing hand calculations it will be very cumbersome. Since we can obtain analytical expression in MatLab, it is more practical and less prompt to commit mistakes if we express this equation analytically in MatLab, then copy the result obtained and use it in the program that contains the equation to be solved. This is the approach used here, and the code can be seen in Appendix A.4.3. The final function (see Appendix A.4.3) contain all the differential equation expressed in the algebraic form and takes into account the liming moment. Some variable is defined inside this function to allow manual turning in order to have a stable response. The program is set to solve the equation iteratively until

tolerances are met. Then this program is evoked in the main program containing the @15s solver, as shown in Appendix A.4.3.

Discussion

The optimum dimension for the current furling model was obtained from equilibrium equations, as discussed earlier. However, the dimensions that resulted from the equilibrium equation when used to analyze the dynamic response of the model shows poor performance. The turbine geometry obtained from CAD also deviates from the optimum dimensions, mainly the tail section. Therefore the model will have dimensions slightly different from optimum.

The dimensions obtained after some tries and errors, in order to have acceptable response, were as follow: $L_1 = 500$ mm, $L_2 = 250$ mm, $L_3 = 2752$ mm, $L_4 = 54$ mm, $L_5 = 750$ mm, $\Delta L_3 = 745$ mm, $\beta = 4.8°$, $\gamma = 17.2°$, $\delta = 24°$, $A_{tail} = 1.424$ m^2, $C_1 = -100$ Nms, $C_3 = -100$ Nms, $Ks = 1750$ Nm, $\psi_{upper} = 30°$, $\psi_{lower} = -30°$.

In the first analysis, static condition (constant wind velocity) was considered. The system response when the yaw and furling angle are given initial displacement was analysed. Four situation were studied namely:

1. Initially, the yaw and furling angle are both aligned with the wind velocity ($\theta = 0°$, and $\psi = 0°$);
2. The turbine is initially displaced 60° while the tail is kept aligned to the wind velocity ($\theta = 60°$, and $\psi = 0°$);
3. The turbine is initially kept in the same direction with the wind velocity while the tail is moved $-30°$ away from it ($\theta = 0°$, and $\psi = -30°$);
4. Both the turbine and tail are shifted away from the inflowing wind by 30° each ($\theta = 30°$, and $\psi = 30°$);

In all four situations, the wind direction is assumed to be constant, and it has a magnitude of 10.5 m/s. Figures 4.26 through 4.29 show the graphs of the four situations above mentioned. In all the graphs, the yaw and furling angles were analyzed with respect to time.

The yaw angle in the first condition, as shown in Figure 4.26, vibrates around its initial position (0°), with a period of about 3.3 s s and a maximum amplitude of around 14°. The furling angle shifts away from its initial and oscillate at about 47.5°, with a period of 3.5° and a maximum amplitude of 18.6°; after one minute, the amplitude is only about 1.2°. The same observation was made in the remaining conditions. Table 4.3 gives a summary of the analysis.

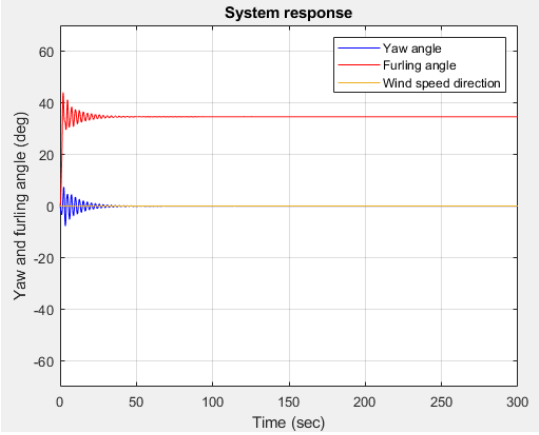

Figure 4.26: Model response at initial condition of $\theta = \psi = 0°$

.

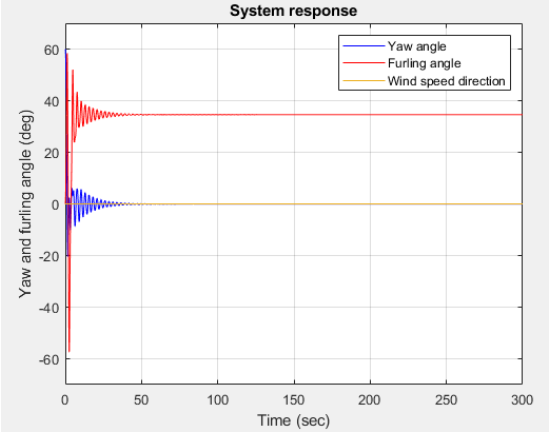

Figure 4.27: Model response at initial condition of $\theta = 30°$, and $\psi = 0°$

.

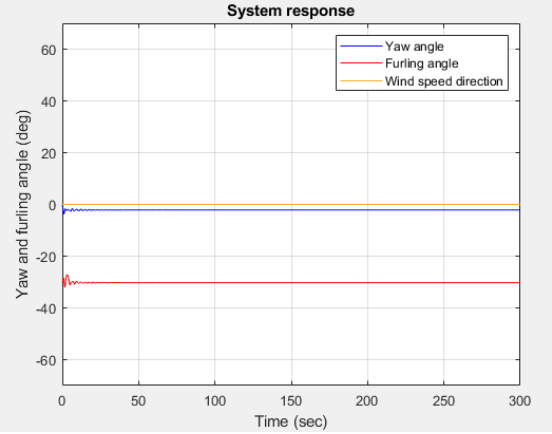

Figure 4.28: Model response at initial condition of $\theta = 0°$, and $\psi = -30°$

.

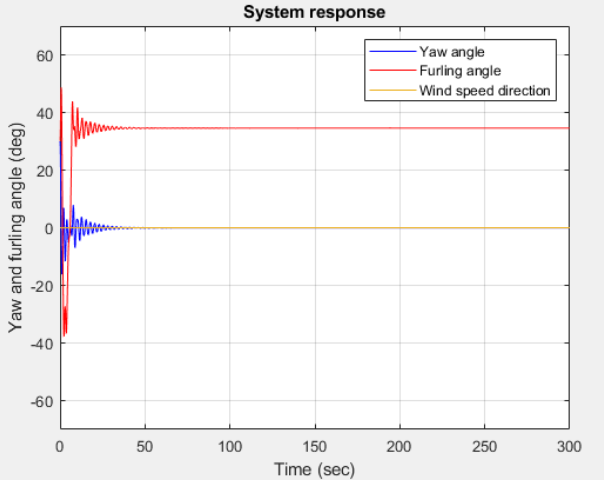

Figure 4.29: Model response at initial condition of $\theta = 30°$, and $\psi = 30°$

.

The yaw angle in the first condition, as shown in Figure 4.26, vibrates around its initial position (0°), with a period of about 3.3 s and a maximum amplitude of around 14°. The furling angle shifts away from its initial and oscillate at about 47.5°, with a period of 3.5° and a maximum amplitude of 18.6°; after one minute the amplitude is only about 1.2°. The same observation was made in the remaining conditions. Table 4.3 gives the summary of the analysis.

Table 4.3: Summary of the dynamic model response to static conditions

	Yaw angle				Furling angle			
Condition	1	2	3	4	1	2	3	4
Period	3.3	3.3	3.3	3.3	3.5	3.5	3.5	3.5
Max. amplitude	14	32	8.3	23	18.7	23	8.8	20
Amplitude_{+60s}	1.1	1.6	0.5	1.7	1.2	1.6	0.6	1.8
S.S. value	0	0	0	0	47.5	47.5	47.5	47.5

From Table 4.3, it can be concluded that it does not matter how and/or by how much the system is displaced. It will always settle at 0° for yaw and $-47.5°$ for furling angle. The model also shows that the turbine and tail have close oscillation period 3.3 and 3.5 s, respectively; consequently, their natural frequency is close to one another. The amplitude of the vibration is directly dependent to the magnitude of the initial displacement of both the turbine and the tail; however, the turbine displacement has more influence to the amplitude of the system oscillation than the tail displacement, which seems to have little effect on the vibration of the turbine, as shown in condition 3. The speed by which the system reaches the steady-state condition also depends on the amplitude; the greater the amplitude of the yaw or furling oscillation, the longer it takes for the system to reach steady-state conditions. The system response, when the magnitude and direction of the wind velocity with time were also analyzed. Two conditions were considered. The first one, the wind velocity is assumed to vary sinusoidally in both magnitude and direction with a long period of oscillation (63.8 s)

for both magnitude and direction, the wind direction is chosen to have an amplitude of 30°. Their equations are shown below.

$$U = 10.5 + 5\sin(0.1t)$$
$$\xi = \frac{\pi}{6}\sin(0.1t).$$

In the second condition, the magnitude and direction of the wind also vary sinusoidally as before, but the period of the variation is chosen to be close to that of the system (3.5 s), and the amplitude of the wind direction was reduced ten times. The equations for the second condition are shown below.

$$U = 10.5 + 5\sin(1.7952t)$$
$$\xi = \frac{\pi}{60}\sin(1.7952t).$$

Figures 4.30 and 4.31 show the results of the analysis. The first condition is shown in Figure 4.30. It can be seen that the turbine model yaws clockwise and counterclockwise around 0° position. When the system reaches a steady-state condition instead of converging in one point, as was the case in the static study, it oscillates around 0° position with an amplitude of about 6.5° and a period of around 63 s. The tail also responds in a similar way. When it reaches the steady-state condition, it oscillates around −41.5° position with a magnitude of 8.3° and a period of 63 s as it was for the turbine. In the second condition, the response of the system is very similar to the first condition, with the conspicuous difference being the amplitude, which is greater in the latter case. In the second condition, when the system reaches the steady-state, the turbine oscillates around 0° position with an amplitude and a period of 17.2° and 3.5 s, respectively. The tail vibrates around −44.5° position, with an amplitude and period of 20.9° and 3.5 s, respectively. Figure 4.31 shows the second condition response.

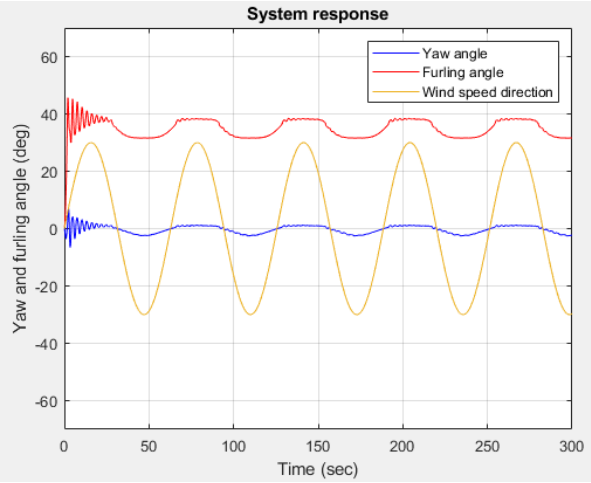

Figure 4.30: Model response when the wind velocity changes slowly

.

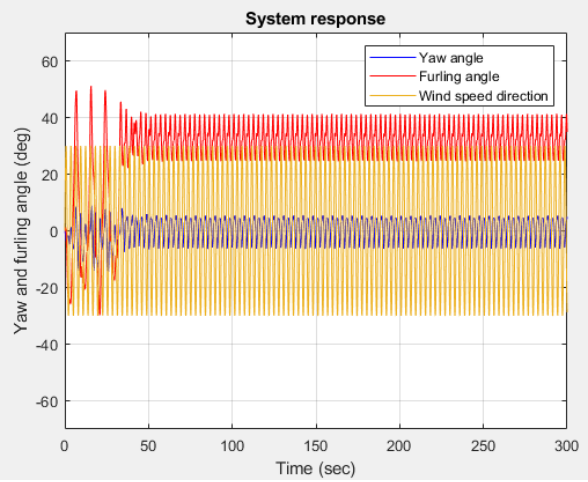

Figure 4.31: Model response to wind frequency close to the system natural frequency

.

Both figures show that the tail and the turbine follow the wind direction in a direct correlation, and when the steady-state condition is reached, the model will oscillate with the same period as the wind. This observation makes us conclude that if the turbine system is built according to this dynamic model, it will follow the wind very closely whenever it changes direction. The system will reach a steady-state at a period of about one minute. It was also shown that when the exciting frequency matches the natural frequency of the turbine components, the system will vibrate with high amplitude, with the tail having the highest. The magnitude of the system vibration does not depend much on the magnitude of the direction, but it depends closely on its direction.

4.10 Generator

Wind turbine generators can operate either at a fixed or variable rotational speed. Variable speed allows the turbine to be operated at the optimum conditions regardless of the wind speed. This is attained by maintaining a constant tip speed ratio; that is, the rotor speed is varied as the wind speed changes. The variable speed generator has the advantage of allowing the turbine to operate at the maximum power coefficient, which means the turbine is able to extract as much power as possible even in low wind speed. It also reduces the stress fluctuations; consequently, the components will have a longer life.

When the wind turbine generator is operating in variable speed mode, the frequency and output voltage have to have a constant value for electrical power quality purposes. In order to maintain the voltage and frequency constant, the generator has to be coupled with power electronics.

The generator normally used in a small wind turbine is a self-excited induction generator. doubly-fed induction generator (DEIG), squirrel cage induction generator (SCIG), and permanent magnet synchronous generator (PMSG).

Permanent magnet synchronous generators have many advantages over induction counterparts. They do not require an external exciter to generate the magnetic field because the magnetic field is generated by the permanent magnet. For this fact, PMSGs do not use brushes or slip rings. Therefore, they are more efficient, lightweight, less expensive, low maintenance. They also can be constructed with enough poles that allow the turbine rotor to drive the generator directly without the need for a gearbox. In small wind turbines up to 10 kW, the permanent magnet synchronous generator is the generator of preference. In the current design, PMSG is used as the turbine's generator.

4.10.1 Electrical Model of a Small Wind Turbine

Figure 4.32 shows the diagram of a wind turbine conversion system (WECS) with a back-to-back converter. The turbine rotor converts the wind energy into mechanical energy, available as shaft rotational energy. This mechanical energy is subsequently converted into electricity by the turbine generator. The output power of the PMSG is connected to a pulse width modulation converter, connected at the generator side of the converter where the AC voltage from the PMSG is converted into DC voltage. The generator side controller is responsible for controlling the speed of the rotor to allow the turbine to operate at an optimum speed by varying the current in the coil of the stator. The other side of the converter, called the grid side, is connected to the grid. In the grid side of the DC voltage is converted into AC voltage with its required frequency; both the frequency and voltage are kept constant. The converter grid side controller maintains the DC-link voltage constant by controlling the power flow.

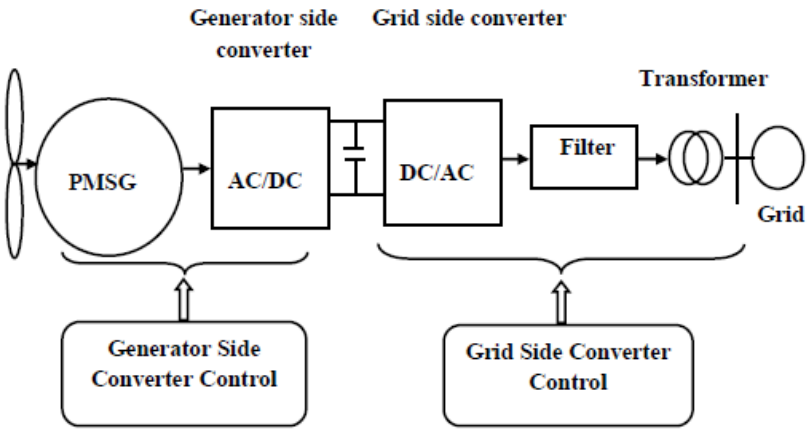

Figure 4.32: SWT electrical model [84]

.

4.10.2 Generator Reference Frame

To create a mathematical model of the dynamics of the PMSG, reference frames must be defined. The equations of the PMSG model are defined with respect to a rotational frame of reference, which has one of the axes (d-axis) attached to one of the poles of the generator

rotor, and it is allowed to rotate with the rotor. The other axis (q-axis) is ahead of d-axis by 90° in the direction of the rotor rotation. A fixed frame of reference is also defined. This frame of reference as one of its axis (α-axis) aligned with one of the stator coils and the other axis (β-axis) is ahead of α-axis by 90° in the direction of the rotor rotation. The other axes, namely, a; b; and c, are aligned with coils A; B and C. Figure 4.31 shows the representation of these reference frames.

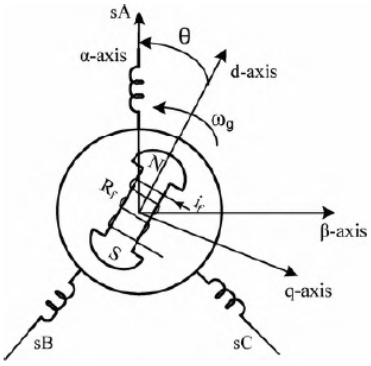

Figure 4.33: Reference frames[85]

.

4.10.3 Steady State Mathematical Model of PMSG

The mathematical model of PMSG assumes that the stator windings are positioned sinusoidally along the air-gap to allow the mutual flux effect with the rotor, the rotor inductances variations as the rotor position varies with respect to the stator slots is negligible, the stator windings are symmetrical, the stator windings resistances are constant, the damper and capacitances of the stator windings are negligible, the power loss is constant, and the magnetic hysteresis and saturation effects are neglected.

The voltages of the stator windings are given by

$$v_a = i_a R_s + \frac{d\psi_a}{dt} \tag{4.117}$$

$$v_b = i_b R_s + \frac{d\psi_b}{dt} \tag{4.118}$$

$$v_c = i_c R_s + \frac{d\psi_c}{dt} \tag{4.119}$$

where, v_a, v_b, and, v_c are the phase voltages of the stator phases a, b, and, c respectively; i_a, i_b, and, i_c are the stator currents of the phases a, b, and, c respectively; and ψ_a, ψ_b, and, ψ_c are the flux linkages of the phases a, b, and, c respectively.

The Fluxes are given by

$$\begin{bmatrix} \psi_a \\ \psi_b \\ \psi_c \end{bmatrix} = \begin{bmatrix} L_{sl} + L_{aa}(\theta) & L_{ab}(\theta) & L_{ac}(\theta) \\ L_{ba}(\theta) & L_{sl} + L_{bb}(\theta) & L_{bc}(\theta) \\ L_{ca}(\theta) & L_{bc}(\theta) & L_{sl} + L_{cc}(\theta) \end{bmatrix} \begin{bmatrix} i_a \\ i_b \\ i_c \end{bmatrix} + \begin{bmatrix} \psi_{ma}(\theta) \\ \psi_{mb}(\theta) \\ \psi_{mc}(\theta) \end{bmatrix} \tag{4.120}$$

where, L_{aa}, L_{bb}, L_{cc} are the self inductances of the stator phases a, b, and c respectively; L_{ab}, L_{bc}, L_{ca} are the mutual inductances between phases a and b, b and c, and c and a respectively; L_{sl} is the leakage inductance while ψ_{ma}, ψ_{mb}, and ψ_{mc} are the permanent magnet flux linkages of the phases a, b, and c respectively. θ (rotor position) is the angle between the permanent magnet pole axis and the a phase.

4.10.4 Equations in the d-q Frame

Figures 4.34 and 4.35 show the equivalent circuits seen from the rotational reference frame d-q. From these Figures we have

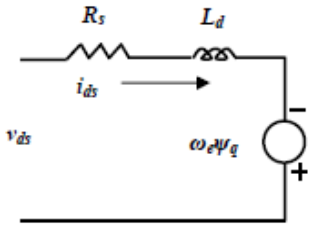

Figure 4.34: PMSG equivalent circuit seen from d-axis

.

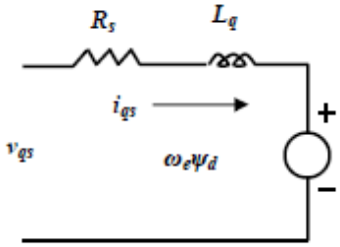

Figure 4.35: PMSG equivalent circuit seen from q-axis

.

$$v_{ds} = R_s i_{ds} + \frac{d\psi_d}{dt} - \omega_e \psi_q \tag{4.121}$$

$$v_{qs} = R_s i_{qs} + \frac{d\psi_q}{dt} + \omega_e \psi_d \tag{4.122}$$

Where, ω_e is the electrical speed in rad/s, ψ_d, and ψ_q are the d-axis and the q-axis flux linkages respectively. v_{ds}, and v_{qs} are respectively the stator d and q axes voltages in the rotating reference frame. i_{ds}, and i_{qs} are respectively the d and q axes stator currents in the rotating reference frame.

But,

$$\psi_d = L_d i_{ds} + \psi_m \tag{4.123}$$
$$\psi_q = L_q i_{qs} \tag{4.124}$$

where L_d, and L_q are the d and q-axes inductances respectively, and ψ_m is the permanent magnet flux linkage.

Therefore,

$$v_{ds} = R_s i_{ds} + \frac{d\left(L_d i_{ds}\right)}{dt} - \omega_e (L_q i_{qs}) \tag{4.125}$$
$$v_{qs} = R_s i_{qs} + \frac{d\left(L_q i_{qs}\right)}{dt} + \omega_e (L_d i_{ds} + \psi_m) \tag{4.126}$$

The mechanical parameters are given by

$$P_{em} = \frac{3}{2}\omega_e \left(\psi_d i_{qs} - psi_q i_d s\right) \tag{4.127}$$
$$\omega_e = p\omega_m \tag{4.128}$$
$$Te = \frac{P_{em}}{\omega_m} = \frac{3}{2} p \left(\psi_d i_{qs} - \omega_q i_{ds}\right) \tag{4.129}$$
$$Te = \frac{3}{2} p \left(\psi_m i_{qs} + \left(L_d - L_q\right) i_{qs} i_{ds}\right) \tag{4.130}$$

4.10.5 Converter Controllers

Usually, there are two philosophies used in the controller of the generator side converter, namely, direct torque control and the field-oriented control. The latter has less current distortion, and therefore, it has better performance, more overall efficiency, and a higher power factor. The field-oriented control can be implemented either with a control strategy that uses sensors to encode the speed or with one than do not use sensors. In the sensor-less strategy, the speed and position of the PMSG rotor are estimated by the stator current.

Figure 4.36 shows the block diagram of field-oriented control without a sensor. The three-phase stator currents are first transformed to $d-q$ the reference frame and subsequently to the $\alpha-\beta$ reference frame. After that, the current is sent to the position and speed estimation block where the position and the speed of the rotor are estimated in this block. The estimated speed is compared to a reference speed, and the error is given to the PI speed controller, which produces the reference q-axis current. This current is compared with the actual q-axis current, and the error is given to the q-axis current controller. The output of this controller is added with the component II to get the q- axis voltage. The reference d-axis current is compared with the actual d-axis current. The error is given to the d-axis current controller. Component I is subtracted from the output of the d-axis current controller to produce the d-axis voltage. The voltages in $d-q$ axis are then transformed to $\alpha-\beta$

axes, which are given as reference voltages for the SVM block. The speed and positions are estimated based on the flux linkage estimation method.

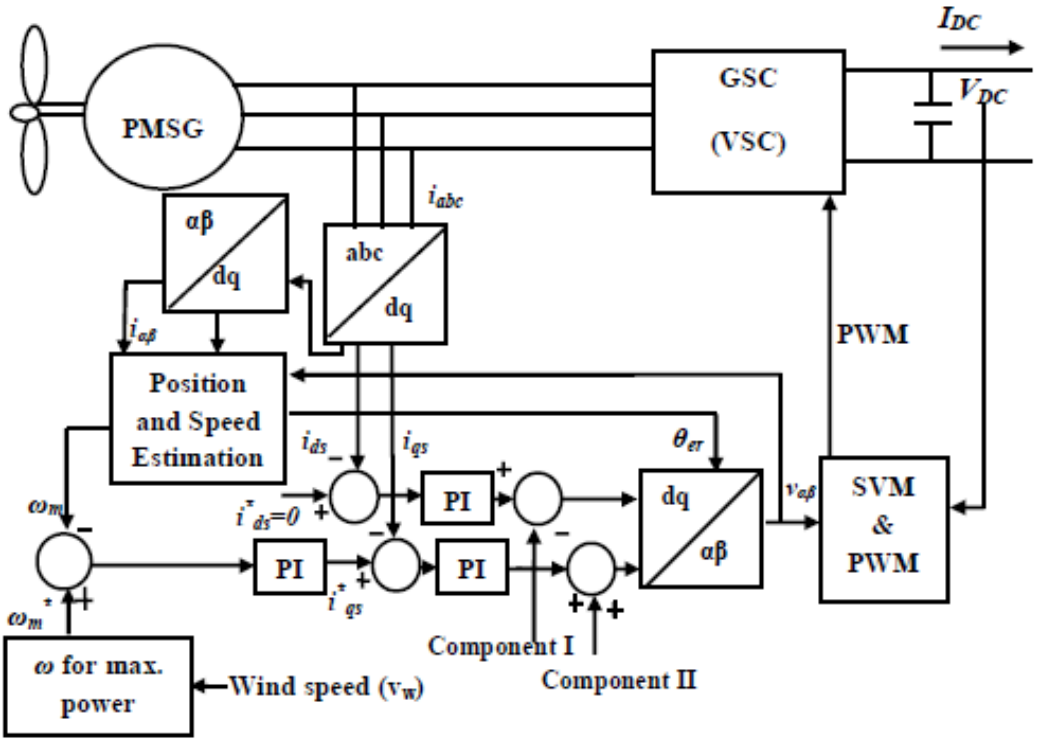

Figure 4.36: Generator side converter controller block diagram

.

In order to have a good electrical power quality in addition to the controller of the generator side converter, it is necessary to have another controller in the grid side, because the controller of the generator side converter only control the speed of the rotor to allow the turbine to operate at optimum speed. Still, the voltage of the DC-link capacitor varies with the variation of the wind speed. The input to the grid side converter is the DC-link voltage. The grid side converter controller controls the DC-link voltage of the system using a hysteresis current controller. Figure 4.37 shows the block diagram of the grid side converter control with the hysteresis current controller.

The DC-link voltage is compared with the reference DC voltage, and the error is given to the PI controller. The PI controller's output is fed to a three-phase reference current generator block, which generates the three reference currents (i^*_{abcg}). These currents are compared with the grid currents (i_{abcg}) in the hysteresis controller to generate the PWM signals. The converter connects the positive side of the DC-link to the grid when the current produced in the hysteresis controller is lower than the reference current, thereby increasing the grid currents. The converter connects the negative side of the DC-link to the grid when the current produced in the hysteresis controller is higher than the reference current, thereby decreasing the grid currents.

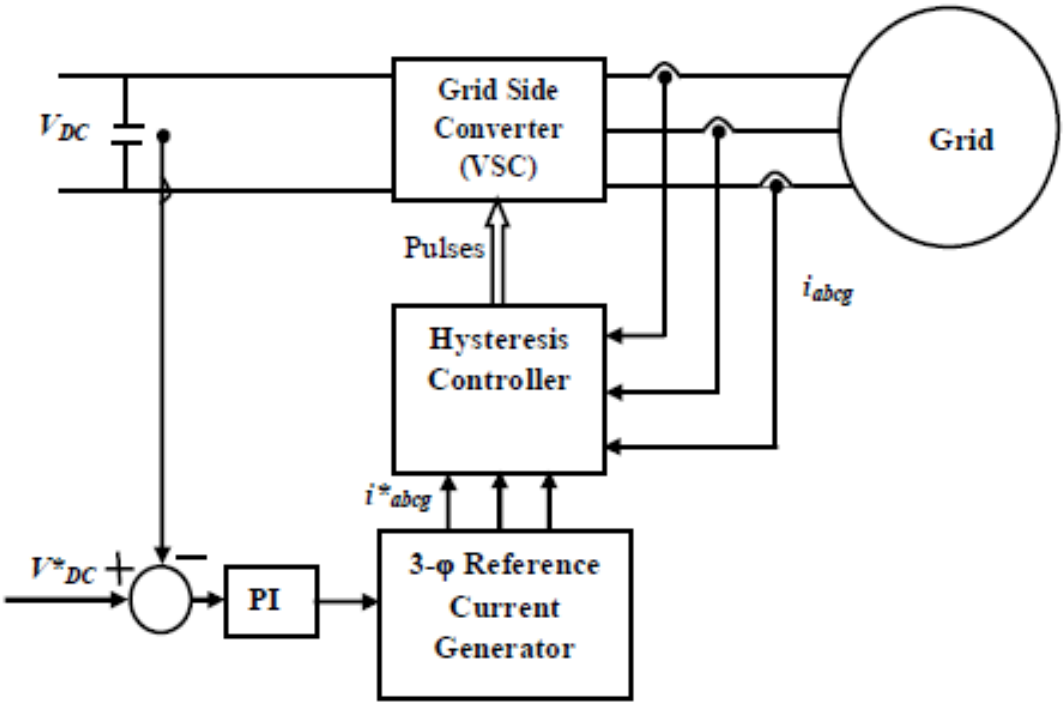

Figure 4.37: grid side converter controller block diagram

.

4.11 Braking System

In the current design, the brakes are used primarily to park the rotor whenever there is an emergency. Secondly, as discussed earlier, the blade gyroscopic loads are too high when the maximum yaw speed is used, and the blades are rotating at a nominal rotational speed. Therefore, the blade's angular velocity needs to be lowered to a safe level while the turbine is yawing freely; hence, it is necessary to use the brake to accomplish that task. Finally, suppose the furling system fails to turn away from inflow wind the rotor from the inflowing wind to protect the turbine against over-speed and high power, which can damage the generator. In that case, the brake is used as an alternative to over-speed and overpower protection.

4.11.1 Disc Brake Theory

There are two assumptions used when designing disc brakes. The first assumes that the contact area's pressure between the disc brake and the disc pad is constant; the second assumption states that the wear on the contact area is uniform.

Constant Wear

For wear to be constant, the product of pressure and velocity at any point of the contact surface must be constant; that is

$$PV = C \tag{4.131}$$

But

$$V = \omega r \tag{4.132}$$

Therefore,

$$P = \frac{r_i}{r} P_i. \tag{4.133}$$

Equation 4.133 allows us to know the pressure at any given point of the disc in contact with the pad, provided that the pressure at one point is known. Equation 4.133 also tells us that the maximum pressure occurs at the inner radius; therefore, we can express Eq. 4.133 in term of maximum pressure as

$$P = \frac{r_i}{r} P_{max}. \tag{4.134}$$

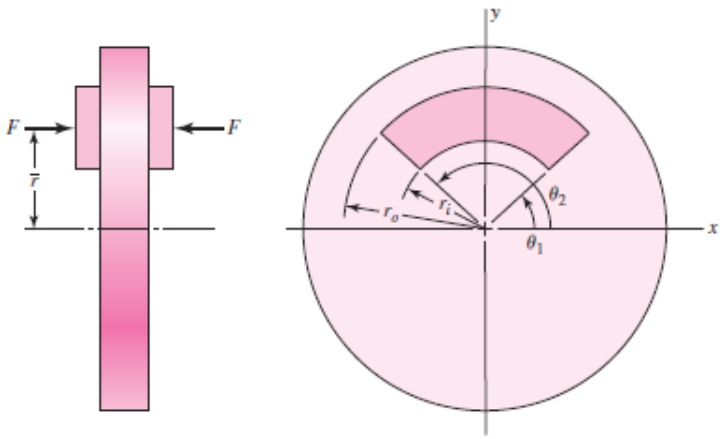

Figure 4.38: Disc brake model [86]

.

The elementary force and torque in any infinitesimal area are given by

$$dF = PdA = P_{max}\frac{r_i}{r} r d\theta dr = P_{max} r_i d\theta dr \tag{4.135}$$

$$dT = r \times \mu dF = \mu P_{max} r_i r d\theta dr \tag{4.136}$$

$$F = \int_{r_i}^{r_o}\int_{\theta_1}^{\theta_2} P_{max} r_i d\theta dr = (\theta_2 - \theta_1) P_{max} r_i (r_o - r_i) \tag{4.137}$$

$$T = \int_{r_i}^{r_o}\int_{\theta_1}^{\theta_2} \mu P_{max} r_i r d\theta dr = \frac{1}{2}(\theta_2 - \theta_1)\mu P_{max} r_i (r_o^2 - r_i^2) \tag{4.138}$$

Constant Pressure

When the pressure on the contact surface is assumed to be constant, the equations for force and torque are as follow:

$$F = \int_{r_i}^{r_o}\int_{\theta_1}^{\theta_2} P_{max} r d\theta dr = \frac{1}{2}(\theta_2 - \theta_1)P_{max}(r_o^2 - r_i^2) \tag{4.139}$$

$$T = \int_{r_i}^{r_o}\int_{\theta_1}^{\theta_2} \mu P_{max} r^2 d\theta dr = \frac{1}{3}(\theta_2 - \theta_1)\mu P_{max}(r_o^3 - r_i^3) \tag{4.140}$$

The kinetic energy absorbed by the brake is transformed into heat and expressed by

$$E = \frac{1}{2} I(\omega_2^2 - \omega_1^2) \tag{4.141}$$

This energy must be carried out of the turbine; otherwise, the disc's temperature will increase to a level that will lower the brake performance or even damage other components. The increase in temperature is given by

$$\Delta T = \frac{E}{mC_p} \tag{4.142}$$

The Newton's cooling mathematical model is given by

$$\frac{T - T_\infty}{T_i - T_\infty} = e^{-\beta t} \tag{4.143}$$

$$T_{max} = T_\infty + \frac{\Delta T}{1 - e^{-\beta t}} \tag{4.144}$$

$$\beta = \frac{h_{CR} A}{mC_P} \tag{4.145}$$

Where

$$h_{CR} = h_r + f_v h_c \tag{4.146}$$

The values of h_r, f_v, and h_c are found from the graph shown in Figures 4.39 and 4.40.

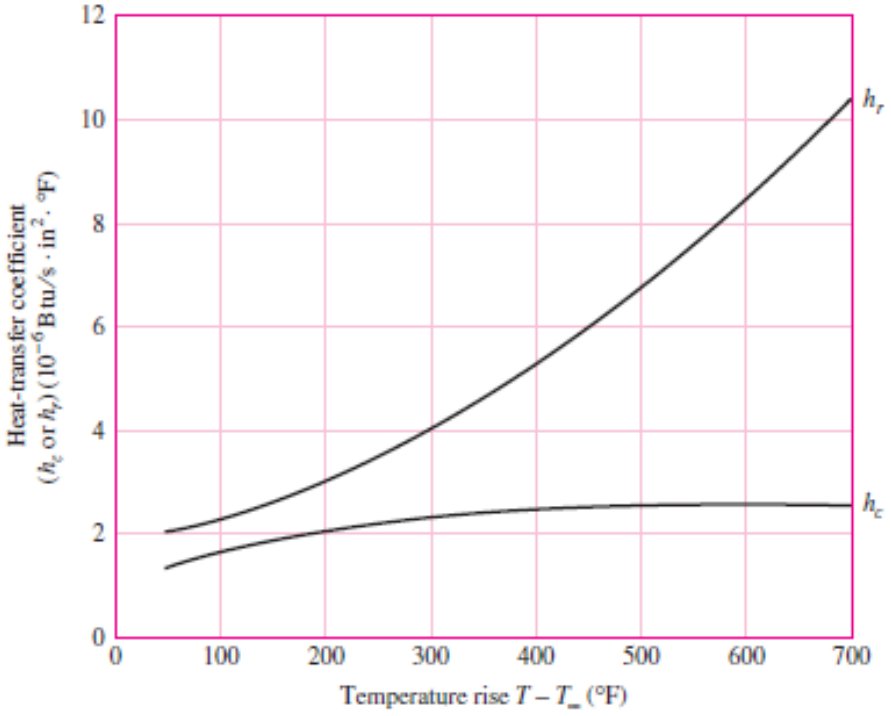

Figure 4.39: Heat-transfer coefficient in still air [86]

.

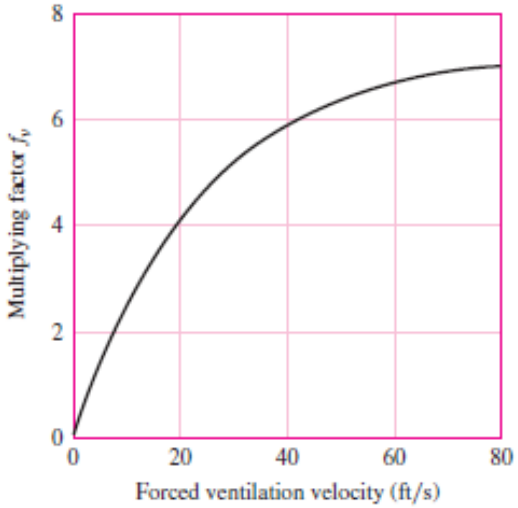

Figure 4.40: Ventilation factors [86]

.

4.11.2 Brake Preliminary Design

We start the turbine brake preliminary design by estimate the dimensions of the brake disc. Let's assume that the difference between the maximum temperature of the disc and the environment temperature to be 200°F and the forced wind speed to be 35 ft/s. From Figure 4.39 and 4.40, we have

Note: English units will be used where appropriate because the graphs to get the values of h_r, h_c and f_v are given in English units.

$$\begin{aligned} h_r &= 3 \times 10^{-6}\ Btu/(in^2 s^\circ F) \\ h_c &= 2 \times 10^{-6}\ Btu/(in^2 s^\circ F) \\ f_v &= 5.6 \end{aligned}$$

Therefore,

$$h_{CR} = (3 + 5.6 \times 2) \times 10^{-6} = 14.2 \times 10^{-6}\ Btu/(in^2 s^\circ F)$$

Given that

$$m = \rho A w$$

and that

$$\begin{aligned} \rho &= 0.282\ lb_m/in^3 \\ C_p &= 0.12\ Btu/(lb_m\ ^\circ F) \end{aligned}$$

Equation 4.145 is modified into

$$\beta = \frac{h_{CR}}{\rho C_p w}. \tag{4.147}$$

Combining Eq. (4.142), (4.144) and (4.147); and solving for A we have

$$A = \frac{0.5I\,|\omega_2^2 - \omega_1^2|}{\rho C_p w \left(1 - e^{-\frac{h_{CR}}{\rho C_p w} t}\right)(T_{max} - T_\infty)} \tag{4.148}$$

From CAD model the moment of inertia was found to be $I = 420\ kgm^2$, and the angular velocities are $\omega_1 = 19.5\ rad/s$, $\omega_2 = 0\ rad/s$. The brakes are assumed to be used once in every 150 s which mean $t = 150\ s$. Knowing that $1\ Btu = 1055.056\ J$, if the values above are used as given, Eq. (4.148), in SI unit, becomes

$$A = \frac{0.5I\,|\omega_2^2 - \omega_1^2|}{1055.056\ \rho C_p w \left(1 - e^{-\frac{h_{CR}}{\rho C_p w} t}\right)(T_{max} - T_\infty)} \tag{4.149}$$

Substituting the values into Eq. (4.149) we have

$$A = \frac{0.5 \times 420 \times |0^2 - 19.5^2|}{1055.056 \times 0.282 \times 0.12w \left(1 - e^{-\frac{14.2 \times 10^{-6}}{0.282 \times 0.12w} \times 150}\right) \times 200}$$

$$A = \frac{11.1829}{w(1 - e^{-\frac{0.0629}{w}})}$$

The graph of the area vs. thickness is shown in Figure 4.41. It can be seen that the smaller the thickness, the lighter the disc, as the mass of the disc varies linearly with the thickness. However, the area and the disc's radius vary exponentially with the disc thickness in inverse order; that is, if the thickness decreases, the area or the radius increases. Therefore, the disc's dimension is only limited by its maximum allowable radius and its ability to withstand the load. Due to space limitations, a radius of 200 mm was chosen, that is,

$$\begin{aligned} r &= 200 \text{ mm} \\ w &= 8.4 \text{ mm} \\ m &= 8.29 \text{ kg} \end{aligned}$$

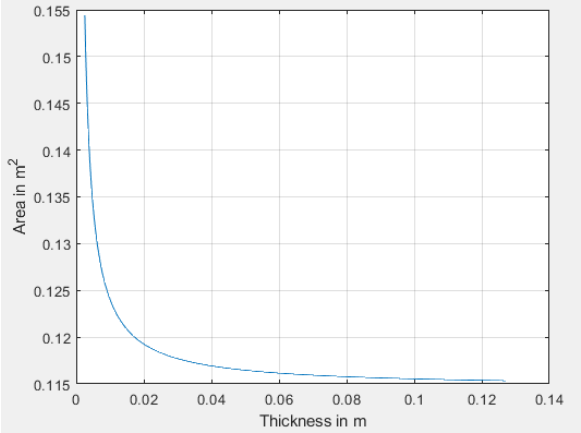

Figure 4.41: Disc area vs thickness

.

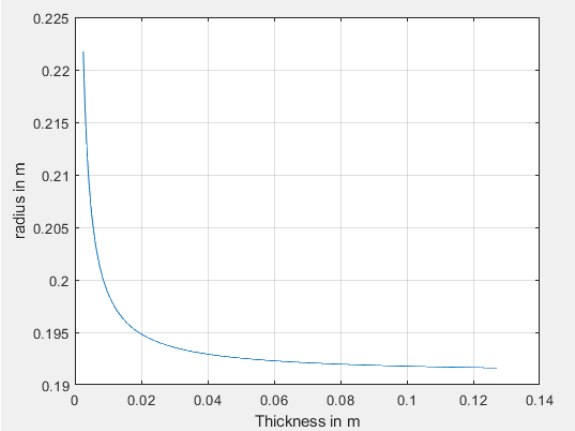

Figure 4.42: Disc radius vs its thickness

.

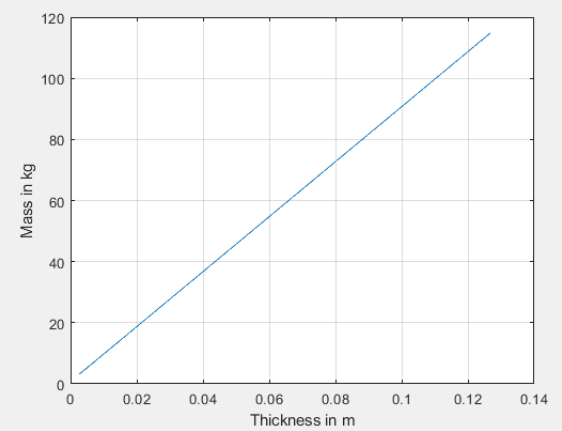

Figure 4.43: Disc mass vs thickness

.

4.11.3 Hydraulic Pressure

The brake pads will be clamped into the disc brake by a brake caliper assembly in the regular operation. Therefore, it is reasonable to assume that the pressure on the contact surface between the disc and the pad is uniform; consequently, using Eq. (4.140) to determine the hydraulic pressure needed to operate the brakes.

It is clear from Eq. (4.140) the brake pad's frictional properties have to be known to determine the pressure on the disc surface. In this design, the commercial brake pad **ACT787** was used for its durability, good frictional properties, and relatively low costs. This brake pad has the dimension of $162.6 \times 94 \times 81.8$ mm. Let's assume a circle with a radius of 200 mm, with a chord length of 162.6 mm as shown in the Figure 4.44.

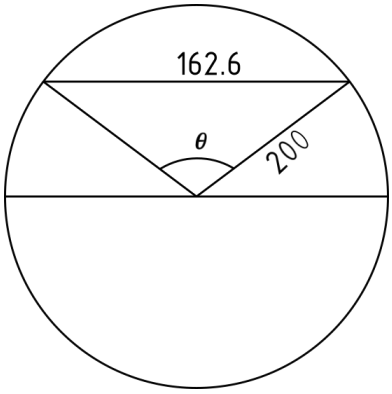

Figure 4.44: Disc brake model

.

The value of θ can be easily calculated.

$$\theta = 2 \arcsin\left(\frac{162.6}{2 \times 200}\right) = 0.8372 \text{ rad}$$

The inner diameter can be assumed to be $r_i = 200 - 94 = 106$ mm.

Now that all the dimensions are found, we can calculate the contact pressure from Eq. (4.140), given a torque of $T = 2367$ Nm and a friction coefficient of 0.45. Since both sides of the disc will contact the pad, we have to multiply the friction coefficient by two.

$$\begin{aligned} 2367 &= \frac{1}{3} \times 0.8372 \times 0.45 \times 2 \times P_{max} \times (0.2^3 - 0.106^3) \\ P_{max} &= 1.3841 \text{ MPa} \end{aligned}$$

Thus, the resultant force is

$$F = \frac{1}{2} \times 0.8372 \times 1.3841 \times 10^6 \times (0.2^2 - 0.106^2) = 16.67 \text{ kN}$$

Let assume that the brake pad is pushed into the disc by two pistons with 70 mm diameter each. Thus, the hydraulic pressure is

$$P = \frac{F}{A} = \frac{16.67 \times 10^3}{2 \times \pi \times 0.035^2} = 2.166 \text{ MPa}$$

From Figure 4.45, the force needed to operate the brake is

$$F_1 = \frac{L_1}{L_2} P A_1 \tag{4.150}$$

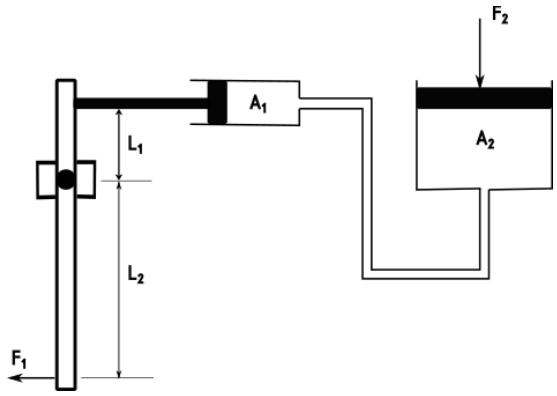

Figure 4.45: Brake system pressure

.

The diameter of cylinder one is assumed to be 10 mm and the mechanical advantage of the lever is set to 10. Therefore

$$F_1 = 0.1 \times 2.166 \times 10^6 \times \pi \times 0.005^2 = 17 \text{ N}$$

The low value of the obtained force, That is needed to operate the brakes allows an inexpensive electromagnet to be used to generate the force needed to operate the brakes.

4.12 Chapter Summary

The chapter started with the discussion of engineering standards to estimate the turbine load. Standard IEC 61400-2 was given special attention; as it is the standard normally used to estimate the small wind turbine wind loads. IEC 61400-2 assumes that wind turbine only needs to withstand fatigue load (load case A), and ultimate strength load (load case B through J). After the brief discussion of the standard, the blade preliminary design based on this standard and on the CAD geometry used in the blade aerodynamic study followed; thus the blade physical and mechanical properties were determined and then optimized for minimum weight using Matlab optimization tools. The main shaft's mechanical and physical properties were determined using the same procedure applied for the blades.

The chapter proceeded by briefly discussing the types of tower used in small wind turbines followed by the mathematical model of the tower chosen in this research; the model assumed the tower is a tapered cantilever with a hollow octagonal cross-sectional area, bearing an extreme wind speed of 52.5 m/s, and the induced load from other components attached to the turbine. The tower buckling was considered according to standard ASCE. The tower mathematical model was solved numerically using Matlab, and the tower dimensions were optimized used graphical methods. The nacelle was modeled as a portal frame fixed at both ends, and load case I (IEC 61400-2) was used to estimate its load. The mainframe was modeled as a cantilever beam with a rectangular cross-sectional area, bearing the inducing load from other components when they are at their worst-case scenario. The mathematical model for both the nacelle and mainframe was solved analytically.

The turbine protection against over-speed was discussed, with particular emphasis on the furling mechanism – furling is the preferred method to protect small wind turbines against over-speed. After the furling mechanism introduction, its mathematical model was derived based on Lagrange formalism, and then the preliminary tail dimensions were obtained from the system equilibrium condition when the turbine operates at the rated speed. The equations were solved numerically and optimized using Matlab, and then a graphical analysis of the system performance was done. The electrical model of the small wind turbine consisted of PMSG, generator-side converter, grid-side converter, and their respective control systems. Their mathematical models were derived; the generator-side converter control system was based on the field-oriented control and the grid-side converter control was based on the hysteresis control. The chapter ends by designing the turbine brake system; the essential theoretical background of the disc brake was discussed first followed by its preliminary design.

Chapter 5

Detail Design

In this Chapter, the connection of the components is discussed, the various bearings used in the design are selected, the CFD and the FEA of the main components are performed. Section 5.1 gives a detailed analysis of how the blades and the main shaft are to be connected to the hub, and the calculations of selecting the main and yaw bearings are given. In Section 5.2 the CFD and FEA of the blades, main shaft, tail, mainframe, and tower are given. The manufacturing processes of the various components are discussed in Section 5.3. Section 5.4 presents the detailed design of the generator side control system. Section 5.5 presents the MatLab Simulink simulation of the turbine system. Finally, Section 5.6 gives the turbine specifications.

5.1 Fitting

5.1.1 Blades and Hub Connection

The blades are connected to the hub through bolts, as shown in Figures 5.1 and 5.2. To estimate the load that the bolts will have to carry, we shall use load case H as design load, since it gives the highest load in the blade root.

In Chapter 4, we found the moment on each blade roots and the thrust induced by the blades to be $M = 3878$ Nm and $F_{th} = 6650\ N$, respectively. Let's now select the type, dimensions, and the material of the bolts to be used in each blade root. Since the blades are to be connected to the hub with the intent of once connected, they will not be disconnected if possible; we choose 10.9 as bolts property class, which gives a minimum proof strength of 830 MPa, see Tab. (8-11) of ref. [86], because it provides a high tension preload. Let's assume that tension forces on the bolts balance the bending moment and the thrust. Initially, we will set the number of bolts to six distributed, as shown in Figure 5.1.

If we further assume that at the connection surface the blade is rigid and that the bolts share the load due to thrust equally, if we take moment about point A, we will have the following expression (see Figure 5.2):

$$M = 3F_1(0.04) + 3F_2(0.13) \tag{5.1}$$

But,

$$\frac{F_{th}}{3} = 3F_1 + 3F_2 \tag{5.2}$$

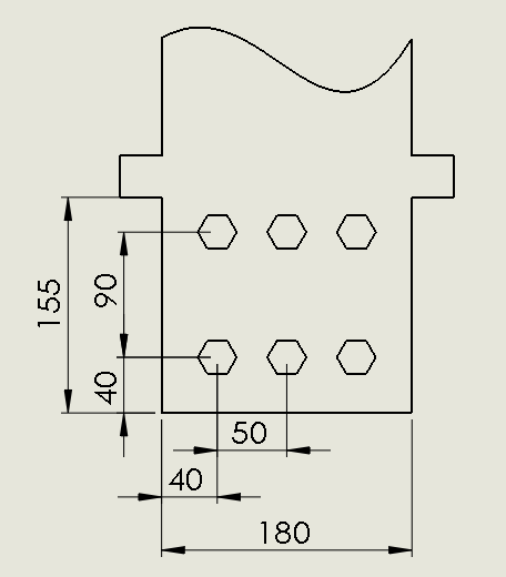

Figure 5.1: Blade and hub connection

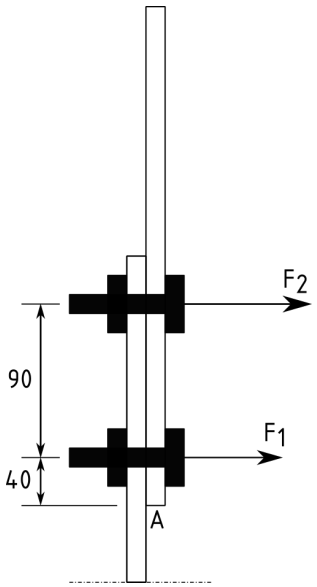

Figure 5.2: Blade and hub connection model

Solving Eqs. (5.1) and (5.2) for F_1 and F_2 simultaneously we have, $F_1 = -13.294$ kN and $F_2 = 14.0333$ kN. This means, in the scenario where load case H is considered to be applied in reverse (downwind), each top bolt will experience a tension force of approximately 14 kN.

The load factor is taken to be 3 as recommended by IEC 61400-2. To take into account the load preload we will used Eq. (8-28) of ref. [86] as expressed below.

$$C = \frac{S_p A_t - F_i}{n_L P} \tag{5.3}$$

Where S_p—minimum proof strength; A_t—tensile stress area; F_i—preload; n_L—load factor; P—external load for each bolt; C—fraction of external load P carried by bolt.

For permanent connection

$$F_i = 0.9 A_i S_p \tag{5.4}$$

The value of C can also be calculated by

$$C = \frac{k_b}{k_b + k_m} \tag{5.5}$$

Where: k_b—effective stiffness of the bolt. k_m—effective stiffness

$$k_b = \frac{A_d A_t E}{A_d l_t + A_t l_d} \tag{5.6}$$

$$k_m = \frac{0.5774 \pi E d}{2 \ln \left(5 \frac{0.5774 l + 0.5 d}{0.5774 l + 2.5 d} \right)} \tag{5.7}$$

Where A_t—tensile-stress area; l_t—length of threaded portion of grip; A_d—major-diameter area of fastener; l_d—length of unthreaded portion in grip; l—thickness of all material squeezed between face of bolt and face of nut; d—diameter of the bolt; E—Young modulus.

The formula to calculate all needed parameter are found in Chapter 8 of ref. [86], and are given below.

$$l_d = L - L_T \tag{5.8}$$

$$L_T = 2d + 6 \tag{5.9}$$

$$l_t = l - l_d \tag{5.10}$$

$$A_d = \frac{\pi d^2}{4} \tag{5.11}$$

Where L—total bolt length; L_T—threaded length.

The bolt's diameter must be estimated and refined iteratively using appropriate Tables to proceed with the calculation. Let $M14 \times 2$ be the initial bolt diameter. From Table 8-1 of ref. [86] a diameter of 14 mm we get $A_t = 115$ mm^2. The blade and hub combined thickness is 45 mm, from the CAD model, using two normal washers 14 N, and a thickness of 2.8 mm. Therefore,

$$l = 2 \times 2.8 + 45 = 50.6 \text{ mm}$$

The bolt's total length is set to be equal to the length of the thickness of all material squeezed between the bolt's face and the nut's face plus the height of the nut, plus two pitches. Therefore, the total bolt length is

$$L = 50.6 + 12.8 + 2 \times 2 = 67.4 \text{ mm}$$

However, 67.4 mm is not a standard size. The next standard size is 80 mm, and this value will be used as the total bolt length. Taking $E = 210$ GPa, all other parameters can be calculated.

$$\begin{aligned}
L_T &= 2 \times 14 + 6 = 34 \text{ mm} \\
l_b &= L - L_T = 80 - 34 = 46 \text{ mm} \\
l_t &= 50.6 - 46 = 4.6 \text{ mm} \\
A_d &= \pi \times 7^2 = 153.94 \text{ mm}^2 \\
k_b &= \frac{153.94 \times 115 \times 210}{153.94 \times 4.6 + 115 \times 46} = 619.7953 \text{ GPamm} \\
k_m &= \frac{0.5774\pi \times 210 \times 14}{2 \ln\left(5 \times \dfrac{0.5774 \times 50.6 + 0.5 \times 14}{0.5774 \times 50.6 + 2.5 \times 14}\right)} = 2572.1 \text{ GPamm} \\
C &= \frac{619.7953}{619.7953 + 2572.1} = 0.1942
\end{aligned}$$

We will check the load factor by Eq. 5.3

$$n_L = \frac{0.1 \times 830 \times 115}{0.1943 \times 14033.3} = 3.5024$$

Let's check the fatigue load factor to see if the bolt will not fail due to fatigue. According to IEC61400-2, only load case A should be considered for fatigue analysis, and the safety factor for fatigue loads should be equal to one, that is, $\gamma_f = 1.0$. From blade preliminary analysis we obtained the following values: $\Delta F = 39$ kN, $\Delta M_x = 1.268$ kNm and $\Delta M_y = 1.578$ kNm.The bolts carry these calculated loads. The analysis of how much load each bolt takes is described in the following paragraph.

Figure 5.3 shows the bolt fatigue analysis model. The axial fatigue load, ΔF, is considered to be equally shared by all the bolts, F_i'. The moment in the x-direction is used for fatigue analysis. The moment is assumed to be applied in the center of geometry formed by the bolts, and it is balanced by the sum of the couple induced by the forces F_i''. Finally, the fatigue load moment in the y-axis is balanced by the couples generated by forces F_i'''. For a detailed analysis of the load carried by bolts, see Ch. 8 of ref. [86].

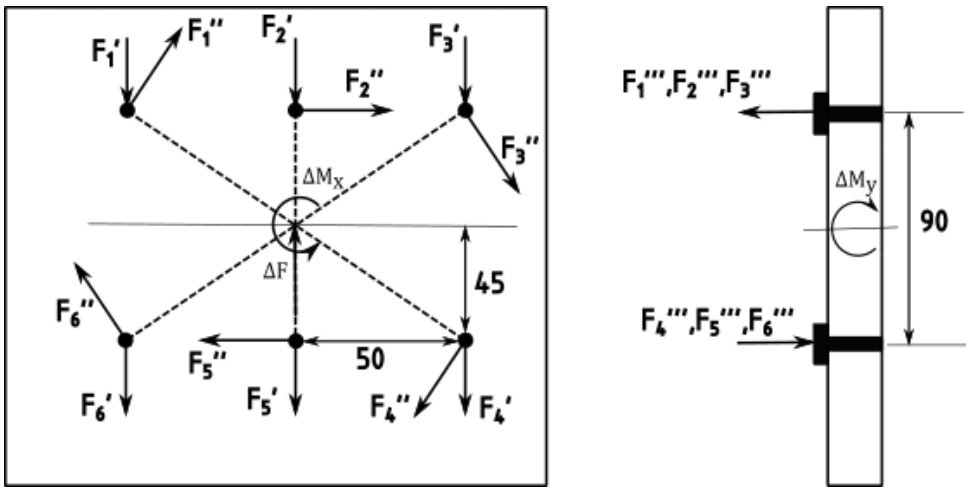

Figure 5.3: Blade and hub connection fatigue model

From geometry formed by the bolts and assuming that all bolts have the same dimensions, we can write

$$F_i' = \frac{\Delta F}{6} \tag{5.12}$$

$$F_1'' = -F_4'',\ F_2'' = -F_5'',\ F_3'' = -F_6'' \tag{5.13}$$

$$F_{1,2,3}''' = -F_{4,5,6}''' \tag{5.14}$$

We can calculate F_i'' from Eq. 8-57 of ref. [86], as

$$F_i'' = \frac{M_x r_i}{\sum_{i=1}^{n} r_i^2} \tag{5.15}$$

In Figure 5.3, we see that the shear force on the bolts one and six are equal and greater than the shear force on any other bolt, and its magnitude is calculated by cosine rule.

We can now calculate the maximum equivalent load on the bolt as

$$F_1' = \frac{39}{6} = 6.5\,\text{kN}$$

$$F_1'' = \frac{1268 \times \sqrt{0.05^2 + 0.045^2}}{4(0.05^2 + 0.045^2) + 2 \times 0.045^2} = 3850.8\ \text{N}$$

$$F_1^S = \sqrt{6500^2 + 3850.8^2 + 2 \times 6500 \times 3850.8 \times \cos\left(\arctan\left(\frac{45}{50}\right)\right)} = 9710.2\ \text{N}$$

The tension force is calculated as

$$F_1''' = \frac{1578}{3 \times 0.09} = 5844.4\ \text{N}$$

Taking the bolt area found earlier, we can calculate the fatigue stresses on the bolts as

$$\begin{aligned} \Delta\sigma &= \frac{5844.4}{115} = 50.82 \text{ MPa} \\ \Delta\tau &= \frac{9710.2}{115} = 84.44 \text{ MPa} \\ \Delta\sigma_{eq} &= \sqrt{\Delta\sigma^2 + 3\Delta\tau^2} = \sqrt{50.82^2 + 3 \times 84.44^2} = 98.55 \text{ MPa} \end{aligned}$$

The fatigue load factor is found from Eq. 8-48 of ref. [86], and can be transformed into

$$n_f = \frac{2S_e(S_{ut} - \sigma_i)}{C\sigma_{eq}(S_{ut} - S_e)} \tag{5.16}$$

Where S_e is the endurance limit; $S_e = 162$ MPa; see Table 8-17 of ref. [86]; and S_{ut} is the minimum tensile strength,S_{ut}. See Tab. 8-11 of ref. [86]. Therefore,

$$n_f = \frac{2 \times 162 \times (1040 - 830)}{0.1942 \times 98553.5 \times (1040 + 162)} = 2.96 \tag{5.17}$$

The load factor turned to be greater than the one defined by IEC61400-2, which means the bolts will not fail due to fatigue. Therefore, the blades and hub will be connected by six $M14 \times 2$ class 10.9 as shown in Figs. 5.1 and 5.2.

5.1.2 Hub and Main Shaft Connection

The main shaft and the hub must be attached to have no relative motion due to sliding and spinning against their connecting surface. In a small wind turbine, the hub and the main shaft are connected by key, with keyways on both components. The shaft is also threaded so that a nut lock the hub, which prevents it from sliding against the shaft. The shaft and hub mate surfaces are machined for tight-fitting [18].

If the stress concentration inherent to using a keyway in the shaft is a concern, shrinking disc fitting can be used. In this type of connection, the hub hole's diameter is made to be just slightly larger than the extremity of the shaft. The shrinking disc is made of two discs and two rings. The ring's inner surface is placed on the outside of the hub section connected to the shaft. The rings are tapered axially in both directions. The tapered rings are located between the two discs, and when bolts pull them together, the rings are compressed, which compresses the hub and clamp it to the shaft [49]. The shaft can also be connected to the hub permanently by putting a flange on one of the shaft's ends and attaching the shaft to the flange by bolts. In the current design, the first fitting method discussed above will be used for simplicity, manufacturability, easiness of assembly, and relatively low cost.

Key Design

The extremity of the main shaft is set to have a diameter of 80 mm. According to Metric Standard, a shaft diameter of 80 mm, would have a keyway width of 22 mm, a keyway depth of 5.4 mm, a key width of 22 mm, and a key depth of 14 mm.

Now let us calculate the length of the key. Let's assume that the load of interest in designing the key is torsion only. Therefore, load case G is used to give the maximum torsion load ($T = 2367$ Nm) that the shaft will be subjected. Using a load factor of 3.3, as specified by IEC61400-2 and using $ASTM - A572$ as the material for the key, we can calculate the length of the key as follows:

$$F = \frac{T_{max}}{r} = \frac{3.3 \times 2367}{0.04} = 195277.5 \text{ N} \tag{5.18}$$

According to distortion-energy theory the shear strength can be calculated by

$$\tau_{sy} = 0.577\sigma_y = 0.577 \times 340 = 196.18 \text{ MPa} \tag{5.19}$$

Therefore

$$l = \frac{F}{\tau_{sy} t} = \frac{195277.5}{196.18 \times 22 \times 10^3} = 45 \text{ mm} \tag{5.20}$$

Or

$$l = \frac{2F}{\sigma_y t} = \frac{2 \times 195277.5}{340 \times 22} = 52 \text{ mm} \tag{5.21}$$

We will use the closest standard larger dimension, which is 60 mm.

Fatigue Analysis of the Threaded Shaft

The maximum tensile force in the thread on the shaft and the maximum shear forces that the nut can take are given by,

$$F_{bolt} = \frac{\pi}{4}(0.9d)^2\sigma_y \tag{5.22}$$

$$F_{nut} = \pi d(0.75t)(0.577\sigma_y) \tag{5.23}$$

See ref. [87].

$$F_{bolt} = \frac{\pi}{4} \times (0.9 \times 0.08)^2 \times \frac{700}{3.3} \times 10^6 = 3454.6 \; kN$$

$$F_{nut} = \pi \times 0.08 \times 0.75 \times 0.022 \times 0.577 \times \frac{700}{3.3} \times 10^6 = 507.56 \; kN$$

Let's test the shaft for fatigue using Goodman theory. Let's assume that the threaded shaft carries only torsion and thrust loads, and let's set the torsion stress concentration to 3 (see ref. [86]). Thus we have

$$\sigma_a = \sqrt{\left(\frac{\Delta F_{x-shaft}}{A}\right)^2 + 3\left(\frac{K_{sc}\Delta M_{x-shaft}}{2W}\right)^2} = \sqrt{\left(\frac{2245.4}{\pi \times 0.05^2}\right)^2 + 3 \times \left(\frac{3 \times 16 \times 821.65}{\pi \times 0.1^3}\right)^2}$$

$$\sigma_a = 21.746 \; MPa$$

$$n_f = \frac{\sigma_e(\sigma_{ut} - \sigma_i)}{\sigma_a(\sigma_{ut} + \sigma_e)} = \frac{162 \times (1040 - 830)}{21.746 \times (1040 + 162)} = 1.3015$$

The threaded blade will not fail due to fatigue because the recommended fatigue factor is 1.25.

5.1.3 Bearings Selection

Main Bearings

The bearings that support the main shaft must be able to carry radial as well as axial load. The bearings should also tolerate some misalignment. Spherical roller bearings are generally used as the primary bearing because they bear axial load in both directions and allow some misalignment. When a bearing is well lubricated and properly sealed against dust and dirt and operates at a reasonable temperature, the only failure to be considered is fatigue failure [86]. Therefore we will consider loading case A to model the bearings mounted on the shaft.

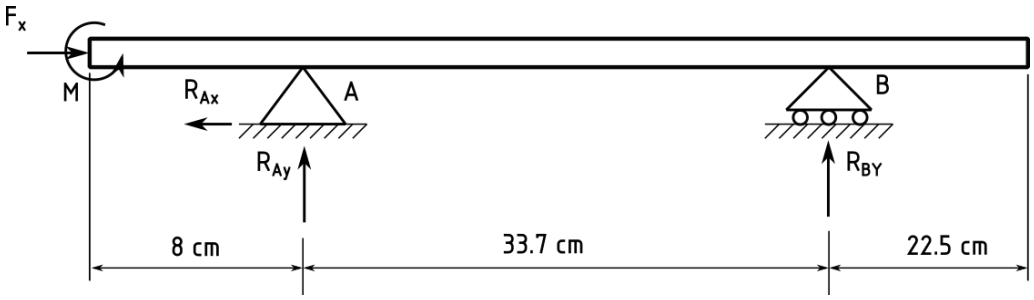

Figure 5.4: Dynamic model of the shaft

The values of the loads represented in Figure 5.5 were obtained in previous sections, and they were as following: $F_x = 2.367$ kN, $M = 1578$ Nm. From Figure 5.4 and using the given values, we can easily find the reactions. However, only the reaction R_A shall be considered because the blades' bearing carries more load. The reaction at A is $R_{Ax} = 2.367$ kN, and $R_{Ay} = 4.6825$ kN. Where R_{Ax}—axial load; and R_{Ay}—radial load.

From SKF catalogue we have the following formula to find the equivalent radial force:

$$\begin{cases} P = F_r + y_1 F_a & \text{if } \dfrac{F_a}{F_r} \leq e \\ P = 0.67 F_r + y_2 F_a & \text{if } \dfrac{F_a}{F_r} > e \end{cases} \tag{5.24}$$

The bearing $SKF\ 24020{-}2RS5/VT143$ was chosen, which gives $e = 0.28$, $y_0 = 2.5$, $y_1 = 2.4$, $y_2 = 3.6$. Therefore the equivalent radial force is

$$P = 4.6825 + 2.4 \times 2.367 = 10.3633 \text{ kN}$$

Since the fatigue load limit for this bearing is $P_u = 45.5$ kN, the factor of safety is

$$n_f = \frac{45}{10.3633} = 4.3422$$

The factor of safety required in IEC61400-2 is 1.25, therefore the bearing will not fail due to fatigue.

Now let's find the life of the bearing. From Eq. (11-3) of ref. [86] we have,

$$C_{10} = F_D \left(\frac{L_D n_D 60}{L_R n_R 60} \right)^{1/a} \tag{5.25}$$

Where C_{10}—dynamic load rating in kN; L_R—rating life in hours; n_R—rating speed in rpm; F_D—desired radial load in kN; L_D—desired life in hours and n_D—desired speed in rpm. Since SKF rates their bearings for one million revolutions the term $L_R n_R 60 = 10^6$. From catalogue $C_{10} = 296$ kN. The desired rotation speed and the equivalent radial load are already known. Taking a to be $a = 10/3$ (see ref. [86]), we have,

$$\begin{aligned} 296 &= 10.3633 \left(\frac{L_D \times 186 \times 60}{10^6} \right)^{0.3} \\ L_D &= 6.38 \times 10^6 \text{ hours} \end{aligned}$$

Therefore, under the given operational conditions, the bearing will take about 729 years before failing due to fatigue.

The bearing static analysis model is shown in Figure 5.5. For the static load analysis load case H is used because it yields the largest static load. The values of the load for case H are as follow: $F_x = 6.65$ kN, $F_y = 1.12$ kN, $q_0 = 4.61$ kN/m, $q_1 = 0.21$ kN/m, $M = 3.88$ kNm. From Figure 5.5 the reaction at A are $R_{Ay} = 13.52$ kN and $R_{Ax} = 6.65$ kN.

The equivalent static load can be determined from SKF catalogue as

$$P_0 = F_r + y_0 F_a \tag{5.26}$$

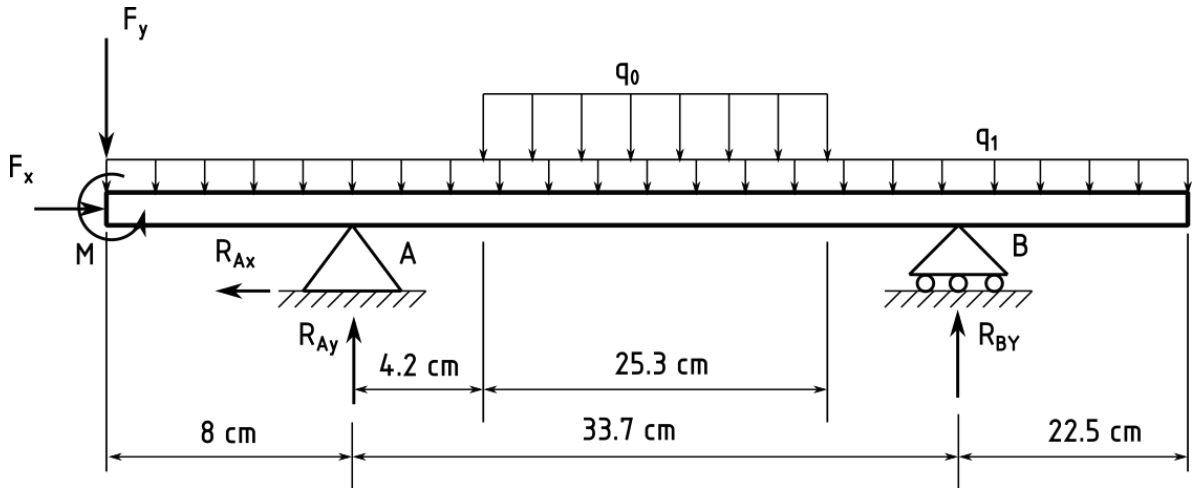

Figure 5.5: Static model of the shaft

Substituting the values, we have

$$P_0 = 13.52 + 2.5 \times 6.65 = 30.15 \text{ kN}$$

Since the static load capacity of bearing $24020 - 2RS5/VT143$ is 415 kN, the bearing will not fail due to static load. Substituting the values we have

Yaw bearing

The yaw bearing has to be able to carry axial, radial, and bending load. In wing turbine rolling or sliding plate, bearings are used as yaw bearing. Figure 5.6 shows the model to calculate the static and dynamic bearing load.

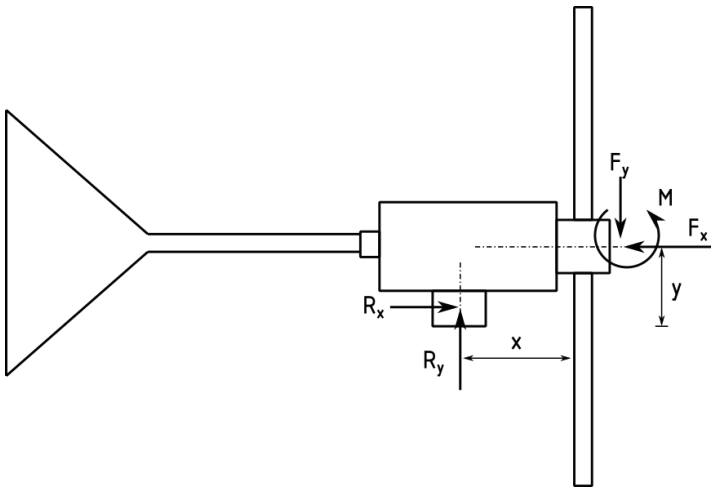

Figure 5.6: Yaw bearing

For dynamic load we have

$$\begin{aligned} R_x &= F_x = F_r = 2.367 \text{ kN} \\ R_y &= F_y = F_a = 0 \text{ kN} \end{aligned}$$

We will use the four-point contact bearings from SKF as the yaw bearing. From the SKF catalog, the equivalent radial force for four points is given by

$$\begin{cases} P = F_r + 0.66F_a & \text{if } \dfrac{F_a}{F_r} \leq 0.95 \\ P = 0.6F_r + 1.07F_a & \text{if } \dfrac{F_a}{F_r} > 0.95 \end{cases} \tag{5.27}$$

Therefore,

$$P = 0.6 \times 2.367 = 1.42 \text{ kN}$$

The maximum yaw rate was calculated previously, $\omega_{yaw} = 2.635$ rad/s. The yaw is assumed to occur 10 percent of time; that is, the bearing life time has to be 10 percent of the turbine life time. Let's take 30000 hours as the yaw bearing life.

Therefore,

$$C_{10} = 1.4202 \times \left(\frac{30000 \times 25.1624 \times 60}{10^6} \right)^{0.3} = 4.46 \text{ kN}$$

For dynamic load we have,

$$\begin{aligned} R_x &= F_x = F_r = 6.65 \text{ kN} \\ R_y &= F_y = F_a = 3.924 \text{ kN} \\ M &= 3.88 \text{ kNm} \end{aligned}$$

The SKF catalog gives the equivalent static load for four-point contact ball bearing as

$$P_0 = F_r + 0.58F_a \tag{5.28}$$

Therefore, the equivalent static load is

$$P_0 = 6.65 + 0.58 \times 3.924 = 8.93 \text{ kN}$$

Since the load calculated for yaw bearings are very low, any bearing with an inner diameter larger than 25 mm will be safe to be used. The bearing $QJ\,216\ N2MA$ was chosen.

5.2 Main Components FEA and CFD Analysis

5.2.1 Turbine Components Computational Analysis

In the previous chapter, we saw that the simple load model load case B and H from IEC 61400-2 dominate the turbine blade's design. It was concluded that to avoid high gyroscopic loads; the turbine will not yaw if the turbine is rotating at a speed greater than the speed considered to be the safe speed. Therefore, the gyroscopic load will not be considered further, as it is assumed that the control system will be designed to mitigate it. Henceforth, only load case H will be regarded as the main component of the wind turbine's computational analysis. The CFD of the blade was done using SolidWorks Flow Simulation.

Blade CFD

Computational domain To set up the computation domain, the blades, hub, and the hub nose were generated separately and then assembled. The airfoil SG6043 was used as the blade cross-section profile, with 287.5 mm of chord length and 3425.9 mm. The hub was modeled as a disc with a 500 mm diameter and a thickness of 15 mm. The hub nose was chosen to be a hollow half ellipsoid with a height of 500 mm and a width of 400 mm. The fluid dominion was left to default as given from external analysis in SolidWorks Flow Simulation. Figures 5.7 to 5.9 show the fluid computational domain.

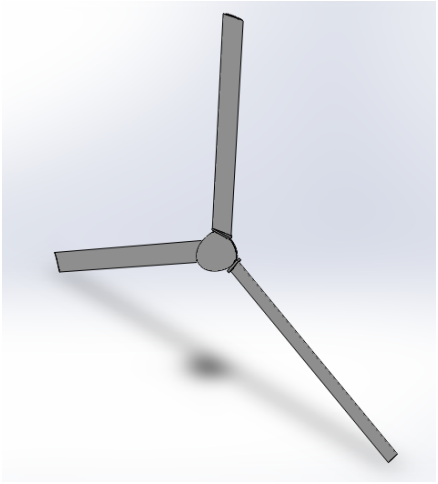

Figure 5.7: Wall boundary of the flow domain

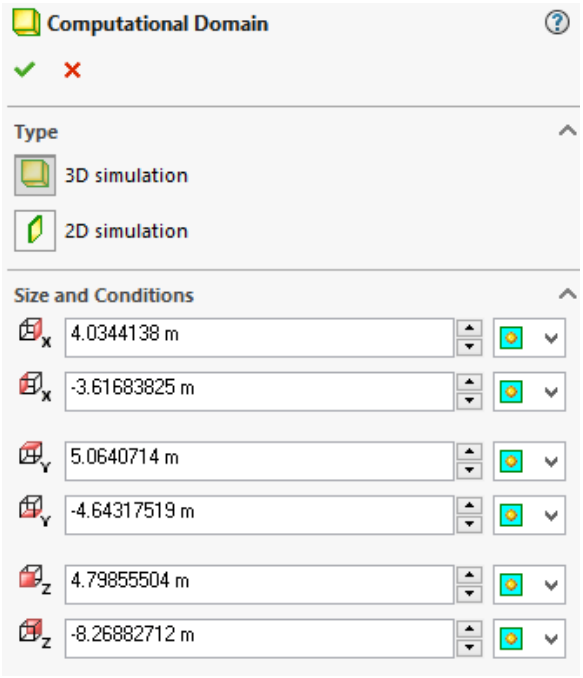

Figure 5.8: Fluid domain

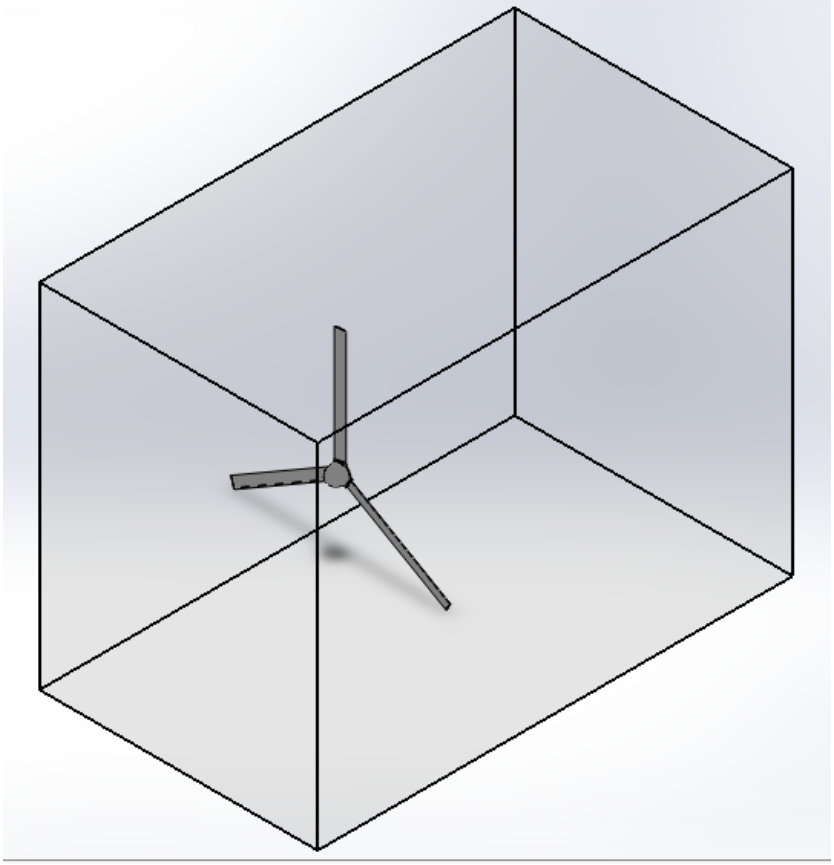

Figure 5.9: Flow domain

General setting The general setting were as following:

- Analysis type: External
- Fluids: Air
- Wall conditions
  - wall thermal conditions: Adiabatic
  - Roughness: 0 micrometer
- Initial and ambient conditions
  - Thermodynamic parameters
    - Pressure: 101325 kPa
    - Temperature: 293.2 K
  - Velocity parameters
    - Velocity in Z direction: $-52.5\ m/s$

For more information see Appendix A.5

Boundary conditions The only boundary condition used was the wall boundary conditions; others were left to default features. The blades, hub disc, and the hub nose were set to be a real wall, as shown in the Figure 5.10.

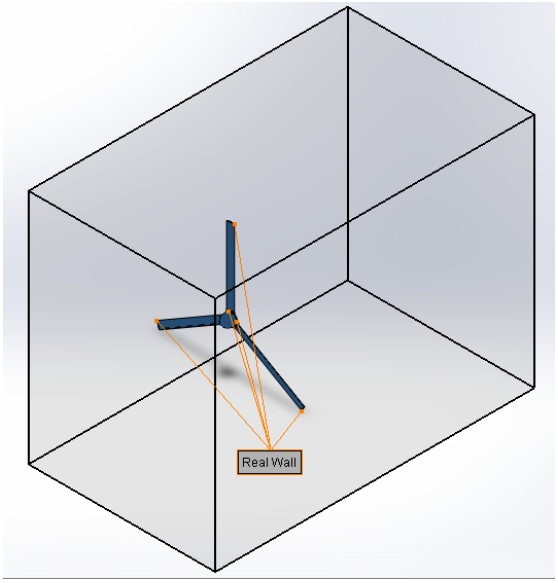

Figure 5.10: Boundary conditions

Meshing and solution Due to low computational capability, the meshing was left to default parameters, which resulted in a total of 2002924 fluid cells, as shown in Figure A.5. The solution converged after 299 iterations, as shown in Figure 5.11.

Parameter	Value
Status	Solver is finished.
Total cells	2,002,924
Fluid cells	2,002,924
Fluid cells contacting solids	973,887
Iterations	299
Last iteration finished	13:59:37
CPU time per last iteration	00:01:33
Travels	
Iterations per 1 travel	264
Cpu time	48 : 26 : 57
Calculation time left	0 : 0 : 0
Run at	NORBERTO

Figure 5.11: Meshing of the flow domain

Post-processing The isopressure lines and velocity field were analyzed for a sanity check. From Figure 5.12, it can be seen that the pressure and velocity field behaves as it is expected.

To show the pressure contour, cut plot was used and isopressure lines were plotted on a plane 2 m from the $xz - plane$. The number of isolines was set to 100, as shown in Figure 5.14. The velocity was set as follows: firstly, the blade, hub, and hub nose surface were chosen; then, the number of velocity lines was set to 500, and the option draw trajectory as lines with arrows was determined. Figure 5.13 shows the velocity trajectory parameters.

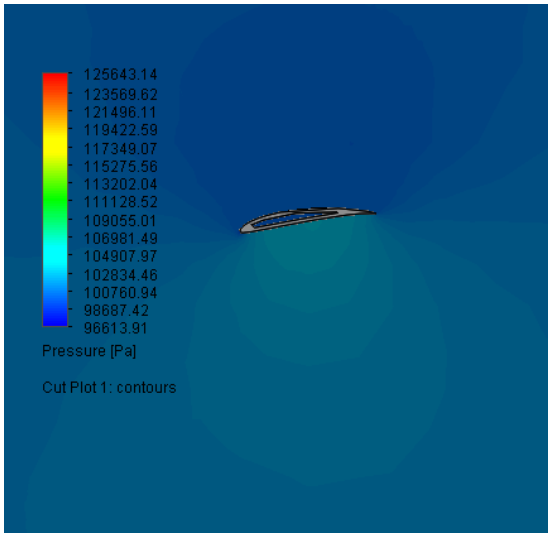

Figure 5.12: Pressure contour

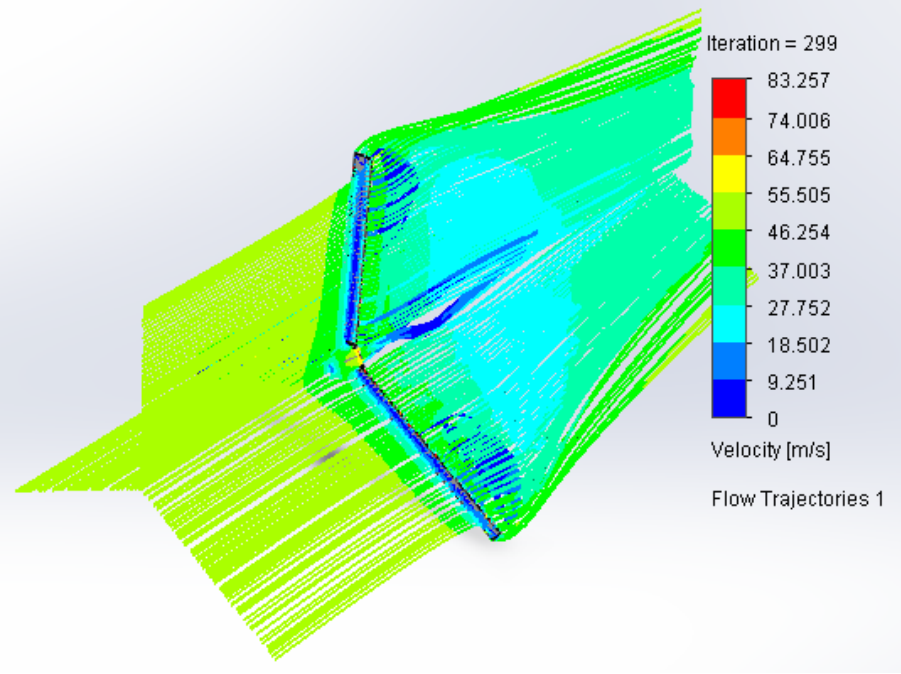

Figure 5.13: Velocity trajectory lines

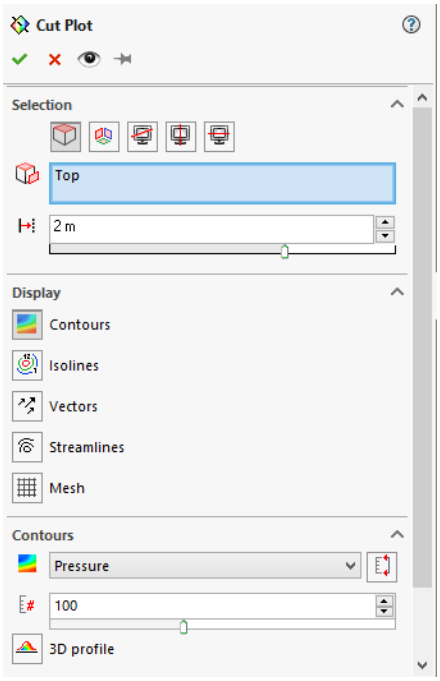

Figure 5.14: Cut plot parameters

5.2.2 Blade FEA

Material Selection To start the blade FEA the material for the blades, hub, and hub nose was assigned. Aluminium 7075-T6 was chosen as the blades and hub nose material, a 1023 carbon steel sheet for the hub disc.

Constraints The hub's hole, where the main shaft is coupled with the hub, was set as a fixed constraint, as shown in Figure 5.15.

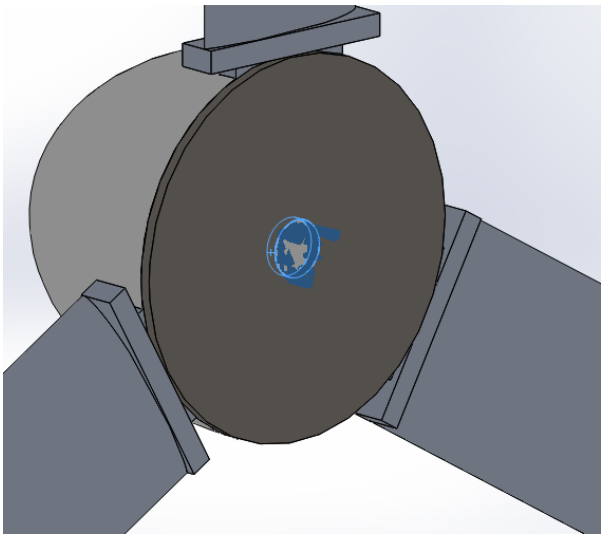

Figure 5.15: Fixed constraint

External Load For External load, the result obtained from Flow Simulation was exported to Solidworks Simulation. Gravity and flow effect from Flow Simulation was used, as shown in Figure 5.16.

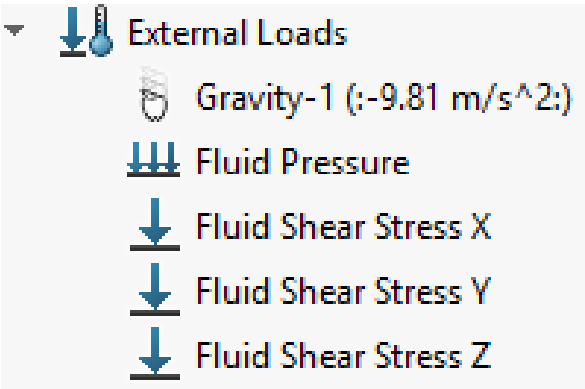

Figure 5.16: External Load

Mesh Since static simulation in SolidWorks Simulation did not take long to converge to a solution, globally, the mesh was set to be as fine as possible, as shown in Figure 5.17. The blades meshing was further refined by applying mesh control on the three-blade surfaces, as shown in Figure 5.18. The details and the final mesh's graphic representation are shown in Figures A.23 and A.24, respectively.

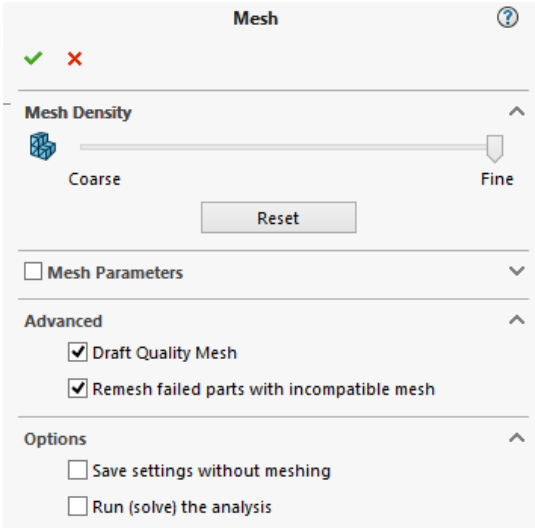

Figure 5.17: Mesh setting

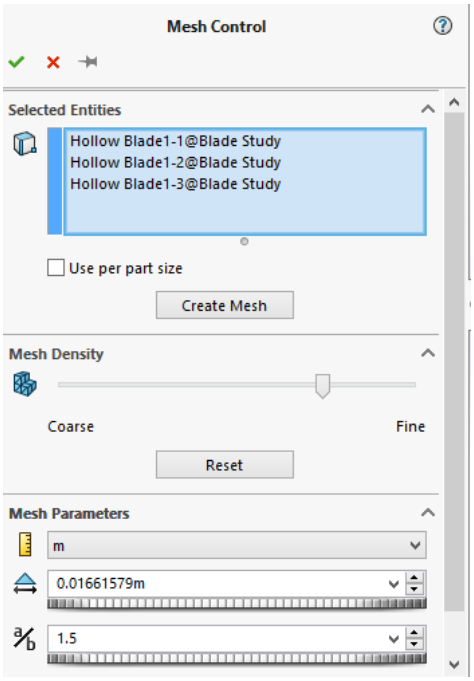

Figure 5.18: Mesh control

Results The mechanical quantities of interest are in this analysis are the Von Mises stresses, the deflection, and the reaction at the fixed surface. The Maximum stress was found to occur near the root of the blade, as shown in Figure 5.19.

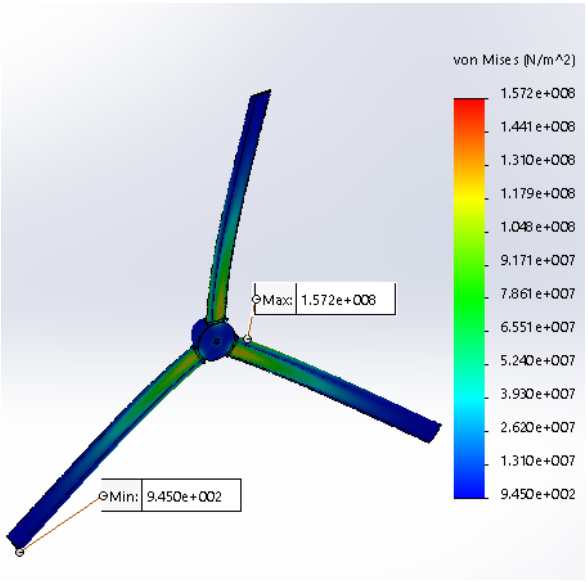

Figure 5.19: Blade Von Moses stress

The blade will experience large deformation at a wind speed of 52.5 m/s. Therefore, a large deflection solver was used. The result shows that the blade will be deflected by 323 mm, as shown in Figure 5.20.

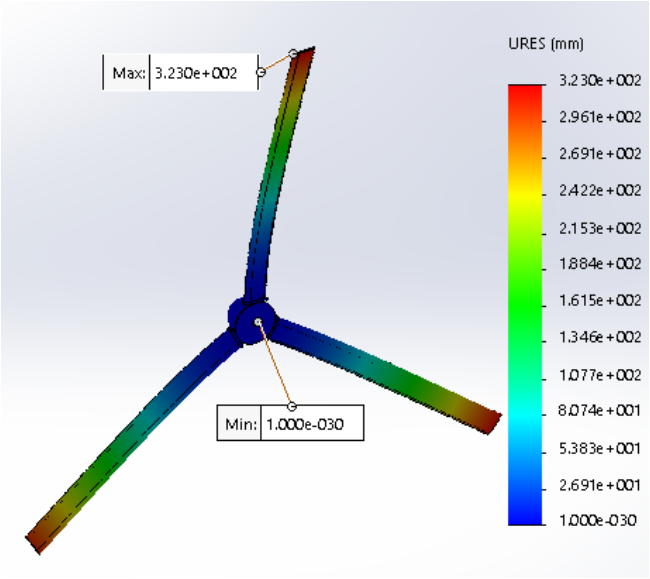

Figure 5.20: Blade deflection

The hub center point was chosen to be where the reaction force and moment are to be obtained. Therefore, this point and the fixed constraint surface were selected in the Free Body Force option, as shown in Figures 5.22 and 5.21.

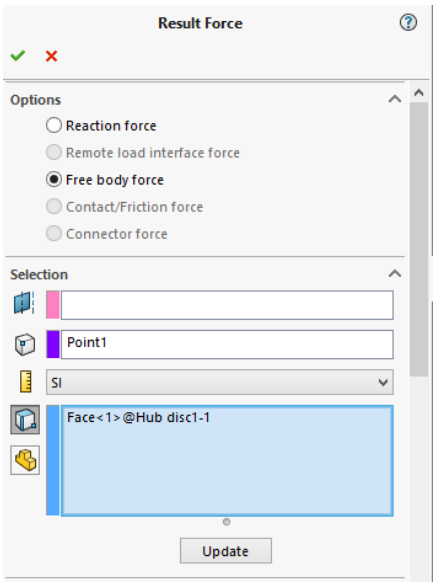

Figure 5.21: Resultant forces parameters

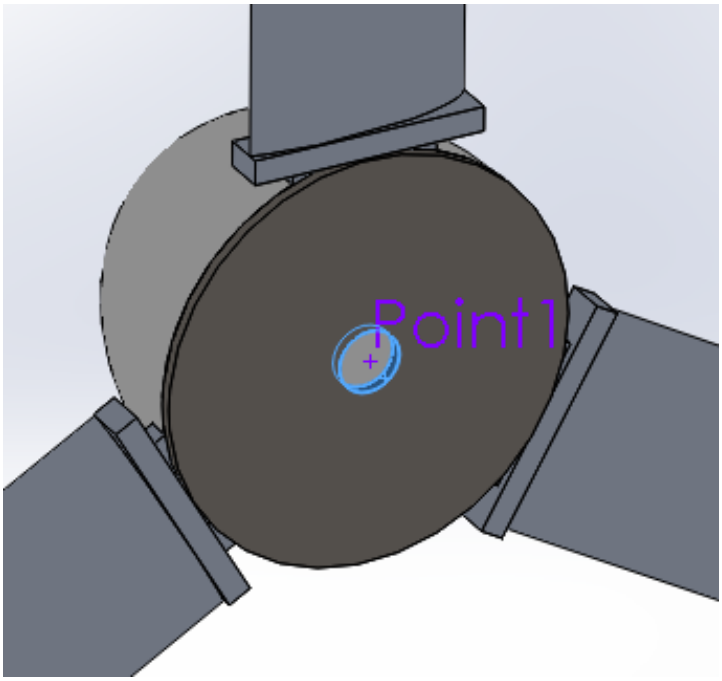

Figure 5.22: Reaction surface

The resultant force and moment were 7.18 kN and 1.94 kNm, respectively. Figure 5.23 shows more details of the forces and moments at the point of consideration.

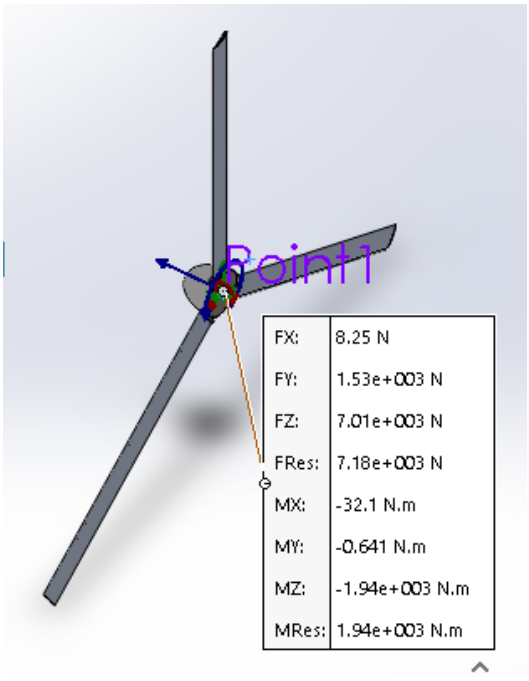

Figure 5.23: Reaction force and moment

The z component of the force reaction coincides with thrust force caused by air through the

blade. According to IEC61400-2 simple load model case H, the load can be calculated by

$$F = 0.5\rho C d_{blade} U^2 A_{proj} B + 0.5\rho C d_{hub} U^2 \left(\frac{\pi d^2}{4}\right) \tag{5.29}$$

$F = 0.5 \cdot 1.225 \cdot 1.5 \cdot 52.5^2 \cdot (3.4259 - 0.375) \cdot 0.2875 \cdot 3 + 0.5 \cdot 1.225 \cdot 1.12 \cdot 52.5^2 \cdot \pi \cdot 0.5^2/4$
$= 7.035$ kN

$$\%err = \frac{|7.010 - 7.035|}{7.010} \times 100\% = 0.36\%$$

The result obtained from Solidworks Simulation shows a good approximation as those obtained from calculation. This fact verifies that the blade FEA analysis is accurate.

5.2.3 Main Shaft FEA

The shaft serves as the hub support; therefore, the reaction force and moment from the previous analysis are applied as the external load for the shaft FEA.

Shaft geometric model The main shaft is modeled as having a 120 mm diameter and 642 mm long, supported at two points that are 337 mm away from each other, and one of the support is 80 mm away from the hub disc. Figure 5.24 shows the shaft model. The shaft is to be made of 10.9 steel grades.

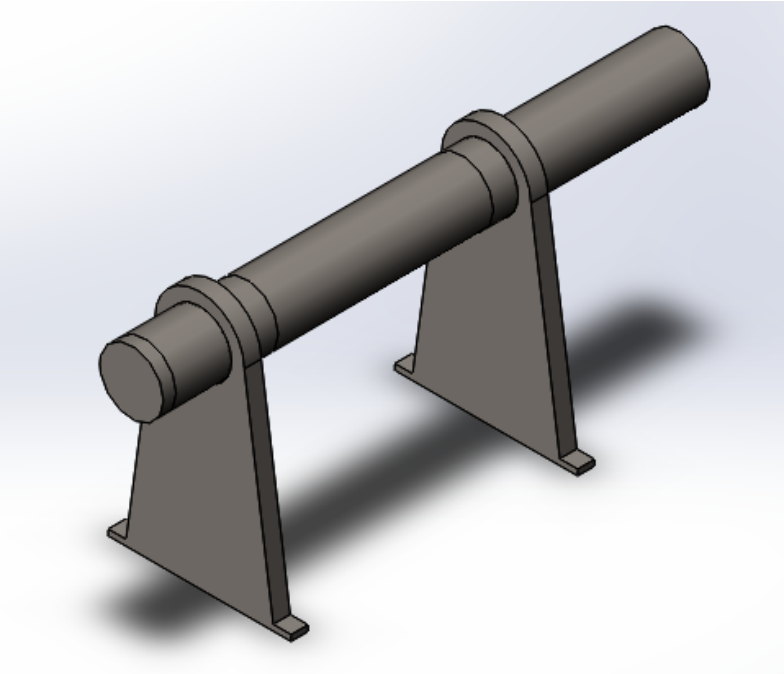

Figure 5.24: Shaft model

Constraint When the maximum limit speed is reached, the brakes clamp the shaft. When the rotor exceed the maximum limit the brake is are applied, this creates torque. The brakes transmit this torque to the supports.

External Load The forces to be considered in this model are the blade reaction forces and moments, the generator's weight, and the shaft's weight. The blades reaction force's vertical component was applied at a middle point of the intersection surface between the hub disc and the shaft. The blade reaction force's axial component was used at the center point of the shaft located at the rotation plane. The weight of the generator is assumed as point load applied at the middle span of the supports.

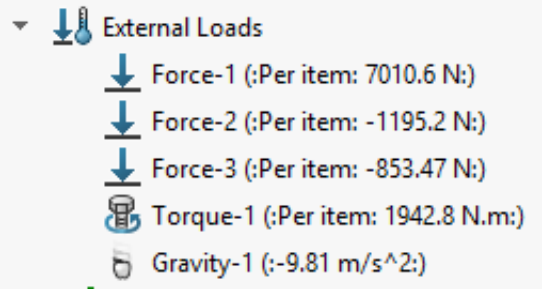

Figure 5.25: Shaft external load

Mesh The global meshing was set to fine setting option as shown in the Figures 5.26 and 5.27.

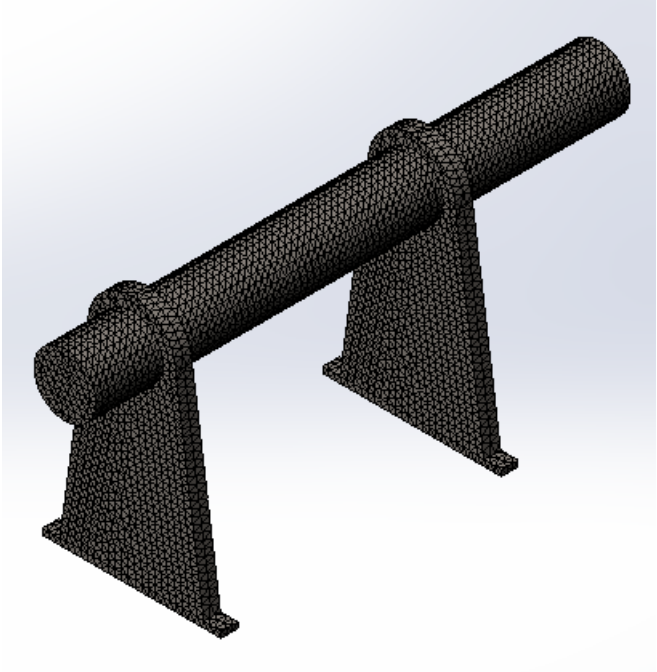

Figure 5.26: Shaft external load

Mesh Details

Study name	Shaft Analysis (-Default-)
Mesh type	Solid Mesh
Mesher Used	Standard mesh
Automatic Transition	Off
Include Mesh Auto Loops	On
Jacobian points	4 points
Element size	8.09682 mm
Tolerance	0.404841 mm
Mesh quality	Draft
Total nodes	11575
Total elements	53508
Maximum Aspect Ratio	3.6308
Percentage of elements with Aspect Ratio < 3	99.9
Percentage of elements with Aspect Ratio > 10	0
Remesh failed parts with incompatible mesh	On
Time to complete mesh(hh:mm:ss)	00:00:03
Computer name	NORBERTO

Figure 5.27: Shaft external load

Results Figure 5.28 shows a maximum Von Mises stress just higher than 50 MPa, which occurs in the shaft support. The shaft experience moderate stress in the region where the external load is applied; in the rest of the shaft, the stress is very low. Since the ultimate strength of 10.9 steel grade is greater than the induced stress, it can be concluded that the shaft will not fail. The displacement of the shaft is minimal, as it can be seen from Figure 5.29.

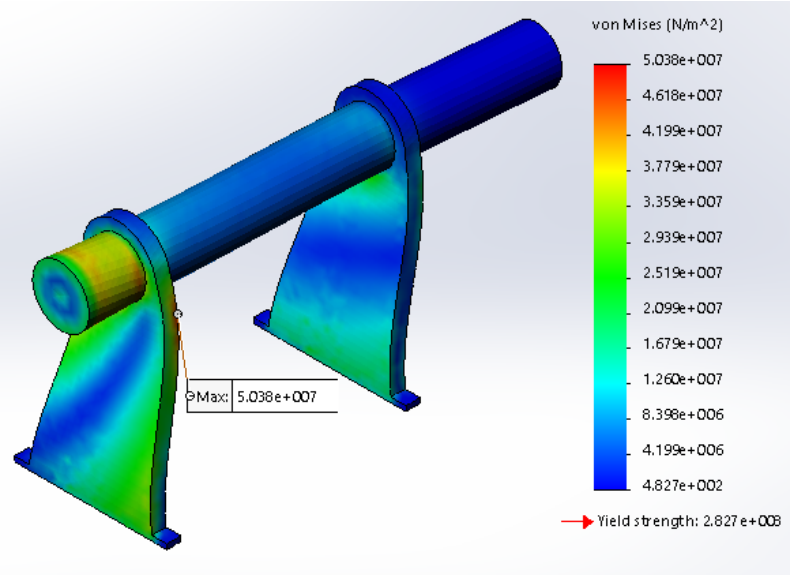

Figure 5.28: Shaft external load

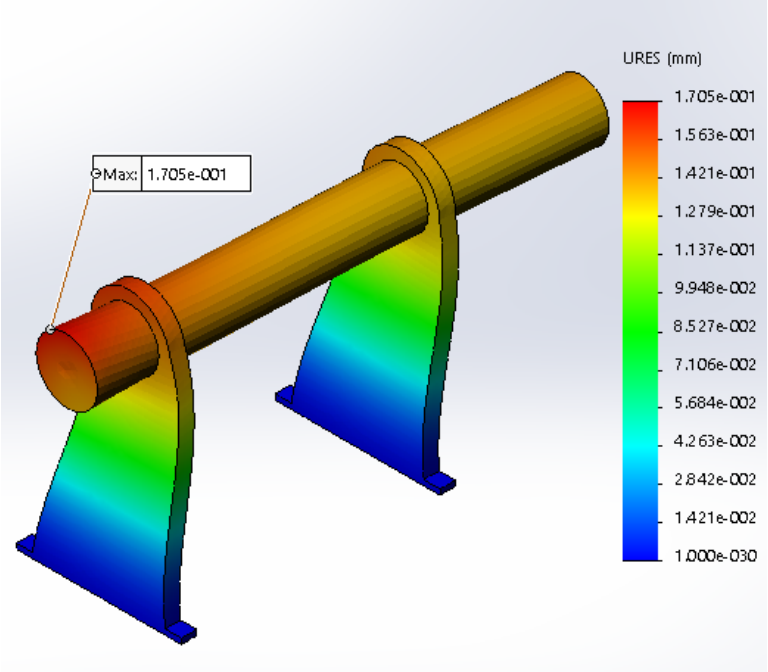

Figure 5.29: Shaft external load

5.2.4 Tail CFD and FEA

The tail was designed by considering the IEC61400-2 simple load model load case I, which requires that the turbine component be exposed to a reference wind speed. This speed should be perpendicular to the maximum projected area.

Tail geometry model The tail is made of a rectangular in one extreme and a triangular shape in the other extreme. The tail's dimensions are as follows: 1 m for the base and 1 m for the height. The tail boom is 3 m long (from the free end to the center of the triangle), and it has a rectangular hollow cross-section with a height of 60 m, a width of 110 m, and a thickness of 1 m. Figure 5.30 shows the tail geometry.

Solidworks Flow Simulation general settings for tail CFD analysis The general setting for the tail CFD analysis is similar to that of the blades: only the wind velocity magnitude and direction changes. In the tail CFD analysis, the value of the speed is 37.5 m/s. The direction of the velocity is parallel to the x-axis (this is so because this direction results in the maximum tail area exposed to the reference wind speed).

Tail computational flow domain The computational domain was left as default, as shown in Figure 5.31. Figure 5.32 shows the flow domain of the tail model.

Boundary condition As in the blade's case, the only boundary condition assigned was the real wall boundary condition, where all tail was set to be a real wall.

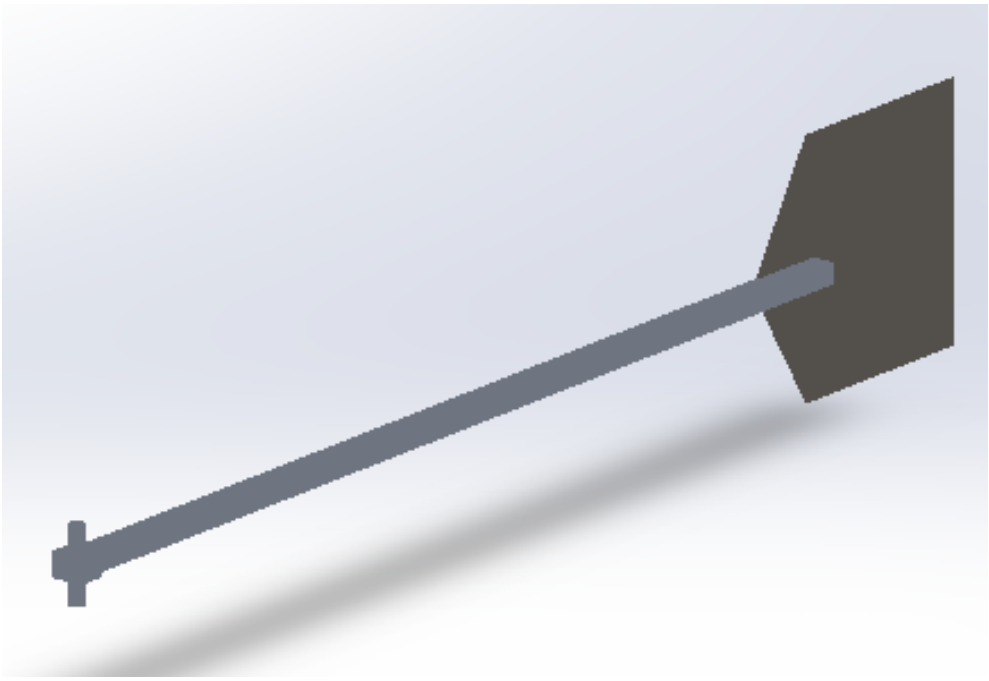

Figure 5.30: Tail geometry

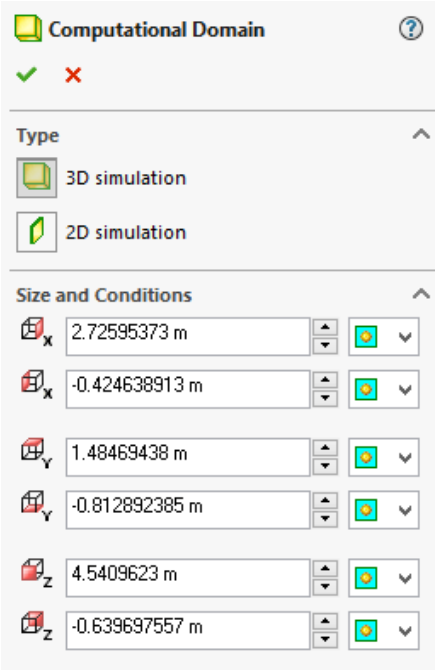

Figure 5.31: Tail computational domain

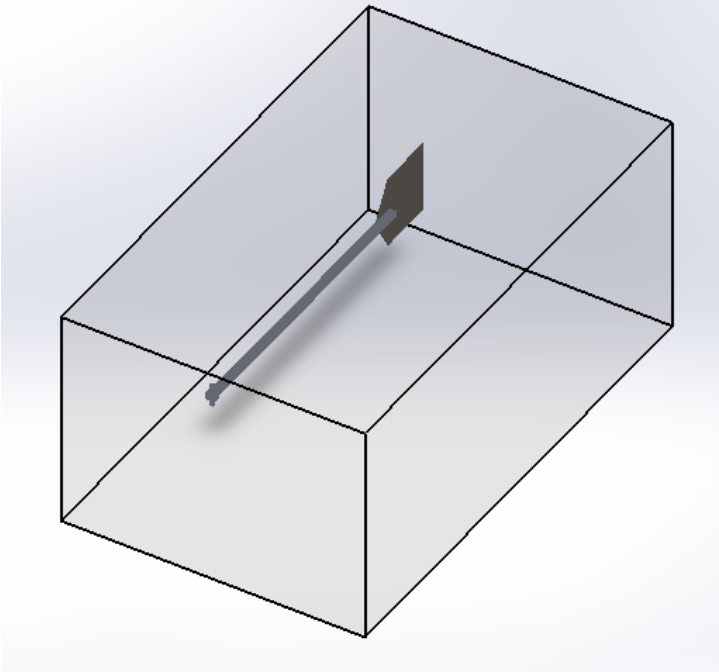

Figure 5.32: Tail computational domain

Mesh Figures 5.33 shows the mesh setting parameters. This setting gave a total number of elements of 513537, of which 38112 are interacting with the wall. Figure 5.34 show detail of meshing done by the SolidWorks Flow Simulation solver.

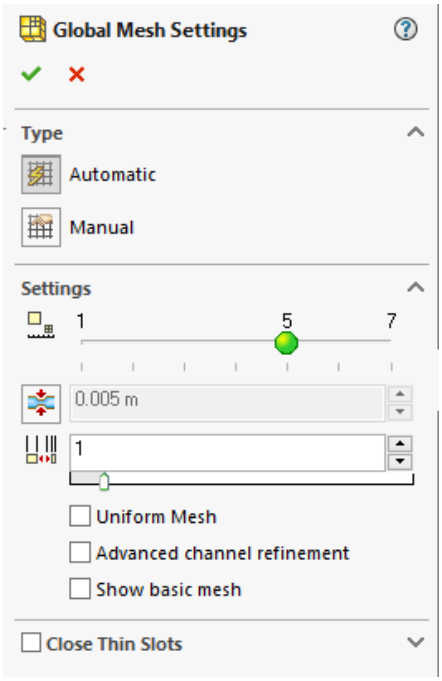

Figure 5.33: Tail CFD mesh parameters

Parameter	Value
Status	Solver is finished.
Total cells	513,537
Fluid cells	513,537
Fluid cells contacting solids	38,112
Iterations	301
Last iteration finished	14:57:46
CPU time per last iteration	00:00:10
Travels	
Iterations per 1 travel	163
Cpu time	1 : 16 : 43
Calculation time left	0 : 0 : 0
Run at	NORBERTO

Figure 5.34: Solver solution detail

Tail CFD Result Figure 5.35 and 5.36 shows the pressure contour and velocity trajectory of the flow field, respectively. The pressure contours are plotted in a middle horizontal plane (xz-plane). The velocity flow trajectory only shows the fluid that passes through the tail.

Tail FEA

The tail geometry used in Flow Simulation was used to run the FEA study. The external loads to be taken into consideration were the wind load and the weight of the tail. The model is assumed to be fixed at the free end of the boom.

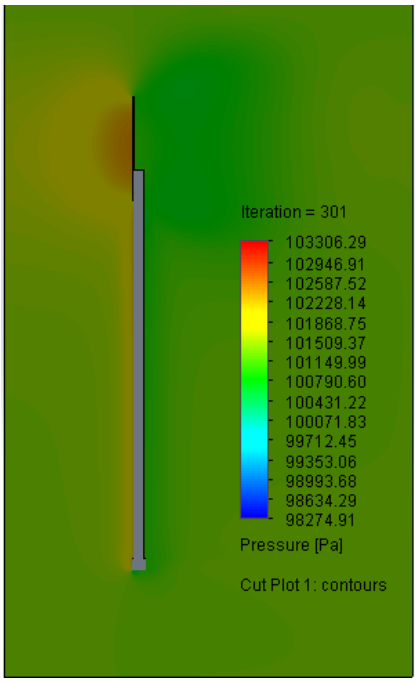

Figure 5.35: Tail pressure contour

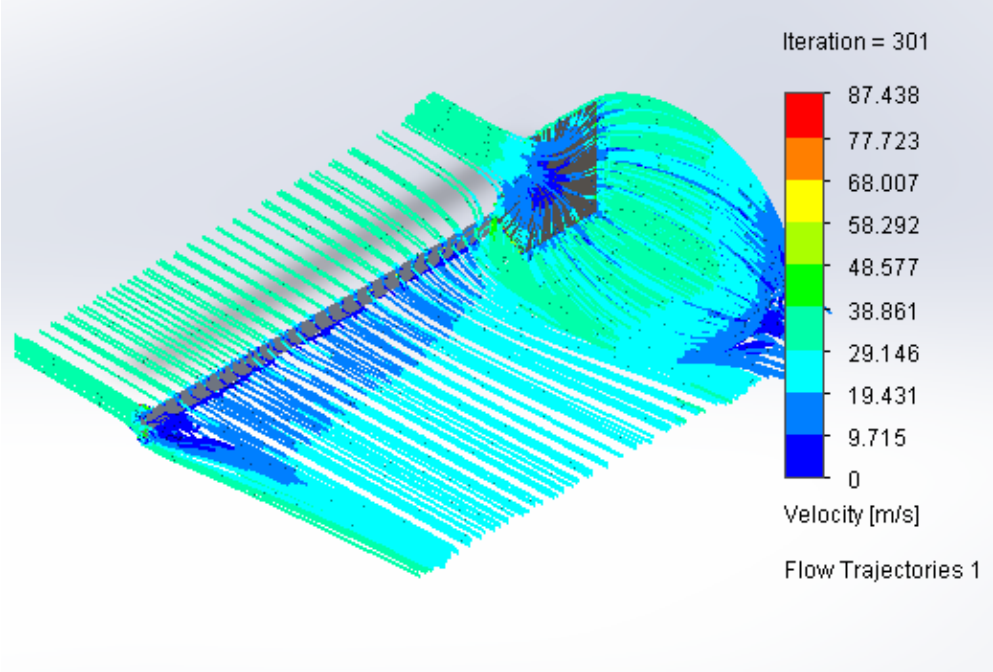

Figure 5.36: Tail velocity trajectory

Tail Geometry Tail Geometry The geometry used for FEA is the same as that used in the CFD study. The tail and the boom were assigned to have the same material, which was AISI 1020 steel.

Constraint The free end of the boom is assumed to be fixed.

External load Two loads are considered in the tail FEA study: the total tail and the wind load weight. The weight of the tail is taken into consideration by activating the gravity effect. The wind load was imported from SolidWorks Flow Simulation corresponding to the tail CFD analysis. Figure 5.37 shows the external loads applied to the tail.

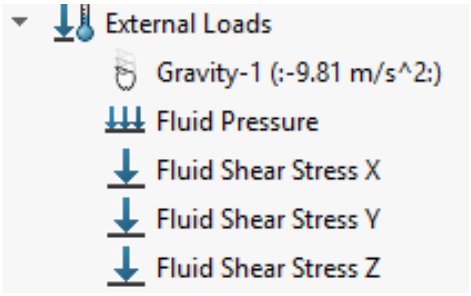

Figure 5.37: Tail Von Mises stress

Mesh The mesh setting, visualization, and details are shown in Figures 5.38, 5.39 and 5.40.

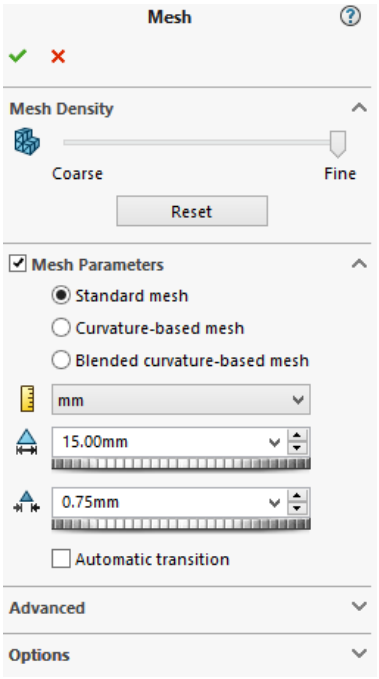

Figure 5.38: Tail mesh parameters

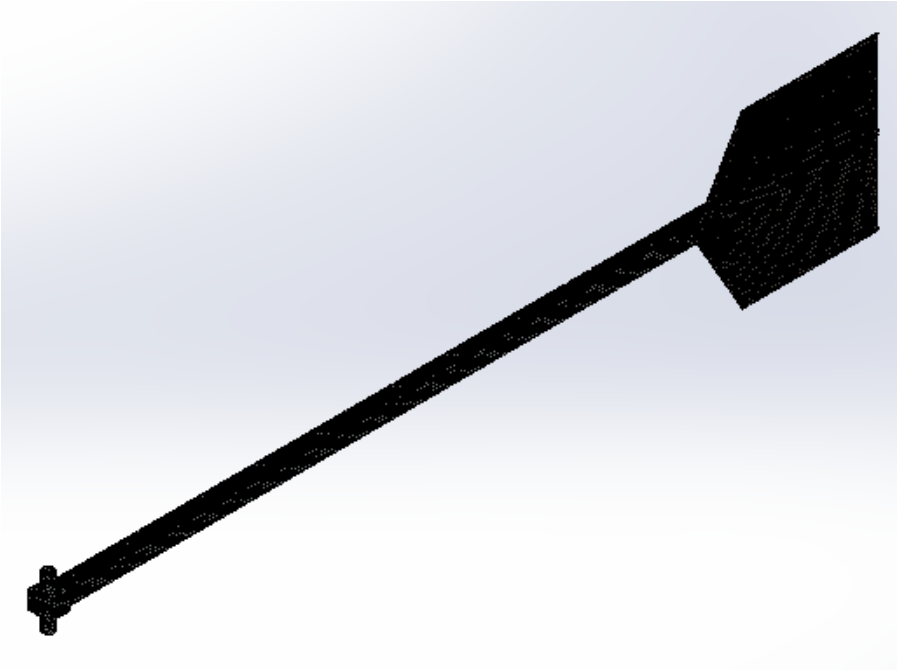

Figure 5.39: Tail FEA mesh

Mesh Details

Study name	Static 1 (-Default-)
Mesh type	Solid Mesh
Mesher Used	Standard mesh
Automatic Transition	Off
Include Mesh Auto Loops	Off
Jacobian points	4 points
Element size	15 mm
Tolerance	0.75 mm
Mesh quality	High
Total nodes	71829
Total elements	36131
Maximum Aspect Ratio	15.971
Percentage of elements with Aspect Ratio < 3	28.4
Percentage of elements with Aspect Ratio > 10	0.0277
% of distorted elements (Jacobian)	0
Remesh failed parts with incompatible mesh	Off
Time to complete mesh(hh:mm:ss)	00:00:09
Computer name	NORBERTO

Figure 5.40: Tail Vmesh detail

Results Figure 5.41 shows that the maximum stress occurs at the tail's fixed support, as it is expected. The ultimate strength of AISI 1020 carbon steel is about 2.6 of the maximum Von Mises stress, which means the factor of safety is less than the one IEC61400-2 prescribes. Higher-strength steel has to be used, or the thickness of the boom has to be increased To increase the tail safety factor, provided that the geometry is not changed.

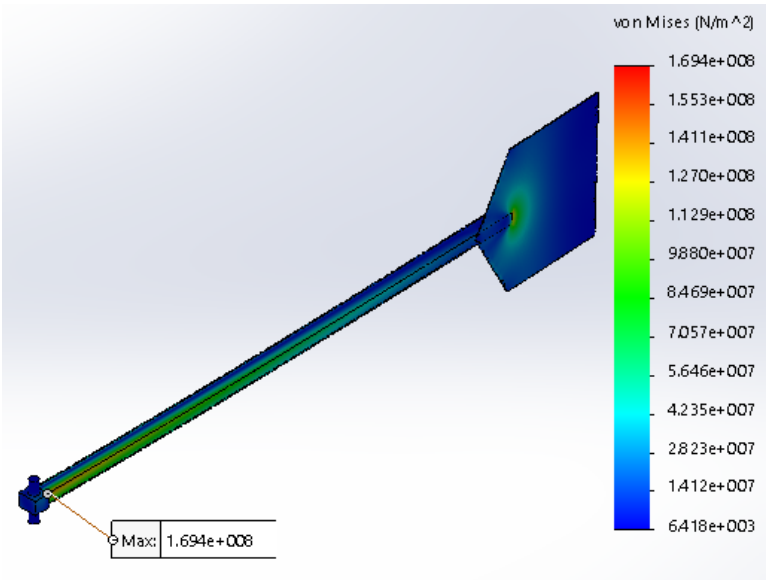

Figure 5.41: Tail Von Mises stress

The maximum tail deflection is around 45 mm, which is acceptable as the tail assembly has

about 3333.3 mm. It can be seen from Figure 5.42 that the maximum deflection occurs at the free end of the tail as it is expected.

A middle point was created on a plane that contains the cross-sectional boom area to obtain the force and moment reaction at the fixed support. This point and the face that comprises it was chosen as the parameters to get the reaction force and moment.

5.2.5 Main Frame FEA

Mainframe geometry The mainframe is modelled as a 800 mm × 600 mm × 10 mm flat plate as shown in the Figures 5.43 and 5.44. The cylinder is given a diameter of 180 mm. The flat plate as three supports, one for the tail and two for the main bearings.

Constraint The bottom part of the mainframe will be connected to the tower. The connection will be such that the mainframe is allowed to yaw about the yaw axis.

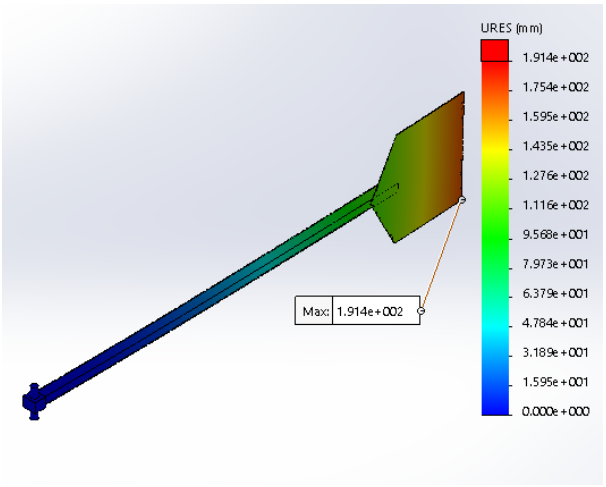

Figure 5.42: Tail displacement

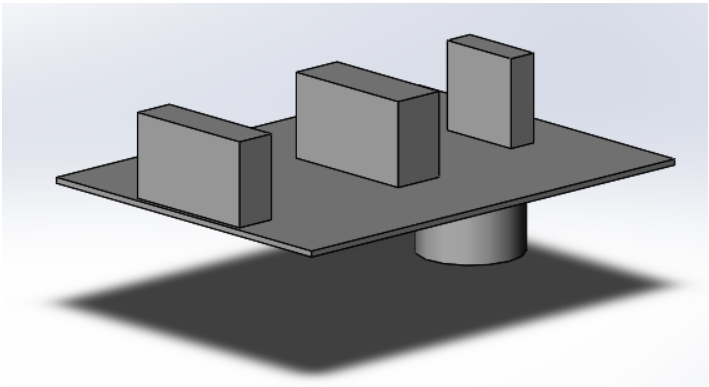

Figure 5.43: Mainframe CAD model

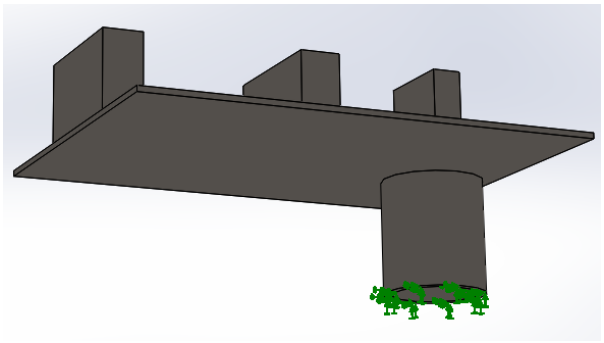

Figure 5.44: Main frame constraint

External load The external load applied to the mainframe are the force and moment reactions from the shaft FEA study and the tail's reactions. Since the shaft reactions happen due to the wind load induced in the blade and hub, it happens that when the blade and hub experience maximum load due to load case H, the tail is assumed to be aligned with the wind, therefore it drag force can be neglected. Thus, only the shaft reaction forces and moment are considered. These loads are assumed to be point loads applied according to the relative position in the general assembly. The first three forces and torques represent the x, y and z force and moment components, respectively, applied at the first bearing support. The last three forces and torques are the x, y and z force and moment components, respectively, applied at the shaft second bearing support.

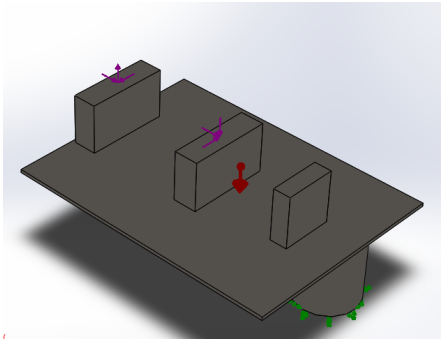

Figure 5.45: Main frame external load

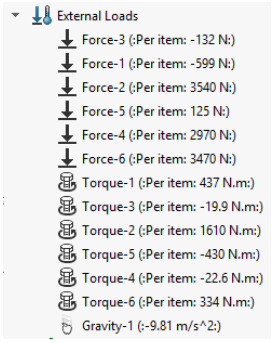

Figure 5.46: Main frame external load

Mesh The mainframe mesh is made as fine as possible, as shown in Figures 5.47 and 5.48 since the time taken for the FEA to converge is not significantly affected by increasing the number of total cells in Solidworks Simulation. Figure 5.49 shows more detailed information about the quantity and quality of the mesh.

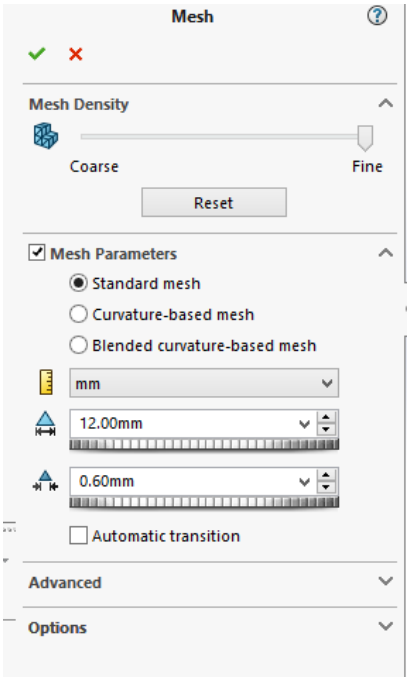

Figure 5.47: Main frame mesh parameters

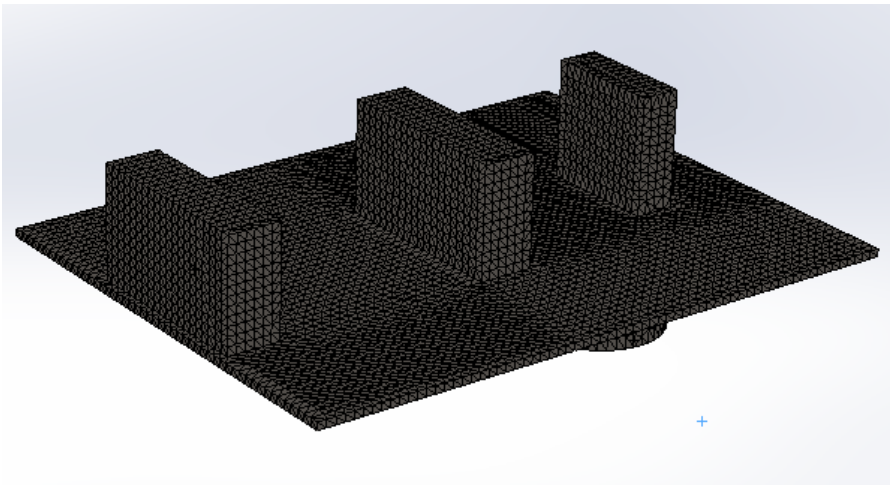

Figure 5.48: Main frame mesh parameters

Mesh Details

Study name	Static 1 (-Default-)
Mesh type	Solid Mesh
Mesher Used	Standard mesh
Automatic Transition	Off
Include Mesh Auto Loops	Off
Jacobian points	4 points
Element size	12 mm
Tolerance	0.6 mm
Mesh quality	Draft
Total nodes	13414
Total elements	45625
Maximum Aspect Ratio	7.8447
Percentage of elements with Aspect Ratio < 3	98.8
Percentage of elements with Aspect Ratio > 10	0
Time to complete mesh(hh:mm:ss)	00:00:08
Computer name	NORBERTO

Figure 5.49: Main frame mesh details

Results The Von Mises stress and the deflection shown in Figures 5.50 and 5.51 indicates that the mainframe is over design. Therefore, the mainframe will be re-evaluated to give an optimum system that would reduce the amount of material and safely bear the loads.

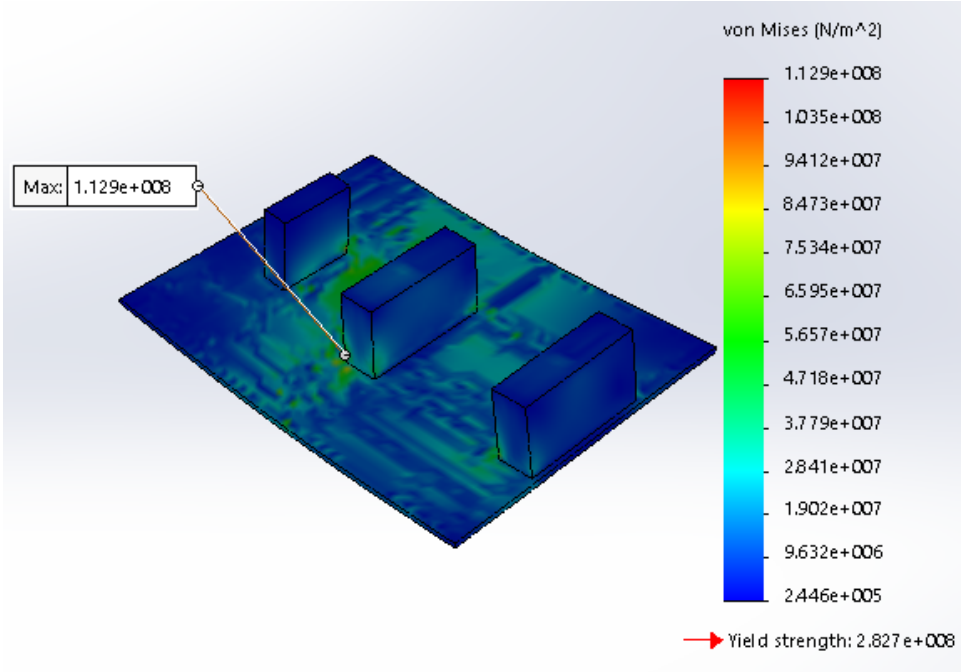

Figure 5.50: Main frame Von Mesis stress

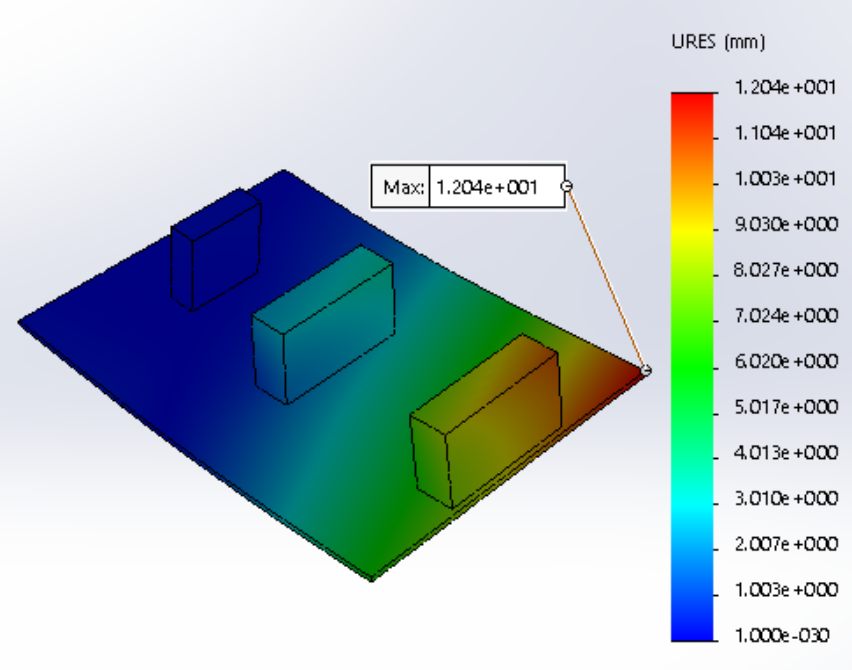

Figure 5.51: Main frame displacement

5.2.6 Tower CFD and FEA

The tower takes the load from all the turbine components and transfers if to the foundation.

Tower CFD

Tower geometry The tower is 20 m high and has an octagonal cross-section. The diameter of each cross-sectional area varies linearly with the height of the tower. The thickness of the tower is considered to be constant throughout the tower height. The tower base and top diameters are set to 750 mm and 150 mm, respectively.

Flow domain The flow domain consists of a rectangular prism with the dimensions left at default settings as shown in Figure A.25, and the tower described in the previous paragraph.

Boundary The surface of the tower that is in contact with the fluid was set as a real wall boundary.

CFD Mesh The global mesh settings are shown in Figure A.27. The settings were chosen to 3 because it gives a reasonably accurate result, and it takes an adequate time (one hour and 38 minutes, as shown in Figure A.27) to converge. The mesh resulted in 598136 fluid cells, of which 64660 were in the boundary between the fluid and the tower.

CFD results The result from the CFD analysis is shown in the Figure below.

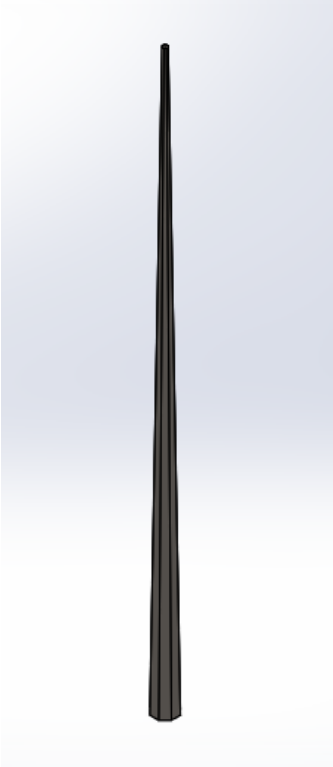

Figure 5.52: Tower geometry

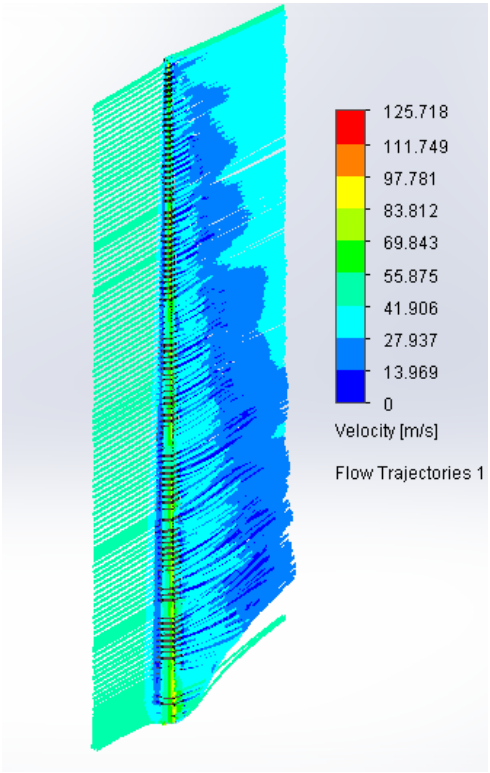

Figure 5.53: Tower geometry

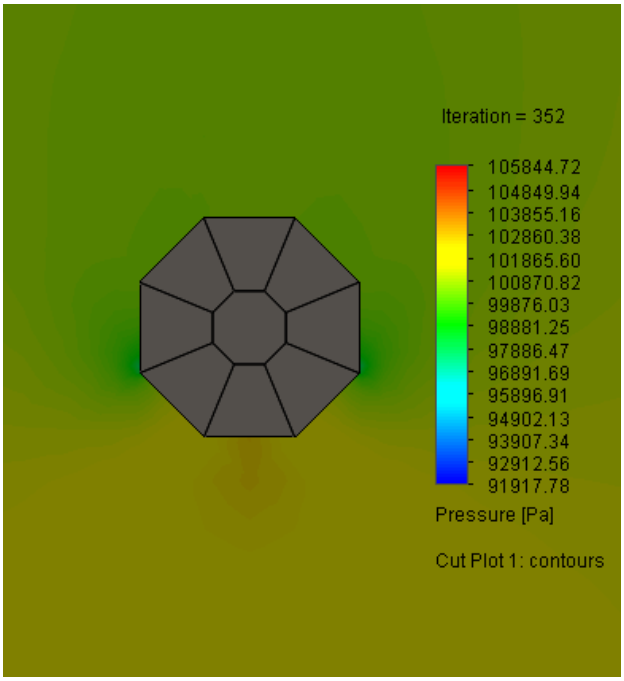

Figure 5.54: Tower geometry

Tower FEA

The stress and deflection induced by air flowing through the blades, hub, and tower are analyzed. This analysis's CAD model is the same as the one used in the tower's CFD analysis. The forces and moments from various components are assumed to be applied at the tower top surface, in the center. The load's effect due to the wind flowing through the tower is imported from Solidworks Flow Simulation of the tower CFD analysis.

Geometry The geometry used in the tower FEA analysis is the same as the one used in its CFD. The tower is chosen to be made of AISI 1020 steel.

FEA constraint FEA constraint The bottom surface of the tower was set as a fixed constraint.

External load Figure 5.55 shows the external forces applied in this analysis. Where Force-2 and Force-3 represent the weight of all the turbine components (excluding the tower), and the axial force in the turbine rotor, respectively. Torque-1 and Torque-2 stand for the flapping moment and the reaction torque due to parking the turbine when the wind speed is 52.5 m/s, respectively. The Fluid Pressure and Shear Stresses represent the wind load that flows through the tower (SolidWorks Flow Simulation). The tower weight is taken into account by including the gravity effect in the analysis.

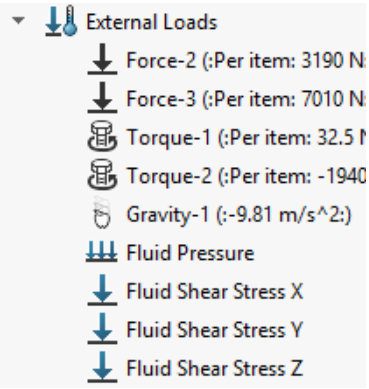

Figure 5.55: Tower external load model

FEA meshing Figure A.29 shows the meshing setting parameters of the tower FEA study. Figure A.30 shows the mesh of a portion of the tower. For more tower meshing details see Figure A.31.

Results It can be seen, from Figure 5.56, that the maximum stress does not occur at the bases of the tower as it was assumed in the preliminary design. The maximum Von Mises stress obtained is 122.3 MPa, and the material strength is 420 MPa, which corresponds to a safety factor of 3.4. Therefore the tower will not fail due to bending and axial load combined. The maximum deflection occurs at the top of the tower as expected. Its magnitude is 364 mm, which is acceptable considering that the tower is 20 m tall (see Figure 5.57).

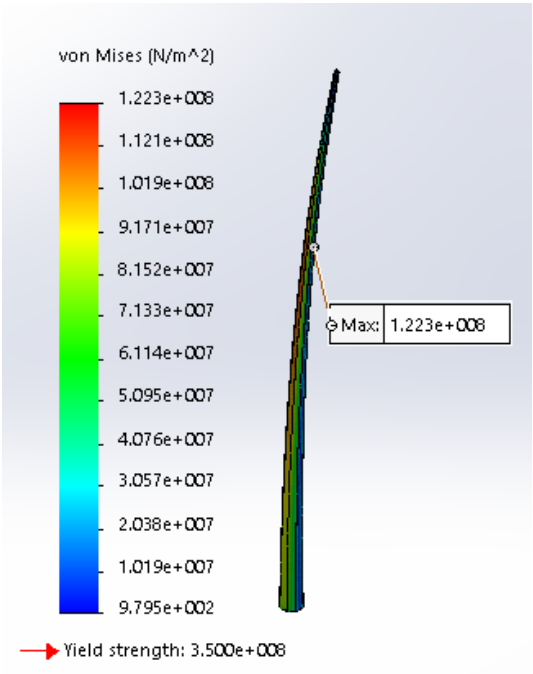

Figure 5.56: Tower geometry

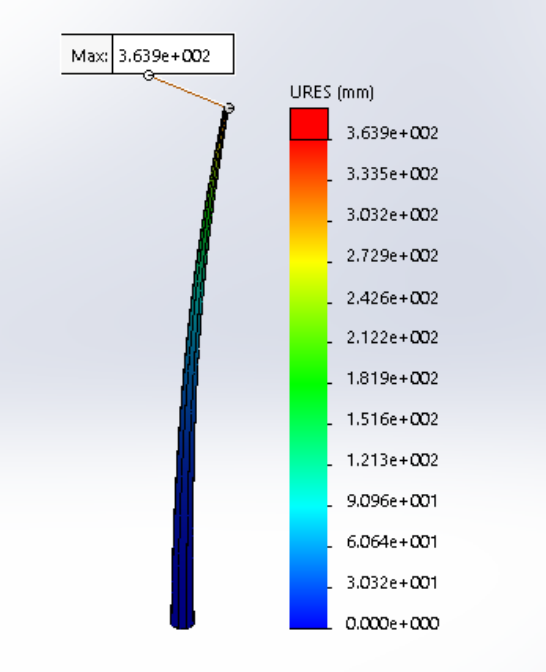

Figure 5.57: Tower geometry

5.3 Turbine Components Materials and Manufacturing Process

5.3.1 Blade

The blade will be made of aluminum 7075 T6. Aluminum 7075 T6 is used in the aircraft industry and in applications where high strength, lightweight, and corrosion-resistant materials are required. At a temperature of $24°C$, it has a tensile strength of 503 MPa, Young modulus of 71 GPa, and a fatigue strength of 154 MPa for a life cycle of 5×10^8.

Extrusion is used to manufacture the blade as it is the most common method to produce aluminum profiles [88]. Extrusion is a process by which the final product is obtained by forcing a block of metal to flow plastically through a die by compressive forces. It can be carried out with the billet hot or cold depending on the aluminum alloy type being extruded. There are two types of extrusion: direct and indirect. The billet is forced through the die by compressive force applied to a ram in the direct extrusion. In the indirect extrusion, the billet is fixed in a container, and the die is forced into the billet.

Figure 5.58 shows a typical extrusion plant. The extrusion process starts at the casting house, where the aluminum is melt. When it is in liquid at a temperature above 700°C, it is cleaned, alloying elements and grain refiners are added. The composition is then poured into a mold, and cooling water is circulated directly over the mold to allow the material to solidify into a log. After casting, the log undergoes a series of thermal process to obtain a good extrudability. Then the log is transported to the extrusion plant. The log is preheated first and then cut into pieces according to the weight needed in the extrusion plant. Alternatively, the log is cut into the desired pieces first and then preheated after, depending on its type. Next, the billet is placed into the extrusion press, and the ram of the extrusion press pushes the billet into the container. The billet is coated to avoid sticking into the dummy block between the billet and the ram. The billet has a smaller diameter than the container bore; therefore, it necessary to give it upsetting for it to fill up the container; this main cause entrapment of air in the container, which is removed by temporarily disengaging the ram from the billet and move it backward. The ram presses the billet against the die opening with a very high compressive load (around 645 MPa).

The log's temperature during extrusion depends on the type of the alloy being extruded; typically, it ranges from 450° to 470°C. The temperature of the product leaving the die is around 550° to 600°C. A puller grips the material leaving the die, and it is directed out of the runout table. While the material is being moved along the table, it is quenched and cooled down further. The material is elongated by 0.5 to 2% on the cooling table to eliminate internal stresses due to uneven cooling over the profile's cross-section. It also straightens up for possible bending and twisting that may have formed during the cooling process, and then it goes into the cutting saw where it is cut into the desired length. The cut section is then transported into the aging oven, where they spend 3 to 6 hrs at a temperature ranging from 170 to 190°C. Finally, the material is packed and ready to be delivered for further treatment

or processing.

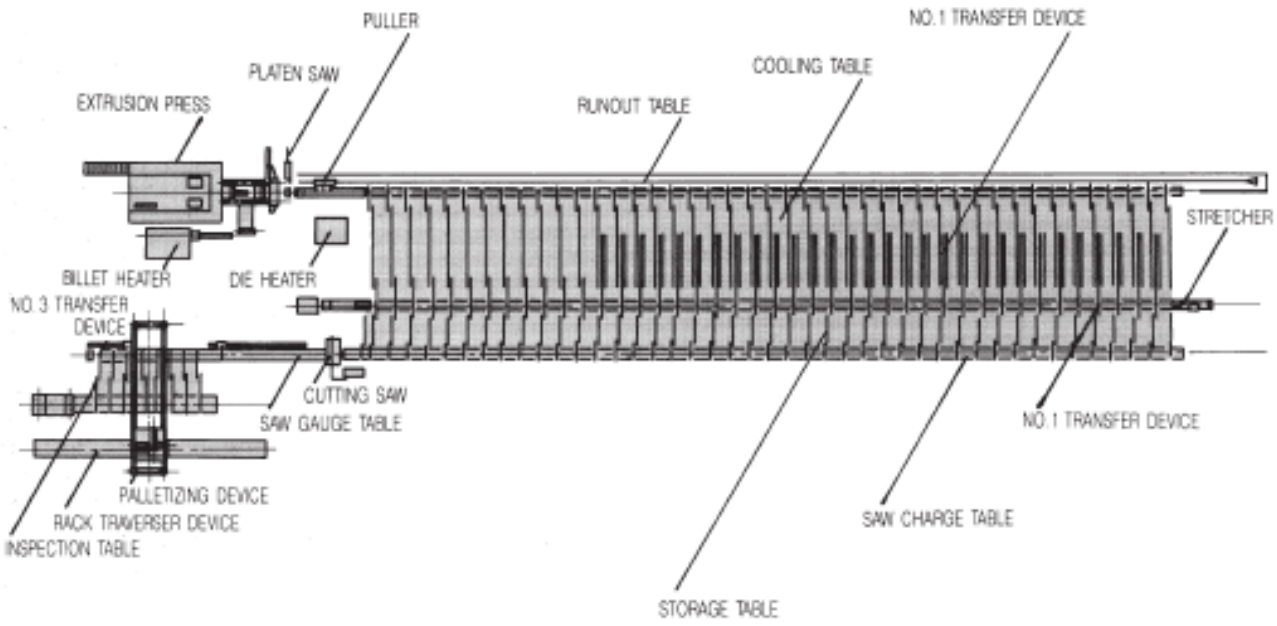

Figure 5.58: Extrusion process [89], p.56

Aluminum 7075 requires a separate solution heat treatment, higher extrusion pressure, and cannot be extruded into hollow shapes without specializing seamless extrusion presses. Aluminum 7075 is sensitive to recrystallization, toughness, and resistance to stress corrosion cracking; therefore, exceptional attention to processing is necessary to minimize these sensitivities. It is also required to have particular practices in tooling design and hydraulic process control.

Aluminum 7075 has a low castability, and it is difficult to have a high-quality product if it is cast. Therefore, the blade's root aluminum 384 will be used because it has relatively high strength and is castable. Bots connect the blade body and root since aluminum welding efficiency ranges from 35 to 65%.

5.3.2 Hub

Steel and aluminum can be considered to be used as the hub material, for they are widely available, they are relatively inexpensive, and have high strength. They can be easily machined into the desired hub features using the normal machining processes. Steel has higher fatigue strength and Young's modulus than aluminum, and it is cheaper than aluminum; however, it is about three times wavier than aluminum. For this reason, aluminum 7075 is used in this design. To fabricate the hub normal machining process (cutting, turning, and drilling) is to be used. The working piece can be obtained from a standard aluminum 7075 plate.

5.3.3 Tower

The vast majority of wind turbine tower is made out of steel, but concrete can also be an alternative which in enormous, it has been proven to be less economic [27]. In the current project, plain carbon steel is chosen as the tower material. The circular tower has a lower drag coefficient than another cross-sectional area. However, circular towers are challenging to manufacture; therefore, more expensive. Tapered octagonal towers, similar to light poles, even though they have a higher drag coefficient than circular towers, are easy to manufacture [82]. The tower is galvanized for corrosion protection. The following paragraph gives a brief description of the tapered octagonal towers' manufacturing process.

The tower is made of steel sheets that arrive at the manufacturing plant in a large roll. A decoiler is used to unwind the sheet and flatten it, and then a shear cutter cuts it into a correct length. A computer-guided plasma cutter marks both end extremes of the cut sheet with short vertical lines to where the sheet's bending will occur. The machine cut the sheet into a trapezoidal shape for tapered towers; for untapped towers, the sheet is cut into a rectangular shape. Then the cut sheet is transferred into a press brake, where it is bent. The press brake bends the sheet along the marked line into a pre-programmed angle, then the angle of the first bending is measured to check its accuracy. After reviewing the first bending angle accuracy, the press brake can proceed with the bending for the remainder of the marked lines, thus transforming the sheet into a multi-sided tapered tower. After that, the tower is moved into the welding side, where hydraulic rollers apply pressure on both sides. This action forces the poles' two edges against each other, allowing a head weld to fill the edges with molten steel. The head deposit is a granular powder that prevents air from penetrating the weld and weakening it. As the weld cools and shrinks, the tower tends to bend; therefore, while the welding is cooling, it is stretched in a hydraulic press. Next, a computer-guided plasma machine cuts the baseplate out of a thick steel sheet. The machine also drills holes in the baseplate where the bolts are to be connected. Then, the baseplate and tower are welded together. A testing device that uses electric current to draw the colored powder into a defective area magnetically is used to check the welding quality. The tower is then sent into a galvanizing plant, where it goes first into a series of washing tanks. After that, the washed tower is submerged into a sulphuric acid solution, which removes any contaminant the washing process cannot remove. The tower is then dipped again into a chemical solution that weakened the tower surface to allow the galvanizing metal to penetrate the steel interior rather than on the surface. The final step consists of putting the tower into a tank containing molten zinc, which galvanizes the steel.

5.3.4 Nacelle

The nacelle is usually made of a lightweight material such as fiberglass [18]. It the current design, the nacelle is suggested to be made of fiberglass vinyl ester for its lightweight, high strength, and good corrosion resistance. Many processes can be used to produce the nacelle. In the current project, the method of manufacturing the nacelle is the vacuum assisted resin transfer molding (VARTM) due to its ability to generate consistent product quality. A mold must be made first to manufacture the nacelle, which increases the initial production cost.

Still, once the mold is created, it can be reused to produce other nacelles, thus reducing the bulk manufacturing process project is to be developed for commercialization purposes. After the VARTM process, the nacelle must be machined to provide a polished final product and locations to attach it to the mainframe.

5.3.5 Main Shaft

The main shaft is subjected to cyclic load. Therefore, fatigue strength is of paramount importance. Usually, the main shaft is made of steel, the condition under which it operates determines the carbon content of carbon in the steel; for extreme conditions, steel alloy is considered. The stress concentration is also considered because the shaft is to be threaded, and it will have a keyway drilled in it. The shaft is to be made of 10.2 steel grades for its high strength and good fatigue resistance. Machining (turning and cutting) is to be used as the main shaft manufacturing process.

5.3.6 Mainframe

The mainframe is to be as stiff as possible to allow the generator, and the main shaft alignment and steel is usually used as the material since it has high Young's modulus [18]. In the current design, plain carbon steel is used as the mainframe material. The mainframe will be machined into pieces according to the shape needed; then, the parts are welded together.

5.3.7 Tail

The tail made is made of a boom and a tail vane. They can be made of steel or aluminum, as its predominant requirement is its strength and moderate fatigue strength. Steel has greater fatigue strength than aluminum, and its higher density can be used for furling stability control, and it is also cheaper than aluminum. Therefore, plain carbon steel will be used as the boom and tail vane material. Machining (cutting, turning) is to be used as the manufacturing process for the boom and the tail vane because both of them have simple shapes that are easily machined. Welding will be used to join the two pieces together.

5.4 Turbine Control

In the previous Chapter, Section 4.10.5 the theoretical background of the control system was given. In This section, we will discuss the application of the control system to the small wind turbine. The q-axis and d-axis current controller, and the q-axis speed controller parameters are defined and their respective control diagrams are designed. The results of the control parameter obtained from MatLab are discussed in this section.

5.4.1 q-axis Current Controller Design

Figure 5.59 shows the block diagram for the design of the **q-axis** current controller. The blocks represent the components of the current control system. The blocks are the PI current

controller block, the delay introduced by the digital calculation with time constant given by the formula $T = 1/f_s$, f_s is sampling frequency (T is taken to be $T = 0.0002\ s$), the delay introduced by the inverter with the time constant of $0.5T_i$ (T_i is taken as $0.0001\ s$), the plant or the stator block, and the delay introduced by digital to analog conversion that is taken to be equal to the delay introduced by the digital calculation.

The value for R_s and L_q are 0.5 Ω and 4.48 mH respectively. The transfer function is given by

$$G_q(s) = K_{pq}\left(1 + \frac{1}{sT_{iq}}\right) \tag{5.30}$$

where K_{pq} is the proportional gain and T_{iq} is the integral time of the $q - axis$ current controller.

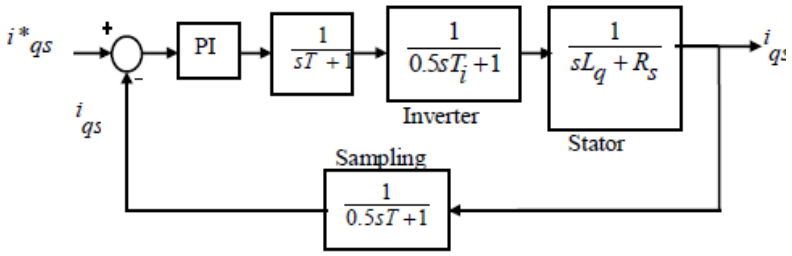

Figure 5.59: Extrusion process

5.4.2 d-axis Current Controller Design

The **d-axis** current controller is implemented in the same way as the **q-axis** current controller except that the L_q is replaced by L_d. The formula below gives the transfer function of the d-axis current controller

$$G_d(s) = K_{pd}\left(1 + \frac{1}{sT_{id}}\right) \tag{5.31}$$

where K_{pd} is the proportional gain of the d-axis current controller and T_{id} is the integral time of the d-axis current controller.

5.4.3 q-axis Speed Controller Design

Figure 5.60 shows the block diagram of the **q-axis** speed controller design. The q-axis controller system is made of the PI speed controller, the delay introduced by the PI controller, the delay introduced by the current controller, the plant, and the filter with the time constant T_f and the delay introduced by digital to analog conversion. The equation that represents the q-axis current loop transfer function is given below

$$GH_q(s) = K_{pq}\left(1 + \frac{1}{sT_{iq}}\right)\left(\frac{1}{sT+1}\right)\left(\frac{1}{0.5sT_i+1}\right)\left(\frac{1}{sL_q+R_s}\right)\left(\frac{1}{0.5sT+1}\right) \tag{5.32}$$

The above transfer function can be simplified since the poles due to digital to analog conversion, digital calculation, and the inverter are far away. The equation below gives the simplified equation

$$GH_q(s) = K_{pq}\left(1+\frac{1}{sT_{iq}}\right)\left(\frac{1}{sL_q+R_s}\right) \tag{5.33}$$

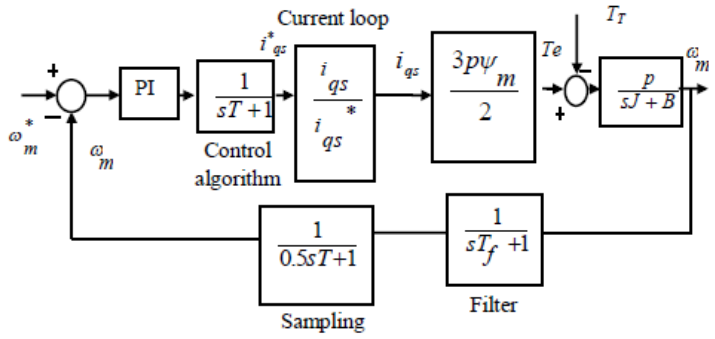

Figure 5.60: Extrusion process

The transfer function of the q-axis current loop is given below

$$\frac{i_{qs}}{i^{\star}_{qs}} = \frac{K_{pq}\left(1+\frac{1}{sT_{iq}}\right)\left(\frac{1}{sL_q+R_s}\right)}{1+K_{pq}\left(1+\frac{1}{sT_{iq}}\right)\left(\frac{1}{sL_q+R_s}\right)} \tag{5.34}$$

In Figure 5.60, T_T is the turbine torque, ω_m is the mechanical speed, J is the moment of inertia and B is the viscous friction coefficient p is the number of the PMSG polar par and Ψ_m is the flux linkage. In the current study, $J = 332$ kgm^2, $p = 19$, $\Psi_m = 0.39$ Vs.

5.5 MatLab Simulink Turbine System Simulation

The SWT is to be parked if the incoming wind speed is less than the cut-in speed. When the wind speed exceed the cut-in speed the turbine starts and operates at the optimum point, that is, at a point of maximum power coefficient. When the inflowing wind speed is greater than the rated speed the turbine is partially turned away from the wind to protected it from rotor over-speed and excessive electrical power, this is done by the furling mechanism. MatLab was used to simulate the SWT control system. Simulink diagram for the control process is found in Appendix A.6. Here a brief explanation of the diagram is given.

Wind speed The wind speed is set to vary in every 5 seconds. Initially, the wind speed is set to be 2.5 m/s. This wind speed is kept for 5 s. After 5 s the wind speed is increased by 5 m/s and remains in this new value for another 5 s. Lastly, an additional increase of 3 m/s is given to the wind speed and it remains at this speed for the final 5 s, as it can be seen in

Figure 5.61. The magnitude of the wind speed gives the rotational speed that the turbine rotor must have in order to obtain optimum power coefficient, this optimum rotor angular velocity is used as a reference speed for the speed controller.

Figure 5.61: Wind speed simulation

Turbine Model The turbine model is obtained from the C_t vs tip speed ratio table obtained from Qblade. The data from the table are then converted into a continuous function with tip speed ratio set as the independent variable. The continuous function is obtained using the linear least square method and the function is chosen to be a polynomial of sixth order. Figure 5.62 shows the C_t data with the fitted curve. This curve allow us to obtain the value of C_t, (consequently, the turbine torque), for any given wind speed. The torque generated by the turbine model drives the PMSG, which is eventually balanced by the generator electromagnetic torque.

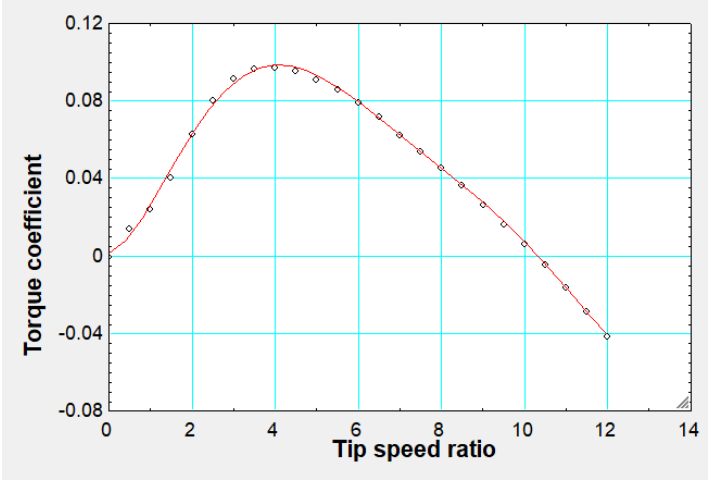

Figure 5.62: Torque coefficient approximation curve

Model Results Figure 5.63 shows the values of the rotor reference angular speed and actual speed plotted against time. As it can be seen the two values are different at the beginning of the period. The reference angular speed is fixed throughout the period whereas the actual speed increases sharply until reaches the value of the reference speed. Once the actual rotor rotational speed equals the reference speed the rotor stops accelerating, therefore maintain its speed until it is disturbed. It is evident that it takes less than 5 s for the rotor to reach the reference speed. The d-current is maintained close to zero throughout the period, as desired, as shown in Figure 5.64. Figure 5.65 shows the q-axis current and its reference counterpart. The currents have very high value at the beginning due to inappropriate generator start-up. To avoid these high current the generator should be started accordingly. From the graph of Figure 5.65, it can be seen that the two current are approximately equal only when the rotor reaches the reference speed. The reference current is maintained constant before the rotor reaches the reference speed, while the actual current decreases its value smoothly. When the reference speed is reached, the reference current drops abruptly into a value that generates an electromagnetic torque that balances the rotor torque and the actual current also experience a sharp drop to reach the reference current. Figure 5.66 shows the rotor torque and the electromagnetic torque plot against time. The rotor torque varies slightly with time due to the adjustment of the tip speed in the process of obtaining optimum rotation, whereas the electromagnetic torque follows the path of the q-axis current, (as it is directly proportional to it). When the rotor reaches the reference speed the electromagnetic torque drops abruptly until it reaches the value of the rotor torque, and the remain equal until disturbance occurs. Figure 5.67 shows the rotor torque and the electromagnetic torque plot against time. The rotor torque varies slightly with time due to the adjustment of the tip speed in the process of obtaining optimum rotation, whereas the electromagnetic torque follows the path of the q-axis current, (as it is directly proportional to it). When the rotor reaches the reference speed the electromagnetic torque drops abruptly until it reaches the value of the rotor torque, and the remain equal until disturbance occurs.

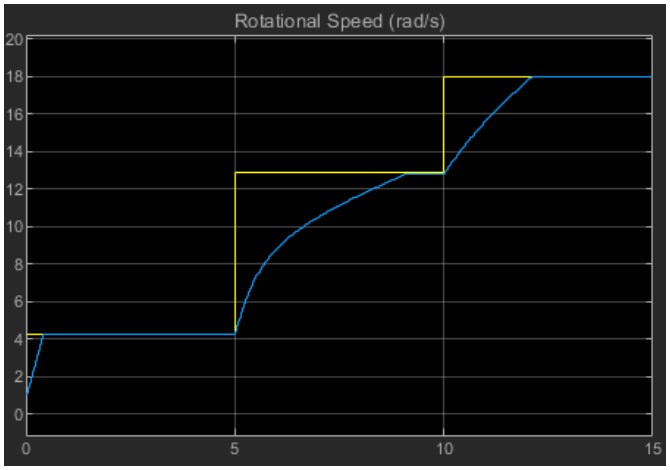

Figure 5.63: Rotor speed

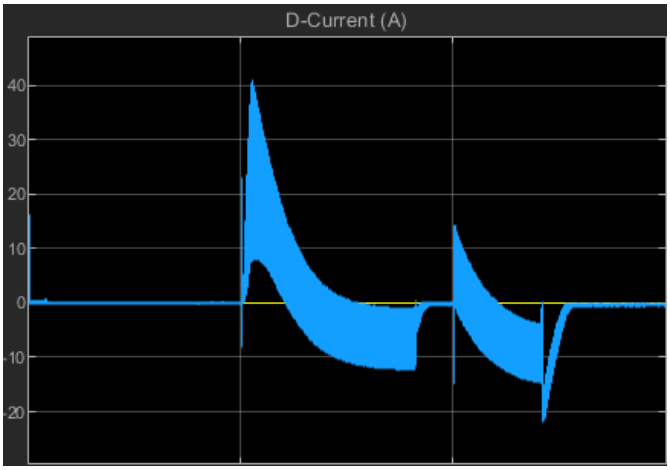

Figure 5.64: D-current

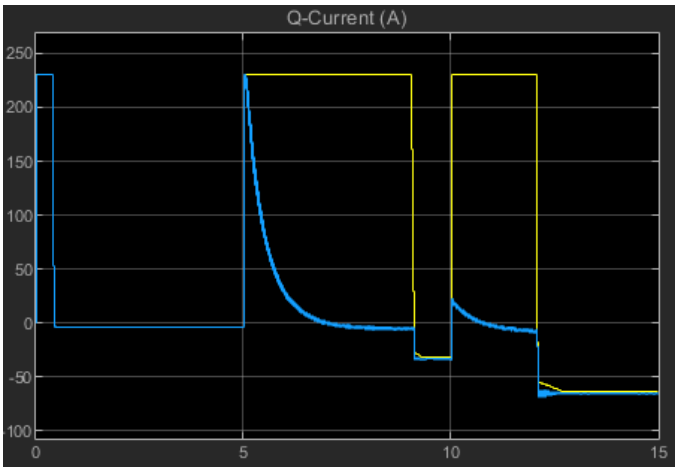

Figure 5.65: Q-current

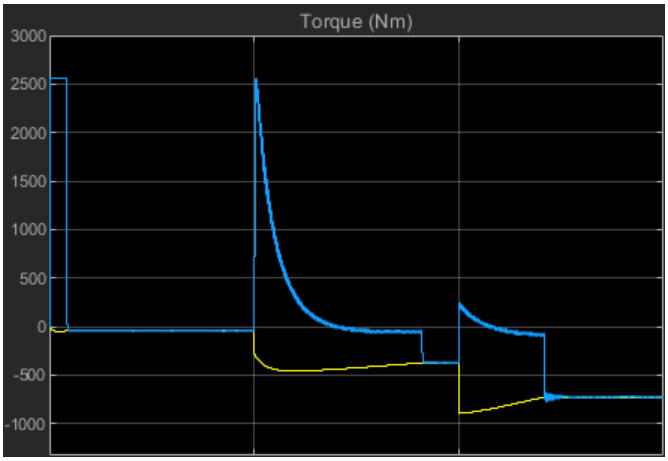

Figure 5.66: Rotor torque

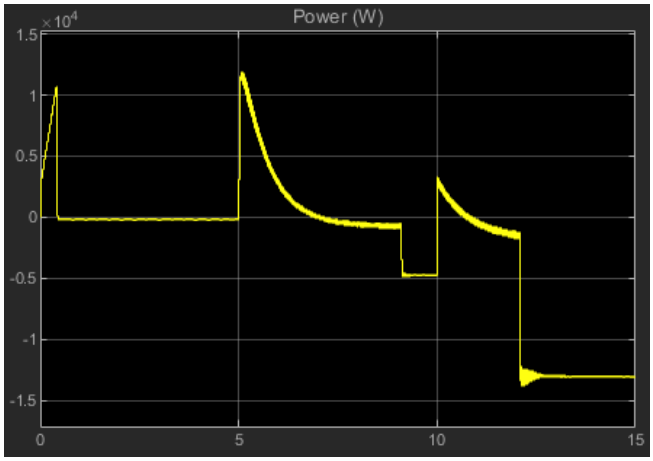

Figure 5.67: Turbine power

5.6 Turbine Specifications

The turbine is designed to operate at an annual wind speed of 7.5 m/s. According to standard IEC 61400-2, an average annual speed of 7.5 m/s corresponds to a rated speed of 10.5 m/s and has a rated power of 10 kW. Table 5.1 shows the summary of the turbine specifications.

Table 5.1: Turbine specification

Power	
Rated Power (kW)	10
Wind speed	
Rated speed (m/s)	10.5
Cut-in speed (m/s)	3
Cut-out speed (m/s)	25
Rotor speed	
Rated rotor speed (rpm)	186
Maximum rotor speed (rpm)	286
Rated tip speed (m/s)	68.25
Rotor	
Rotor diameter (m)	7
No. blades	3
Blade materials	Aluminium 7075
Generator	
Generator type	PMSG
Voltage (V)	380
No. phases	3
Slip rings	None
Control System	
Power control	Variable torque and furling

Wind orientation system	Passive yaw by tail
Bakes	Yes
Controller	Yes
Tower	
Tower height (m)	20
Tower material	Steel
Annual Yield (kWh per year)	
Average wind speed 3 m/s	3140
Average wind speed 5 m/s	14530
Average wind speed 6 m/s	25110
Average wind speed 7.5 m/s	49040
Average wind speed 8.5 m/s	71390
Average wind speed 10 m/s	116240

5.7 Chapter Summary

In this chapter, the detailed design of the turbine main components was studied. The chapter started by studying the concepts of blades and hub connection which resulted in the decision to connect the blade to the hub by bolts – six bolts for each blade. The main shaft was set to be connected to the hub via keyway, key, and a bolt, thus the main shaft is threaded on one extreme; all the necessary calculations were done to ensure these components are connected safely. To estimate the bearing load on the main and yaw bearing simple mechanical structures were modeled, and catalogs from bearing manufacturing were used to obtain the bearing dimensions, consequently selecting the respective bearings.

The second part of this chapter dealt with the turbine main components CFD and FEA studies. Firstly, the blades, hub, and hub nose were combined as a simple component (rotor), and then the aerodynamic loads were determined using Solidwork Flow Simulation (CFD software package) and the results were exported to Solidwork Simulation (FEA software package); the load used in CFD was the same as that used in the preliminary design. In the FEA study, the surface area where the main shaft is connected to the hub is considered to be fixed, and in addition to the imported CFD results, the weights of the components were also considered. The maximum Von Mises stress and deflection were found to be 157.2 MPa (near the blade root), and 323 mm (at the blade tip), respectively. Since the blade material used is aluminum 7075 T6 the blade would not fail due to ultimate strength. The resultant force obtained from FEA was compared with the one calculated from IEC 61400-2, and the error obtained was about 0.36%. The small error obtained served as a verification of the model used for CFD and FEA. The FEA of the main shaft and its support was done by applying the resultant load from the rotor FEA study and the induced weight from the other components attached to the main shaft; the all structure was fixed at both supports. The maximum Von Mises stress was 50.4 MPa and occurred at the support nearest to where the rotor would be connected, which is consistent with what is expected. The tail CFD was set using load case I, and considering the wind to strike the tail worse position possible;

therefore, the wind would flow normal to the tail surface. The CFD results were exported to the FEA study. In the FEA, the boom-free extreme is fixed, and in addition to the imported load from CFD gravity was taken into account. The maximum Von Mises stress and deflection were 169.4 MPa (at the fixed area), and 45 mm (at the tail tip), respectively. The mainframe FEA study was similar to that of the main shaft – the maximum Von Mises stress and deflection were 112.9 MPa (at the main shaft support further from the rotor) 12 mm (at the nearest to the rotor). The tower CFD was done by considering load case H, and the result was exported to the tower FEA study. In the FEA study, in addition to the load from the CFD, the induction load from the turbine and gravity was also taken into account, the tower root was set as fixed support. The maximum Von Mises stress and deflection were 122.3 MPa (at the first third from the top), 364 mm (at the tower tip).

The third part of this chapter was dedicated to the description of the material used for the turbine main components and their processes thereof. The blade and the hub were chosen to be made of aluminum 7075 T6. Extrusion would be used to obtain the desired blade shape, whereas machining would be the most suitable process to manufacture the hub. The tower would be made of plain carbon steel, and the process used to fabricate the light poles was suggested to ideal to manufacture the tower for this project. The nacelle is made of fiberglass vinylester and vacuum-assisted resin transfer molding (VARTM) is used as the manufacturing process. The mainframe and the main shaft were both made of plain carbon steel and machined into shape. The tail was suggested to be made of aluminum and machined into shape.

The last part of the chapter described the design of the turbine control. The design was based on the theoretical described in Section 4.10.5. To calculate the control parameter, the following parameters were used: $R_s = 0.5\ \Omega$; $L_q = 4.48$ mH; $T = 0.0002$ s; $T_i = 0.0001$ s; $p = 19$; $J = 332$ kgm^2; and $\psi = 0.39$ Vs. These parameters were also used to simulate the turbine control in Matlab Simulink. The system was simulated considering three different wind speeds ($2.5, 5, 7.5$ m/s). In all of the wind conditions, the turbine was chosen to operate at the maximum power coefficient condition, after the transient conditions settled the turbine. The turbine's final specifications would be as follow: $P = 10$ kW; $U = 10.5$ m/s; $N = 186$ rpm; $B = 3$.

Chapter 6

Cost and Benefits Analysis

In this chapter, the economic and environmental impact of a small wind turbine is analysed. The chapter starts by giving the estimated costs of the components in Section 6.1. In Section 6.2 a brief theory of the wind distribution model is given followed by the calculation of the average mean power. Section 6.3 defines and determines the economic parameters of interest to evaluate the cost of producing electricity from the designed turbine. The final section gives the simplified qualitative benefits of the project.

6.1 Turbine Estimated Cost

Table 6.1 shows the market prices of the material used to design the turbine components. Aluminum 7075 is used as blades, hub, and tail material; mild steel is as mainframe, tower, and alternator supports. The rotor shaft is made of 4340 steel. The aluminum and steel prices are given in R/kg. Fiberglass is used in the nacelle and hub nose, and the price is given in R/m^2. Table 6.3 shows the estimated manufacturing process cost of the blades, hub nacelle, mainframe, and tower. The total cost of a component is the sum of the costs of the material needed and the manufacturing process cost. Table 6.4 shows the total cost of the main turbine components.

Table 6.1: Turbine Material price

Material	**Price**
Aluminium 7075	R150/kg
Mild steel	R2/kg
Round bar of steel 4340	R50/kg
Fibreglass vinyl ester	R200/kg

Table 6.2: Material process price

Process	**Price**
Blade	R150/kg
Hub	R100/kg

Hub nose	R200/kg
Nacelle	R200/kg
Mainframe	R50/kg
Tower	R50/kg

Table 6.3: Turbine components

Component	**Material**	**Property**
Blade	Aluminium 7075	35 kg
Hub	Aluminium 7075	9.2 kg
Hub nose	Fiberglass vinylester	7.43 kg
Nacelle	Fiberglass vinylester	59.11 kg
Mainframe	Mild Steel	66 kg
Tower	Mild steel	844.2 kg
Tail	Mild steel	36.2 kg
Rotor shaft	Steel 4340	29.7 kg

Table 6.4: Turbine Component prices

Components	**Price**
Alternator	R93469
Converter	R41210
Controller	R25000
Blades	R31500
Tower	R43904
Nacelle	R5912
Hub	R2325
Hub nose	R800
Mainframe	R3432
Tail	R1882
Rotor shaft	R2970
Brakes	R4000
Bearings	R27598
Ancillary	R20000
Total SWT Cost	**R304002**

Assuming that the installation cost is about 30% of the turbine system cost, the initial investment is estimated to be

$$\textbf{Intial investment} = \text{R}395\ 202.6$$

6.2 Estimative of Wind Turbine Energy Production

The wind speed can be modelled as a random variable. Therefore to estimate the energy potential of a given site and thereby predict the power produced by an installed wind turbine in that site, statical analysis is used.

There are two methods used in wind turbine analysis to analyze wind data: the Rayleigh and the Weibull probability distribution. The Rayleigh used only one parameter to analyze the wind data, the value of the mean wind speed. In contrast, the Weibull distribution is based in two-parameter, with this method, a wide variety of wind regime can be generated [18].

6.2.1 Rayleigh Distribution

The Rayleigh distribution is the simplest between the two since it only requires the knowledge of the value of the mean wind speed.To calculate the probability density and the cumulative distribution function, the following formulae are used [18]:

$$p(U) = \frac{\pi}{2}\left(\frac{U}{\bar{U}^2}\right) exp\left[-\frac{\pi}{4}\left(\frac{U}{\bar{U}}\right)^2\right] \tag{6.1}$$

$$F(U) = 1 - exp\left[-\frac{\pi}{4}\left(\frac{U}{\bar{U}}\right)^2\right] \tag{6.2}$$

6.2.2 Weibull Distribution

Two parameters must be known to use the Weibull probability density function: a shape factor, k, and a scale factor, c. These parameters are functions of the mean wind speed and the standard deviation of the main speed, σ_U. The Weibull probability density function and the cumulative distribution function are given by [18]

$$p(U) = \left(\frac{k}{c}\right)\left(\frac{U}{c}\right)^{k-1} exp\left[-\left(\frac{U}{c}\right)^k\right] \tag{6.3}$$

$$F(U) = 1 - exp\left[-\left(\frac{U}{c}\right)^k\right] \tag{6.4}$$

6.2.3 Average mean Power

When the wind regime probability density function, $p(U)$, is known, and the turbine's power curve, $P_w(U)$, is given, the average wind turbine power can be calculated by:

$$\bar{P}_w = \int_0^\infty P_w(U)p(U)dU \tag{6.5}$$

But,

$$P_w(U) = 0.5\rho A C_p \eta U^3 \tag{6.6}$$

Therefore, for a constant C_p

$$\bar{P}_w = 0.5\rho\pi R^2\eta C_p \int_0^\infty U^3 p(U) dU \tag{6.7}$$

We use the Rayleigh distribution method to estimate the mean average power. From Eqs. 6.1 and 6.7, we can plot the average mean power produced by the turbine as a function of annual mean speed and maintaining other parameters constant. The other parameters were obtained in the previous sections; that is: $C_p = 0.45$, $\eta = 0.655$, $R = 3.5$ m, $\rho = 1.225$ kg/m^3. These parameters are assumed to be constant throughout the turbine operation. Figures (6.1) and (6.2) shows the average mean power and the average annual energy produced, respectively, as a function of annual mean speed.

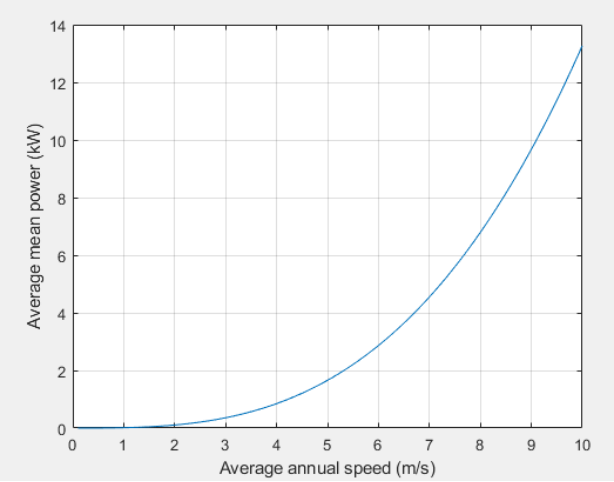

Figure 6.1: Average mean power vs Annual mean speed

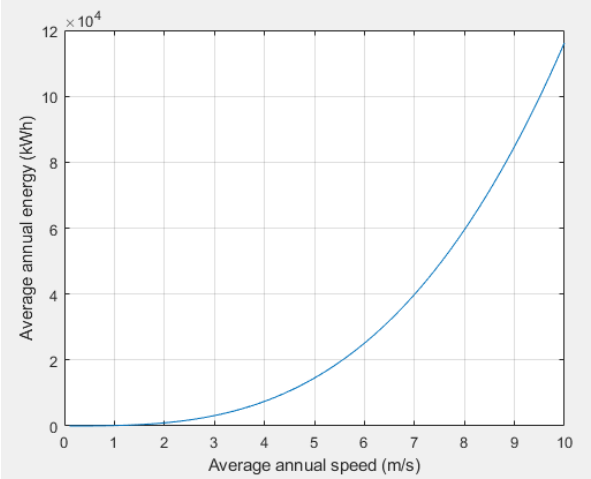

Figure 6.2: Average annual energy vs Annual mean speed

6.3 Quantitative Costs and Benefits

6.3.1 Simple Payback Period

The simple payback period (SPP) is the period (typically measured in years) when positive cash flow exceeds the initial investment. The value of money changes from over the years due to several economic factors that is today's money will have less buying power in the future. However, SPP does not take into account the value of money in the future. The SPP is an essential parameter as a shorter payback is very attractive to investors. The formula to calculate the SPP is given by [18]:

$$SPP = \frac{C_c}{AAR} \tag{6.8}$$

Where SPP is simple payback period, C_c is the installed capital cost, and AAR is the average annual return [18]. The average annual return is given by:

$$AAR = E_a P_e \tag{6.9}$$

Where E_a is the annual energy production (kWh/year), and P_e is the price obtained for electricity (R/kWh). Therefore,

$$SPP = \frac{C_c}{E_a P_e} \tag{6.10}$$

The electricity price from the grid is around R1.3 in South Africa. Assuming that the price remains the same throughout the years, in regions where the annual average wind speed is 7.5 m/s, the simple payback period would be:

$$\begin{aligned} AAR &= 1.3 \times 49038 = \text{R}63749.4/yr \\ SPP &= \frac{395202.6}{63749.4} = 6.2 \text{ yrs.} \end{aligned}$$

It takes three years and seven months for the wind turbine to start having positive cash flow when installed in a site with an average annual speed of 7.5 m/s.

According to Figure 6.3, a wind speed of 7.5 m/s can be found in the Cape provinces, in some areas of KwaZulu Natal, Free State, and Mpumalanga.

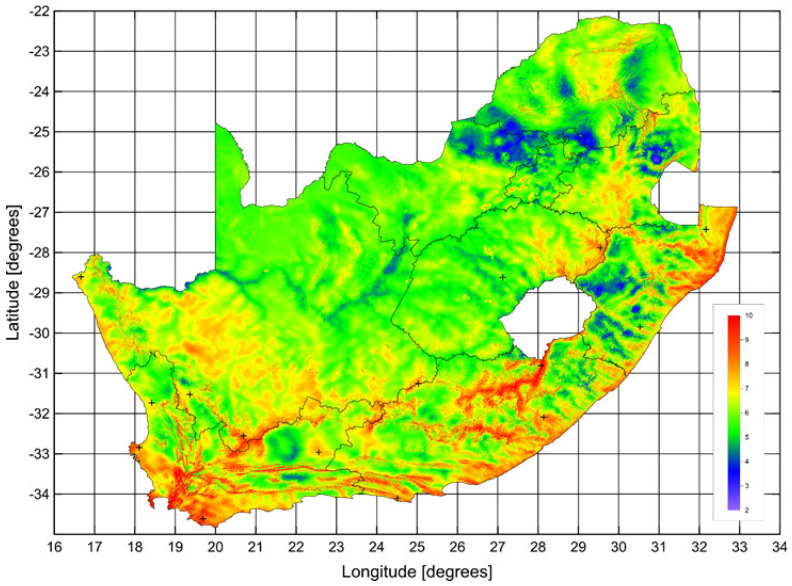

Figure 6.3: WASA high resolution wind resource map [90]

6.3.2 Net Present Value

The net present value (NPV) represents the sum of all the relevant costs of an investment; it considers the amount of money over time. It calculates the value of the total present value of cash inflows and outflows at a given target rate of return or capital cost. When the NPV is positive, the project is said to be fanancially viable, whereas a negative NPV value represents a no viable project [16].

The NPV is calculated as the difference of the total benefits over a period of time and the total cost of the investment. To proceed with the calculations, we assume that the annual wind speed distribution and the price of electricity remain the same; consequently, the total revenue is constant. Since the cost is projected in the future, the discount must be included in the equation. The NPV is given by [16]:

$$NPV = AAR \times \frac{(1+i)^n - 1}{i(1+i)^n} - C_c \tag{6.11}$$

Where i is the discount rate, and n is the lifetime of the wind turbine. Where i is the discount rate, and n is the lifetime of the wind turbine. It is assumed a 10% discount rate and that it remains constant throughout the turbine lifetime, and that the turbine is to be operational for 20 years. The annual operating and maintenance cost is taken to be one percent of the initial turbine system cost. Therefore the net present value at a site of an annual mean speed of 7.5 m/s is

$$NPV = 63749.4 \times \frac{(1+0.1)^{20} - 1}{0.1(1+0.1)^{20}} - 395202.6 - 0.0225 \times 395202.6 \times 20 = -\text{R}30309$$

6.3.3 Levelised Cost of Energy

The levelised cost of energy (LCOE) is the cost associated to the production of electricity over the lifetime of the of the system, that is, it is cost to produce one kWh of electricity during the lifetime of the turbine. It encompass the total installation cost, financing costs, operations and maintenance costs. The value of LCOE is used to compare the cost of energy production with other sources.

The levelised cost of energy (LCOE) is the cost associated with the production of electricity over the lifetime of the turbine; that is, it is the cost to produce one kWh of electricity during the turbine's lifetime. It encompasses the total installation cost, financing costs, operations, and maintenance costs. The value of LCOE is used to compare the cost of energy production with other sources.

The following formula calculates the LCOE:

$$LCOE = \frac{C_c \times CRF + O\&M}{E_a} \tag{6.12}$$

Where $O\&M$ is the annual operations and maintenance cost, and CRF is the Capital Recovery Factor for the system. The CRF is given by:

$$CRF = \frac{i(1+i)^n}{(1+i)^n - 1} \tag{6.13}$$

Taking the parameters from the last section, we have

$$\begin{aligned} CRF &= \frac{0.1(1+0.1)^{20}}{(1+0.1)^{20}-1} = 0.1175 \\ LCOE &= \frac{395202.6 \times 0.1175 + 0.0225 \times 395202.6}{49038} = \text{R1.13/kWh} \end{aligned}$$

The levelised cost is slightly below the national grid line's average energy cost, around R1.3/kWh.

6.3.4 Sensitivity Study

A sensitivity study is a method of evaluating the effect of the deviation of any variable from its estimated value. Due to the uncertainty of the estimated values used to calculate the net present value, it is necessary to do a sensitivity study to define a suitable range of the specific variable to know which range of value yields a viable investment. The variable that causes a considerable change in the NPV when changed is of critical importance in the design as it would influence whether the project is economically feasible or not.

In the current study, we analyzed the effect of varying the average annual wind speed, the power coefficient, the discount rate, and the operations and maintenance costs on the NPV, assuming a constant price of grid electricity.

The average mean speed is a critical parameter for knowing how much power the turbine generates at a particular wind site. Studying the effect of varying this parameter on the NPV determines the location where the turbine's installation would result in a positive NPV over the turbine lifetime.

The power coefficient determines how efficiently the turbine extracts power from the inflowing wind. The increase in the power coefficient would result in more energy being extracted, consequently increasing the turbine revenue. However, increasing the power coefficient also increases the initial capital cost and complexity of the design. Therefore, it is crucial to know how much income is gained or lost by increasing or decreasing the power coefficient to set an acceptable range of it, which would result in an optimum operation point.

The discount rate is used to compare future costs and benefits of an investment with the present market value. Since it is impossible to predict the future's amount of the discount rate with a great degree of accuracy, it is necessary to analyze its effect from the assumed value on the NPV.

The Danish Wind Industry Association estimate the wind turbines' annual operation and maintenance costs to be generally in the range of 1.5% to 3% of the original turbine cost. Most of the cost is due to the regular service of the turbine [18]. We will analyze the effect of varying the O&M on the NPV to evaluate the importance of estimate its values accurately to determine if the investment is greatly affected by it.

Table 6.5: Sensitivity analysis scenario

Scenario	**Discount rate (%)**	**Av. wind speed (m/s)**	C_p	**O&M (%)**
Base	10	7.5	0.45	2.25
Best case	5	10	0.5	1.5
Worse case	15	5	0.4	3
4	5	7.5	0.45	2.25
5	15	7.5	0.45	2.25
6	10	5	0.45	2.25
7	10	10	0.45	2.25
8	10	7.5	0.5	2.25
9	10	7.5	0.4	2.25
10	10	7.5	0.45	1.5
11	10	7.5	0.45	3

The base case scenario is considered when the turbine is installed in a wind site of an average annual speed of 7.5 m/s, it has a power coefficient of 0.45, the discount rate is 10%, and the annual O&M costs is 2.25% of the initial capital cost. In the best-case scenario, the wind site has an average annual speed of 7.5 m/s, the power coefficient is 0.5, the discount rate is set to 5%, and the annual O&M costs are 1.5% of the initial capital cost. The worst-case

scenario is defined as when the wind site's mean speed is 5 m/s, the power coefficient is 0.4, the discount rate is 15%, and the O&M cost is 3% of the initial capital cost. The other case scenario is set by varying one variable at a time from its best to worst-case scenario while others variable are kept constant. Table 6.5 shows all the scenarios considered in this study.

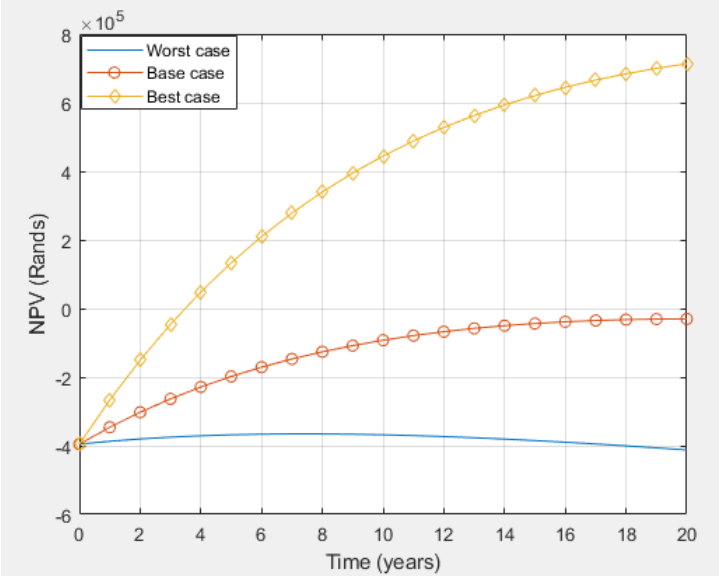

Figure 6.4: Sensibility study best, base and worse case scenario

It can be seen that the base case scenario has a negative NPV, which means the turbine would not be economically feasible under those conditions. The best-case scenario has a positive NPV, that is for an average wind speed of 10 m/s the turbine is economically feasible over a period of 20 years. The worst-case scenario shows a negative NPV signifying the installation would be economically infeasible. The value of other cases would range in between the best and the worst-case scenario.

Figure 6.5 shows the effect of varying the discount rate. reducing the discount rate by 5% from the base case increases the NPV by more than R200 000 over 20 years. When the discount rate is increasing by 5% from the base case, the NPV decreases by R143 700 from the base case during 20 years. Thus reducing the discount rate increases the NPV considerably.

The average wind speed has a significant impact on the NPV, as shown in Fig. (6.6). A deviation of 2.5 m/s from the base value can determine the project's economic feasibility. When the average annual wind speed is 5 m/s, the NPV results in a negative value of R412 230, which is about R381 930 apart from the base value. However, if the annual average wind speed increases to 10 m/s, the NPV is R713450 (positive), which is a significant increase.

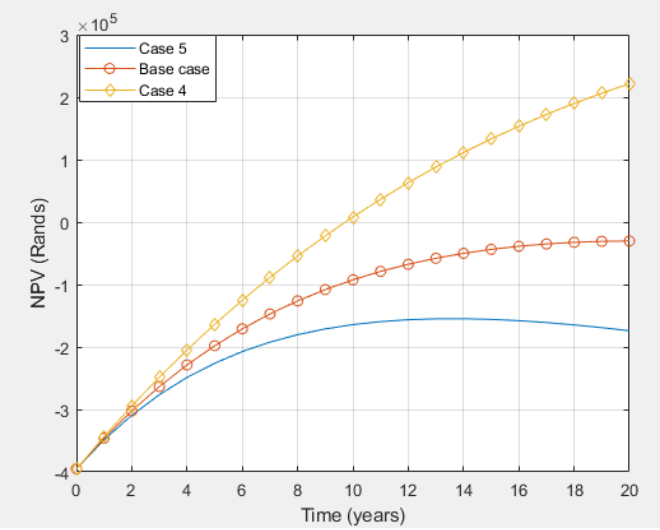

Figure 6.5: Sensibility study scenario 4 and 5

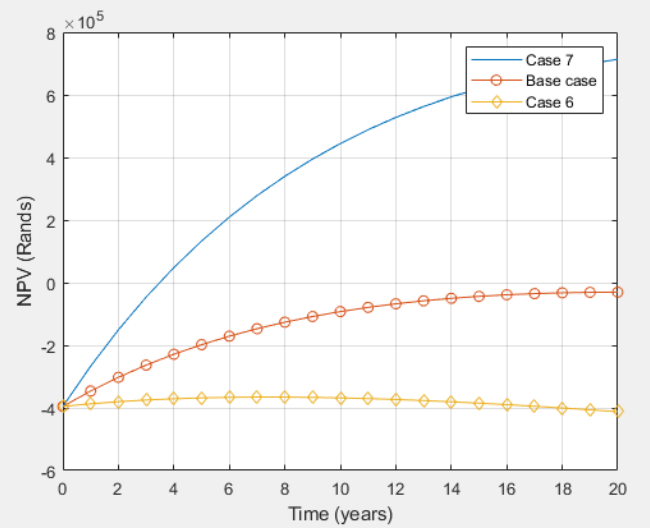

Figure 6.6: Sensibility study scenario 6 and 7

Figure 6.7 depicts the deviation of the power coefficient. It can be seen that the power coefficient affects the NPV moderately. An increase of 5% in the C_p from the base values gives an increase of the NPV of about R60 304, whereas an decrease of 5% in C_p decreases around R60 304; therefore the NPV is linearly dependent to C_p. The operation and maintenance cost has low effect in the NPV if compared with others parameters, as can be seen in figure 6.8. A 50% decrease of the base value yields a small deviation in NPV. However and increase of 50% of the base value gives a moderate increase in the NPV.

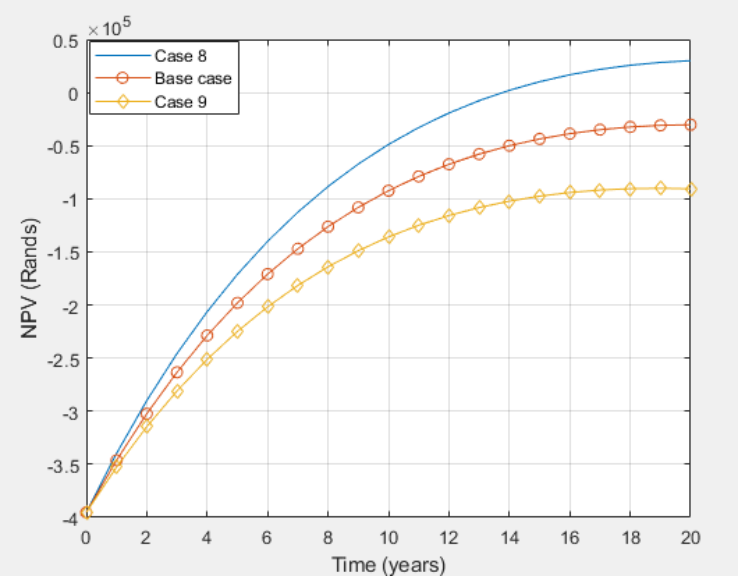

Figure 6.7: Sensibility study scenario 8 and 9

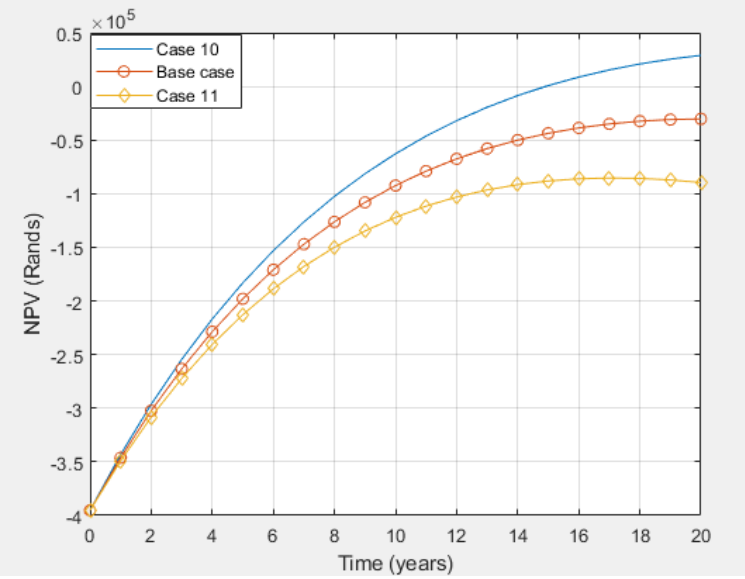

Figure 6.8: Sensibility study scenario 10 and 11

In all case scenarios studied in this section, only when the average wind speed of 10 m/s resulted in a positive NPV. Therefore the turbine will not gives a positive NPV at the rated speed when compared with the grid price electricity.

The annual average wind speed has the most significant impact on the economic feasibility of the turbine. A small increase from the base value can determine whether the project is feasible or not.

The change in discount rate has a significant impact on the result of the NPV. When the

discount rate increases, the NPV decrease; when it drops, the NPV decreases.

The change in the power coefficient has a moderate effect on the NPV; this implies that any attempt to design a very efficient blade may be offset by the extra costs required. The change in the operation and maintenance costs has little impact on the NPV results.

6.4 Qualitative Costs and Benefits

Wind energy is green energy; that is, it reduces greenhouse gases (GHGs) emissions and does not pollute the environment (air or water) when electricity is produced. Therefore, using a wind turbine to produce electricity has fewer environmental impacts than conventional electricity generation sources. However, wind turbines cannot be considered zero-emission machines, in the real sense of the word, because of the emission and pollution associated with the manufacturing and installation of the wind turbine systems. The indirect emission related to the production and installation of a small wind turbine is small. The small wind turbine has low energy density; therefore, it reduces only a small fraction of GHGs emissions.

The production of electricity using a wind turbine is not done without a negative environmental impact. Some of the effects are listed below.

- Avian and bat interact with turbine
- Visual impact of wind turbine
- Wind turbine noise
- Electromagnetic interference effect of wind turbine
- Other impact consideration

See reference [18] for more information on qualitative cost and benefits of wind turbines.

6.5 Chapter Summary

The chapter started by estimating the manufacturing costs of all the components based on the current material and manufacturing prices available in the market. The total manufacturing cost of the turbine was estimated to be R304002. The installation costs were assumed to be 30% of the manufacturing cost; which implies that the total turbine initial investment was estimated to be R395203. The total energy that the turbine ought to produce estimated using the Rayleigh distribution method taking the annual wind speed of 7.5 m/s; the turbine is estimated to yield R63749.4 per year, which means it would take 6.2 years for the turbine to return all the initial investment. The other two important economical parameters studied were the NPV and the LCOE. Assuming a discount rate of 10%, the NPV was found to be –R30309; that is, it would be more expensive for the customer to install this turbine than to use the electricity from the grid considering an average electricity price of R1.3/kWh if a discount rate of 10% is taken into account. The LCOE was calculated to be R1.13/kWh,

which is lower than the grid average cost of electricity.

A sensibility study was done to analyze the effect of changing some parameters on the NPV. The parameters studied were discount rate, wind speed, power coefficient, and operational and maintenance costs. Each parameter was varied while maintaining the others constant. It was found that the NPV varies considerably with the wind speed. The variation with discount rate is also meaningful, but it is less sensitive to the discount rate than wind speed. The power coefficient and operations and maintenance have a moderate effect on the NPV.

Chapter 7

Conclusion

This chapter presents the conclusion and recommendation of the study. Section 7.1 gives a summary of the research. In Section 7.2, the summary of the main findings and conclusions of each research objective is presented. Section 7.3 gives recommendations on how the study could be improved in each objective of the current design project.

7.1 Introduction

The overall aim of this research was to lower the Levelized Cost of Energy (LCOE) of small wind turbines, for this reason, a 10 kW wind turbine intended to be installed in a wind site with an average annual speed of 7.5 m/s was designed optimized and simulated. To accomplish the above-mentioned aim the following specific objectives had to be carried out:

- Identification of the small wind turbine components that need to be design and those, which need to be selected.
- Modelling or selection of the components or system preliminarily.
- Detailed design of the components or system. The turbine model simulation.
- Analysis of the economic aspects of the design.

This section reviews the aim and the specific objects of the research project summarize the research findings and provide conclusions based on the findings. Chapter one introduced the projects. The next chapter reviewed the literature available on the research topic under study. Chapter three gave the theoretical background of the turbine blade design and the analysis of the aerodynamic blade performance. Chapter four presented the preliminary design of the turbine components and systems essential for good turbine performance, Chapter five presented the mechanical analysis of the fundamental components, and Chapter six studied the economic aspect of the designed turbine. The previous chapters are extensive and require to be summarized; hence, the summary in this chapter. Recommendations based on the conclusion will be presented wherever applicable, as well as recommendations for future work in terms of how to progress from this research. This structure was adopted to enable the evaluation of whether the research objectives stated at the beginning of the research were met.

7.2 Research Objectives: Summary of Findings and Conclusion

In this section, the findings of each objective are summarized and conclusions thereof are drawn.

7.2.1 Research Objective 1: Literature Review

From the literature review, it was found that the costs of producing electricity using small wind turbine is less competitive when compared to the cost of the traditional ways of producing electricity such as photovoltaic technology or large wind turbines; even though the price of small wind turbines has been dropping considerably in the last decades. The cost of photovoltaic technology has dropped substantially to the extent that this technology has reached a level of competing with the traditional technologies for electricity generation, while small wind turbines are still not economically feasible. Therefore, PV technology constitutes the main competitor for small wind turbines.

Small wind turbines share many similarities with large counterparts. However, they have considerable differences. The main differences between them are that small wind turbines experience more fatigue load they have higher centrifugal and gyroscopic loads, they experience low load variations due to gravity and wind shear, they need thin airfoil near the root of the blade, they have more options for blade material to be used, they require more maintenance, and they have low reliability than their larger counterpart. Little is known about the various key aspects of small wind turbine blade behaviour. The large wind turbine has developed to a stage of maturity and plenty of literature is available on the topic; however, a little study was done on the small wind turbine.

There are many approaches used to design the turbine's blades, the most common ones are the blade element momentum theory, the vortex model method, the actuator type model, and the computational fluid dynamics method. All of them have their advantages and disadvantages. The BEM has several limitations. Therefore, several models such as tip loss, turbulent wake state, dynamic inflow, dynamic stall, stall delay, radial flow, and skewed wake model have to be developed to overcome those limitations. However, BEM needs very little computational time compared to other models, and if reliable aerodynamic data for airfoil is available, this method can provide accurate results. When designing the blades of a wind turbine the BEM method is preferred.

Large wind turbines use pitch or stall control to regulate the turbine blade rotational speed and the output power and a separate yaw control mechanism to orient the turbine to the wind. However, in small wind turbine, furling is the predominant method to control the wind turbine blade rotational speed and power and the turbine alignment to the wind. Furling is obtained by offsetting the turbine from the yaw axis and by a tail attached to the turbine. The turbine offset tends to rotate the turbine due to the thrust generated on the blades; the aerodynamic forces on the tail vane balance this rotation. When the wind speed increases

the thrust on the blades increases and the turbine is rotated away from the wind until a new equilibrium is reached. The tail tends to be aligned with the wind and it is kept in that way due to its weight.

The main towers used in modern turbines are lattice towers, tubular steel towers, and guyed towers. Lattice towers consume less material than a tubular tower; therefore, they need a lighter foundation. However, lattice towers have many problems; the major ones are aesthetics, intense avian activities, and not maintenance-friendly. The tubular tower allows optimum bending resistance in all directions due to their circular cross-section; they have good aesthetics and reduce avian activity significantly. Tower with guyed steel poles can be used to support a small wind turbine. In this system, the load is shared by the tower and the guy wires, which makes it possible to design a much lighter tower than it would have been needed otherwise, therefore, less expensive.

The vast majority of wind turbine projects are large-scale turbines because large wind turbines are economically feasible; therefore, most of the studies done on wind turbines are centered on large turbine achievements, which creates a scarcity of studies pertaining to small wind turbine achievements, as well as a database. The interest to develop the small wind turbine technology to a stage of maturity is propelled mainly by climate change and the need to lower greenhouse gas emissions by reducing or replace the use of fossil fuel to generate electricity. The decentralization of energy production to supply the electricity in remote areas as well as the desire of people to be independent of the electricity supplied by the grid also has influenced the growing need for small wind turbines. Currently, many small wind turbines are not economically feasible. Thus, the future of small wind turbine depends on reducing the technology costs, improving their certification and safety, creating incentive policies, having a deeper understanding of the final users, and attracting investors. Currently, the main concern about small wind turbine performance is reliability. Most small wind turbines do not have the performance claimed by the manufacturer, often the performance is far below the claimed one, which results in client dissatisfaction.

7.2.2 Research Objective 2: Modelling and Selection of the Turbine Components or Systems

The preliminary modeling process started by designing the blade aerodynamically. The blades' aerodynamic design aimed to produce blades capable of yielding the rated power at the rated wind speed with an acceptable power coefficient and relatively low costs. The design resulted in uniform cross-sectional blades with a rotor diameter of 7.0 m. The blade design was done using three different methods, namely: calculations, Qblade, and CFD. The calculations and Qblade are based on the blade element momentum method with the Prandtl tip and root lost as well as the Glauert correction model included. The CFD model had a one-third tapered cone with the general settings chosen to Pressure-based, Absolute, and Steady options. The air density and viscosity were set to 1.225 kg/m^3 and 1.7894 kg/ms respectively. The inlet velocities were varied in order to obtain the range of tip speed ratio needed and 0 kPa gauge pressure was set as the outlet. The $k-\omega$ SST model was cho-

sen as the turbulence model. The Qblade was used to verify the algorithm developed to calculate the blade aerodynamic parameters. The values of the power coefficient obtained from calculations and Qblade are very similar. The slight differences are due to the fact that the graphic method was to obtain the lift coefficient in the calculations whereas Qblade obtains the lift coefficient iteratively. The power coefficient from the CFD model shows a considerable difference at the low tip speed ratio and a very close approximation to the two previous methods when the tip speed ratio is moderate or high.

The maximum power coefficient obtained from the three methods is relatively high where the lowest is about 77.4 percent of the Betz limit. Therefore, the blades have a considerably high power coefficient even though they are not twisted and optimized for maximum power coefficient. The three methods used to design the turbine's blades showed that the turbine rotor could make use of blades with a uniform cross-sectional area with a high lift to drag coefficient airfoil (SG6043) and still have a relatively high power coefficient. The power coefficient obtained from calculations and that found from Qblade are very similar. Therefore, Qblade can be used to estimate the turbine's blades aerodynamic parameters, since the time taken to compute the results from Qblade is quite fast, the turbine's blades model can quickly be set, and the software is available for free for everyone.

After the blades' aerodynamic design, the blade's structure was analyzed and optimized preliminarily. When the optimum blade design was obtained, other turbine components were also analyzed preliminarily. To estimate the blade's loads standard IEC 61400-2 was used, which establishes one load case for fatigue analysis and nine load cases for ultimate stress analysis. The blade was considered to be a cantilever rigidly attached to the hub with a rectangular cross-section root. The maximum stress was considered to occur at the blade's root. The analysis resulted in the design of a blade made of aluminum with a rectangular root cross-sectional area and a hollow cross-sectional area throughout the blade's body. Load case A, B, C, and H dominated the design. It was found that the fatigue stresses were in acceptable range but the stresses due to gyroscopic loads (load case B and C) on the interface between the blade body and root were extremely high.

It is concluded that the blade will not fail due to fatigue, therefore it is expected that they will operate throughout the turbine life span (20 years). If the blades are allowed to rotate at the designed rotational yaw speed prescribed by IEC 61400-2 while rotating at the rotor rated speed the blade will fail at the interface between blade's root and body due to gyroscopic loads and designing the blades to bear those loads is not economically feasible; therefore, the rotor speed must be reduced to acceptable levels when the turbine is yawing. Hence, for ultimate stress analysis, only load case H is considered in the blade design and other components.

The main shaft preliminary design was done using the standard IEC 61400-2 to estimate the load and CAD software to determine the physical and geometric properties. Here again, load case A provided the method to estimate the fatigue load, and load case B yielded the highest load among the ultimate stresses load cases; therefore it was used to estimate the dimensions of the main shaft. The analysis done resulted in a design of a shaft of 120 mm

diameter made out of steel ASTM-A574. Both the fatigue and the ultimate stresses criteria were met; therefore, the shaft will not fail due to fatigue or stress load conditions throughout the turbine life span.

The tower was modeled considering only load case H since it gives the maximum load on the tower among all the other load cases. A tapered octal cross-section tower was chosen for ease of manufacturing and cost reduction. The graphical optimization method was used to obtain the suitable dimensions for the tower. The ultimate stress and the tower buckling were analyzed by developing a computer program that does the stress and buckling calculations; the program also estimates the tower's natural frequency. The analysis resulted in a design of a tower made of plain carbon steel which has a height of 20 m, 500 and 200 mm base and top diameters, respectively, and 4.7 mm thick. The load cases A, B, and H were compared to see which one would dominate the tower design, and it turned out that the load case H clear gives the highest stress which occurs at the base of the tower, as expected. However, the maximum load does not occur at the base of the tower but at about 6 m down from the top of the tower. The tower ultimate and buckling criteria are met; therefore, it will not fail due to fatigue or buckling throughout the turbine life span.

The nacelle was model as a rectangular frame with the ends separated at a distance equal to the yaw bearing fixed at both ends, and a rectangular cross-sectional area whose dimensions are the nacelle length and thickness. The load case I was used to estimating the nacelle load according to standard IEC 61400-2. The fiberglass vinyl ester was used as the nacelle material which was estimated to have a tensile strength of 550 MPa. The nacelle's thickness for it to meet the ultimate stress criteria according to standard IEC 61400-2 was found to be 2.5 mm.

The mainframe is modeled as a cantilever beam with a rectangular cross-sectional area with a length equal to the length of the mainframe. Plain carbon steel was used as the mainframe material. The load used for the mainframe design are load from the main bearings supports, and the weight of the turbine (except the weight of the rotor) applied at the center of mass. The calculations to estimate the mainframe thickness was quite straightforward. The thickness for the mainframe to bear the load according to standard IEC 61400-2 was found to be 15 mm.

Furling was used for over-speed protection and power control because they are cost-effective and easy to implement. The furling model consisted of a turbine rotor and a tail system (tail boom and vane). The rotor is responsible to generate thrust, and when offset from the yaw axis the rotor thrust tends to create torque in the yaw axis, this torque is balanced by the torque generated by the aerodynamic forces on the tail. Lagrange formalism was used to generate the system mathematical model and computer codes to optimize the tail system dimensions and analyse the system response was created. The rotor thrust was obtained from Qblade, and the lift and drag forces on the tail vane were obtained from XFoil. The analysis resulted in a design of a tail system with a tail boom of 2.752 m and a delta shape tail vane with an area of 1.424 m^2. From the system response, analysis it was concluded that the system follows the wind direction and turn away from the wind for wind speed higher than the rated wind speed; therefore the turbine will align the wind for wind speed up to

the rated wind speed and will furl for wind speed greater than the rated wind speed.

A permanent magnet synchronous generator was selected to be the turbine generator because they do not require an external exciter to generate the magnetic field, they are more efficient, lightweight, less expensive, low maintenance, and they do not use brushes or slip rings. The variable speed method is chosen for the turbine to be allowed to operate at the maximum power coefficient; therefore, the generator frequency and output put voltage are controlled by power electronics to maintain electrical power quality. The turbine will operate at the maximum power coefficient by varying the electromagnetic torque by changing the current that passes in the stator windings. The output frequency is maintained fixed by control of the DC bus voltage.

In a wind turbine, brakes are used to park the turbine when the wind speed is beyond the cut-out speed or below the cut-in speed. Here the brake system is also designed to control the turbine to prevent high gyroscopic load. The brake was dimensioned by assuming that the temperature difference between the maximum temperature of the disc and the environment temperature is about 111.1°C and a forced wind speed of 10.67 m/s, the pressure on the disc was assumed to be constant when the brakes are deployed, the brakes are assumed to be used once in every 150 s. After optimization, the brake disc dimensions were 400 mm in diameter, and 8.4 mm thick made out of steel. The force needed to actuate the brake was found to be very small which allows the use of a solenoid to generate this force; consequently, the brakes can be controlled by electric circuitry.

7.2.3 Research Objective 3: Detailed Design of the Components or System

In the detailed design, the components were analysed further to see if they will bear the loads as specified by IEC 61400-2. For that, Computational Fluid Dynamics was used to simulate the wind loads and Finite Element Analysis to do the stress analysis. The components analysed were the rotor (the blades, hub, and hub cover), the main shaft, the tail, the mainframe, and the tower. Load case H was used for the analysis.

The rotor CFD was done SolidWorks Flow Simulation. The flow domain was considered to be a rectangular parallelepiped with a proper dimension that would allow the flow to stabilize and yet not too big that would require a lot of computer power for the simulation to converge to a solution. The rotor was considered as a real wall and the inlet was set to velocity parallel to the axis of rotation with a magnitude of 52.5 m/s and the outlet set into ambient pressure of magnitude of 101.325 kPa. After the CFD simulation was done, the results were exported to SolidWorks Simulation. In SolidWorks Simulation, the rotor was fixed at the connection point between the hub and the main shaft, as the turbine is supposed to be parked when the wind speed is 52.5 m/s. The results from SolidWorks Flow Simulation and gravity were used as the load, and a sufficiently fine mesh was applied to the model. The simulation result showed that the maximum Von-Mises stress of 157.2 MPa, maximum blade deflection of 323 mm, and a resultant force and moment of 7.18 kN and 1.94 kNm.

The maximum stress occurs near the blade root and the maximum deflection happens at the blade tip; therefore the sanity check is consistent with what was expected; furthermore, the resultant force from the simulation was compared to that obtained from the calculation and an error of 0.36% was obtained. Therefore, it was concluded that the CFD and FEA simulation were verified to be quite accurate.

The circular shaft is modelled as a circular beam fixed in both of the support of the bearing. The resultant force and moment obtained from the rotor FEA analysis are transferred to the main shaft and serves as load. The gravity effect as well as the weight of the generator were taken into consideration. After suitable meshing, the simulation gave 50.38 MPa for the Von-Mises stress and a maximum deflection of 0.1705 mm. The Von-Mises stress and deflection are relatively small; therefore, the shaft will safely bear the load in case of load H occurrence.

The model for the turbine tail for stress analysis was done according to load case I of IEC 61400-2, that is the tail is truck by the reference wind in the most unfavourable way when it is unable to rotate; therefore, the tail is treated as a cantilever. The CFD analysis was done in SolidWorks Flow Simulation. The fluid domain was a rectangular parallelepiped with the tail boom and vane considered as real wall and the inlet a 37.5 m/s velocity whose direction is perpendicular to the tail vane surface area, and the output is an ambient pressure of 101.325 kPa. The results obtained from CFD were exported to SolidWorks Simulation. In the SolidWorks Simulation, one end of the tail boom was fixed, the load from SolidWorks Flow Simulation and gravity were used as the simulation load and a suitable mesh was applied. The finite element analysis gave the maximum Von Mises stress of 169.4 MPa and a maximum deflection of 191.4 mm. The maximum Von-Mises stress and deflection occur at the fixed extreme and at the free end of the tail boom, respectively, as expected, confirming that the sanity check is correct. We concluded that the tail would not fail even if the reference wind struck it in the most unfavourable position.

The mainframe is modelled as a flat plate fixed at the point where the yaw bearing is to be attached. The loads to do the mainframe FEA analysis are taken from the main bearings support reactions obtained from load case H and the gravity effect. choosing plain carbon steel as the mainframe material and after a suitable mesh, the FEA results were as follows: 112.9 MPa for Von-Mises stress and 12.0 mm for maximum deflection. The maximum stress occurs at the second main bearing support, and the maximum deflection happens at the first bearing support. The mainframe will safely bear the stress caused by load case H, with very small deflection.

The tower was modelled as a tapered octagonal cross-section cantilever beam with a base top diameter of 500 mm and 200 mm, respectively, a thickness of 4.7 mm, and a length of 19001.5 mm. The CFD was done in SolidWorks Flow Simulation. The flow domain was a rectangular parallelepiped with a suitable dimension to allow optimum convergence time, the inlet was set to the velocity of 52.5 m/s in the horizontal direction, the outlet was chosen to be ambient pressure of 101.325 kPa, and the tower was treated as a real wall. The result from the SolidWorks Flow Simulation was exported to Solidwork Simulation. In the SolidWorks Simulation, the base of the tower was fixed, the loads from the nacelle, Solidworks

Flow Simulation, and gravity were used in the FEA study. After a suitable mesh, the result obtains in the SolidWorks Simulation were 122.3 MPa for the maximum Von-Mises stress and 363.9 mm for the maximum deflection. The maximum Von-Mises stress does not occur at the fixed end of the tower but somewhere in between the top and the middle of the tower; this is due to the variation of the area and the second moment along the length of the tower. The maximum deflection occurred at the free end of the tower. Therefore the tower will bear safely the induced load due to load case H of standard IEC 61400-2, with acceptable deflection.

7.2.4 Research Objective 4: Turbine Model Simulation

The turbine operation was simulated in MatLab Simulink. The turbine system model consisted of a turbine model, a permanent magnet synchronous generator, a voltage source, an AC to DC and DC to AC inverter, a DC bus voltage, a generator side control system, and filters. The turbine model was obtained from the Qblade data, that is, the torque coefficient from Qblade was converted into a continuous function, with the tip speed ratio as the independent variable, using the linear least square method and a polynomial of sixth order. The C_t obtained was multiply with other parameters to convert it into torque and this torque represented the torque generated by the blades, and it was fed into the permanent magnet synchronous generator. The control system was designed in such a way that the turbine is to produce maximum power for a given wind speed in the range between cut-in and rated speed, and it is to produce no power when the wind speed is below the cut-in speed.

To simulate the turbine operational modes, the wind speed was incremented each 5 s; starting at 2.5 m/s, then increased to 7.5 m/s, and finally increased to 10.5 m/s. The control was achieved by monitoring the following variables: rotor angular velocity, generator stator currents, turbine and generator torque, and the power output. For each wind speed, there is a corresponding rotor angular speed that would result in an optimum power being generated, and this angular speed is set as reference for the PI controller. The power losses were not taken into account in the simulation. The results showed that when the wind speed increases the rotor angular speed quickly increases until it equals the reference angular velocity, after that the rotor angular velocity remains constant until disturbance on the wind speed occurs. When the two angular speeds have the same value, the torques and the current in the stator also have the same value. The power had a slightly higher value than expected because the system was considered ideal. It was concluded that the turbine would operate at an optimum point when the wind speed is in the range between cut-in and rated value and will not produce power when the wind is below the cut-in value, and the turbine takes less than 5 s to reach the maximum power coefficient when the wind is disturbed.

7.2.5 Research Objective 5: Analysis of the Economic Aspects of the Design

To start the analysis of the cost and benefits of the designed small wind turbine, the estimated cost of the components was done first. Then the Rayleigh distribution was used to estimate the mean wind speed, consequently calculating the average annual power produced

by the turbine. To calculate the economic parameters the following assumptions were made: the discount rate was set to 10%, the average price of electricity from the grid was R1.3/kWh. The economical parameters of interest determined in the study were simple payback period, net present value, and the levelised cost of energy. A sensitivity study was done to find the parameter that influences the economic feasibility of the turbine the most.

At an average wind speed of 7.5 m/s the turbine has a simple payback period of 6.2 years, a net present value of -R30 306, the LCOE is R1.13/kWh, the overall cost was about R50692/kW is which approximately $3400/kW. The feasibility study reviled that the economic feasibility of the turbine depends greatly on the site average wind speed, moderately to the discount rate, and has little dependence on the power coefficient and maintenance costs. The economical analysis of the project has shown that the turbine is economically feasible because the price of electricity from the designed turbine is lower than the average price from the grid when the average wind speed is 7.5 m/s, and the cost of the turbine is also lower than the current average price of small wind turbine ($4710/kW).

7.3 Recommendations

Designing a small wind turbine is a multidisciplinary process; therefore it was not possible to cover every single aspect pertaining to small wind turbines due to the limitations of the scope of the current study. The recommendations below will improve the current study.

7.3.1 Literature Review

From the literature review, it is believed that three additional reviews (namely factors behind the price difference between small and large wind turbine, wind turbine noise and noise mitigation in the small wind turbine, and small wind turbine market in South Africa) would improve the current study. It is a clear fact that the price of wind turbines increases as the turbines' power decreases. Therefore, a thorough study of the parameters that affect this trend is recommended. Such a study would help to pinpoint the areas that need to be developed in order to make a small wind turbine commercially competitive with other technology. Noise is a major concern in small wind turbines as many of them are installed near residential areas. A study that explains how noise is produced in a wind turbine, which factors influence the noise generation, and methods to mitigate noise in small wind turbines while keeping them cheap and efficient is recommended. Knowledge of the current state of the art of small wind turbine technology in South Africa, as well as the market trend, would allow setting strategic policies to develop small wind turbines toward a stage of maturity.

7.3.2 Preliminary Design

In addition to the components preliminary design done in this study, the full electrical and electronic system needed for the proper turbine functionality, the heat transfer of the entire system, and the interaction of the turbine with the environment should be studied. Preliminary studies on electrical systems such as the generator protection against short

circuit and overload, the grid connection and power control, the electrical control of the brake system, and the turbine supervisory control system, as well as their feasibility if implemented in the design, are recommended. The impact of the heat generated by the brakes, the generator, and the turbine moving parts should be estimated. The turbine's interaction with the environment such as the possibility of the turbine being destroyed by lighting and appropriate lighting protection, the possibility of the water from the rain entering the turbine, and turbine corrosion prevention and protection should be studied as well.

7.3.3 Detailed Design

The results obtained from the CFD and FEA study were verified by the calculations with the formulae given by standard IEC 61400-2. The turbine model should be further verified in existing software designed to generate turbine aeroelastic models. FAST would be a good candidate for this verification because it is freely available to the public, and it has many certified models available that can be edited to match the model that one desires to verify. After the model has been verified in an existing wind turbine software, it should be validated by constructing a prototype and test it in a wind tunnel, or in a vehicle-based test. In both cases, measurement instruments should be available and mounted on the turbine to measure the power from the generator, the rotor speed, the wind speed, the blade stresses, the generator current, the yaw and furling rate, and the deflection of the blade. The result obtained should be compared with those from the analysis done in this study to validate the accuracy of the analysis. To accurately estimate the installation cost two things must be done: the detailed design of the turbine foundation, and the step-by-step description of the turbine site installation procedure. The turbine installation and foundation should be done with the goal of reducing costs.

7.3.4 Cost and Benefits of the Designed Turbine

The project economical study showed that for a wind site where the average speed is about 7.5 m/s, using the Rayleigh distribution model, and an average price of the energy of R1.3/kWh the designed turbine is economically feasible. For a more accurate wind distribution model, and to study regions in South Africa where the designed turbine can be implemented and yield a positive NPV, a thorough study of the county's wind map should be conducted.

Bibliography

[1] IRENA. Future of Wind: Deployment, investiment, technology, grid integration and socio-economic aspect (A Global Energy Transformation paper). Technical report, International Renewable Energy Agency, Abu Dhabi, 2019.

[2] WWEA. World wind resource assessment report. Technical report, World Wind Energy Association, Bonn, 2014.

[3] Alexandra Niez. Comparative study on rural electrification policies in emerging economies. 2010.

[4] Sector Mining Board. Designing Sustainable Off-Grid Rural Electrification Projects: Principles and Practices. 2008.

[5] S. ROLLAND. Rural Electrification with Reneawable Energy. Technical report, Alliance for Rural Electrification, 2011.

[6] DoE. The South Africa Energy Sector Report 2019. Technical report, Department of Energy, Pretoria, 2019.

[7] SANEDI. Annual Report 2018/2019. Technical report, South Africa National Energy Development Intitute, Sandton, 2019.

[8] DoE. State of Renewablw Energy in South Africa. Technical report, Department of Energy, Pretoria, 2015.

[9] DoE. State of Renewablw Energy in South Africa. Technical report, Department of Energy, Pretoria, 2017.

[10] South Africa. Carbon Tax Act No. 15 of 2019. Technical report.

[11] Statistic South Africa. Millennium Development Goals 7: Ensure environmental sustainability. Technical report, Statistics South Africa, 2015.

[12] National Development Commission. National Development plan 2030. Our future-make it work. Technical report, NPC, 2011.

[13] Noor Jamal. Options for the supply of electricity to rural homes in South Africa. *Journal of Enegy Southern Africa*, 26(3):58–65, 2017.

[14] C. G. Monyei, A. O. Adewumi, and K. E. H. Jenkins. Energy (in)justice in off-grid rural electrification policy: South Africa in focus. *Energy research & social science*, 44:152–171, 2018.

[15] Caio C. M. Chagas, Marcio G. Pereira, Luiz P. Rosa, Neilton F. da Silva, Marcos A. V. Freitas, and Julian D. Hunt. From Megawatts to Kilowatts: A Review of Small Wind Turbine Applications, Lessons From The US to Brazil. *Sustainability (Basel, Switzerland)*, 12(7):2760, 2020.

[16] Olatayo Kunle Ibukun. *A development path for small wind energy system in South Africa*. PhD thesis, North-West University, May 2017.

[17] Sathyajith Mathew. *Wind energy: fundamentals, resource analysis and economics*, volume 1. Springer, 2006.

[18] James F Manwell, Jon G McGowan, and Anthony L Rogers. *Wind energy explained: theory, design and application*. John Wiley & Sons, 2010.

[19] Hugh P Vowles. An inquiry into origins of the windmill. *Transactions of the Newcomen Society*, 11(1):1–14, 1930.

[20] Ahmad Hemami. *Wind turbine technology*. Cengage Learning, 2012.

[21] Lin Wang, Xiongwei Liu, and Athanasios Kolios. State of the art in the aeroelasticity of wind turbine blades: Aeroelastic modelling. *Renewable and Sustainable Energy Reviews*, 64:195–210, 2016.

[22] Xiongwei Liu, Lin Wang, and Xinzi Tang. Optimized linearization of chord and twist angle profiles for fixed-pitch fixed-speed wind turbine blades. *Renewable Energy*, 57:111–119, 2013.

[23] Guanpeng Xu and Lakshmi N Sankar. Application of a viscous flow methodology to the nrel phase vi rotor. In *ASME 2002 Wind Energy Symposium*, pages 83–93. American Society of Mechanical Engineers, 2002.

[24] O De Vries. Fluid dynamic aspects of wind energy conversion. Technical report, Advisory Group for Aerospace Research and Development NEUILLY-SUR-SEINE (France), 1979.

[25] H Glauert. The analysis of experimental results in the windmill brake and vortex ring states of an airscrew, r and m 1026. *British. ARC*, 1926.

[26] Marshall L Buhl Jr. New empirical relationship between thrust coefficient and induction factor for the turbulent windmill state. Technical report, National Renewable Energy Lab.(NREL), Golden, CO (United States), 2005.

[27] Tony Burton, Nick Jenkins, David Sharpe, and Ervin Bossanyi. *Wind Energy Handbook, Second Edition*. 2011.

[28] Patrick J Moriarty and A Craig Hansen. Aerodyn theory manual. Technical report, National Renewable Energy Lab., Golden, CO (US), 2005.

[29] A Spera David and PHD Spera. Wind turbine technology. *New York: The American Society of Engineers*, 1998.

[30] EA Bossanyi. Gh bladed–theory manual, version 3.81. *Garrad Hassan and Partners*, 16, 2008.

[31] Stig Øye. Dynamic stall simulated as time lag of separation. In *Proceedings of the 4th IEA Symposium on the aerodynamics of wind turbines*, 1991.

[32] Dale M Pitt and David A Peters. Theoretical prediction of dynamic-inflow derivatives. 1980.

[33] CT Tran and D Petot. Semi-empirical model for the dynamic stall of airfoils in view of the application to the calculation of responses of a helicopter blade in forward flight. 1980.

[34] J Gordon Leishman and TS Beddoes. A semi-empirical model for dynamic stall. *Journal of the American Helicopter society*, 34(3):3–17, 1989.

[35] H Snel. Heuristic modelling of dynamic stall characteristics. In *EWEC-CONFERENCE-*, pages 429–433. Bookshop for Scientific Publications, 1997.

[36] FJ Tarzanin. Prediction of control loads due to blade stall. *Journal of the American Helicopter Society*, 17(2):33–46, 1972.

[37] Morten Hartvig Hansen, Mac Gaunaa, and Helge Aagaard Madsen. A beddoes-leishman type dynamic stall model in state-space and indicial formulations. 2004.

[38] Q Wang, Y Xu, and JZ Xu. A new stall delay model for hawt based on inviscid theory. In *Fluid-Structure-Sound Interactions and Control*, pages 363–368. Springer, 2014.

[39] Horia Dumitrescu, Florin Frunzulică, and Vladimir Cardoş. Improved stall-delay model for horizontal-axis wind turbines. *Journal of Aircraft*, 50(1):315–319, 2012.

[40] R Lanzafame and M Messina. Bem theory: How to take into account the radial flow inside of a 1-d numerical code. *Renewable Energy*, 39(1):440–446, 2012.

[41] Ken Chaney, A Eggers, Jr, P Moriarty, and W Holley. Skewed wake induction effects on thrust distribution on small wind turbine rotors. In *20th 2001 ASME Wind Energy Symposium*, page 54, 2001.

[42] Mac Gaunaa, Niels Sorensen, and Mads Dossing. Prediction of steady aerodynamic performance of rotors with winglets using simple prescribed wake methods. In *49th AIAA Aerospace Sciences Meeting including the New Horizons Forum and Aerospace Exposition*, page 543, 2011.

[43] Yong-Xing Qiu, Xiao-Dong Wang, Shun Kang, Ming Zhao, and Jun-Yu Liang. Predictions of unsteady hawt aerodynamics in yawing and pitching using the free vortex method. *Renewable Energy*, 70:93–106, 2014.

[44] VA Riziotis, DI Manolas, and SG Voutsinas. Free-wake aeroelastic modelling of swept rotor blades. *EWEA, editor*, 2011.

[45] Min-Soo Jeong, Seung-Jae Yoo, and In Lee. Wind turbine aerodynamics prediction using free-wake method in axial flow. In *International Journal of Modern Physics: Conference Series*, volume 19, pages 166–172. World Scientific, 2012.

[46] Wen Zhong Shen, Jens Nørkær Sørensen, and Jianhui Zhang. Actuator surface model for wind turbine flow computations. In *2007 European Wind Energy Conference and Exhibition*, 2007.

[47] Wen Zhong Shen, Jian Hui Zhang, and Jens Nørkær Sørensen. The actuator surface model: a new navier–stokes based model for rotor computations. *Journal of Solar Energy Engineering*, 131(1):011002, 2009.

[48] Taewoo Kim, Sejong Oh, and Kwanjung Yee. Improved actuator surface method for wind turbine application. *Renewable Energy*, 76:16–26, 2015.

[49] H Bijl, AH Van Zuijlen, and A Van Mameren. Validation of adaptive unstructured hexahedral mesh computations of flow around a wind turbine airfoil. *International journal for numerical methods in fluids*, 48(9):929–945, 2005.

[50] CKG Lam and K Bremhorst. A modified form of the k-ε model for predicting wall turbulence. *Journal of fluids engineering*, 103(3):456–460, 1981.

[51] Philippe Spalart and Steven Allmaras. A one-equation turbulence model for aerodynamic flows. In *30th aerospace sciences meeting and exhibit*, page 439, 1992.

[52] Siri Kalvig, Eirik Manger, and Bjørn Hjertager. Comparing different cfd wind turbine modelling approaches with wind tunnel measurements. In *Journal of Physics: Conference Series*, volume 555, page 012056. IOP Publishing, 2014.

[53] SC Cakmakcioglu, IO Sert, O Tugluk, and N Sezer-Uzol. 2-d and 3-d cfd investigation of nrel s826 airfoil at low reynolds numbers. In *Journal of Physics: Conference Series*, volume 524, page 012028. IOP Publishing, 2014.

[54] Wen Zhong Shen, Wei Jun Zhu, and Jens Nørkær Sørensen. Study of tip loss corrections using cfd rotor computations. In *Journal of Physics: Conference Series*, volume 555, page 012094. IOP Publishing, 2014.

[55] M Carrión, R Steijl, M Woodgate, GN Barakos, X Munduate, and S Gomez-Iradi. Aeroelastic analysis of wind turbines using a tightly coupled cfd–csd method. *Journal of Fluids and Structures*, 50:392–415, 2014.

[56] Povl Brøndsted and Rogier PL Nijssen. *Advances in wind turbine blade design and materials*. Elsevier, 2013.

[57] JF Maxwell, JG McGowan, and AL Rogers. Wind energy explained, 2002.

[58] Constantine H Houpis and Mario Garcia-Sanz. *Wind energy systems: control engineering design*. CRC press, 2012.

[59] AK Sleiti and A Mehrabian. Case study of a cost-effective small wind turbine. *Energy Sources, Part B: Economics, Planning, and Policy*, 10(2):132–138, 2015.

[60] Jakub Bukala, Krzysztof Damaziak, Hamid R. Karimi, Krzysztof Kroszczynski, Marcin Krzeszowiec, and Jerzy Malachowski. Modern small wind turbine design solutions comparison in terms of estimated cost to energy output ratio. *Renewable Energy*, 83:1166–1173, 2015.

[61] Zdenko Simic, Juraj George Havelka, and Maja Bozicevic Vrhovcak. Small wind turbines–a unique segment of the wind power market. *Renewable Energy*, 50:1027–1036, 2013.

[62] Ricardo Luiz Utsch de Freitas Pinto and Bruna Patrícia Furtado Gonçalves. A revised theoretical analysis of aerodynamic optimization of horizontal-axis wind turbines based on bem theory. *Renewable energy*, 105:625–636, 2017.

[63] Xin Shen, Jin-Ge Chen, Xiao-Cheng Zhu, Peng-Yin Liu, and Zhao-Hui Du. Multi-objective optimization of wind turbine blades using lifting surface method. *Energy*, 90:1111–1121, 2015.

[64] Tuhfe Göçmen and Barış Özerdem. Airfoil optimization for noise emission problem and aerodynamic performance criterion on small scale wind turbines. *Energy*, 46(1):62–71, 2012.

[65] Saud A. Bassyouni, M. Gutub. Materials selection strategy and surface treatment of polymer composites for wind turbine blades fabrication. *Polymers and Polymer Composites*, 21(7):463–472, 2013.

[66] Lorenzo Scappatici, Nicola Bartolini, Francesco Castellani, Davide Astolfi, Alberto Garinei, and Marcello Pennicchi. Optimizing the design of horizontal-axis small wind turbines: From the laboratory to market. *Journal of Wind Engineering and Industrial Aerodynamics*, 154:58–68, 2016.

[67] Abolfazl Pourrajabian, Peyman Amir Nazmi Afshar, Mehdi Ahmadizadeh, and David Wood. Aero-structural design and optimization of a small wind turbine blade. *Renewable Energy*, 87:837–848, 2016.

[68] RC Adhikari, DH Wood, and L Sudak. Low-cost bamboo lattice towers for small wind turbines. *Energy for sustainable development*, 28:21–28, 2015.

[69] MJ Clifton Smith and DH Wood. Optimisation of self-supporting towers for small wind turbines. *Wind Engineering*, 34(5):561–578, 2010.

[70] DH Wood. An improved determination of the tower height that maximises the power output per unit cost of a small wind turbine. *Wind Engineering*, 25(3):191–196, 2001.

[71] J Zico Kolter, Zachary Jackowski, and Russ Tedrake. Design, analysis, and learning control of a fully actuated micro wind turbine. In *2012 American Control Conference (ACC)*, pages 2256–2263. IEEE, 2012.

[72] Etienne Audierne, Jorge Elizondo, Leonardo Bergami, Humberto Ibarra, and Oliver Probst. Analysis of the furling behavior of small wind turbines. *Applied Energy*, 87(7):2278–2292, 2010.

[73] KC Latoufis, GM Messinis, PC Kotsampopoulos, and ND Hatziargyriou. Axial flux permanent magnet generator design for low cost manufacturing of small wind turbines. *Wind engineering*, 36(4):411–431, 2012.

[74] Haining Wang, Chem Nayar, Jianhui Su, and Ming Ding. Control and interfacing of a grid-connected small-scale wind turbine generator. *IEEE Transactions on Energy Conversion*, 26(2):428–434, 2011.

[75] Mohd Hasan Ali. *Wind energy systems: solutions for power quality and stabilization*. Crc Press, 2016.

[76] Sailendra Nath Bhadra, Debaprasad Kastha, and Soumitro Banerjee. *Wind electrical systems*. Oxford University Press, 2005.

[77] Robert Elliott Wilson and Peter Lissaman. Applied aerodynamics of wind power machines. 1974.

[78] DA Spera. Wind turbine technology: fundamental concepts of wind turbine engineering-chapter 5-aerodynamic behavior of wind turbines. *The American Society of Mechanical Engineers (ASME)*, pages 215–260, 1994.

[79] Matthew Cable. *An evaluation of turbulence models for the numerical study of forced and natural convective flow in Atria*. PhD thesis, 2009.

[80] TJ Chung. *Computational fluid dynamics*. Cambridge university press, 2010.

[81] British Standard. Wind turbines part 2: Design requirements for small wind turbine. *BS EN: 61400-61402*, 2006.

[82] David Wood. *Small Wind Turbines Analysis, Design, and Application*. Springer, 2011.

[83] William A Sirignano. Small wind turbines: Analysis, design, and application, 2013.

[84] Porselvi. *Study of Multilevel Inverter Based Wind Electric System with a Single DC Source*. PhD thesis, Anna University, 2015.

[85] Rolan ., A. Luna, G. Vazquez, D. Aguilar, and G. Azevedo. Modeling of a variable speed wind turbine with a permanent magnet synchronous generator. pages 734–739. IEEE, 2009.

[86] Richard G. Budynas, J. K. Nisbett, and Joseph E. Shigley. *Shigley's mechanical engineering design.* McGraw-Hill Education, New York, NY, t edition, 2015.

[87] Marshek M. Kurt Juvinall C. Robert. *Fundamentals of Machine Component Design/ Robert C. Juvinal, Kert M.* Wiley, 2017.

[88] Inc Marcel Dekker. *Handbook of Aluminum Volume 1 Physical Metarllurgy and Processes.* Marcel Dakker, 2003.

[89] Pradip K. Saha. *Aluminum Extrusion Technology.* ASM International, 2000.

[90] WASA. WASA high resolution wind resource map, May 2019. http://www.wasaproject.info/ Accessed: 21-May-2021.

Appendix A

Blade Aerodynamics

A.1 Matlab Code to Calculate C_p Based on BEM

A.1.1 Main Program

```
clc
clear
B=3;
R=3.5;
R_h=0.15;
C=0.25;
r=0.25:0.155:3.35;
Sig=B*C./(2*pi*r);
Lam=1:0.5:11;
A=load('Airfoil parameter for matlab.txt');
for n=1:length(Lam)
for N=1:length(r)
fi=(A(N,(3*n-2))+7.5)*(pi/180);
F_t=(2/pi)*acos(exp(-(B*(R-r(N))./(2*r(N)*sin(fi)))));
F_h=(2/pi)*acos(exp(-(B*(r(N)-R_h)./(2*r(N)*sin(fi)))));
F=F_h*F_t;
a_0=1/(1+4*F*((sin(fi))^2)/(Sig(N)*A(N,(3*n-1))*cos(fi)));
Ct=Sig(N)*((1-a_0)^2)*(A(N,(3*n- 1))*cos(fi)+A(N,(3*n))*sin(fi))/(sin(fi))^2;
a(N,n)=a_0;
Cl(N,n)=A(N,3*n-1);
f(N,n)=F;
fi_i(N,n)=fi;
if a_0>0.4
a_0=(1/F)*(0.143+sqrt(0.0203-0.6427*(0.889-Ct)));
end
a_1=1/(-1+4*F*(cos(fi))/(Sig(N)*A(N,(3*n-1))));
Cp_i(N)=(8*Lam(n)/((R^2)*length(r)))*(F*r(N)^2)*(cos(fi)-(r(N)/R)*Lam(n)*sin(fi))*(sin(fi)+(r(N)/F
(A(N,(3*n))/A(N,(3*n-1)))*cot(fi))*sin(fi)^2;
```

```
end
Cp(n)=sum(Cp_i);
end
plot(Lam,Cp),xlabel('Tip speed ratio'),ylabel('Cp'),title('Power coefficient vs Tip speed ratio'),grid
```

Note: Airfoil parameter for matlab.txt is a txt file given in appendix A.1.5

A.1.2 Program to Find C_l, C_d and Angle of Attack of Each Blade Element

```
clear
clc
C_mean=0.25;
R=3.5;
B=3;
C=C_mean;
R_h=0.15;
r=2.73;
Lam=2.5;
Airfoil_data=load('XFOIL SG6043.txt');
alfa_x=(pi/180)*Airfoil_data(:,1)';
alpha=(pi/180)*(-5):pi/1800:pi-7.5*pi/180;
for n=1:length(alpha)
alfa=alpha(n);
[Cl,Cd,alfa_0]=airfoil_parameters(alfa,C_mean,R,Airfoil_data);
Cl_g(n)=Cl;
Cd_g(n)=Cd;
end
lam_r=Lam*r/R;
Sig=B*C/(2*pi*r);
fi=alpha+7.5*(pi/180);
F_t=(2/pi)*acos(exp(-(B*(R-r)./(2*r*sin(fi)))));
F_h=(2/pi)*acos(exp(-(B*(r-R_h)./(2*r*sin(fi)))));
F=F_h.*F_t;
Cl_t=4*F.*sin(fi).*((cos(fi)-lam_r*sin(fi))./(Sig*(sin(fi)+lam_r*cos(fi))));
plot(alpha*180/pi,Cl_g,alpha*180/pi,Cl_t,alpha*180/pi,Cd_g),grid,axis([-10 180 -2 2])
```

Note: airfoil_parameters (alfa,C_mean,R,Airfoil_data) is a function, which is given in appendix A.1.3; XFOIL SG6043.txt is a txt file containing the angle of attack, Cl, and Cd obtained from XFOIL software, it is given in appendix A.1.4

A.1.3 Airfoil Parameter Function

```
function [Cl,Cd,alfa_0]=airfoil_parameters(alfa,C_mean,R,Airfoil_data)
alfa_0=(pi/180)*Airfoil_data(:,1);
```

```
Cl_0=Airfoil_data(:,2);
Cd_0=Airfoil_data(:,3);
N_1=0;
for n_1=1:length(alfa_0)
if alfa==alfa_0(n_1)
N_1=1+N_1;
Cl=Cl_0(n_1);
Cd=Cd_0(n_1);
break
end
if N_1==0
for n_2=1:(length(alfa_0)-1)
N_2=0;
if (alfa>alfa_0(n_2))&&(alfa<alfa_0(n_2+1))
N_2=N_2+1;
Cl=Cl_0(n_2)+(alfa-alfa_0(n_2))*(Cl_0(n_2+1)-Cl_0(n_2))/(alfa_0(n_2+1)-alfa_0(n_2));
Cd=Cd_0(n_2)+(alfa-alfa_0(n_2))*(Cd_0(n_2+1)-Cd_0(n_2))/(alfa_0(n_2+1)-alfa_0(n_2));
break
end
end
end
end
if ((N_1==0)&&(N_2==0))
[Cl_stall,index_i]=max(Cl_0);
Cd_max=max(Cd_0);
alfa_stall=alfa_0(index_i);
Cd_stall=Cd_0(index_i);
AR=R/C_mean;
B_2= (Cd_stall-Cd_max*((sin(alfa_stall))^2))/cos(alfa_stall);
A_2=(Cl_stall-0.5*Cd_max*sin(2*alfa_stall))*(sin(alfa_stall)/(cos(alfa_stall))^2);
B_1=1.11+0.018*AR;
A_1=B_1/2;
Cl=A_1*sin(2*alfa)+A_2*(((cos(alfa))^2)/(sin(alfa)));
Cd=B_1*((sin(alfa))^2)+B_2*cos(alfa);
end
end
```

A.1.4 Text Files Data used in MatLab

XFoil Data

Table A.1: Xfoil aerodynamic parameters

α	C_l	C_d	α	C_l	C_d
-0.5	0.198169	0.036727	7.4	1.42056	0.014584
-4.9	0.213153	0.035366	7.5	1.42611	0.014867
-4.8	0.227996	0.033993	7.6	1.43121	0.015175
-4.7	0.226869	0.027367	7.7	1.43821	0.015375
-4.6	0.235279	0.02657	7.8	1.44411	0.015636
-4.5	0.245025	0.026149	7.9	1.44905	0.015957
-4.4	0.25569	0.025649	8	1.45524	0.01621
-4.3	0.267078	0.025041	8.1	1.46149	0.016462
-4.2	0.279313	0.024342	8.2	1.46669	0.016774
-4.1	0.292307	0.023619	8.3	1.47129	0.017123
-4	0.305692	0.022892	8.4	1.47779	0.017357
-3.9	0.319419	0.022176	8.5	1.48372	0.017627
-3.8	0.33351	0.021498	8.6	1.48857	0.017966
-3.7	0.344322	0.020984	8.7	1.4931	0.018327
-3.6	0.353995	0.020642	8.8	1.49964	0.018562
-3.5	0.364549	0.020655	8.9	1.50564	0.018826
-3.4	0.376132	0.02184	9	1.51084	0.019141
-3.3	0.38755	0.021555	9.1	1.51536	0.019503
-3.2	0.399171	0.020986	9.2	1.51981	0.019878
-3.1	0.415175	0.013752	9.3	1.52628	0.020123
-3	0.428254	0.012458	9.4	1.53269	0.020376
-2.9	0.441266	0.011648	9.5	1.53829	0.020681
-2.8	0.454163	0.011278	9.6	1.54303	0.021042
-2.7	0.467211	0.011034	9.7	1.54711	0.02145
-2.6	0.480506	0.010827	9.8	1.55082	0.02189
-2.5	0.491386	0.01066	9.9	1.55704	0.022161
-2.4	0.501402	0.010495	10	1.5635	0.022417
-2.3	0.511848	0.010329	10.1	1.56921	0.022725
-2.2	0.522676	0.010158	10.2	1.574	0.023094
-2.1	0.533792	0.00998	10.3	1.57792	0.023518
-2	0.54514	0.009799	10.4	1.58122	0.023989
-1.9	0.556684	0.009616	10.5	1.58375	0.024523
-1.8	0.56841	0.00944	10.6	1.5902	0.024783
-1.7	0.580538	0.009279	10.7	1.59645	0.02506
-1.6	0.592963	0.009142	10.8	1.60188	0.025397
-1.5	0.605629	0.009032	10.9	1.60668	0.02578
-1.4	0.618642	0.008913	11	1.61091	0.026211
-1.2	0.642192	0.008579	11.1	1.6152	0.026645
-1.1	0.652487	0.008506	11.2	1.61879	0.027142
-1	0.663003	0.008437	11.3	1.62167	0.027702
-0.9	0.673751	0.008356	11.4	1.62309	0.028376

Table A.1: Continuation of table A.1

α	C_l	C_d	α	C_l	C_d
-0.8	0.684725	0.008251	11.5	1.62746	0.028818
-0.7	0.695875	0.008126	11.6	1.633	0.029171
-0.6	0.707193	0.007989	11.7	1.6384	0.029539
-0.5	0.718903	0.007815	11.8	1.6436	0.029925
-0.4	0.730719	0.007652	11.9	1.64846	0.030342
-0.3	0.74261	0.007655	12	1.65298	0.030789
-0.2	0.754749	0.007579	12.1	1.65676	0.031296
-0.1	0.766549	0.007538	12.2	1.65985	0.031861
0	0.776231	0.007447	12.3	1.66243	0.032474
0.1	0.78575	0.007354	12.4	1.66438	0.03315
0.2	0.795035	0.007265	12.5	1.66536	0.033915
0.3	0.8038	0.007174	12.6	1.66757	0.034575
0.4	0.811626	0.007081	12.7	1.67339	0.034913
0.5	0.818786	0.007001	12.8	1.67837	0.035319
0.6	0.82549	0.006929	12.9	1.68276	0.035779
0.7	0.835833	0.006813	13	1.68676	0.036279
0.8	0.847881	0.006845	13.1	1.69041	0.036819
0.9	0.860221	0.006901	13.2	1.69378	0.037393
1	0.871156	0.006929	13.3	1.69687	0.038005
1.1	0.88136	0.006941	13.4	1.69952	0.038668
1.2	0.891757	0.006956	13.5	1.7013	0.039421
1.3	0.902292	0.006972	13.6	1.7026	0.040234
1.4	0.912942	0.006989	13.7	1.70364	0.041086
1.5	0.923834	0.007011	13.8	1.70425	0.041994
1.6	0.934878	0.007039	13.9	1.70432	0.042973
1.7	0.946068	0.007078	14	1.70849	0.043537
1.8	0.95757	0.007136	14.1	1.71207	0.044166
1.9	0.968295	0.00717	14.2	1.71515	0.044852
2	0.978435	0.007186	14.3	1.71811	0.045559
2.1	0.988722	0.007206	14.4	1.72105	0.046271
2.2	0.999121	0.00723	14.5	1.72394	0.046993
2.3	1.0096	0.007259	14.6	1.72578	0.047835
2.4	1.02013	0.007296	14.7	1.72814	0.048628
2.5	1.03067	0.007345	14.8	1.73024	0.049453
2.6	1.04134	0.007416	14.9	1.73153	0.050374
2.7	1.05143	0.007437	15	1.7327	0.051317
2.8	1.06155	0.007465	15.1	1.73402	0.052253
2.9	1.07169	0.007501	15.2	1.73532	0.053196
3	1.08179	0.007548	15.3	1.73645	0.05416
3.1	1.09179	0.007609	15.4	1.73725	0.055172
3.2	1.10162	0.00769	15.5	1.73695	0.056335
3.3	1.11172	0.007737	15.6	1.73604	0.05758

Table A.1: Continuation of table A.1

α	C_l	C_d	α	C_l	C_d
3.4	1.12166	0.007779	15.7	1.73501	0.058846
3.5	1.13128	0.007837	15.8	1.73355	0.060178
3.6	1.14044	0.007923	15.9	1.7313	0.061618
3.7	1.14916	0.00804	16	1.72826	0.063179
3.8	1.15913	0.008088	16.1	1.729	0.064253
3.9	1.16884	0.008152	16.2	1.73	0.065294
4	1.17817	0.008237	16.3	1.73105	0.066327
4.1	1.18698	0.008347	16.4	1.73202	0.067374
4.2	1.19589	0.008455	16.5	1.73286	0.06845
4.3	1.20579	0.00852	16.6	1.73282	0.069675
4.4	1.21512	0.008607	16.7	1.73224	0.071004
4.5	1.2235	0.008733	16.8	1.73204	0.072285
4.6	1.23105	0.008891	16.9	1.73207	0.073537
4.7	1.24055	0.008972	17	1.73212	0.074793
4.8	1.24899	0.009096	17.1	1.73213	0.076076
4.9	1.25599	0.009276	17.2	1.73094	0.077566
5	1.26441	0.009404	17.3	1.7295	0.079106
5.1	1.27315	0.009521	17.4	1.72851	0.080572
5.2	1.28068	0.009687	17.5	1.72774	0.08201
5.3	1.28765	0.009872	17.6	1.72698	0.08346
5.4	1.29653	0.009987	17.7	1.72544	0.08505
5.5	1.30419	0.010151	17.8	1.72284	0.086831
5.6	1.3103	0.010374	17.9	1.72086	0.088505
5.7	1.31854	0.010515	18	1.71929	0.090123
5.8	1.32528	0.01072	18.1	1.71767	0.091748
5.9	1.33041	0.010981	18.2	1.71518	0.093535
6	1.33711	0.011175	18.3	1.71158	0.095531
6.1	1.3411	0.01147	18.4	1.70883	0.097382
6.2	1.34775	0.011671	18.5	1.70637	0.099182
6.3	1.35295	0.011939	18.6	1.7037	0.101014
6.4	1.35869	0.012184	18.7	1.69922	0.103196
6.5	1.36547	0.01239	18.8	1.69505	0.105334
6.6	1.37079	0.012665	18.9	1.69151	0.107351
6.7	1.37735	0.012882	19	1.68789	0.109373
6.8	1.38407	0.013096	19.1	1.68284	0.111683
6.9	1.38932	0.013381	19.2	1.67753	0.11407
7	1.39571	0.013611	19.3	1.67299	0.116293
7.1	1.40239	0.013827	19.4	1.66841	0.118513
7.2	1.40773	0.014115	19.5	1.66229	0.121067
7.3	1.41372	0.014372			

A.1.5 Aerodynamics Parameters for Each Blade With TSR Varing from 1-11

The first set of 3 columns represent the angle of attack, lift coefficient and drag coefficient, respectively, when the tip speed ratio is one. The second set represents the same as the previous set but this time corresponds to a tip speed ratio of 1.5. The subsequent sets follow the same logic with the tip speed ratio incrementing by 0.5.

Table A.2: Airfoil Parameters used in MatLab

α	C_l	C_d	α	C_l	C_d	α	C_l	C_d	α	C_l	C_d
54	0.8954	0.9986	47	1.012	0.8048	40.5	1.109	0.6222	32.75	1.203	0.4142
62.5	0.7416	0.214	53.25	0.9366	0.9783	44.25	1.061	0.7273	36.75	1.154	0.5194
63.75	0.7066	1.243	52.5	0.9448	0.9579	42.5	1.084	0.6781	34	1.187	0.4465
63.25	0.7556	1.231	50.25	0.9723	0.8958	39.25	1.124	0.5876	30.5	1.232	0.3578
62.5	0.6952	1.214	48	1.007	0.8329	36.25	1.16	0.506	27.5	1.278	0.2865
61.25	0.7415	1.184	45.5	1.044	0.7625	33.5	1.193	0.4335	24.5	1.336	0.2202
59.75	0.8813	1.148	43	1.077	0.6921	30.75	1.229	0.364	22.5	1.386	0.1792
58.5	0.7279	1.116	40.75	1.106	0.6292	28.5	1.262	0.3097	20.25	1.456	0.1364
57	0.9419	1.078	38.5	0.133	0.567	26.75	1.291	0.2694	18.5	1.527	0.1057
55.75	0.7359	1.045	36.75	1.154	0.5194	24.75	1.331	0.2255	17.25	1.589	0.08523
54.5	0.7151	1.012	35	1.175	0.4727	23.75	1.354	0.2045	15.75	1.699	0.0687
53.25	1.004	0.9783	33.75	1.19	0.44	22.75	1.379	0.1842	15.5	1.697	0.06571
52.25	1	0.951	32.75	1.203	0.4142	22	1.4	0.1694	15.25	1.698	0.06235
51.5	1.184	0.9304	32	1.212	0.3952	21.75	1.407	0.1645	15.25	1.698	0.06235
51.25	1.029	0.9235	31.75	1.216	0.3889	21.75	1.407	0.1645	15.75	1.699	0.0687
52	0.9432	0.9442	32.5	1.206	0.4078	22.75	1.379	0.1842	17	1.602	0.08129
53.75	0.9125	0.9919	34.25	1.184	0.453	25	1.325	0.2308	19.75	1.475	0.1274
57	0.8512	1.078	37.75	1.142	0.5465	29	1.254	0.3215	23.75	1.354	0.2045
55.75	0.8754	1.045	36.75	1.154	0.5194	28.25	1.266	0.3038	23.25	1.366	0.1942
54.25	0.9034	1.005	35.5	1.169	0.4859	27.25	1.283	0.2807	22.75	1.379	0.1645
26.5	1.276	0.2638	18.5	1.527	0.1057	12	1.649	0.0333	8.5	1.488	0.01887
29.75	1.243	0.3395	23.5	1.36	0.1993	15.75	1.699	0.0687	11.25	1.621	0.02931
26.75	1.291	0.2694	20	1.465	0.1319	13.5	1.688	0.0437	9.5	1.541	0.0221
23.25	1.366	0.1942	16	1.699	0.072	11.25	1.621	0.0293	8	1.461	0.01739
20	1.465	0.1319	13.75	1.694	0.0457	9.5	1.541	0.0221	6.5	1.36	0.01281
17.5	1.575	0.0892	12	1.649	0.0333	8.25	1.475	0.0181	5.5	1.304	0.01057
15.25	1.698	0.0624	10.75	1.599	0.0271	7.25	1.419	0.0153	4.75	1.252	0.00937
14	1.695	0.0482	9.75	1.553	0.0231	6.75	1.375	0.0134	4.25	1.212	0.00874
13	1.677	0.0399	9	1.514	0.0205	6.25	1.346	0.0122	4	1.191	0.00848
12	1.649	0.0333	8.5	1.488	0.0189	6	1.333	0.116	3.75	1.169	0.00825
11.5	1.628	0.0308	8.25	1.475	0.0181	5.75	1.319	0.0111	3.5	1.147	0.00805
11.25	1.621	0.0293	8	1.461	0.0174	5.75	1.319	0.0111	4	1.191	0.00848
11	1.611	0.0281	8.25	1.475	0.0181	6	1.333	0.116	4.25	1.212	0.00874
11.25	1.621	0.0293	8.5	1.488	0.0189	6.5	1.36	0.0128	4.75	1.252	0.00937

Table A.2: Continuation of table A.2

α	C_l	C_d	α	C_l	C_d	α	C_l	C_d	α	C_l	C_d
12	1.649	0.0333	9.25	1.528	0.0213	7.25	1.419	0.0153	6	1.333	0.0116
13.5	1.688	0.0437	11	1.611	0.0281	9.25	1.528	0.0213	7.75	1.446	0.0167
16.25	1.698	0.0756	14	1.695	0.0482	12.25	1.652	0.0352	10.75	1.599	0.02713
20.75	1.439	0.1456	18.5	1.527	0.1057	16.75	1.684	0.0848	15.5	1.697	0.06571
20.25	1.456	0.1364	18	1.55	0.0974	16.25	1.698	0.0756	15.25	1.698	0.06235
19.75	1.475	0.1274	17.75	1.563	0.0933	16	1.699	0.072	15	1.704	0.05853
6.25	1.346	0.0122	2.75	1.076	0.0076	1.5	0.949	0.0071	0.5	0.841	0.00682
8	1.461	0.0174	3.5	1.147	0.0081	2	1.001	0.0073	1	0.896	0.00695
6.75	1.375	0.0134	2.5	1.051	0.0075	1.25	0.922	0.007	0	0.797	0.0071
5.25	1.289	0.0101	1.5	0.9485	0.0071	0.25	0.818	0.007	-0.75	0.721	0.0074
4	1.191	0.0085	0.75	0.8683	0.0069	-0.25	0.773	0.0072	-1.25	0.664	0.00812
3.25	1.124	0.0079	0.25	0.8177	0.007	-0.75	0.721	0.0074	-1.75	0.607	0.00863
2.75	1.076	0.0076	0	0.7967	0.0071	-1	0.692	0.0076	-1.75	0.607	0.00863
2.5	1.051	0.0075	0	0.7967	0.0071	-1.25	0.664	0.0081	-2	0.579	0.00878
2.25	1.026	0.0073	0	0.7967	0.0071	-1.25	0.664	0.0081	-2.25	0.551	0.00903
2	1.001	0.0073	0	0.7967	0.0071	-1.25	0.664	0.0081	-2	0.579	0.00878
2.25	1.026	0.0073	0	0.7967	0.0071	-1.25	0.664	0.0081	-2	0.579	0.00878
2.5	1.051	0.0075	0.25	0.8177	0.007	-1.25	0.664	0.0081	-2	0.579	0.00878
2.75	1.076	0.0076	0.5	0.8411	0.0068	-0.75	0.721	0.0074	-1.75	0.554	0.00863
3.5	1.147	0.0081	1	0.8957	0.007	-0.25	0.773	0.0072	0.25	0.67	0.00697
4.5	1.233	0.009	2	1.001	0.0073	1.25	0.922	0.007	1	0.715	0.00695
6.5	1.36	0.0128	3	1.1	0.0077	3.25	0.94	0.0079	3.25	0.814	0.00695
9.5	1.541	0.0221	6.75	1.305	0.0134	7	1.112	0.014	6	0.948	0.0116
14.25	1.693	0.0511	11.75	1.613	0.0319	11.5	1.363	0.0308	11	1.161	0.02614
14.25	1.693	0.0511	12.75	1.672	0.0379	12	1.649	0.0333	11.25	1.516	0.02931
14.25	1.693	0.0511	12.5	1.664	0.0379	12.25	1.652	0.0352	12	1.649	0.03328
-0.75	0.721	0.0074									
0	0.7967	0.0071									
-1	0.6919	0.0076									
-1.5	0.6369	0.0084									
-2	0.5791	0.0088									
-2.25	0.5511	0.009									
-2.5	0.5204	0.0093									
-2.75	0.4925	0.0096									
-2.75	0.4925	0.0096									
-2.75	0.4925	0.0096									
-2.75	0.4925	0.0096									
-2.75	0.4362	0.0096									
-2	0.4664	0.0088									
0	0.575	0.0071									
1	0.6256	0.007									
3	0.6993	0.0077									

Table A.2: Continuation of table A.2

α	C_l	C_d	α	C_l	C_d	α	C_l	C_d	α	C_l	C_d
6.5	0.8208	0.0128									
11.25	0.9998	0.0293									
10.75	1.335	0.0271									
11.25	1.621	0.0293									

A.2 CFD-ANSYS Fluent

A.2.1 Project Layout

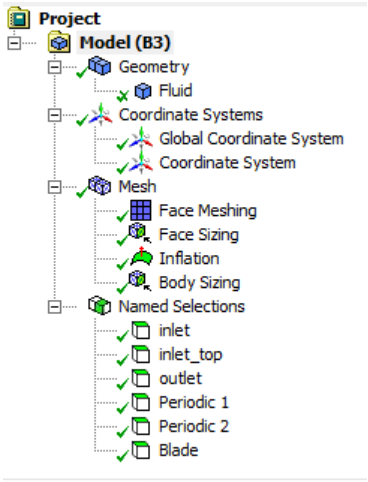

Figure A.1: Project layout

A.2.2 Meshing Details

Display	
Display Style	Body Color
Defaults	
Physics Preference	CFD
Solver Preference	Fluent
Export Format	Standard
Export Preview Surface Mesh	No
Element Order	Linear
Sizing	
Size Function	Proximity and Curvature
Max Face Size	Default (1.52690 m)
Mesh Defeaturing	Yes
Defeature Size	Default (7.6345e-003 m)
Growth Rate	Default (1.20)
Min Size	Default (1.5269e-002 m)
Max Tet Size	Default (3.05380 m)
Curvature Normal Angle	Default (18.0 °)
Proximity Min Size	Default (1.5269e-002 m)
Num Cells Across Gap	Default (3)
Proximity Size Function Sou...	Faces and Edges
Bounding Box Diagonal	30.5380 m
Average Surface Area	97.3020 m²
Minimum Edge Length	0.256080 m
Quality	
Check Mesh Quality	Yes, Errors
Target Skewness	Default (0.900000)
Smoothing	Medium
Mesh Metric	None

Figure A.2: General meshing

Inflation	
Use Automatic Inflation	None
Inflation Option	Smooth Transition
Transition Ratio	0.272
Maximum Layers	5
Growth Rate	1.2
Inflation Algorithm	Pre
View Advanced Options	No
Assembly Meshing	
Method	None
Advanced	
Number of CPUs for Parallel...	Program Controlled
Straight Sided Elements	
Number of Retries	0
Rigid Body Behavior	Dimensionally Reduced
Triangle Surface Mesher	Program Controlled
Topology Checking	Yes
Pinch Tolerance	Default (1.3742e-002 m)
Generate Pinch on Refresh	No
Statistics	
Nodes	463365
Elements	2191755

Figure A.3: General meshing

Scope	
Scoping Method	Geometry Selection
Geometry	2 Faces
Definition	
Suppressed	No
Mapped Mesh	Yes
Constrain Boundary	No
Advanced	
Specified Sides	No Selection
Specified Corners	No Selection
Specified Ends	No Selection

Figure A.4: Face meshing

Scope	
Scoping Method	Named Selection
Named Selection	Blade
Definition	
Suppressed	No
Type	Element Size
Element Size	8.5e-003 m
Advanced	
Defeature Size	Default (4.25e-003 m)
Size Function	Uniform
Behavior	Hard

Figure A.5: Face sizing

Scope	
Scoping Method	Geometry Selection
Geometry	1 Body
Definition	
Suppressed	No
Boundary Scoping Method	Named Selections
Boundary	Blade
Inflation Option	Smooth Transition
Transition Ratio	Default (0.272)
Maximum Layers	5
Growth Rate	1.2
Inflation Algorithm	Pre

Figure A.6: Inflation

Title Page	
Author	
Subject	
Prepared for	
Information	
First Saved	Tuesday, February 26, 2019
Last Saved	Friday, March 1, 2019
Product Version	19.0 Release
Project Data Management	
Save Project Before Solution	No
Save Project After Solution	No

Figure A.7: Sphere of influence

A.2.3 Ansys Fluent General Settings

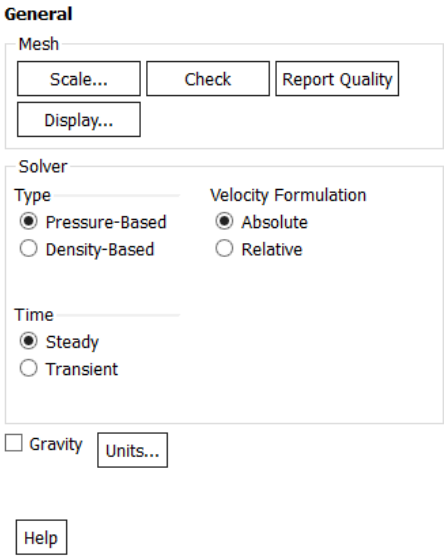

Figure A.8: General settings

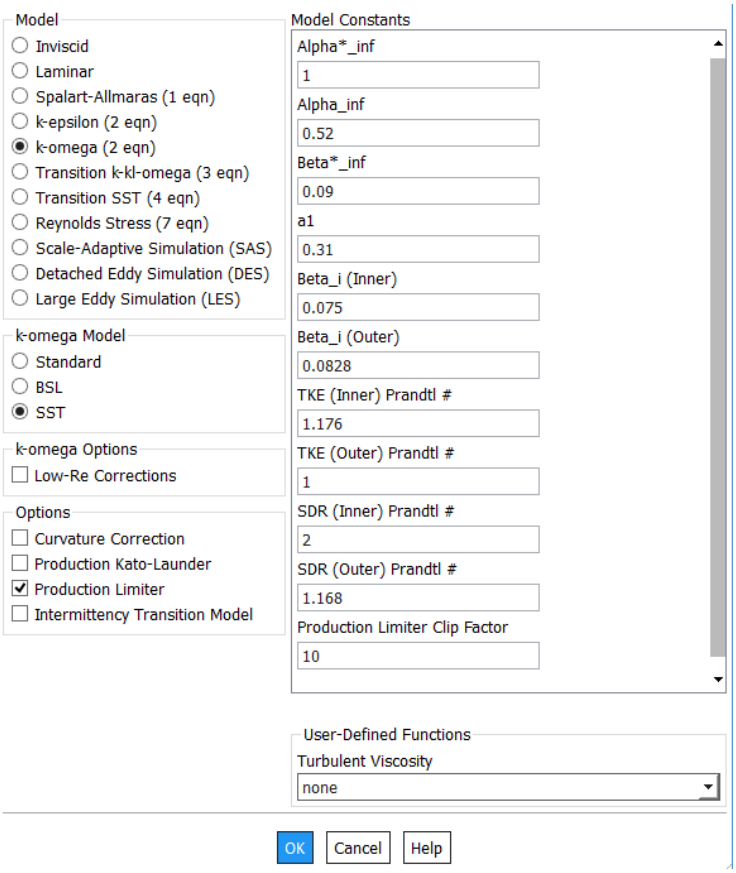

Figure A.9: Turbulence model

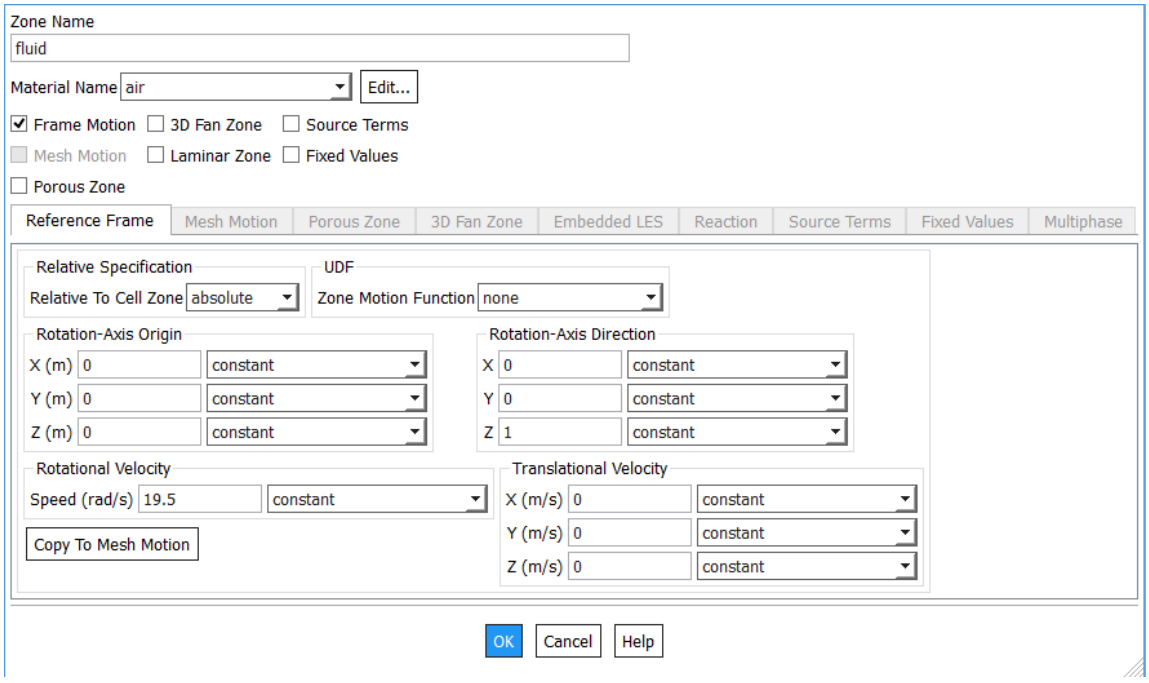

Figure A.10: Cell zone

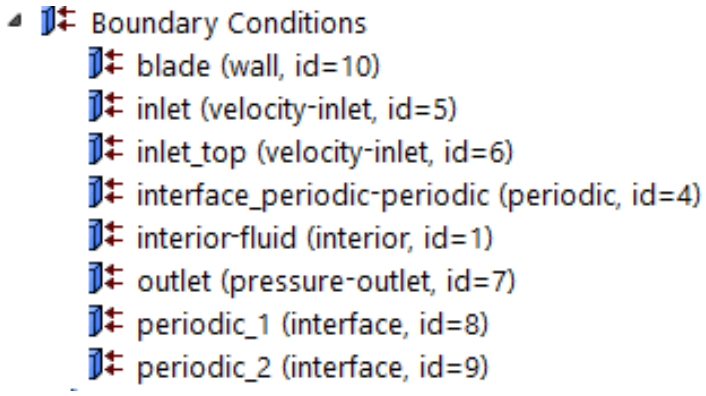

Figure A.11: Boundary conditions

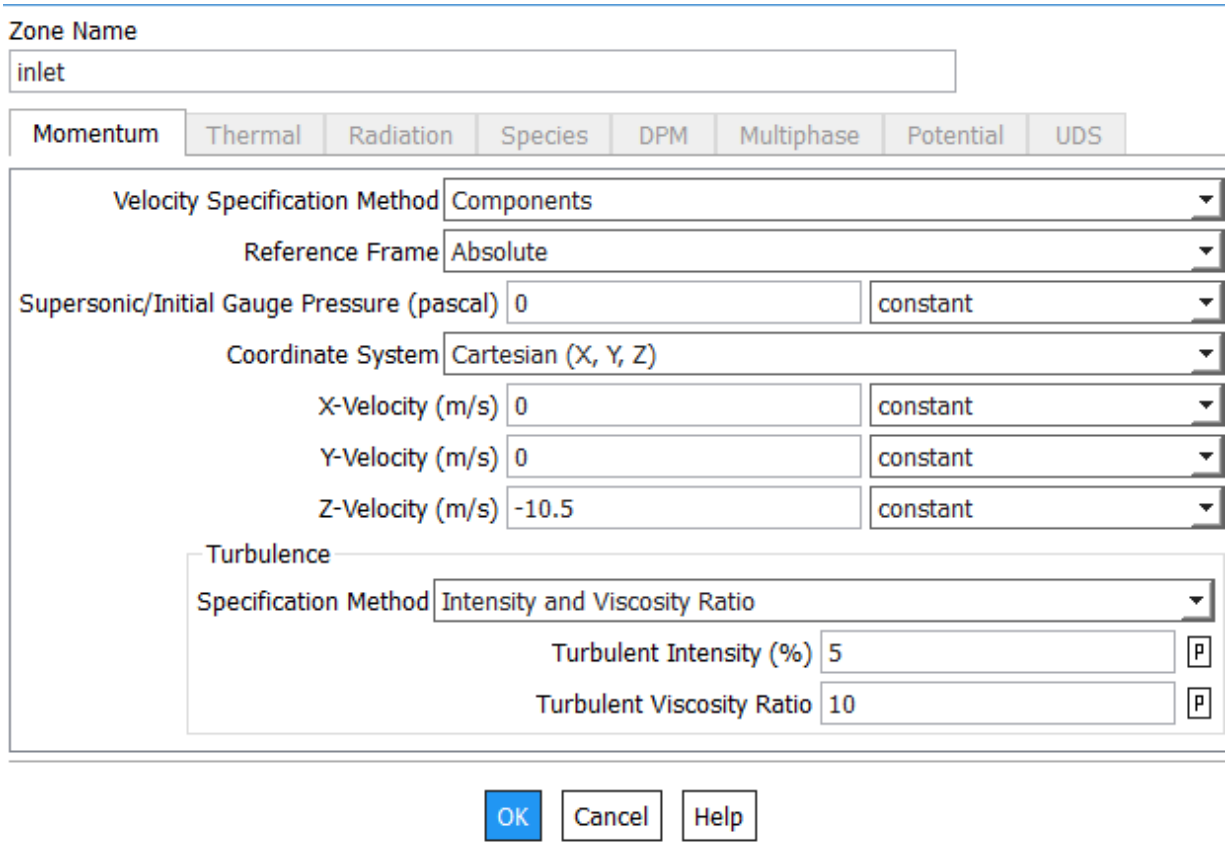

Figure A.12: Inlet boundary conditions

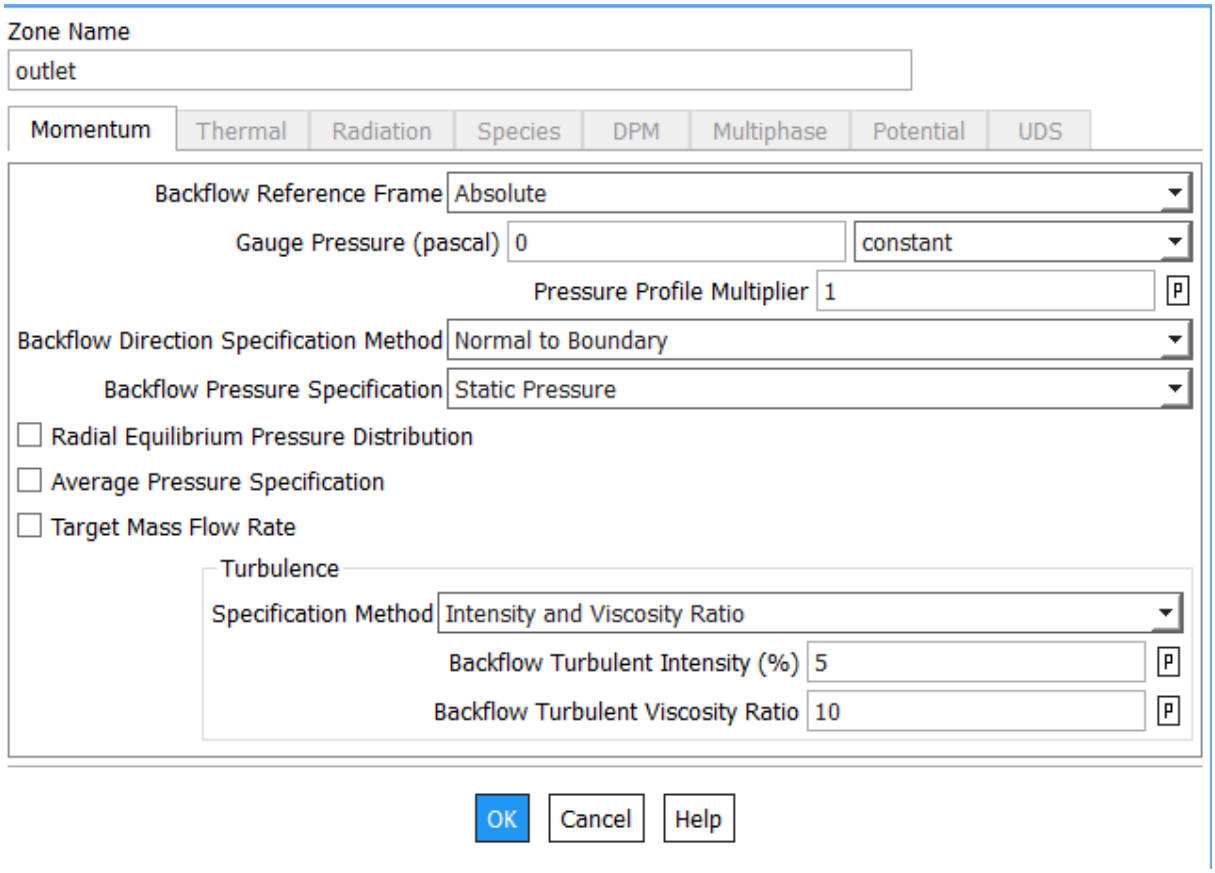

Figure A.13: Outlet boundary conditions

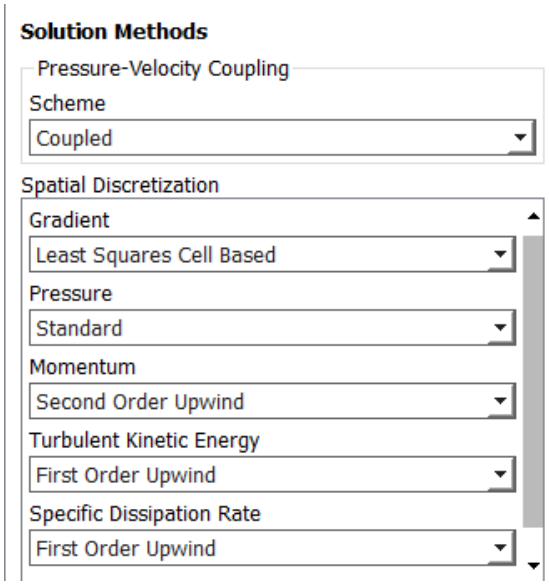

Figure A.14: Solution Method

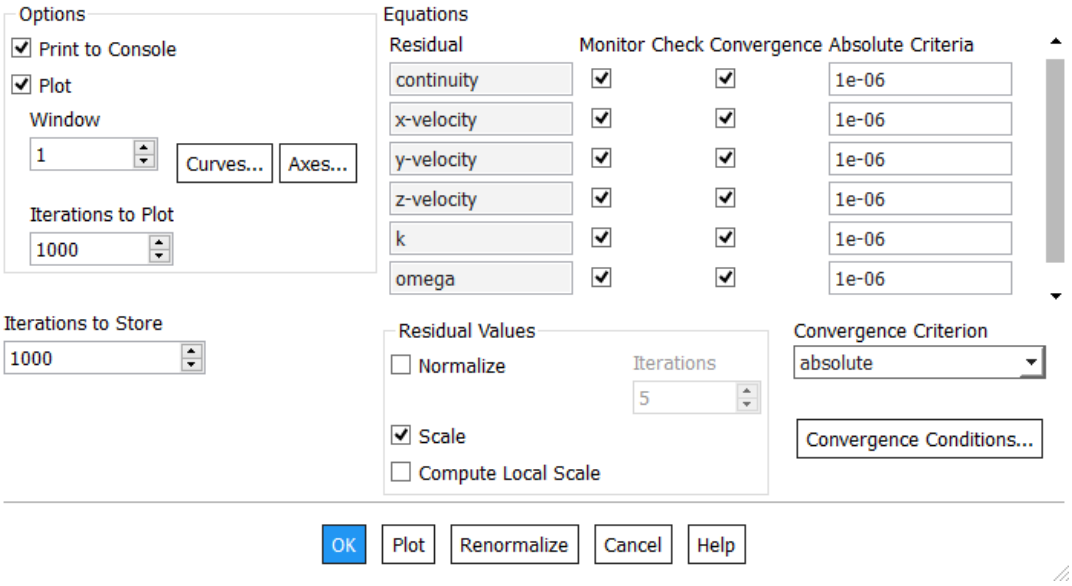

Figure A.15: Residuals

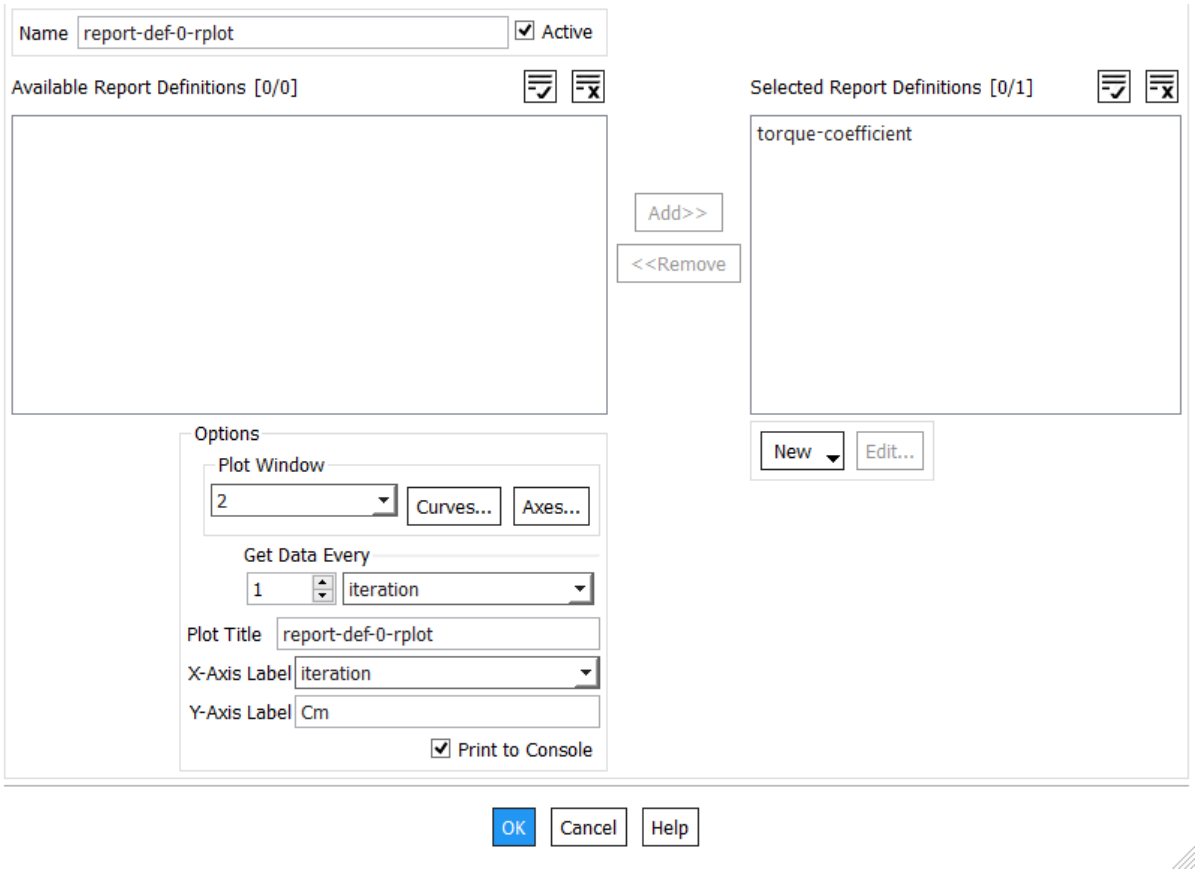

Figure A.16: Torque coefficient

A.3 Blade Optimization Problem

A.3.1 Blade Constraints Function

clear all
clc

function[g,h,gg,gh]=nlcons(x)

$U = 10.5$; %Rated wind speed (m/s)
$eff = 1$; %Efficiency
$Cp = 0.45$; %Power coefficient
$rho\_a = 1.225$; %Air density (kg/mˆ 3)
$U\_e50 = 52.5$; %Extreme wind speed (m/s)
$Cd = 1.5$; %Drag coefficient
$x1 = x(1); x2 = x(2); x3 = x(3);$
$g(1) = -572 * 10^6/3.3 + (10^4/(8.486546 * x1^3)) * (0.25 * Cd * rho\_a * U\_e50^2 * x1 * (x2 - x3)^2);$
$g(2) = 10^4 - 0.5 * rho\_a * pi * Cp * eff * (x2 - x3)^2 * U^3;$
$h = [\,];$

if nargout>2
$gg(1,1) = -(1407374883553280000 * Cd * U\_e50^2 * rho\_a * (x2 - x3)^2)/(2388750337703911 * x1^3);$
$gg(1,2) = (703687441776640000 * Cd * U\_e50^2 * rho\_a * (2 * x2 - 2 * x3))/(2388750337703911 * x1^2);$
$gg(1,3) = -(703687441776640000 * Cd * U\_e50^2 * rho\_a * (2 * x2 - 2 * x3))/(2388750337703911 * x1^2);$
$gg(2,1) = 0;$
$gg(2,2) = -(Cp * U^3 * eff * rho\_a * pi * (2 * x2 - 2 * x3))/2;$
$gg(2,3) = (Cp * U^3 * eff * rho\_a * pi * (2 * x2 - 2 * x3))/2;$
$gh = [\,];$
end

A.3.2 Blade Objective Function

$objective = @(x)6.87 * 10^-2 * x(1)^2 * x(2);$
$x0 = [0.1\ 1\ 0.5];$
$lb = [0.1\ 1\ 0.5];$
$ub = [0.5\ 5\ 0.75];$
$A = [\,];$
$b = [\,];$
$Aeq = [\,];$
$beq = [\,];$
$nonlincon = @nlcons;$
$options = optimoptions(@fmincon,'MaxFunctionEvaluations', 1e6,$

$'MaxIterations', 1e4, 'StepTolerance', 1e-6000, 'OptimalityTolerance', 1e-90000);$
$x = fmincon(objective, x0, A, b, Aeq, beq, lb, ub, nonlincon, options);\ disp(x)$

A.3.3 Tower MatLab Code

Main Program

```
clc
clear
%rho-Density of the tower material in kg/m^3;
%rho_a-Density of air in kg/m^3;
%Sig_y-Tower material yield stress in MPa;
%Sig_u-Tower material ultimate stress in MPa;
%E-Tower material modulus of elasticity stress in GPa;
%m_tw-Mass of the tower in kg;
%m_t-Mass of the turbine in kg;
%H-turbine height in m;
%c-Rotor blade main chord m;
%R-Rotor blade radius in m
%t,t_c-thickness of the tower in m;
%C_d-Drag coefficient;
%A-Elemental cross sectional area of the tower in m^2;
%I-Elemental second moment of area of the tower in m^4;
%d-Elemental tower diameter in m;
%d_h-Tower base diameter in m;
%d_o-Tower top diameter in m;
%U-Wind speed in m/s;
%F-Thrust in N;
%M_0-Moment at the top of the tower in Nm;
%M-Moment at the elemental section in Nm;
%Sig_H- Load case H maximum stress in MPa
%Fa-Buckling load in MPa;
%Fa_B-Load case B buckling load in MPa;
%Fa_A-Load case A buckling load MPa;
%CF_y-Yield stress capacity factor;
%CF_yB-Load case B yield stress capacity factor;
%CF_yA-Load case A yield stress capacity factor;
%CF_BU- Buckling capacity factor;
%CF_BUB- Buckling capacity factor (Load case B);
%CF_BUA- Buckling capacity factor (Load case A);
%d_deflH-Load case H deflection in m;
%d_deflB-Load case B deflection in m;
%d_deflA-Load case A deflection in m;
%f_nHU-Load case H natural frequency 1 rad/s;
%f_nBU-Load case B natural frequency 1 rad/s;
```

```
%f_nAU-Load case A natural frequency 1 rad/s;
%f_n2H-Load case H natural frequency 2 rad/s;
%f_n2B-Load case B natural frequency 2 rad/s;
%f_n2A-Load case A natural frequency 2 rad/s;
%y-Tower element height in m;
%Sig_wH-Load case H stress due to overall weight in MPa;
%Sig_wB-Load case B stress due to overall weight in MPa;
%Sig_wA-Load case A stress due to overall weight in MPa;
%Sig_bH-Loaa case H stress due to bending in MPa;
%Sig_bB-Loaa case B stress due to bending in MPa;
%Sig_bA-Loaa case A stress due to bending in MPa;
%SigH-Load case H total stress in MPa;
%SigB-Load case B total stress in MPa;
%SigA-Load case A total stress in MPa;
%Properties of steel ASTM-A572
rho=7850;
Sig_y=345*10^6;
Sig_u=450*10^6;
E=200*10^9;
R=3.5;
c=0.25;
rho_a=1.225;
H=20;
m_t=438.39;
C_d=1.4;
t=0.002:0.00001:0.01;
d=linspace(0.15,0.75,length(t));
[t,d]=meshgrid(t,d);
A=2/(1+sqrt(2))*(d-t).*t;
I=((10+6*sqrt(2))/(24*(1+sqrt(2))^3))*(d.^4-(d-2*t).^4);
[C,h]=contour(t,d,A);
xlabel('t(m)'),ylabel('d(m)'),zlabel('A(m^2)'),clabel(C),grid
[C,p]=contour(t,d,I);
xlabel('t(m)'),ylabel('d(m)'),zlabel('A(m^2)'),clabel(C),grid
d_h=input('Enter the value of the base diameter in meters; ');
d_0=input('Enter the value of the top diameter in meters; ');
t_c=input('Enter the value of the thickness in meters; ');
d1=(d_h-d_0)/H;
m_tw=((8*rho*t_c)/(1+sqrt(2)))*(((d_h-d_0)*(H^2))/(2*H)+(d_0-t_c)*(H));
N=0;
while N~=1
N=input('Enter #1 to calculate the parameters for load case H: ');
end
U=52.5;
M_0=0;
```

```
F=0.5*C_d*rho_a*U^2*R*c;
[Sig_H,Fa,CF_y,CF_BU,d_deflH,f_nHU,f_n2H]=
tower_design(M_0,F,m_tw,m_t,t_c,U,C_d,rho_a,E,Sig_y,H,d_h,d_0);
fprintf('The tower mass is %5.3f kg\n',m_tw)
fprintf('The maximum buckling factor for load case H is, CF=%5.3f\n',Sig_H/Fa)
fprintf('The maximum stress factor for load case H is, CF=%5.3f\n',Sig_H/Sig_y)
fprintf('The maximum deflection for the load case H is %5.3f m\n',d_deflH)
fprintf('The maximum stress for the load case H is %5.3f MPa\n',Sig_H*10^-6)
fprintf('The natural frequency of turbine+tower for load case H is %5.3a Hz\n',f_nHU/(2*pi))

fprintf('The natural frequency of turbine+0.23tower for the load case H is %5.3f Hz\n',f_n2H/(2*pi))

y=0:0.1:20;
M=M_0+F*y+0.25*C_d*rho_a*U^2*((y.^3).*(d_h-d_0)/(3*H)+d_0*(y.^2));
d=d1*y+d_0;
A=(8/(1+sqrt(2)))*(d-t_c).*t_c;
m_tw=((8*rho*t_c)/(1+sqrt(2)))*(((d_h-d_0)*(y.^2))/(2*H)+(d_0-t_c).*(y));
I=((10+6*sqrt(2))/(24*(1+sqrt(2))^3))*(d.^4-(d-2*t_c).^4);
Sig_wH=(m_tw+m_t)*9.81./A;
Sig_bH=H.*d./(2*I);
SigH=Sig_wg+SiH_bH;
while N~=2
N=input('Enter #2 to calculate the parameters for load case B: ');
end
U=10.5;
M_0=4653;
[Sig_B,Fa_B,CF_yB,CF_BUB,d_deflB,f_nBU,f_n2B]=
tower_design(M_0,F,m_tw,m_t,t_c,U,C_d,rho_a,E,Sig_u,H,d_h,d_0);
fprintf('The maximum buckling factor for load case B is, CF=%5.3f\n',Sig_B/Fa_B)
fprintf('The maximum stress factor for load case B is, CF=%5.3f\n',Sig_B/Sig_y)
fprintf('The maximum deflection for the load case B is %5.3f m\n',d_deflB)
fprintf('The maximum stress for the load case B is %5.3f MPa\n',Sig_B*10^-6)
fprintf('The natural frequency of turbine+tower for the load case B is %5.3f Hz\n',f_nBU/(2*pi))

fprintf('The natural frequency of turbine+0.23tower for the load case B is %5.3f Hz\n',f_n2B/(2*pi))

y=0:0.1:20;
M=M_0+F*y+0.25*C_d*rho_a*U^2*((y.^3).*(d_h-d_0)/(3*H)+d_0*(y.^2));
d=d1*y+d_0;
A=(8/(1+sqrt(2)))*(d-t_c).*t_c;
m_tw=((8*rho*t_c)/(1+sqrt(2)))*(((d_h-d_0)*(y.^2))/(2*H)+(d_0-t_c).*(y));
I=((10+6*sqrt(2))/(24*(1+sqrt(2))^3))*(d.^4-(d-2*t_c).^4);
Sig_wB=(m_twB+m_t)*9.81./A;
Sig_bB=M.*d./(2*I);
SigB=Sig_wB+Sig_bB;
```

```
while N~=3
N=input('Enter #3 to calculate the parameters for load case A: ');
end
U=10.5;
M_0=sqrt(1027^2+450^2+(31452/4)^2);
F=2319;
[Sig_A,Fa_A,CF_yA,CF_BUA,d_deflA,f_nAU,f_n2A]=
tower_design(M_0,F,m_tw,m_t,t_c,U,C_d,rho_a,E,Sig_y,H,d_h,d_0);
fpiintf('The maximum buckling factor for load case B is, CF=%5.3f\n',Sig_A/Fa_A)
firintf('The maximum stress factor for load case H is, CF=%5.3f\n',Sig_A/Sig_y)
fprintf('The maximum deflection for the load case H is %5.3f m\n',d_deflA)
fprintf('The maximum stress for the load case H is %5.3f MPa\n',Sig_A*10^-6)
fprintf('The natural frequency of turbine+tower for the load case H is %5.3f Hz\n',f_nAU/(2*pi))

fprintf('The natural frequency of turbine+0.23tower for the load case H is %5.3f Hz\n',f_n2A/(2*pi))

y=0:0.1:20;
M=M_0+F*y+0.25*C_d*rho_a*U^2*((y.^3).*(d_h-d_0)/(3*H)+d_0*(y.^2));
d=d1*y+d_0;
A=(8/(1+sqrt(2)))*(t-t_c).*d_c;
m_tw=((8*rho*t_c)/(1+sqrt(2)))*(((d_h-d_0)*(y.^2))/(2*H)+(d_0-t_c).*(y));
I=((10+6*sqrt(2))/(24*(1+sqrt(2))^3))*(d.^4-(d-2*t_c).^4);
Sig_wA=(m_tw+m_t)*9.81./A;
Sig_bA=M.*d./(2*I);
SigA=Sig_wA+Sig_bA;
plot(y,SigA*10^-6,'k',y,SigB*10^-6,'k',y,SigH*10^-6,'k')
xlabel('Tower height (m)'),ylabel('Stress (Mpa)'),
gtext('Load Case A'),gtext('Load Case B'),gtext('Load Case H'),grid.
```

Tower Design Function

```
function [Sig,Fa,CF_y,CF_BU,d_defl,f_n,f_n2]=
tower_design(M_0,F,m_tw,m_t,t_c,U,C_d,rho_a,E,Sig_y,H,d_h,d_0)
d1=(d_h-d_0)/H;
A_b=8/(1+sqrt(2))*(d_h-t_c).*t_c;
Sig_w=(m_tw+m_t)*9.81/A_b;
M=M_0+F*H+0.25*C_d*rho_a*U^2*((H^3)*d1/3+d_0*(H^2));
I_b=((10+6*sqrt(2))/(24*(1+sqrt(2))^3))*(d_h.^4-(d_h-2*t_c).^4);
Sig_b=M*d_h/(2*I_b);
Sig=Sig_w+Sig_b;
a=d_h/(1+sqrt(2));
n=a*sqrt(Sig_y*10^-6)/t_c;
if Sig_w<=6.9*10^6
if n<=680
Fa=n;
```

```
elseif n>680&&n<960
Fa=1.42*Sig_y*(1-n*4.34*10^-4);
else
Fa=0.00001;
end
elseif Sig_w>6.9*10^6
if n<=630
Fa=n;
elseif n>630&&n<960
Fa=1.45*Sig_y*(1-n*4.91*10^-4);
else
Fa=0.00001;
end
end
CF_BU=Sig/Fa;
CF_y=Sig/Sig_y;
[s,x]=ode45(@(s,x)deflection(s,x,U,E,C_d,d_h,d_0,H,F,M_0,rho_a,t_c),[0 20],[0 0]);
D_defl=x(:,2);
d_defl=max(D_defl);
F_w=0.25*rho_a*U^2*C_d*H*(d_0+d_h);
Fh=F+F_w;
k_t=Fh/max(d_defl);
f_n=sqrt(k_t/(m_t+m_tw));
f_n2=sqrt(k_t/(m_t+0.23*m_tw));
```

Differential Equation Function

```
function xdot=deflection(s,x,U,E,C_d,d_h,d_0,H,F,M_0,rho_a,t_c)
xdot(1)=x(2);
xdot(2)=(M_0+F*s+0.25*C_d*rho_a*U^2*((s^3)*(d_h-d_0)/
(3*H)+d_0*(s^2)))/(E*(((5+3*sqrt(2))*((((d_h-d_0)/(H))*s+d_0)^4-
(((d_h-d_0)/(H))*s+d_0-2*t_c)^4))/(12*(1+sqrt(2))^3)));
xdot=[xdot(1);xdot(2)];
```

A.4 Tail Design

A.4.1 Tail Equilibrium

Turbine System Equilibrium Transcript Code

```
function[g,h]=nlcons(x)

%g - inequality constraint
%h - equality constraint
```

$\%L1 = x1; L2 = x2; L3 = x3; L4 = x4; L5 = x5; L6 = x6; D\_L3 = x7; psi = x8; beta = x9; gamma = x10; delta = x11; rho = x12; A\_tail = x13; U\_tail = x14; F_r = x15; CD = x17; CL = x16; M_R = x18;$

$x1 = x(1); x2 = x(2); x3 = x(3); x4 = x(4); x5 = x(5); x6 = x(6); x7 = x(7); x8 = x(8); x9 = x(9); x10 = x(10); x11 = x(11); x12 = x(12); x13 = x(13); x14 = x(14); x15 = x(15); x16 = x(16); x17 = x(17); x18 = x(18);$

$g = -((-(cos(x(9))*sin(x(10))*((x(12)*x(13)*x(14)^2*(x(3)+x(7))*(cos(x(8))*cos(x(9))*sin(x(11))+cos(x(11))*sin(x(8))*sin(x(10))+cos(x(8))*cos(x(10))*cos(x(11))*sin(x(9)))*(x(17)*cos(x(8))+x(16)*sin(x(8))+x(16)*cos(x(8))*sin(x(10))*sin(x(11))-x(17)*sin(x(8))*sin(x(10))*sin(x(11))))/2-(x(12)*x(13)*x(14)^2*cos(x(11))*sin(x(10))*(x(3)+x(7))*(x(16)*cos(x(8))-x(17)*sin(x(8)))*(sin(x(8))*sin(x(10))*sin(x(11))-cos(x(8))*cos(x(9))*cos(x(11))+cos(x(8))*cos(x(10))*sin(x(9))*sin(x(11))))/2-(sin(x(9))*sin(x(11))-cos(x(9))*cos(x(10))*cos(x(11)))*((x(12)*x(13)*x(14)^2*(x(3)+x(7))*(cos(x(10))*sin(x(8))-cos(x(8))*sin(x(9))*sin(x(10)))*(x(17)*cos(x(8))+x(16)*sin(x(8))+x(16)*cos(x(8))*sin(x(10))*sin(x(11))-x(17)*sin(x(8))*sin(x(10))*sin(x(11))))/2-(x(12)*x(13)*x(14)^2*cos(x(10))*(x(3)+x(7))*(x(16)*cos(x(8))-x(17)*sin(x(8)))*(sin(x(8))*sin(x(10))*sin(x(11))-cos(x(8))*cos(x(9))*cos(x(11))+cos(x(8))*cos(x(10))*sin(x(9))*sin(x(11))))/2)+(x(12)*x(13)*x(14)^2*cos(x(8))*(x(3)+x(7))*(cos(x(11))*sin(x(9))+cos(x(9))*cos(x(10))*sin(x(11)))^2*(x(16)*cos(x(8))-x(17)*sin(x(8))))/2)/(x(3)*(sin(x(9))*sin(x(11))-cos(x(9))*cos(x(10))*cos(x(11)))*(cos(x(10))*sin(x(8))-cos(x(8))*sin(x(9))*sin(x(10)))-x(3)*cos(x(9))*sin(x(10))*(cos(x(8))*cos(x(9))*sin(x(11))+cos(x(11))*sin(x(8))*sin(x(10))+cos(x(8))*cos(x(10))*cos(x(11))*sin(x(9))));$

$h = x4*x15+(x12*x13*x14^2*(x17*cos(x8)+x16*sin(x8)+sin(x10)*sin(x11)*(x16*cos(x8)-x17*sin(x8)))*(x1-x3*cos(x10)*sin(x8)-x7*cos(x10)*sin(x8)+x3*cos(x8)*sin(x9)*sin(x10)+x7*cos(x8)*sin(x9)*sin(x10)))/2+(x12*x13*x14^2*cos(x10)*(x16*cos(x8)-x17*sin(x8))*(x2*cos(x9)-x3*cos(x8)*(cos(x9)*cos(x11)-cos(x10)*sin(x9)*sin(x11))-x7*cos(x8)*(cos(x9)*cos(x11)-cos(x10)*sin(x9)*sin(x11))+x3*sin(x8)*sin(x10)*sin(x11)+x7*sin(x8)*sin(x10)*sin(x11)))/2;$

end

Turbine System Equilibrium Executable

$P1 = createOptimProblem('fmincon','objective',@(x)-(cos(x(9))*sin(x(10))*((x(12)*x(13)*x(14)^2*(x(3)+x(7))*(cos(x(8))*cos(x(9))*sin(x(11))+cos(x(11))*sin(x(8))*sin(x(10))+cos(x(8))*cos(x(10))*cos(x(11))*sin(x(9)))*(x(17)*cos(x(8))+x(16)*sin(x(8))+x(16)*cos(x(8))*sin(x(10))*sin(x(11))-x(17)*sin(x(8))*sin(x(10))*sin(x(11))))/2-(x(12)*x(13)*x(14)^2*cos(x(11))*sin(x(10))*(x(3)+x(7))*(x(16)*cos(x(8))-x(17)*sin(x(8)))*(sin(x(8))*sin(x(10))*sin(x(11))-cos(x(8))*cos(x(9))*$

$cos(x(11)) + cos(x(8)) * cos(x(10)) * sin(x(9)) * sin(x(11))))/2) - (sin(x(9)) * sin(x(11)) - cos(x(9)) * cos(x(10)) * cos(x(11))) * ((x(12) * x(13) * x(14)^2 * (x(3) + x(7)) * (cos(x(10)) * sin(x(8)) - cos(x(8)) * sin(x(9)) * sin(x(10))) * (x(17) * cos(x(8)) + x(16) * sin(x(8)) + x(16) * cos(x(8)) * sin(x(10)) * sin(x(11)) - x(17) * sin(x(8)) * sin(x(10)) * sin(x(11))))/2 - (x(12) * x(13) * x(14)^2 * cos(x(10)) * (x(3) + x(7)) * (x(16) * cos(x(8)) - x(17) * sin(x(8))) * (sin(x(8)) * sin(x(10)) * sin(x(11)) - cos(x(8)) * cos(x(9)) * cos(x(11)) + cos(x(8)) * cos(x(10)) * sin(x(9)) * sin(x(11))))/2) + (x(12) * x(13) * x(14)^2 * cos(x(8)) * (x(3) + x(7)) * (cos(x(11)) * sin(x(9)) + cos(x(9)) * cos(x(10)) * sin(x(11)))^2 * (x(16) * cos(x(8)) - x(17) * sin(x(8))))/2)/(x(3) * (sin(x(9)) * sin(x(11)) - cos(x(9)) * cos(x(10)) * cos(x(11))) * (cos(x(10)) * sin(x(8)) - cos(x(8)) * sin(x(9)) * sin(x(10))) - x(3) * cos(x(9)) * sin(x(10)) * (cos(x(8)) * cos(x(9)) * sin(x(11)) + cos(x(11)) * sin(x(8)) * sin(x(10)) + cos(x(8)) * cos(x(10)) * cos(x(11)) * sin(x(9)))),$
'nonlcon',@nlcons,'x0',[0.5 0.5 1 0.1 0.75 0.2384 0.4 $4 * pi/180$ $15 * pi/180$ $10 * pi/180$ $5 * pi/180$ 1.225 0.5 10.5 2500 0.5450 0.0118 350],'lb',[0.2 0.2 0.5 0.05 0.25 0.2384 0.01 $5 * pi/180$ $0 * pi/180$ $0 * pi/180$ $0 * pi/180$ 1.225 0.05 10.5 2500 0.5450 0.0118 350],'ub',[1 1 2.5 1 1 0.2384 1 $5 * pi/180$ $30 * pi/180$ $30 * pi/180$ $30 * pi/180$ 1.225 10 10.5 2500 0.5450 0.0118 350],'options',optimset('MaxFunEvals',1e6,'MaxIter',1e6));

P1 =
struct with fields:
objective: [$function\_handle$]
x0: [1×18 *double*]
Aineq: [ ]
bineq: [ ]
Aeq: [ ]
beq: [ ]
lb: [1×18*double*]
ub: [1 1 2.5 1 1 0.2384 1 0.0873 0.5236 0.5236 0.5236 1.225 10 10.5 2500 0.5450 0.0118 350]
nonlcon: @nlcons
solver: 'fmincon'
options: [1×1 *optim.options.Fmincon*]

A.4.2 Turbine System Equilibrium Global Optimization

gs=GlobalSearch;

gs =
GlobalSearch with properties:
NumTrialPoints: 1000
BasinRadiusFactor: 0.2000
DistanceThresholdFactor: 0.7500
MaxWaitCycle: 20
NumStageOnePoints: 200
PenaltyThresholdFactor: 0.2000

Display: 'final'
FunctionTolerance: 1.0000e-06
MaxTime: Inf
OutputFcn: [ ]
PlotFcn: [ ]
StartPointsToRun: 'all'
XTolerance: 1.0000e-06

A.4.3 System Response

Angle Transformation

$function[alfa] = alfa\_one\_circ(alfa)$
$if\ rem(alfa, 360) \geq 0$
$if\ rem(alfa, 360) \geq 180$
$alfa = rem(alfa, 360);$
$else$
$alfa = rem(alfa, 360) - 360;$
end
$else$
$if\ rem(alfa, 360) \geq -180$
$alfa = rem(alfa, 360);$
$else$
$alfa = rem(alfa, 360) + 360;$
end
end

Lift and drag coefficient function

$function[CL, CD] = Tail_C L_C D(alfa)$
$alfa = alfa\_one\_circ(alfa);$
$B = load('naca0006\_Parameters.txt');$
$for\ n = 1 : (length(B(:, 1)) - 1)$
$if\ alfa \geq B(n, 1)\ \&\&\ alfa \leq B(n + 1, 1)$
$CL = (alfa - B(n, 1)) * (B(n + 1, 2) - B(n, 2))/(B(n + 1, 1) - B(n, 1)) + B(n, 2);$
$CD = (alfa - B(n, 1)) * (B(n + 1, 3) - B(n, 3))/(B(n + 1, 1) - B(n, 1)) + B(n, 3);$
$break$
$end\theta$
end

Thrust function

$function[F\_th] = thrust(U)$
$B = load('ThrustvsSpeed.txt');$

$for\ n = 1 : (length(B(:,1)) - 1)$
$if\ U \geq B(n,1)\ \&\&\ U \leq B(n+1,1)$
$F_th = (U - B(n,1)) * (B(n+1,2) - B(n,2))/(B(n+1,1) - B(n,1)) + B(n,2);$
$break$
end
end

Limit moment

$function[M\_lim] = Moment\_lim(x2)$
$y\_up = 30 * pi/180; y\_low = -30 * pi/180; Ks = 5000;$
$if x2 > y\_up$
$M\_lim = -Ks * (x2 - y\_up);$
$elseify_low > x2$
$M\_lim = -Ks * (x2 - y\_low);$
$else$
$M\_lim = 0;$
end

Analytical equations generator

clear
clc
$syms\ x1\ x2\ x3\ x4\ C1\ C2\ C3\ C0\ Fr\_0\ CL\ CD\ M\_lim\ U\ MT\ L1\ L2\ real$
$beta = 0.0842; gamma = 0.2998; delta = 0.4193; miu = 0;$
$L3 = 2.7522; L4 = 0.054; D\_L3 = 0.745; L5 = 0.75; L6 = 0.2384;$
$J\_ot = 330; J\_gy = 353 + 325 * (0.375 - L1)\wedge^2; A\_tail = 1.424; rho = 1.225; g = 9.81;$

%Coordinamate system matrices transformation
$R0 = [cos(x1), sin(x1), 0; -sin(x1), cos(x1), 0; 1, 0, 0];$
$R1 = [1, 0, 0; 0, cos(beta), sin(beta); 0, -sin(beta), cos(beta)];$
$R2 = [cos(gamma), 0, -sin(gamma); 0, 1, 0; sin(gamma), 0, cos(gamma)];$
$R3 = [1, 0, 0; 0, cos(delta), sin(delta); 0, -sin(delta), cos(delta)];$
$R = R1 * R2 * R3;$

%Coordinator system
$x\_B = [1, 0, 0]; y\_B = [0, 1, 0]; z\_B = [0, 0, 1]; x\_C = [1, 0, 0]; y\_C = [0, 1, 0]; z\_C = [0, 0, 1]; x\_A = x\_B; y\_A = y\_B; z\_A = z\_B;$

%Yaw Radius
$r\_T\_B = L1 * x\_B - L2 * cos(beta) * y\_B - L2 * sin(beta) * z\_B - L3 * sin(x2) * (R' * x\_C')' + L3 * cos(x2) * (R' * y\_C')';$
$r\_R\_B = -L4 * x\_B + L5 * y\_B;$
$r\_R\_B2 = -L4 * x\_B + L6 * y\_B;$
$r\_T\_2 = r\_T\_B + (R' * (-D\_L3 * sin(x2) * x\_C' + D\_L3 * cos(x2) * y\_C'))';$

%Furling Radius
$r\_fB\_ae_B = (R' * ((L3 + D\_L3) * cos(x2) * y\_C' - (L3 + D\_L3) * sin(x2) * x\_C'))';$
$r\_fT\_g\_B = (R' * (L3 * cos(x2) * y\_C' - L3 * sin(x2) * x\_C'))';$
$r\_fB\_th\_B = (L5 + L2 * cos(beta)) * y\_B - (L1 + L4) * x\_B + L2 * sin(beta) * z\_B;$
$r\_fB\_g\_B = (L6 + L2 * cos(beta)) * y\_B - (L1 + L4) * x\_B + L2 * sin(beta) * z\_B;$
$r\_fB\_R\_B = -L1 * x\_B + L2 * cos(beta) * y\_B + L2 * sin(beta) * z\_B;$

$J1 = MT * dot((diff(R0', x1) * r\_T\_B'), (diff(R0', x1) * r\_T\_B')) + J\_ot + J\_gy;$
$J2 = MT * dot((R0' * diff(r\_T\_B', x2)), (R0' * diff(r\_T\_B', x2))) + J\_ot;$
$J3 = MT*dot((R0'*diff(r\_T\_B', x2)), (diff(R0', x1)*r\_T\_B')) + J\_ot*(dot(z\_B, (R'*z\_C')'));$

%Forces
$C = (R'*(CL*cos(miu) - CD*sin(miu))*x\_C' + (CL*sin(miu) + CD*cos(miu))*y\_C')';$
$F = 0.5 * rho * U\^2 * A\_tail * C;$
$F\_r\_A = Fr\_0 * cos(miu - x1)\^2 * (cos(x1) * (R0 * y\_A')' + sin(x1) * (R0 * x\_A')');$

%Potential energy
$V = MT * g * (dot(r\_T\_B, z\_B));$

%Moment tail
$M\_ae\_T = dot(cross(r\_T\_2, F), z\_B);$
$M\_ae\_R = dot(cross(r\_R\_B, F\_r\_A), z\_B);$
$Q\_ae = M\_ae\_T + M\_ae\_R;$
$M\_f = dot(cross(r\_fB\_ae\_B, F), (R' * z\_C')');$
$Q\_f = M\_f + M\_lim;$

$f1 = Q\_ae - diff(J3, x2) * x4\^2 - diff(J1, x2) * x3 * x4 + C1 * x3 + C0;$
$f2 = Q\_f - 0.5 * diff(J2, x2) * x4\^2 + 0.5 * diff(J1, x2) * x3\^2 - diff(J3, x1) * x3\^2 - diff(V, x2) + C3 * x4 + C2;$

%Equation of motion
$Eq1 = (J3 * f2 - J2 * f1)/(J3\^2 - J1 * J2);$
$Eq2 = (J3 * f1 - J1 * f2)/(J3\^2 - J1 * J2);$

System mathematical model

```
function xdot=xdot(t,x)
x1=x(1);x2=x(2);x3=x(3);x4=x(4);
C0=0;C1=-100;C2=0;C3=-100;U=10.5+0*sin(t);miu=0*pi/180*sin(t);
MT=35;L1=0.5;L2=0.25;

err=10;
count=0;
```

while $err > 10\hat{} - 9 || count > 1000\ count = count + 1;$
$M\_lim = Moment\_lim(x2);$
$alfa = (miu - x1 - x2) * 180/pi;$
$[CL, CD] = Tail\_CL_CD(alfa);$
$Fr\_0 = thrust(U);$
$b = x2;$
$xdot(1) = x(3);$
$xdot(3) = ((MT * ((cos(x1) * ((11922291920736161 0289 * cos(x2))/ 360287970189639680000 + (4350212399888777169 * sin(x2))/180143985094819 8400) + sin(x1) * ((29604859120706813361 * cos(x2))/11258999068426240000 + (98513293664129735061 * sin(x2))/144115188075855872 0000))^2 + ((4179311912382387957 * cos(x2))/5629499534213120000 - (59379532932789619407 * sin(x2))/ 450359962737049600 00 + sin(x1) * ((11922291920736161 0289 * cos(x2))/ 360287970189639680000 + (4350212399888777169 * sin(x2))/180143985094819 8400) - cos(x1) * ((29604859120706813361 * cos(x2))/11258999068426240000 + (98513293664129735061 * sin(x2))/144115188075855872 0000))^2) + 330) * (C0 + C1 * x3 - (27 * Fr_0 * cos(x1)^2 * (cos(x1)^2 - sin(x1)^2))/500 + (4361 * U^2 * (CD + (8663826699176049 * CL)/72057594037927936) * (L1 + (62590053521218390643 * cos(x2))/ 720575940379279360000 - (18809336770026863543 * sin(x2))/5629499534213120000))/5000 + MT * x4^2 * ((cos(x1) * (L1 + (98513293664129735061 * cos(x2))/144115188075855872 0 - (29604859120706813361 * sin(x2))/11258999068426240000) + sin(x1) * ((8975289213922057 * L2)/9007199254740992 - (4350212399888777169 * cos(x2))/180143985094819 8400 + (11922291920736161 0289 * sin(x2))/360287970189639680000)) * (cos(x1) * ((4350212399888777169 * cos(x2))/ 180143985094819 8400 - (11922291920736161 0289 * sin(x2))/360287970189639680000) + sin(x1) * ((98513293664129735061 * cos(x2))/144115188075855872 0000 - (29604859120706813361 * sin(x2))/11258999068426240000)) - (cos(x1) * ((11922291920736161 0289 * cos(x2))/360287970189639680000 + (4350212399888777169 * sin(x2))/180143985094819 8400) + sin(x1) * ((29604859120706813361 * cos(x2))/ 11258999068426240000 + (98513293664129735061 * sin(x2))/144115188075855872 0000)) * ((4179311912382387957 * cos(x2))/5629499534213120000 - (59379532932789619407 * sin(x2))/450359962737049600 00 + sin(x1) * ((11922291920736161 0289 * cos(x2))/ 360287970189639680000 + (cos(x1) * ((11922291920736161 0289 * cos(x2))/ 360287970189639680000 + (4350212399888777169 * sin(x2))/180143985094819 8400) + sin(x1) * ((29604859120706813361 * cos(x2))/11258999068426240000 + (98513293664129735061 * sin(x2))/144115188075855872 0000)) * (sin(x1) * ((11922291920736161 0289 * cos(x2))/360287970189639680000 + (4350212399888777169 * sin(x2))/180143985094819 8400) - cos(x1) * ((29604859120706813361 * cos(x2))/ 11258999068426240000 + (98513293664129735061 * sin(x2))/144115188075855872 0000)) - (sin(x1) * (L1 + (98513293664129735061 * cos(x2))/144115188075855872 0000 - (29604859120706813361 * sin(x2))/11258999068426240000) - cos(x1) * ((8975289213922057 * L2)/9007199254740992 - (4350212399888777169 * cos(x2))/180143985094819 8400 + (11922291920736161 0289 * sin(x2))/360287970189639680000)) * ((59379532932789619407 * cos(x2))/450359962737049600 00 + (4179311912382387957 * sin(x2))/ 562949953421312000 0 - sin(x1) * ((4350212399888777169 * cos(x2))/

$$180143985094819840000 - (119222919207361610289 * sin(x2))/360287970189639680000) + cos(x1) * ((985132936641297350 61 * cos(x2))/1441151880758558720000 - (29604859120706813361*sin(x2))/11258999068426240000)))+(9382079109468963961*CL*U^2 * ((8975289213922057 * L2)/9007199254740992 - (2763891215189853847 * cos(x2))/900719925474099200 + (75747836830896196407 * sin(x2))/180143985094819840000))/11258999068426240000 - (3 * Fr_0 * cos(x1)^3 * sin(x1))/2 - MT * x3 * x4 * (2 * (cos(x1) * (L1 + (98513293664129735061 * cos(x2))/1441151880758558720000 - (29604859120706813361 * sin(x2))/11258999068426240000) + sin(x1) * ((8975289213922057 * L2)/9007199254740992 - (4350212399888777169 * cos(x2))/180143985094819840000 + (119222919207361610289 * sin(x2))/360287970189639680000)) * (sin(x1) * ((119222919207361610289 * cos(x2))/360287970189639680000 + (4350212399888777169 * sin(x2))/180143985094819840000) - cos(x1) * ((29604859120706813361 * cos(x2))/11258999068426240000 + (98513293664129735061 * sin(x2))/1441151880758558720000)) - 2 * (sin(x1) * (L1 + (98513293664129735061 * cos(x2))/1441151880758558720000 - (29604859120706813361 * sin(x2))/11258999068426240000) - cos(x1) * ((8975289213922057 * L2)/9007199254740992 - (4350212399888777169 * cos(x2))/180143985094819840000 + (119222919207361610289 * sin(x2))/360287970189639680000)) * (cos(x1) * ((119222919207361610289 * cos(x2))/360287970189639680000 + (4350212399888777169 * sin(x2))/180143985094819840000) + sin(x1) * ((29604859120706813361 * cos(x2))/11258999068426240000 + (98513293664129735061 * sin(x2))/1441151880758558720000)))) + (MT * ((cos(x1) * (L1 + (98513293664129735061 * cos(x2))/1441151880758558720000 - (29604859120706813361 * sin(x2))/11258999068426240000) + sin(x1) * ((8975289213922057 * L2)/9007199254740992 - (4350212399888777169 * cos(x2))/180143985094819840000 + (119222919207361610289 * sin(x2))/360287970189639680000)) * (cos(x1) * ((119222919207361610289 * cos(x2))/360287970189639680000 + (4350212399888777169 * sin(x2))/180143985094819840000) + sin(x1) * ((29604859120706813361 * cos(x2))/11258999068426240000 + (98513293664129735061 * sin(x2))/1441151880758558720000)) + (sin(x1) * (L1 + (98513293664129735061 * cos(x2))/1441151880758558720000 - (29604859120706813361 * sin(x2))/11258999068426240000) - cos(x1) * ((8975289213922057 * L2)/9007199254740992 - (4350212399888777169 * cos(x2))/180143985094819840000 + (119222919207361610289 * sin(x2))/360287970189639680000)) * ((4179311912382387957 * cos(x2))/5629499534213120000 - (59379532932789619407 * sin(x2))/4503599627370496000 + sin(x1) * ((119222919207361610289 * cos(x2))/360287970189639680000 + (4350212399888777169 * sin(x2))/180143985094819840000) - cos(x1) * ((29604859120706813361 * cos(x2))/11258999068426240000 + (98513293664129735061 * sin(x2))/1441151880758558720000))) - 606160741091217/2199023255552) * (C2 + M_lim + C3 * x4 - (981 * MT * ((4179311912382387957 * cos(x2))/5629499534213120000 - (59379532932789619407*sin(x2))/4503599627370496000))/100 - MT*x3^2*((cos(x1)*(L1+(98513293664129735061 * cos(x2))/1441151880758558720000 - (29604859120706813361*sin(x2))/11258999068426240000) + sin(x1)*((8975289213922057*L2)/9007199254740992 - (4350212399888777169 * cos(x2))/180143985094819840000 + (119222919207361610289 * sin(x2))/360287970189639680000)) * (sin(x1) * ((119222919207361610289 * cos(x2))/360287970189639680000 + (4350212399888777169 * sin(x2))/180143985094819840000) - cos(x1) * ((29604859120706813361 * cos(x2))/$$

$$1125899906842624000 + (98513293664129735061 * sin(x2))/144115188075855872000)) - (cos(x1) * (L1 + (98513293664129735061 * cos(x2))/144115188075855872000 - (29604859120706813361 * sin(x2))/1125899906842624000) + sin(x1) * ((8975289213922057 * L2)/9007199254740992 - (4350212399888777169 * cos(x2))/1801439850948198400 + (119222919207361610289 * sin(x2))/360287970189639680000)) * ((4179311912382387957 * cos(x2))/5629499534213120000 - (59379532932789619407 * sin(x2))/45035996273704960000 + sin(x1) * ((119222919207361610289 * cos(x2))/360287970189639680000 + (4350212399888777169 * sin(x2))/1801439850948198400) - cos(x1) * ((29604859120706813361 * cos(x2))/1125899906842624000 + (98513293664129735061 * sin(x2))/144115188075855872000))) + (MT * x4^2 * (2 * ((4179311912382387957 * cos(x2))/5629499534213120000 - (59379532932789619407 * sin(x2))/45035996273704960000 + sin(x1) * ((119222919207361610289 * cos(x2))/360287970189639680000 + (4350212399888777169 * sin(x2))/1801439850948198400) - cos(x1) * ((29604859120706813361 * cos(x2))/1125899906842624000 + (98513293664129735061 * sin(x2))/144115188075855872000)) * ((59379532932789619407 * cos(x2))/45035996273704960000 + (4179311912382387957 * sin(x2))/5629499534213120000 - sin(x1) * ((4350212399888777169 * cos(x2))/1801439850948198400 - (119222919207361610289 * sin(x2))/360287970189639680000) + cos(x1) * ((98513293664129735061 * cos(x2))/144115188075855872000 - (29604859120706813361 * sin(x2))/1125899906842624000)) - 2 * (cos(x1) * ((4350212399888777169 * cos(x2))/1801439850948198400 - (119222919207361610289 * sin(x2))/360287970189639680000) + sin(x1) * ((98513293664129735061 * cos(x2))/144115188075855872000 - (29604859120706813361 * sin(x2))/1125899906842624000)) * (cos(x1) * ((119222919207361610289 * cos(x2))/360287970189639680000 + (4350212399888777169 * sin(x2))/1801439850948198400) + sin(x1) * ((29604859120706813361 * cos(x2))/1125899906842624000 + (98513293664129735061 * sin(x2))/144115188075855872000))))/2 + (32811032723689316649 * U^2 * ((62590053521218390643 * cos(x2))/720575940379279360000 - (18809336770026863543 * sin(x2))/5629499534213120000) * (CD + (8663826699176049 * CL)/72057594037927936))/45035996273704960000 - (23119094775128810843 * U^2 * ((37726564670545719241 * cos(x2))/22517998136852480000 + (2655310228178127891 * sin(x2))/2814749767106560000) * (CD + (8663826699176049 * CL)/72057594037927936))/900719925474099200000 + (MT * x3^2 * (2 * (cos(x1) * (L1 + (98513293664129735061 * cos(x2))/144115188075855872000 - (29604859120706813361 * sin(x2))/1125899906842624000) + sin(x1) * ((8975289213922057 * L2)/9007199254740992 - (4350212399888777169 * cos(x2))/1801439850948198400 + (119222919207361610289 * sin(x2))/360287970189639680000)) * (sin(x1) * ((119222919207361610289 * cos(x2))/360287970189639680000 + (4350212399888777169 * sin(x2))/1801439850948198400) - cos(x1) * ((29604859120706813361 * cos(x2))/1125899906842624000 + (98513293664129735061 * sin(x2))/144115188075855872000)) - 2 * (sin(x1) * (L1 + (98513293664129735061 * cos(x2))/144115188075855872000 - (29604859120706813361 * sin(x2))/1125899906842624000) - cos(x1) * ((8975289213922057 * L2)/9007199254740992 - (4350212399888777169 * cos(x2))/1801439850948198400 + (119222919207361610289 * sin(x2))/360287970189639680000)) * (cos(x1) * ((119222919207361610289 * cos(x2))/360287970189639680000 + (4350212399888777169 * sin(x2))/1801439850948198400) +$$

$sin(x1) * ((29604859120706813361 * cos(x2))/11258999068426240000 + (98513293664129735061 * sin(x2))/1441151880758558720000))))/2 - (97012200202285139730881009856348 3 * CL * U^2 * ((2763891215189853847 * cos(x2))/900719925474099200 - (75747836830896196407 * sin(x2))/18014398509481984000))/126765060022822940149670320537600 0 - (554015582862242531835129350972072 7 * CL * U^2 * ((62590053521218390643 * cos(x2))/720575940379279360000 - (18809336770026863543 * sin(x2))/5629499534213120000))/5070602400912917605986812821504000 0 - (39244625969932379872663585320030571 * CL * U^2 * ((37726564670545719241 * cos(x2))/22517998136852480000 + (2655310228178127891 * sin(x2))/2814749767106560000))/10141204801825835211973625643008000 0))/((MT * ((cos(x1) * ((119222919207361610289 * cos(x2))/360287970189639680000 + (4350212399888777169 * sin(x2))/1801439850948198400) + sin(x1) * ((29604859120706813361 * cos(x2))/11258999068426240000 + (98513293664129735061 * sin(x2))/144115188075855872000 0))^2 + ((4179311912382387957 * cos(x2))/5629499534213120000 - (59379532932789619407 * sin(x2))/45035996273704960000 + sin(x1) * ((119222919207361610289 * cos(x2))/360287970189639680000 + (4350212399888777169 * sin(x2))/1801439850948198400) - cos(x1) * ((29604859120706813361 * cos(x2))/11258999068426240000 + (98513293664129735061 * sin(x2))/144115188075855872000 0))^2) + 330) * (325 * (L1 - 3/8)^2 + MT * ((cos(x1) * (L1 + (98513293664129735061 * cos(x2))/144115188075855872000 - (29604859120706813361 * sin(x2))/11258999068426240000) + sin(x1) * ((8975289213922057 * L2)/9007199254740992 - (4350212399888777169 * cos(x2))/1801439850948198400 + (119222919207361610289 * sin(x2))/360287970189639680000))^2 + (sin(x1) * (L1 + (98513293664129735061 * cos(x2))/144115188075855872000 - (29604859120706813361 * sin(x2))/11258999068426240000) - cos(x1) * ((8975289213922057 * L2)/9007199254740992 - (4350212399888777169 * cos(x2))/1801439850948198400 + (119222919207361610289 * sin(x2))/360287970189639680000))^2) + 683) - (MT * ((cos(x1) * (L1 + (98513293664129735061 * cos(x2))/144115188075855872000 - (29604859120706813361 * sin(x2))/11258999068426240000) + sin(x1) * ((8975289213922057 * L2)/9007199254740992 - (4350212399888777169 * cos(x2))/1801439850948198400 + (119222919207361610289 * sin(x2))/360287970189639680000)) * (cos(x1) * ((119222919207361610289 * cos(x2))/360287970189639680000 + (4350212399888777169 * sin(x2))/1801439850948198400) + sin(x1) * ((29604859120706813361 * cos(x2))/11258999068426240000 + (98513293664129735061 * sin(x2))/144115188075855872000)) + (sin(x1) * (L1 + (98513293664129735061 * cos(x2))/144115188075855872000 - (29604859120706813361 * sin(x2))/11258999068426240000) - cos(x1) * ((8975289213922057 * L2)/9007199254740992 - (4350212399888777169 * cos(x2))/1801439850948198400 + (119222919207361610289 * sin(x2))/360287970189639680000)) * ((4179311912382387957 * cos(x2))/5629499534213120000 - (59379532932789619407 * sin(x2))/45035996273704960000 + sin(x1) * ((119222919207361610289 * cos(x2))/360287970189639680000 + (4350212399888777169 * sin(x2))/1801439850948198400) - cos(x1) * ((29604859120706813361 * cos(x2))/11258999068426240000 + (98513293664129735061 * sin(x2))/144115188075855872000))) - 606160741091217/2199023255552)^2)$

$xdot(2) = x(4);$

$$xdot(4) = ((325 * (L1 - 3/8)^2 + MT * ((cos(x1) * (L1 + (98513293664129735061 * cos(x2))/ 144115188807585587200000 - (29604859120706813361 * sin(x2))/11258999068426240000) + sin(x1) * ((8975289213922057 * L2)/9007199254740992 - (4350212399888777169 * cos(x2))/ 1801439850948198400 + (119222919207361610289 * sin(x2))/360287970189639680000))^2 + (sin(x1) * (L1 + (98513293664129735061 * cos(x2))/144115188807585587200000 - (29604859120706813361 * sin(x2))/11258999068426240000) - cos(x1) * ((8975289213922057 * L2)/9007199254740992 - (4350212399888777169 * cos(x2))/1801439850948198400 + (119222919207361610289 * sin(x2))/360287970189639680000))^2) + 683) * (C2 + M\_lim + C3 * x4 - (981 * MT * ((4179311912382387957 * cos(x2))/56294995342131200000 - (59379532932789619407 * sin(x2))/45035996273704960000))/100 - MT * x3^2 * ((cos(x1) * (L1 + (98513293664129735061 * cos(x2))/144115188807585587200000 - (29604859120706813361 * sin(x2))/11258999068426240000) + sin(x1) * ((8975289213922057 * L2)/9007199254740992 - (4350212399888777169 * cos(x2))/1801439850948198400 + (119222919207361610289 * sin(x2))/360287970189639680000)) * (sin(x1) * ((119222919207361610289 * cos(x2))/ 360287970189639680000 + (4350212399888777169 * sin(x2))/1801439850948198400) - cos(x1) * ((29604859120706813361 * cos(x2))/11258999068426240000 + (98513293664129735061 * sin(x2))/144115188807585587200000)) - (cos(x1) * (L1 + (98513293664129735061 * cos(x2))/ 144115188807585587200000 - (29604859120706813361 * sin(x2))/11258999068426240000) + sin(x1) * ((8975289213922057 * L2)/9007199254740992 - (4350212399888777169 * cos(x2))/ 1801439850948198400 + (119222919207361610289 * sin(x2))/360287970189639680000)) * ((4179311912382387957 * cos(x2))/56294995342131200000 - (59379532932789619407 * sin(x2))/ 45035996273704960000 + sin(x1) * ((119222919207361610289 * cos(x2))/ 360287970189639680000 + (4350212399888777169 * sin(x2))/1801439850948198400) - cos(x1) * ((29604859120706813361 * cos(x2))/11258999068426240000 + (98513293664129735061 * sin(x2))/144115188807585587200000))) + (MT * x4^2 * (2 * ((4179311912382387957 * cos(x2))/ 56294995342131200000 - (59379532932789619407 * sin(x2))/45035996273704960000 + sin(x1) * ((119222919207361610289 * cos(x2))/360287970189639680000 + (4350212399888777169 * sin(x2))/1801439850948198400) - cos(x1) * ((29604859120706813361 * cos(x2))/ 11258999068426240000 + (98513293664129735061 * sin(x2))/144115188807585587200000)) * ((59379532932789619407 * cos(x2))/45035996273704960000 + (4179311912382387957 * sin(x2))/ 56294995342131200000 - sin(x1) * ((4350212399888777169 * cos(x2))/1801439850948198400 - (119222919207361610289 * sin(x2))/360287970189639680000) + cos(x1) * ((98513293664129735061 * cos(x2))/144115188807585587200000 - (29604859120706813361 * sin(x2))/11258999068426240000)) - 2 * (cos(x1) * ((4350212399888777169 * cos(x2))/ 1801439850948198400 - (119222919207361610289 * sin(x2))/360287970189639680000) + sin(x1) * ((98513293664129735061 * cos(x2))/144115188807585587200000 - (29604859120706813361 * sin(x2))/11258999068426240000)) * (cos(x1) * ((119222919207361610289 * cos(x2))/360287970189639680000 + (4350212399888777169 * sin(x2))/1801439850948198400) + sin(x1) * ((29604859120706813361 * cos(x2))/ 11258999068426240000 + (98513293664129735061 * sin(x2))/144115188807585587200000))))/2 + (32811032723689316649 * U^2 * ((625900535212183906 43 * cos(x2))/72057594037927936000 - (18809336770026863543 * sin(x2))/562949534213120000) * (CD + (8663826699176049 * CL)/ 72057594037927936))/45035996273704960000 - (23119094775128810843 * U^2 * ((37726564670545719241 * cos(x2))/22517998136852480000 + (26553102281781278 91 * sin(x2)) /2814749767106560000) * (CD + (8663826699176049 * CL)/72057594037927936))/$$

$$9007199254740992 + (MT * x3^2 * (2 * (cos(x1) * (L1 + (98513293664129735061 * cos(x2))/144115188075855872000 - (29604859120706813361 * sin(x2))/11258999068426240000) + sin(x1) * ((8975289213922057 * L2)/9007199254740992 - (4350212399888777169*cos(x2))/180143985094819840+(119222919207361610289*sin(x2))/360287970189639680000)) * (sin(x1) * ((119222919207361610289 * cos(x2))/360287970189639680000+(4350212399888777169*sin(x2))/180143985094819840)-cos(x1)*((29604859120706813361 * cos(x2))/11258999068426240000 + (98513293664129735061 * sin(x2))/144115188075855872000)) - 2 * (sin(x1) * (L1 + (98513293664129735061 * cos(x2))/144115188075855872000 - (29604859120706813361 * sin(x2))/11258999068426240000) - cos(x1) * ((8975289213922057 * L2)/9007199254740992 - (4350212399888777169*cos(x2))/180143985094819840+(119222919207361610289*sin(x2))/360287970189639680000)) * (cos(x1) * ((119222919207361610289 * cos(x2))/360287970189639680000+(4350212399888777169*sin(x2))/180143985094819840)+sin(x1)*((29604859120706813361 * cos(x2))/11258999068426240000 + (98513293664129735061 * sin(x2))/144115188075855872000))))/2-(97012200202285139730881009856348 3*CL*U^2*((2763891215189853847*cos(x2))/90071992547409920-(75747836830896196407*sin(x2))/180143985094819840000))/126765060022822940149670320537600 0 - (554015582862242531835129350972072 7 * CL * U^2 * ((62590053521218390643 * cos(x2))/72057594037927936000 - (18809336770026863543 * sin(x2))/5629499534213120000))/507060240091291760598681282150400 00 - (392446259699323798726635853200305 71 * CL * U^2 * ((37726564670545719241 * cos(x2))/22517998136852480000 + (2655310228178127891 * sin(x2))/2814749767106560000))/10141204801825835211973625643008000 0) + (MT * ((cos(x1) * (L1 + (98513293664129735061 * cos(x2))/144115188075855872000 - (29604859120706813361 * sin(x2))/11258999068426240000) + sin(x1) * ((8975289213922057 * L2)/9007199254740992 - (4350212399888777169 * cos(x2))/180143985094819840 + (119222919207361610289 * sin(x2))/360287970189639680000)) * (cos(x1) * ((119222919207361610289 * cos(x2))/360287970189639680000 + (4350212399888777169 * sin(x2))/180143985094819840) + sin(x1) * ((29604859120706813361 * cos(x2))/11258999068426240000 + (98513293664129735061 * sin(x2))/144115188075855872000)) + (sin(x1) * (L1 + (98513293664129735061 * cos(x2))/144115188075855872000 - (29604859120706813361 * sin(x2))/11258999068426240000) - cos(x1) * ((8975289213922057 * L2)/9007199254740992 - (4350212399888777169 * cos(x2))/180143985094819840 + (119222919207361610289 * sin(x2))/360287970189639680000)) * ((4179311912382387957 * cos(x2))/5629499534213120000-(59379532932789619407*sin(x2))/450359962737049600+ sin(x1) * ((119222919207361610289 * cos(x2))/360287970189639680000 + (4350212399888777169*sin(x2))/180143985094819840)-cos(x1)*((29604859120706813361* cos(x2))/11258999068426240000 + (98513293664129735061 * sin(x2))/144115188075855872000))) - 606160741091217/2199023255552) * (C0 + C1 * x3 - (27 * Fr_0 * cos(x1)^2 * (cos(x1)^2 - sin(x1)^2))/500 + (4361 * U^2 * (CD + (8663826699176049 * CL)/72057594037927936)*(L1+(625900535212183906 43*cos(x2))/72057594037927936000-(18809336770026863543*sin(x2))/5629499534213120000))/5000+MT*x4^2*((cos(x1)*(L1+(98513293664129735061 * cos(x2))/144115188075855872000 - (29604859120706813361 * sin(x2))/11258999068426240000)+sin(x1)*((8975289213922057*L2)/9007199254740992-(4350212399888777169 * cos(x2))/180143985094819840 + (119222919207361610289 * sin(x2))/360287970189639680000)) * (cos(x1) * ((4350212399888777169 * cos(x2))/$$

$$180143985094819840 - (11922291920736161 0289 * sin(x2))/360287970189639680000) + sin(x1) * ((98513293664129735061 * cos(x2))/1441151880758558720000 - (29604859120706813361 * sin(x2))/11258999068426240000)) - (cos(x1) * ((11922291920736161 0289 * cos(x2))/360287970189639680000 + (4350212399888777169 * sin(x2))/180143985094819840 0) + sin(x1) * ((29604859120706813361 * cos(x2))/11258999068426240000 + (98513293664129735061 * sin(x2))/1441151880758558720000)) * ((4179311912382387957 * cos(x2))/5629499534213120000 - (59379532932789619407 * sin(x2))/45035996273704960000 + sin(x1) * ((11922291920736161 0289 * cos(x2))/360287970189639680000+(4350212399888777169 * sin(x2))/180143985094819840 0) - cos(x1) * ((29604859120706813361 * cos(x2))/11258999068426240000 + (98513293664129735061 * sin(x2))/1441151880758558720000)) + (cos(x1) * ((11922291920736161 0289 * cos(x2))/360287970189639680000+(4350212399888777169 * sin(x2))/180143985094819840 0)+sin(x1) * ((29604859120706813361 * cos(x2))/11258999068426240000 + (98513293664129735061 * sin(x2))/1441151880758558720000)) * (sin(x1) * ((11922291920736161 0289 * cos(x2))/360287970189639680000+(4350212399888777169 * sin(x2))/180143985094819840 0) - cos(x1) * ((29604859120706813361 * cos(x2))/11258999068426240000 + (98513293664129735061 * sin(x2))/1441151880758558720000)) - (sin(x1) * (L1 + (98513293664129735061 * cos(x2))/1441151880758558720000 - (29604859120706813361 * sin(x2))/11258999068426240000) - cos(x1) * ((8975289213922057 * L2)/9007199254740992 - (4350212399888777169 * cos(x2))/180143985094819840 0 + (11922291920736161 0289 * sin(x2))/360287970189639680000)) * ((59379532932789619407 * cos(x2))/45035996273704960000+(4179311912382387957 * sin(x2))/5629499534213120000 - sin(x1) * ((4350212399888777169 * cos(x2))/180143985094819840 0 - (11922291920736161 0289 * sin(x2))/360287970189639680000) + cos(x1) * ((98513293664129735061 * cos(x2))/1441151880758558720000 - (29604859120706813361 * sin(x2))/11258999068426240000)))+(9382079109468963961 * CL * U^2 * ((8975289213922057 * L2)/9007199254740992 - (2763891215189853847 * cos(x2))/900719925474099200 + (75747836830896196407 * sin(x2))/180143985094819840 0))/11258999068426240000 - (3 * Fr_0 * cos(x1)^3 * sin(x1))/2 - MT * x3 * x4 * (2 * (cos(x1) * (L1 + (98513293664129735061 * cos(x2))/1441151880758558720000 - (29604859120706813361 * sin(x2))/11258999068426240000) + sin(x1) * ((8975289213922057 * L2)/9007199254740992 - (4350212399888777169 * cos(x2))/180143985094819840+(11922291920736161 0289 * sin(x2))/360287970189639680000)) * (sin(x1) * ((11922291920736161 0289 * cos(x2))/360287970189639680000+(4350212399888777169 * sin(x2))/180143985094819840 0) - cos(x1) * ((29604859120706813361 * cos(x2))/11258999068426240000 + (98513293664129735061 * sin(x2))/1441151880758558720000)) - 2 * (sin(x1) * (L1 + (98513293664129735061 * cos(x2))/1441151880758558720000 - (29604859120706813361 * sin(x2))/11258999068426240000) - cos(x1) * ((8975289213922057 * L2)/9007199254740992 - (4350212399888777169 * cos(x2))/180143985094819840 0 + (11922291920736161 0289 * sin(x2))/360287970189639680000)) * (cos(x1) * ((11922291920736161 0289 * cos(x2))/360287970189639680000 + (4350212399888777169 * sin(x2))/180143985094819840 0)+sin(x1) * ((29604859120706813361 * cos(x2))/11258999068426240000 + (98513293664129735061 * sin(x2))/1441151880758558720000)))))/((MT * ((cos(x1) * ((11922291920736161 0289 * cos(x2))/360287970189639680000+(4350212399888777169 * sin(x2))/180143985094819840 0)+sin(x1) * ((29604859120706813361 * cos(x2))/11258999068426240000 + (98513293664129735061 * sin(x2))/1441151880758558720000))^2 + ((4179311912382387957 * cos(x2))/$$

$5629499534213120000 - (59379532932789619407 * sin(x2))/45035996273704960000 + sin(x1) * ((119222919207361610289 * cos(x2))/360287970189639680000 + (435021239988877716 9*sin(x2))/180143985094819840 0)-cos(x1)*((29604859120706813361*cos(x2))/1125899906842624000 0 + (985132936641297350 61 * sin(x2))/144115188075855872 0000))^2) + 330) * (325 * (L1 - 3/8)^2 + MT * ((cos(x1) * (L1 + (985132936641297350 61 * cos(x2))/144115188075855872 0000 - (29604859120706813361 * sin(x2))/1125899906842624 0000)+sin(x1)*((8975289213922057*L2)/9007199254740992-(435021239988877716 9 * cos(x2))/180143985094819840 0 + (119222919207361610289 * sin(x2))/360287970189639680000))^2 + (sin(x1) * (L1 + (985132936641297350 61 * cos(x2))/144115188075855872 0000 - (29604859120706813361 * sin(x2))/1125899906842624 0000) - cos(x1) * ((8975289213922057 * L2)/9007199254740992 - (435021239988877716 9 * cos(x2))/180143985094819840 0 + (119222919207361610289 * sin(x2))/360287970189639680000))^2) + 683)-(MT*((cos(x1)*(L1+(985132936641297350 61*cos(x2))/144115188075855872 0000-(29604859120706813361*sin(x2))/1125899906842624 0000)+sin(x1)*((8975289213922057* L2)/9007199254740992 - (435021239988877716 9 * cos(x2))/180143985094819840 0 + (119222919207361610289 * sin(x2))/360287970189639680000)) * (cos(x1) * ((119222919207361610289 * cos(x2))/360287970189639680000 + (435021239988877716 9 * sin(x2))/180143985094819840 0) + sin(x1) * ((29604859120706813361 * cos(x2))/1125899906842624 0000 + (985132936641297350 61 * sin(x2))/144115188075855872 0000)) + (sin(x1) * (L1 + (985132936641297350 61 * cos(x2))/144115188075855872 0000 - (29604859120706813361 * sin(x2))/1125899906842624 0000) - cos(x1) * ((8975289213922057 * L2)/9007199254740992 - (435021239988877716 9 * cos(x2))/180143985094819840 0 + (119222919207361610289 * sin(x2))/360287970189639680000)) * ((417931191238238795 7*cos(x2))/5629499534213120000-(59379532932789619407*sin(x2))/45035996273704960000 + sin(x1) * ((119222919207361610289 * cos(x2))/360287970189639680000+(435021239988877716 9*sin(x2))/180143985094819840 0)-cos(x1)*((29604859120706813361 * cos(x2))/1125899906842624 0000 + (985132936641297350 61 * sin(x2))/144115188075855872 0000))) - 606160741091217/2199023255552)^2);$
$err = abs(b - x2);$
end

$xdot = [xdot(1); xdot(2); xdot(3); xdot(4)];$

Final differential equation program

clear
clc
close all
$[t, x] = ode15s(@xdot, [0, 120], [0, 4.5 * pi/180, 0, 0]);$
$plot(t, x(:, 1) * 180/pi,' bl', t, x(:, 2) * 180/pi,' red', t, 30 * sin(t)), axis([0, 120, -50, 50]), grid$

Table A.3: Thrust vs wind speed

Wind speed	Thrust
1.00E-02	0.00E+00
5.10E-01	0.00E+00
1.01E+00	4.41E+01
1.51E+00	8.94E+01
2.01E+00	1.47E+02
2.51E+00	2.15E+02
3.01E+00	2.93E+02
3.51E+00	3.81E+02
4.01E+00	4.80E+02
4.51E+00	5.88E+02
5.01E+00	7.06E+02
5.51E+00	8.33E+02
6.01E+00	9.67E+02
6.51E+00	1.11E+03
7.01E+00	1.26E+03
7.51E+00	1.42E+03
8.01E+00	1.58E+03
8.51E+00	1.75E+03
9.01E+00	1.93E+03
9.51E+00	2.10E+03
1.00E+01	2.30E+03
1.05E+01	2.45E+03
1.10E+01	2.61E+03
1.15E+01	2.78E+03
1.20E+01	2.93E+03
1.25E+01	3.09E+03
1.30E+01	3.24E+03
1.35E+01	3.38E+03
1.40E+01	3.52E+03
1.45E+01	3.67E+03
1.50E+01	3.80E+03
1.55E+01	3.93E+03
1.60E+01	4.06E+03
1.65E+01	4.18E+03
1.70E+01	4.31E+03
1.75E+01	4.42E+03
1.80E+01	4.53E+03
1.85E+01	4.64E+03
1.90E+01	4.75E+03
1.95E+01	4.85E+03

A.4.4 Thrust vs wind speed

Table A.4: NACA0006 lift and drag vs angle of attack

α	C_L	C_D	α	C_L	C_D
-180	0.0000	0.0000	1	0.1208	0.0053
-170	0.3077	0.0543	2	0.2381	0.0070
-160	0.5783	0.2106	3	0.3383	0.0088
-150	0.7792	0.4500	4	0.4418	0.0100
-140	0.8861	0.7437	5	0.5449	0.0118
-130	0.8861	1.0563	6	0.6419	0.0166
-120	0.7792	1.3500	7	0.7219	0.0296
-110	0.5783	1.5894	8	0.7555	0.0560
-100	0.3077	1.7457	9	0.7380	0.0873
-90	0.0000	1.8000	10	0.7263	0.1090
-80	-0.3100	1.7493	20	0.7644	0.2301
-70	-0.5875	1.5966	30	0.8875	0.4680
-60	-0.8002	1.3604	40	0.9521	0.7597
-50	-0.9252	1.0697	50	0.9252	1.0697
-40	-0.9521	0.7596	60	0.8002	1.3604
-30	-0.8874	0.4680	70	0.5875	1.5966
-20	-0.7644	0.2301	80	0.3100	1.7493
-10	-0.7251	0.1089	90	0.0000	1.8000
-9	-0.7373	0.0872	100	-0.3078	1.7457
-8	-0.7554	0.0560	110	-0.5785	1.5894
-7	-0.7218	0.0296	120	-0.7794	1.3500
-6	-0.6418	0.0166	130	-0.8863	1.0563
-5	-0.5449	0.0118	140	-0.8863	0.7437
-4	-0.4419	0.0100	150	-0.7794	0.4500
-3	-0.3383	0.0088	160	-0.5785	0.2106
-2	-0.2381	0.0070	170	-0.3078	0.0543
-1	-0.1208	0.0053	180	0.0000	0.0000
0	0.0000	0.0047			

A.5 Components CFD Analysis

This section gives more details on the CFD of the turbine's components.

Blade CFD

Bade CFD Analysis General Settings

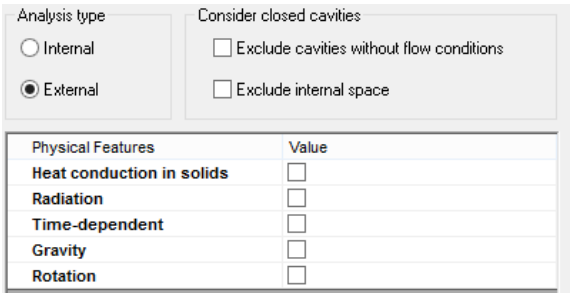

Figure A.17: Analysis type

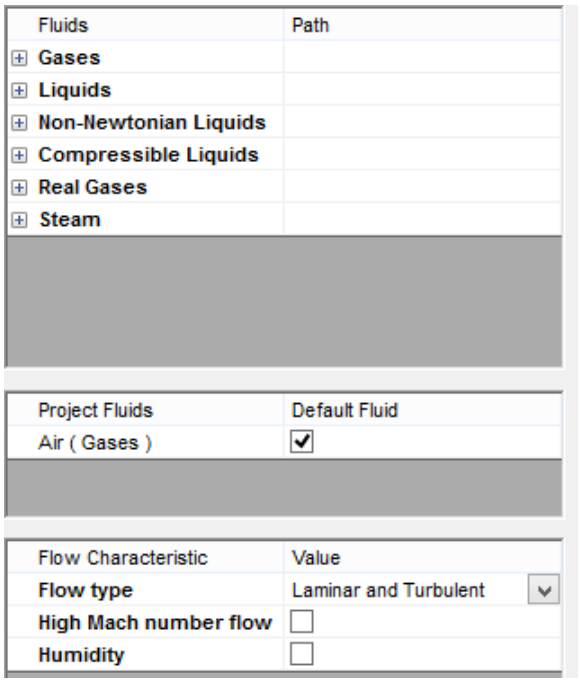

Figure A.18: Fluids

Figure A.19: Wall conditions

Parameter	Value
Parameter Definition	User Defined
Thermodynamic Parameters	
Parameters	Pressure, temperature
Pressure	101325 Pa
Temperature	293.2 K
Velocity Parameters	
Parameter	Velocity
Defined by	3D Vector
Velocity in X direction	0 m/s
Velocity in Y direction	0 m/s
Velocity in Z direction	-52.5 m/s
Turbulence Parameters	
Parameters	Turbulence intensity and length
Turbulence intensity	0.1 %
Turbulence length	0.00415 m

Figure A.20: Initial and ambient conditions

Meshing

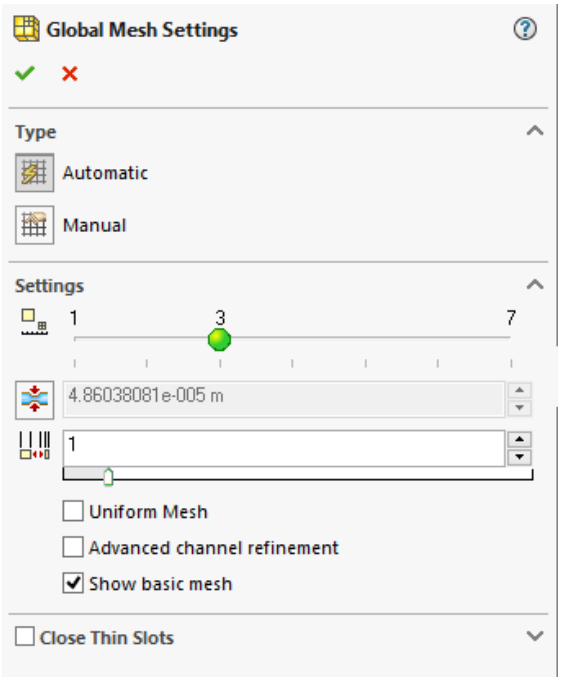

Figure A.21: Mesh settings

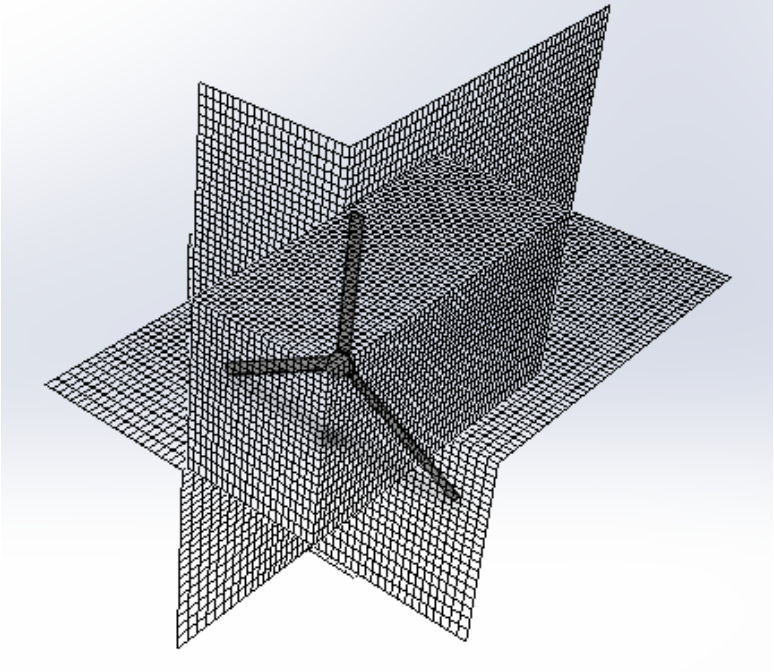

Figure A.22: Meshing of the flow domain

Blade Mesh for FEA Simulation

Mesh Details

Study name	Blade FEA (-Default-)
Mesh type	Solid Mesh
Mesher Used	Curvature-based mesh
Jacobian points	4 points
Mesh Control	Defined
Max Element Size	0.0664675 m
Min Element Size	0.00332337 m
Mesh quality	Draft
Total nodes	87627
Total elements	275763
Maximum Aspect Ratio	1.5352e+005
Percentage of elements with Aspect Ratio < 3	81
Percentage of elements with Aspect Ratio > 10	7.2
Remesh failed parts with incompatible mesh	On
Time to complete mesh(hh:mm:ss)	00:00:44
Computer name	NORBERTO

Figure A.23: Mesh details

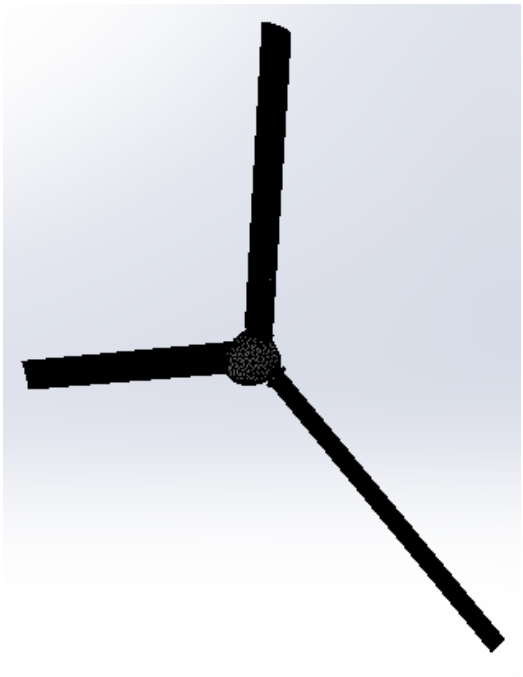

Figure A.24: Blade mesh

A.5.1 Tower CFD and FEA anaysis

Tower CFD Flow Domain

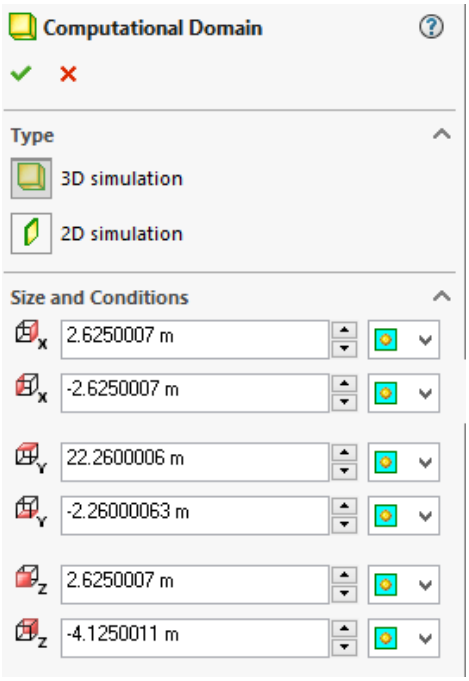

Figure A.25: Flow domain dimensions

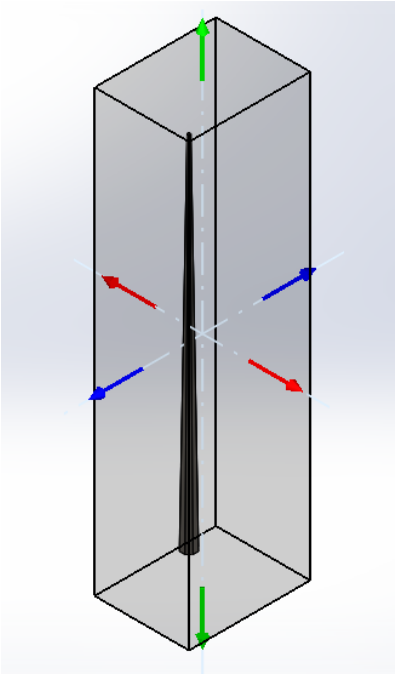

Figure A.26: Flow domain

Tower CFD Mesh

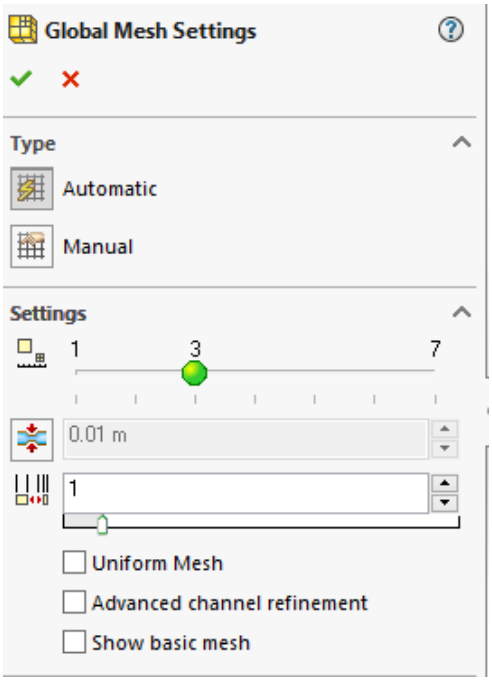

Figure A.27: Tower CFD Mesh settings

Parameter	Value
Status	Solver is finished.
Total cells	598,136
Fluid cells	598,136
Fluid cells contacting solids	64,660
Iterations	352
Last iteration finished	15:14:56
CPU time per last iteration	00:00:13
Travels	
Iterations per 1 travel	173
Cpu time	1 : 38 : 5
Calculation time left	0 : 0 : 0
Run at	NORBERTO

Figure A.28: Final status of the tower CFD analysis

Tower FEA Mesh

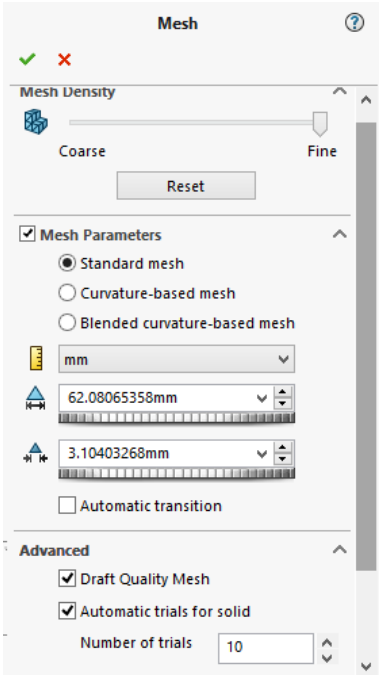

Figure A.29: Tower FEA meshing parameters

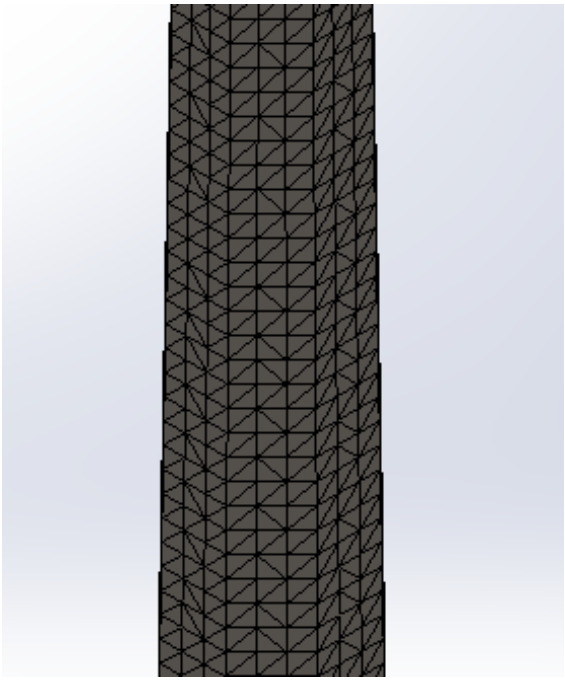

Figure A.30: Tower portion meshing

Mesh Details

Study name	Tower FEA (-Default-)
Mesh type	Solid Mesh
Mesher Used	Standard mesh
Automatic Transition	Off
Include Mesh Auto Loops	On
Jacobian points	4 points
Mesh Control	Defined
Element size	62.0807 mm
Tolerance	3.10403 mm
Mesh quality	Draft
Total nodes	33915
Total elements	111722
Maximum Aspect Ratio	174.65
Percentage of elements with Aspect Ratio < 3	0.0277
Percentage of elements with Aspect Ratio > 10	95.3
Time to complete mesh(hh:mm:ss)	00:02:32
Computer name	NORBERTO

Figure A.31: Tower meshing details

A.6 SWT Control System

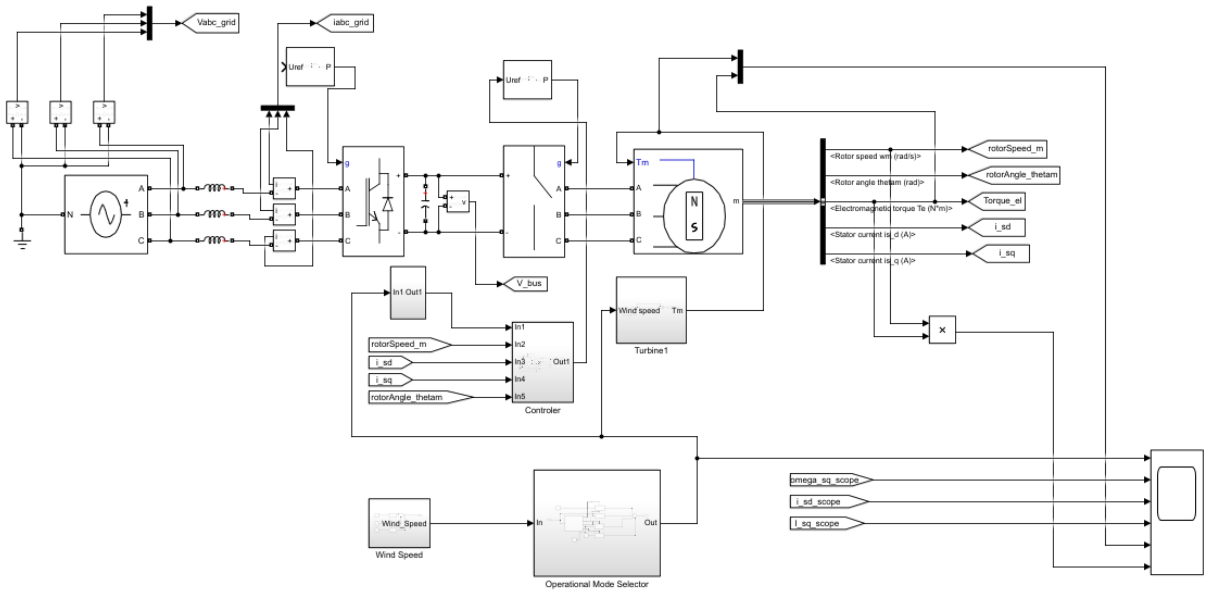

Figure A.32: SWT control system Simulink diagram

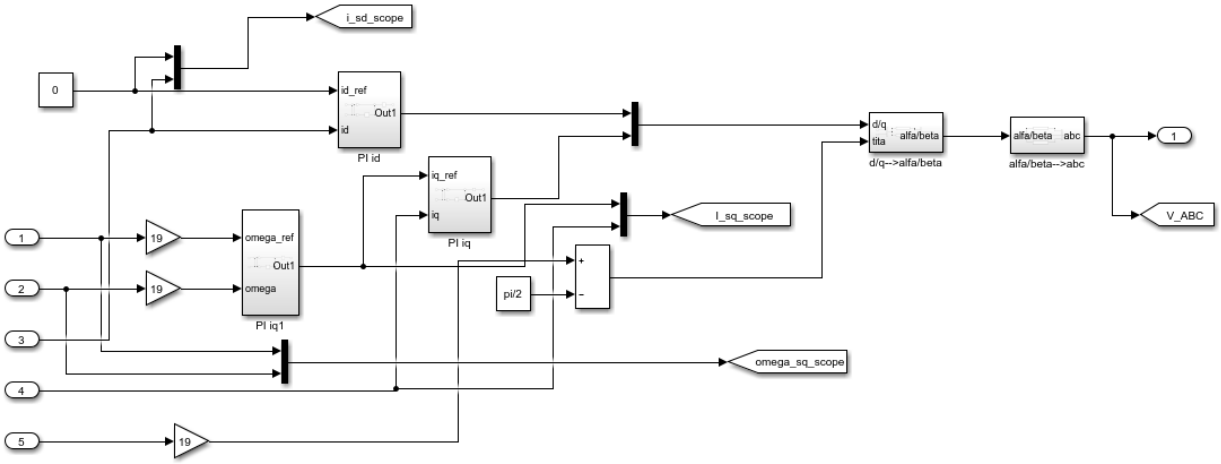

Figure A.33: SWT controller Simulink diagram

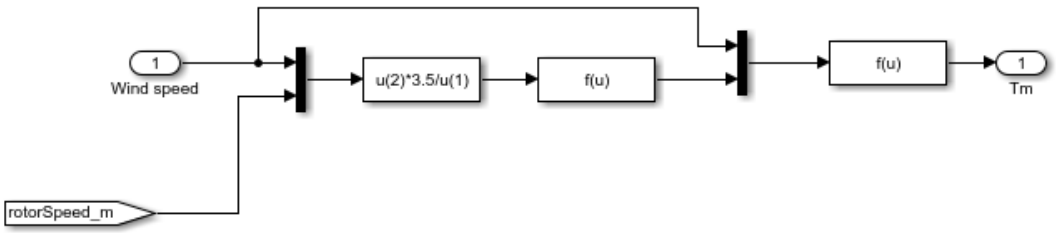

Figure A.34: SWT Simulink turbine model

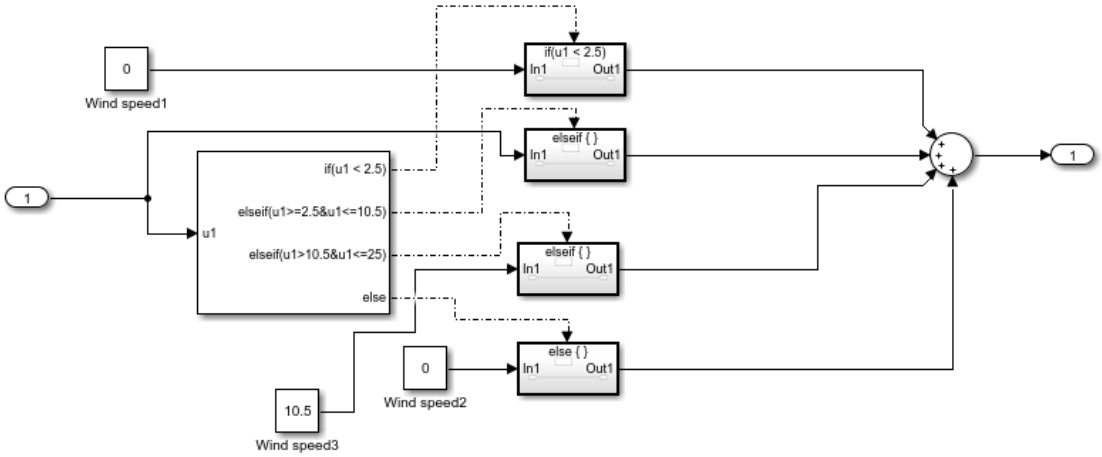

Figure A.35: SWT Simulink operational mode selector

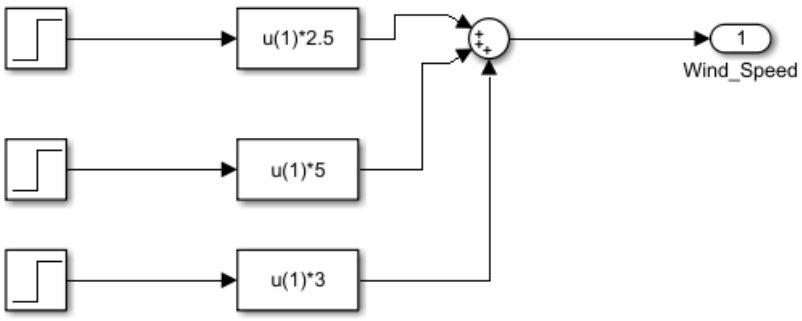

Figure A.36: SWT Simulink wind speed simulator

A.7 Engineering Drawing

SWT-000 - General Assembly

SWT-001 Rotor

1. SWT-001-01 Blade
2. SWT-001-02 Hub nose
3. SWT-001-03 Hub
4. SWT-001-04 Main Shaft

SWT-002 Nacelle

1. SWT-002-00 Inner components
    (a) SWT-002-00-01 Mainframe
    (b) SWT-002-00-02 Bearing Support
    (c) SWT-002-00-03 Alternator
        i. SWT-002-00-03A Alternator support
        ii. SWT-002-00-03B Alternator rotor cover
    (d) SWT-002-00-04 Brake support
    (e) SWT-002-00-05 Brake pads Assembly
    (f) SWT-002-00-06 Brake disc with a shaft
2. SWT-002-01 Nacelle Front Cover
3. SWT-002-02 Nacelle
4. SWT-002-03 Nacelle rear cover
5. SWT-002-06 Brakes Disc

SWT-003 Tail

1. SWT-003-01 Tail support
2. SWT-003-02 Nuckle
3. SWT-003-03 Tail
4. SWT-003-04 Nuckle pin

SWT-004 Tower

1. SWT-004-01 Tower
2. SWT-004-02 Nacelle shaft

SWT-005 Tower Base

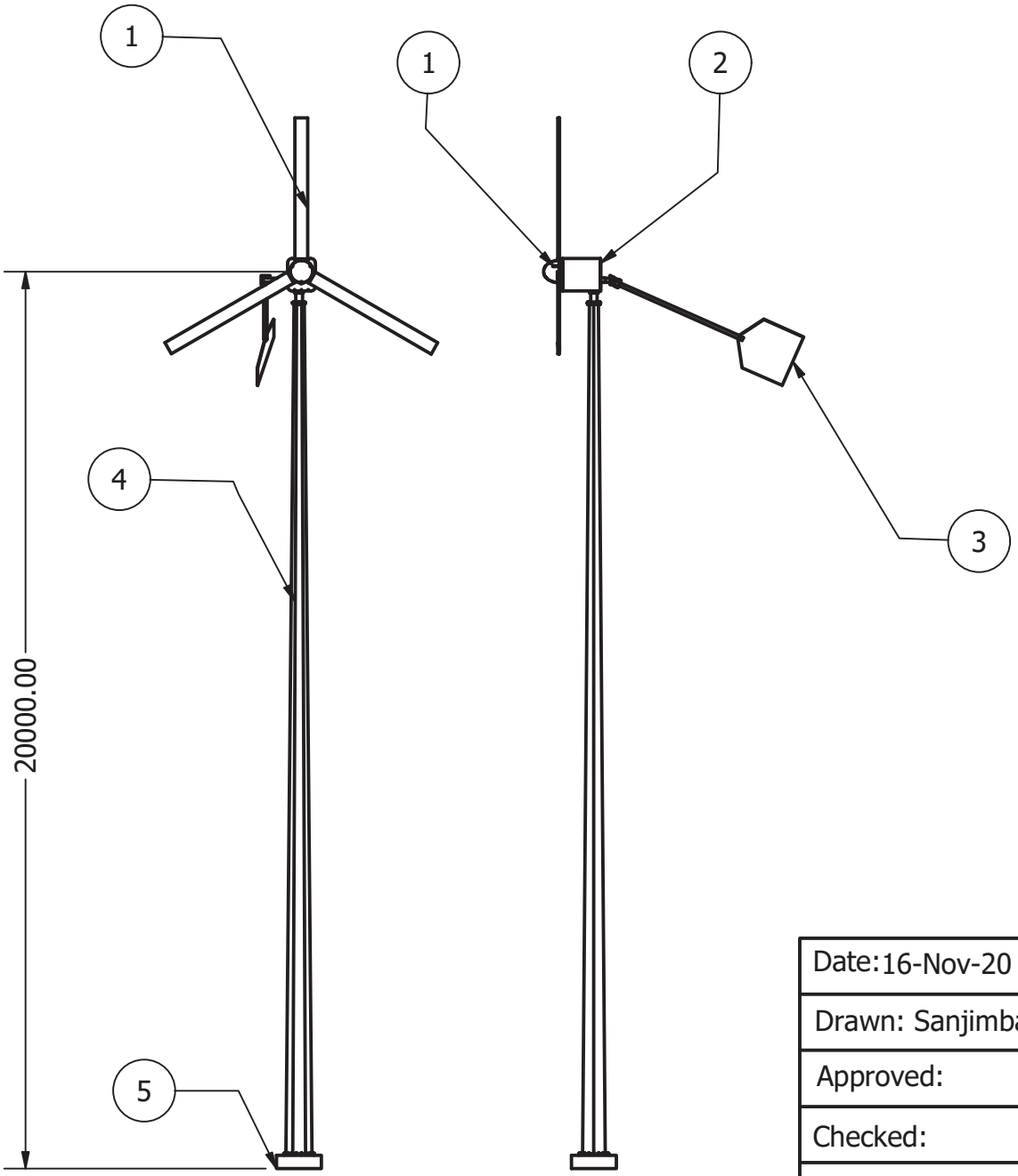

PARTS LIST			
ITEM	QTY	PART NUMBER	DESCRIPTION
1	1	SWT-001	Rotor
2	1	SWT-002	Nacelle
3	1	SWT-003	Tail
4	1	SWT-004	Tower
5	1	SWT-005	Tower Base

Date: 16-Nov-20	Durban University of Technology
Drawn: Sanjimba	
Approved:	Drawing Title: **Small Wind Turbine General Assembly**
Checked:	
Scale: 1:150	DWGNO: SWT-000
Mass:	Sheet No: 1 of 1 — A4

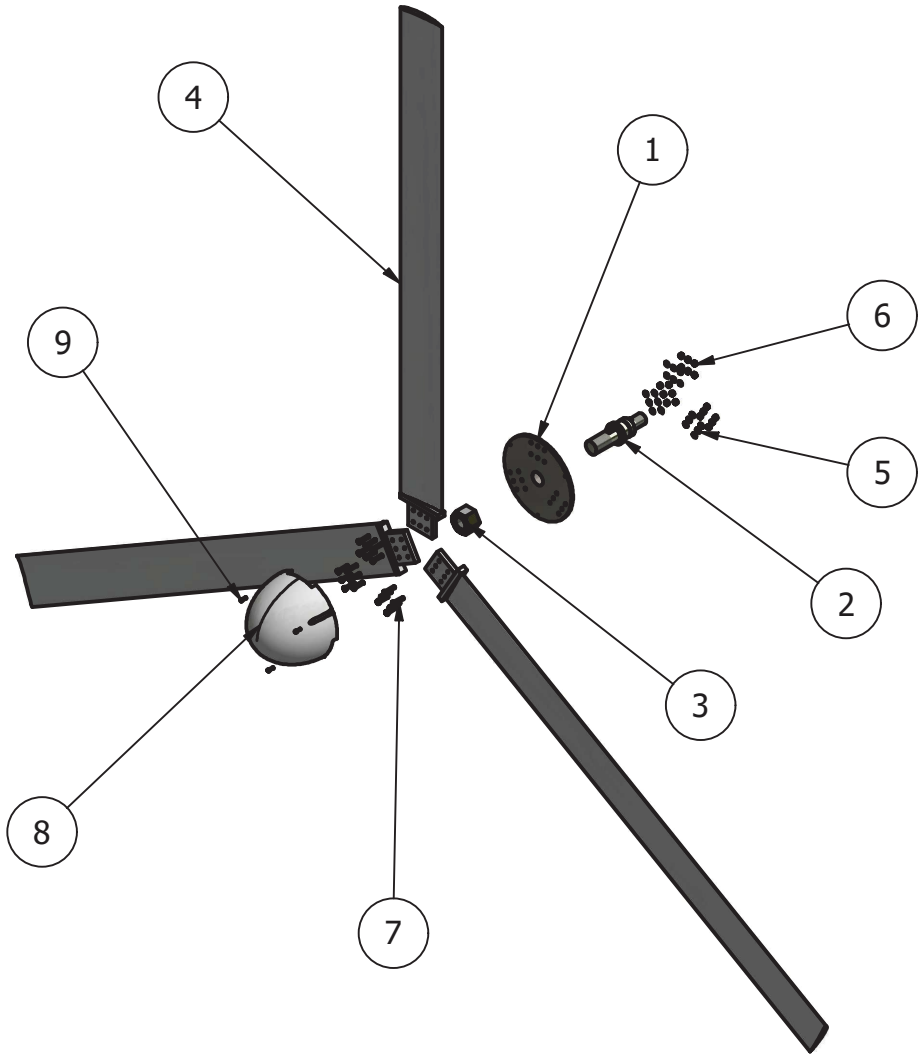

PARTS LIST			
ITEM	QTY	PART NUMBER	DESCRIPTION
1	1	SWT-001-03	Hub
2	1	SWT-001-04	Main Shaft
3	1	ANSI B18.2.4.6M - M80 x 6	Heavy Hex Nut
4	3	SWT-001-01	Blade
5	18	ISO 7089 - 14	Plain washers - Normal series - Product grade A
6	18	ISO 8673 - M14x1.5	Hexagon nuts, style1, with metric fine pitch thread - product A and B
7	18	ISO 8765 - M14 x 1.5 x 65	Hexagon head bolts with metric fine pitch thread - Product grades A and B
8	1	SWT-001-02	Hub Nose
9	3	ANSI B18.3.1M - M8x1.25 x 30, FSHCSM	Forged Socket Head Cap Screw - Metric

Date: 16-Nov-20	Durban University of Technology	
Drawn: Sanjimba		
Approved:		
Checked:	Drawing Title: **Turbine Rotor Assembly**	DWGNO: SWT-001
Scale: 1:40		Sheet No: 1 of 1
Not Scale		A4

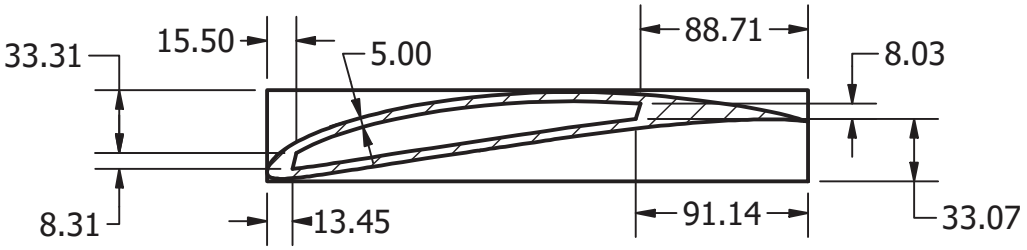

SECTION A-A
SCALE 1 / 4

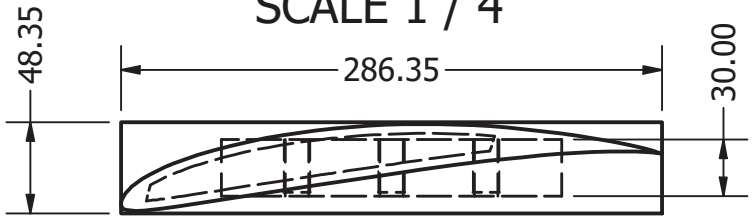

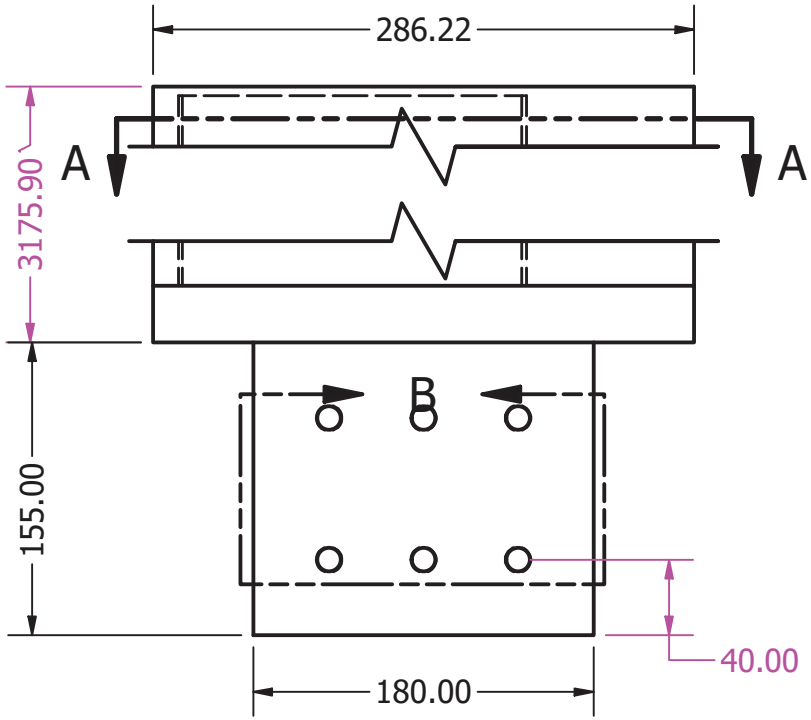

The blade cross-sectional area is made of airfoil SG6043 with a chord length of 278.25mm rotated 7° from horizontal line in counter-clockwise direction

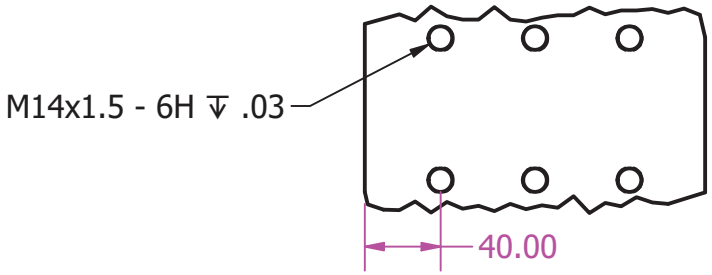

DETAIL B
SCALE 1 / 4

Date: 16-Nov-20	Durban University of Technology
Drawn: Sanjimba	
Approved:	Drawing Title: **Small Wind Turbine Blade**
Checked:	
Scale: 1/4	DWGNO: SWT-001-01
Not to Scale	Sheet No: 1 of 1 — A4

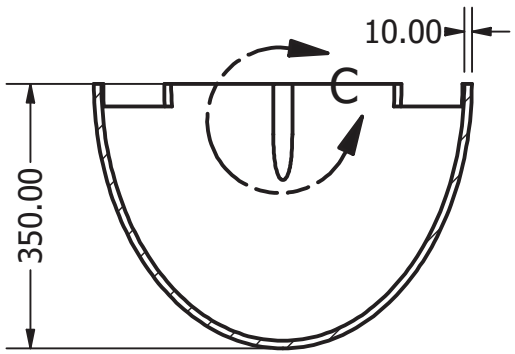

SECTION A-A
SCALE 1:10

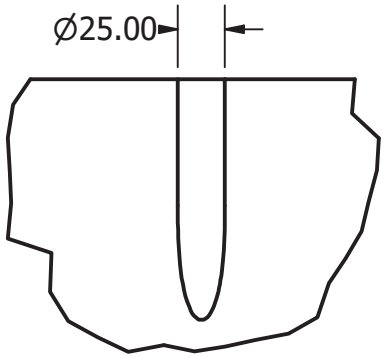

DETAIL C
SCALE 1/4

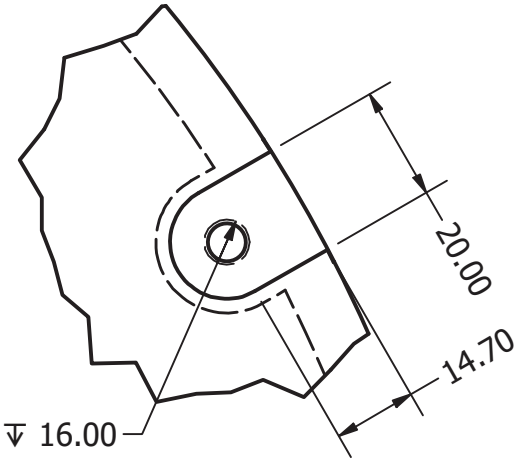

DETAIL B
SCALE 3/4

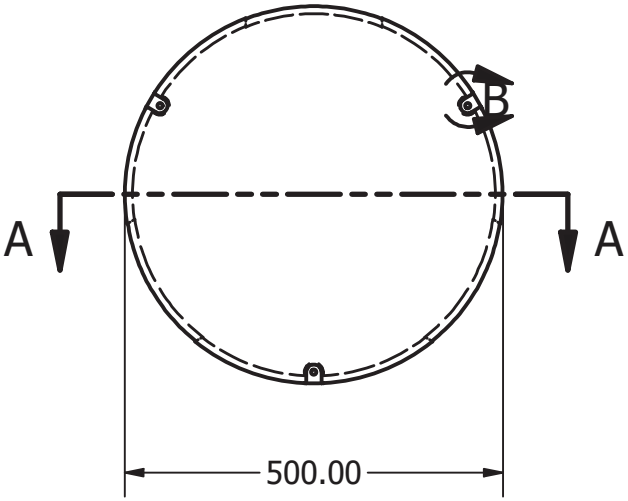

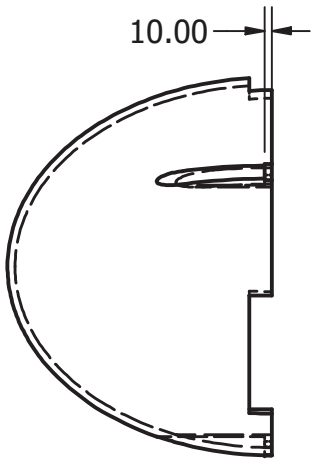

Date: 16-Nov-20	Durban University of Technology
Drawn: Sanjimba	
Approved:	
Checked:	Drawing Title: **Hub Nose**
Scale: **Not to Scale**	DWGNO: SWT-001-02
	Sheet No: 1 of 1 — A4

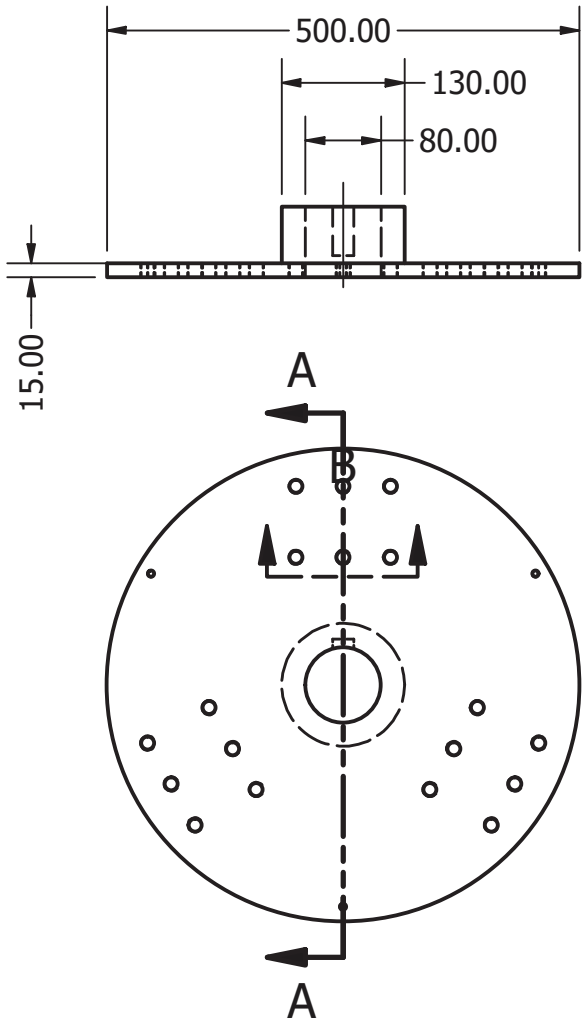

SECTION A-A
SCALE 1:8

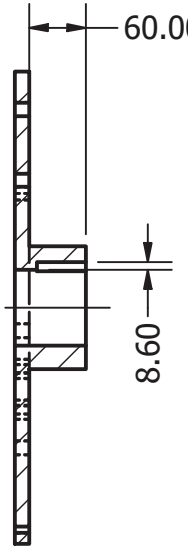

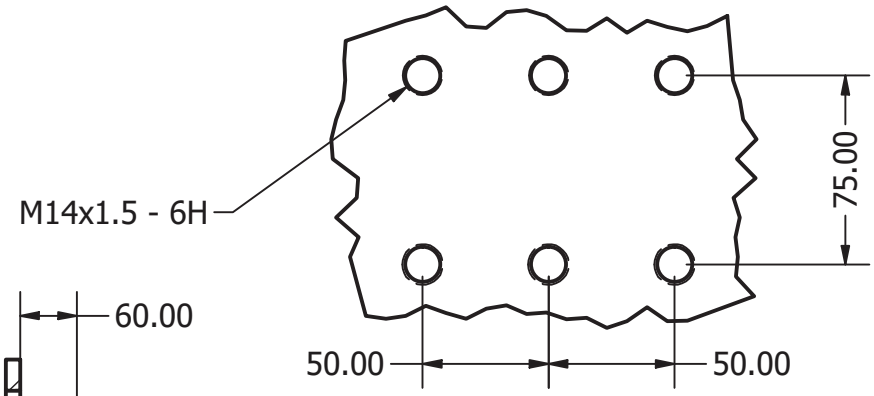

DETAIL B
SCALE 1 / 3

Date: 16-Nov-20	Durban University of Technology
Drawn: Sanjimba	
Approved:	
Checked:	Drawing Title: **Hub**
Scale: 1/8	DWGNO: SWT-001-03
Not to Scale	Sheet No: 1 of 1 | A4

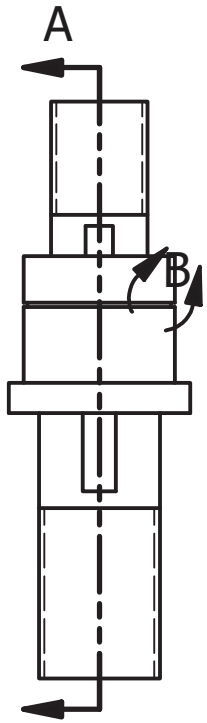

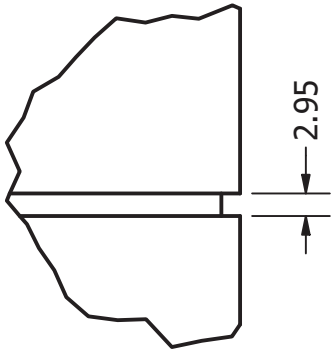

DETAIL B
SCALE 1

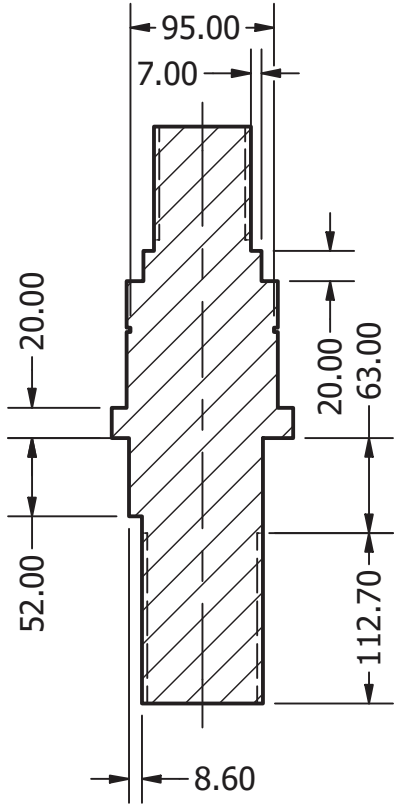

SECTION A-A
SCALE 1 / 5

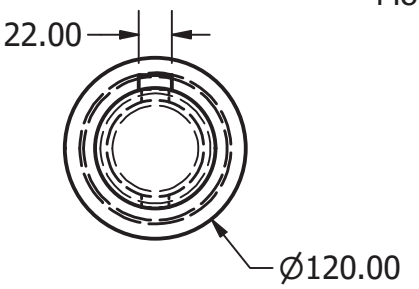

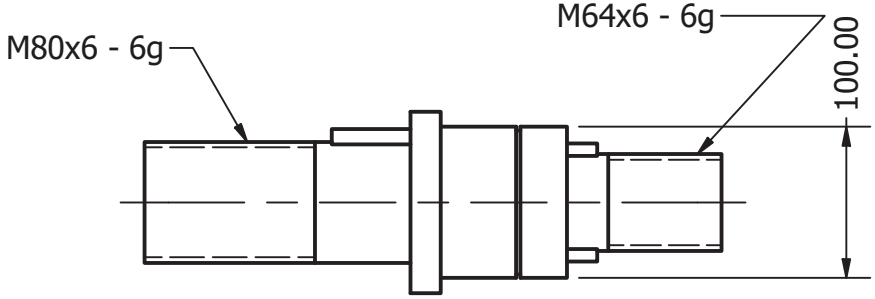

Date: 16-Nov-20	Durban University of Technology
Drawn: Sanjimba	
Approved:	
Checked:	Drawing Title: **Main Shaft**
Scale: **Not to Scale**	DWGNO: SWT-001-04
	Sheet No: 1 of 1 — A4

PARTS LIST			
ITEM	QTY	PART NUMBER	DESCRIPTION
1	1	SWT-002-02	Nacelle
2	1	SWT-002-01	Nacelle Front Cover
3	1	SWT-002-03	Nacelle rear cover
4	12	JIS B 1101 - M10 x 30	Slotted Pan Head Screw
5	1	SWT-002-00	Inner components

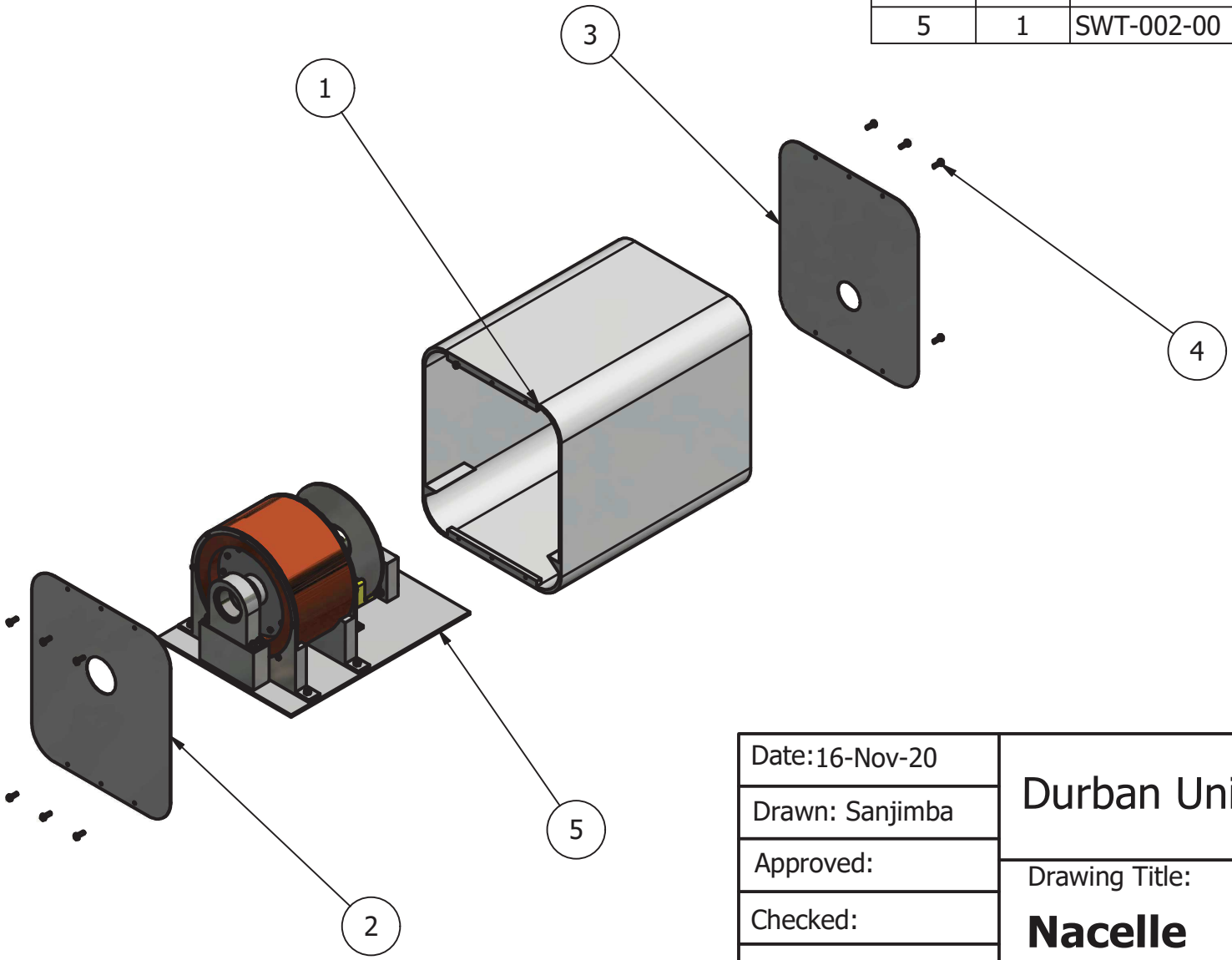

Date: 16-Nov-20	Durban University of Technology
Drawn: Sanjimba	
Approved:	Drawing Title: **Nacelle Assembly**
Checked:	
Scale: 1/20	DWGNO: SWT-002
Not to Scale	Sheet No: 1 of 1 — A4

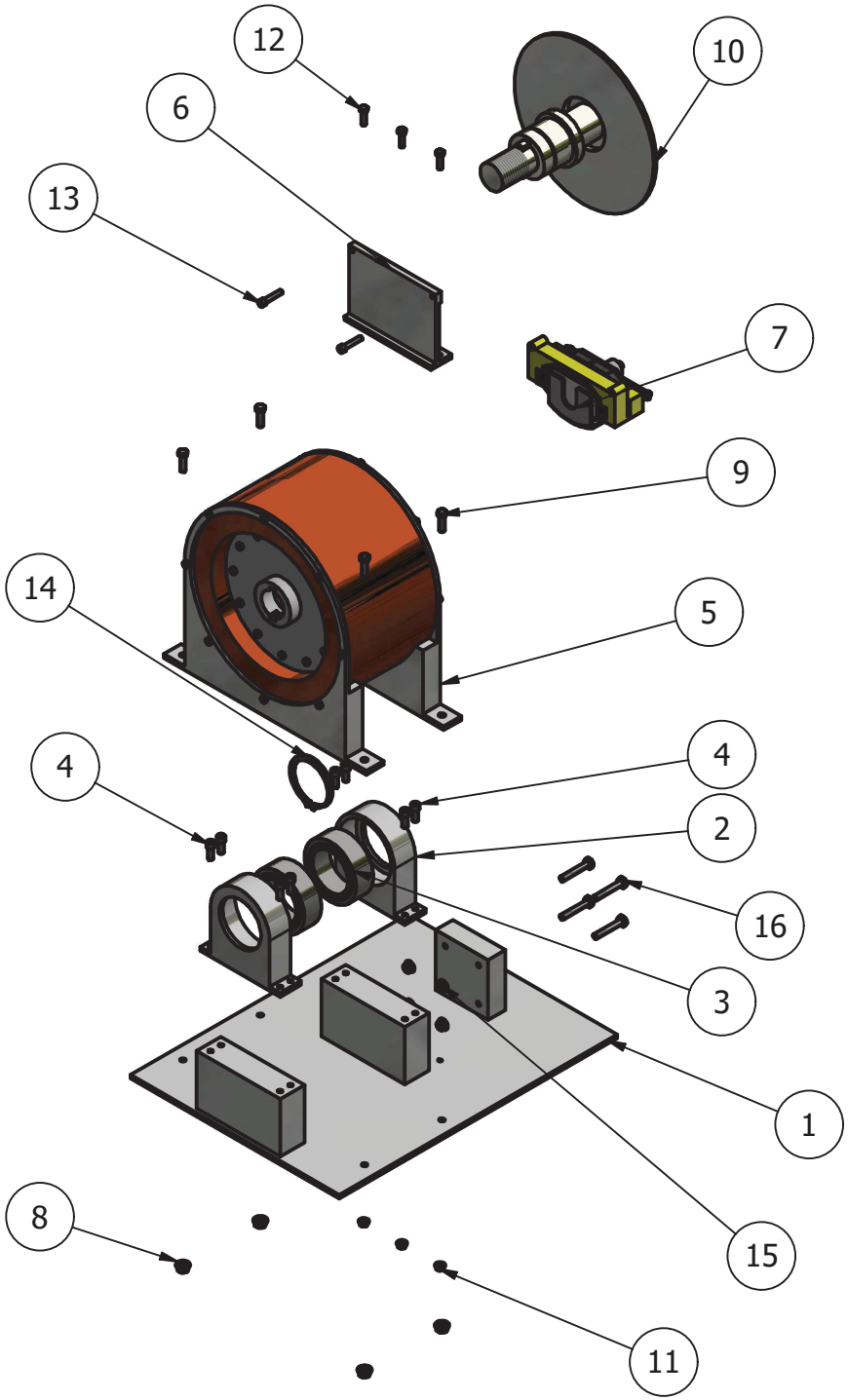

PARTS LIST

ITEM	QTY	PART NUMBER	DESCRIPTION
1	1	SWT-002-00-01	Mainframe
2	2	SWT-002-00-02	Bearing support
3	2	DIN 635 SKF - SKF 24020 CC/W33	Spherical Roller Bearings Double Row with Cylindrical Bore SKF
4	8	ANSI B18.3.1M - M12x1.75 x 30, FSHCSM	Forged Socket Head Cap Screw - Metric
5	1	SWT-002-00-03	Alternator
6	1	SWT-002-00-04	Brake support
7	1	SWT-002-00-05	Brake pads assembly
8	4	ANSI B18.2.4.4M - M14 x 2	Metric Hex Flange Nuts
9	4	ANSI B18.2.3.5M - M12 x 1.75 x 40	Hex Bolt
10	1	SWT-002-00-06	Brake disc with a shaft
11	3	ANSI B18.2.4.4M - M10 x 1.5	Metric Hex Flange Nuts
12	3	ANSI B18.2.3.5M - M10 x 1.5 x 35	Hex Bolt
13	2	ANSI B18.3.1M - M10x1.5 x 50, FSHCSM	Forged Socket Head Cap Screw - Metric
14	2	MS 16624 - 4.250, IERRS5100	Industrial External Retaining Rings, Series 5100
15	4	ANSI B18.2.4.4M - M12 x 1.75	Metric Hex Flange Nuts
16	4	ANSI B18.2.3.3M - M12x1.75 x 75	Heavy Hex Screw (Regular Thread - Metric)

Date: 16-Nov-20	Durban University of Technology
Drawn: Sanjimba	
Approved:	Drawing Title: **Inner Turbine Components**
Checked:	DWGNO: SWT-002-00
Scale: 1/15	Sheet No: 1 of 1
Not to Scale	A4

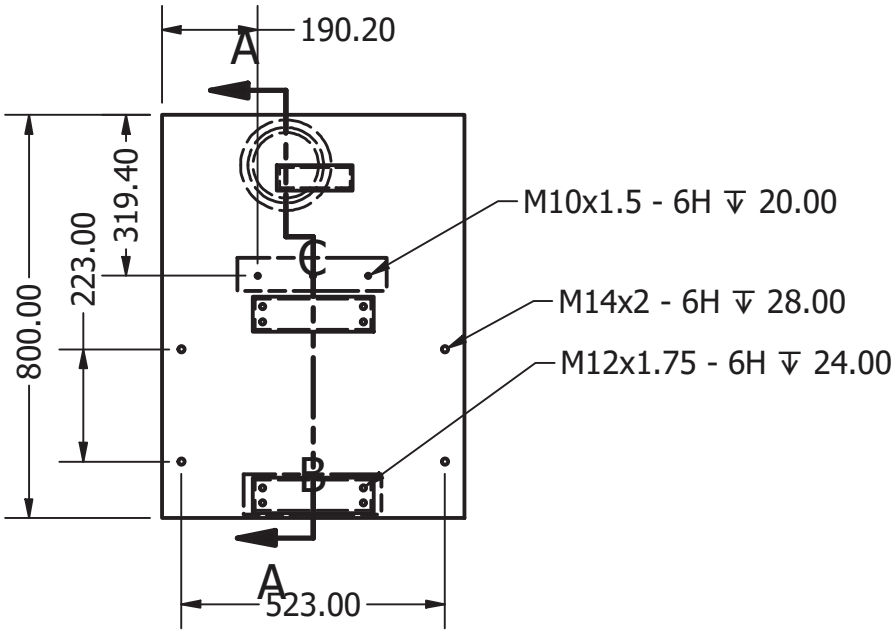

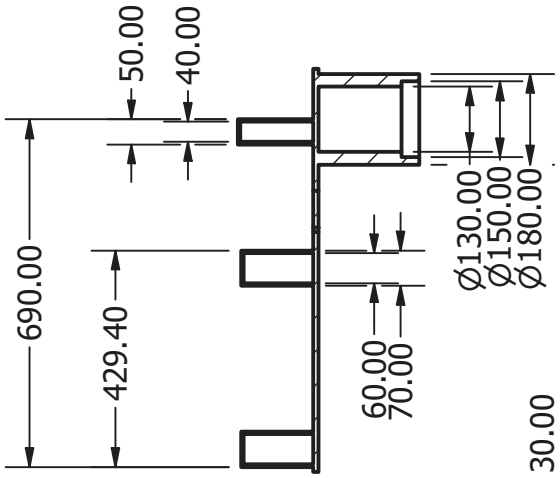

SECTION A-A
SCALE 1:15

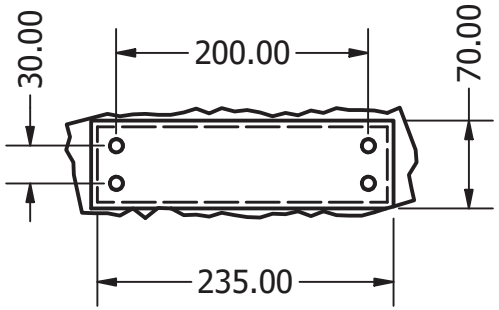

DETAIL B
SCALE 1 / 6

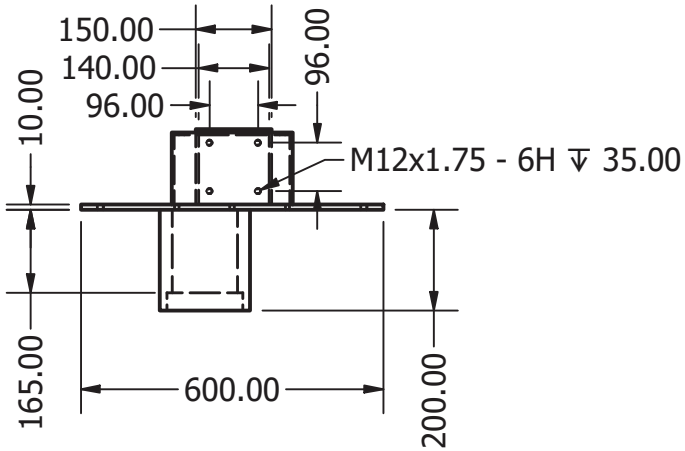

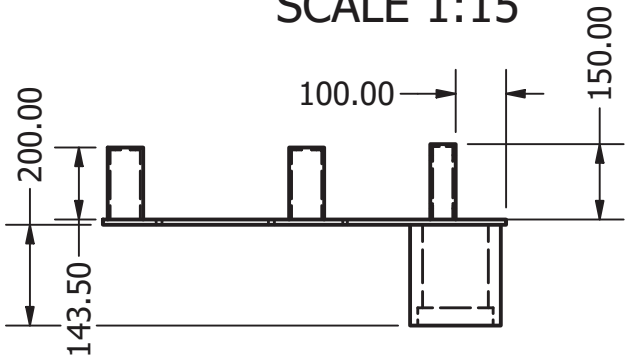

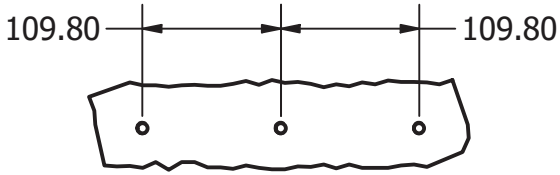

DETAIL C SCALE 1 / 6

Date: 16-Nov-20	Durban University of Technology
Drawn: Sanjimba	
Approved:	
Checked:	Drawing Title: **Mainframe**
Scale: 1/15	DWGNO: SWT-002-00-01
Not to Scale	Sheet No: 1 of 1 — A4

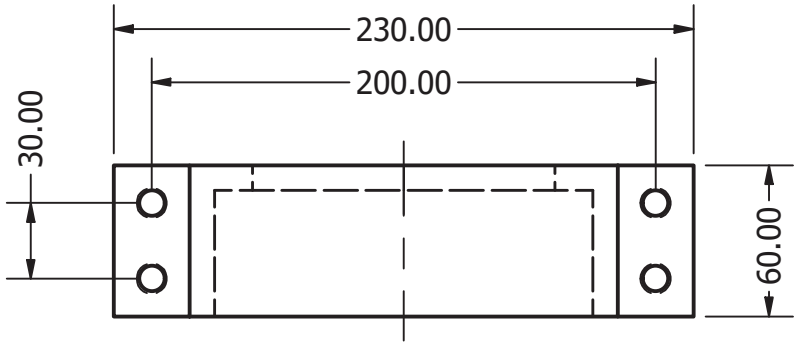

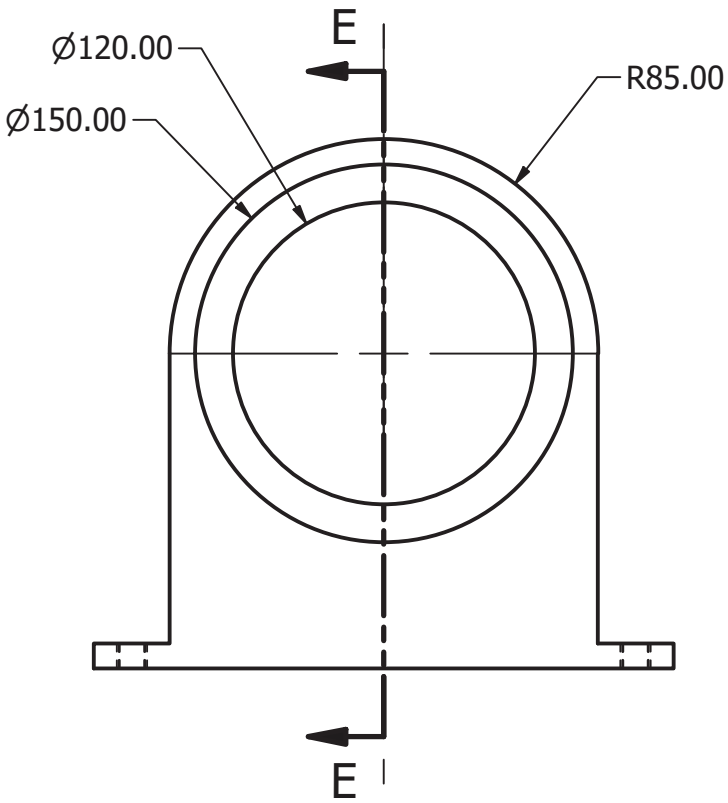

SECTION E-E
SCALE 1 / 3

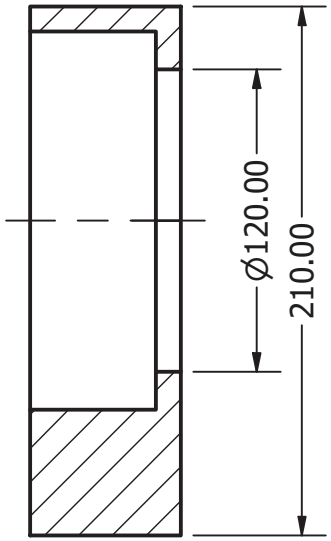

Date: 16-Nov-20	Durban University of Technology
Drawn: Sanjimba	
Approved:	Drawing Title: **Main Bearing Support**
Checked:	
Scale: 1/3	DWGNO: SWT-002-00-02
Not to scale	Sheet No: 1 of 1 — A4

PARTS LIST			
ITEM	QTY	PART NUMBER	DESCRIPTION
1	2	SWT-002-00-03A	Alternator support
2	1	GES 043-150-200	Alternator
3	2	SWT-002-00-03B	Alternator rotor cover
4	24	ISO 4017 - M8 x 25(3)	Hexagon head screws
5	16	ANSI B18.2.3.5M - M8 x 1.25 x 25	Hex Bolt

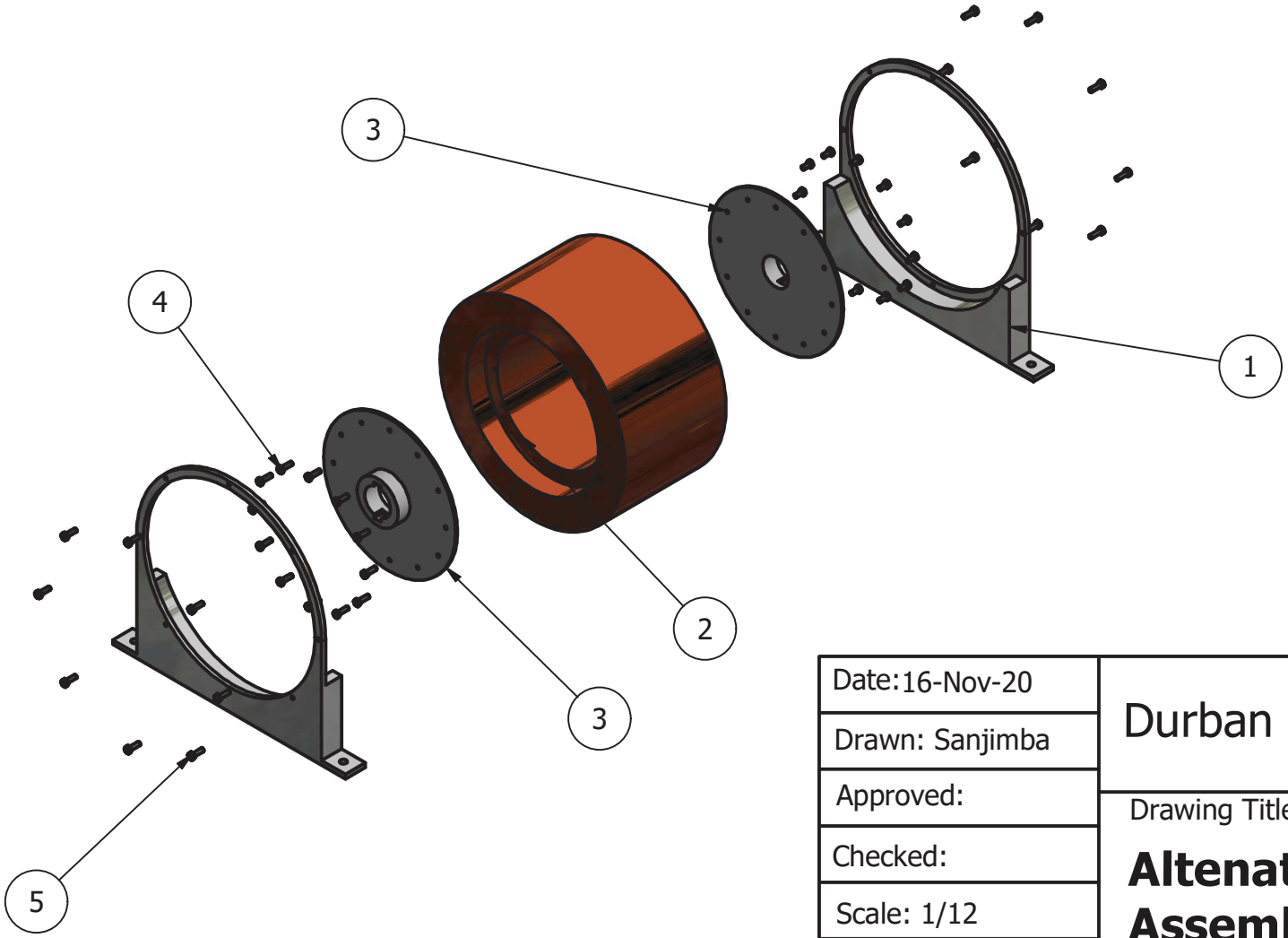

Date: 16-Nov-20	Durban University of Technology	
Drawn: Sanjimba		
Approved:	Drawing Title: **Altenator Assembly**	
Checked:		DWGNO: SWT-002-00-03
Scale: 1/12		Sheet No: 1 of 1 | A4
Not to scale		

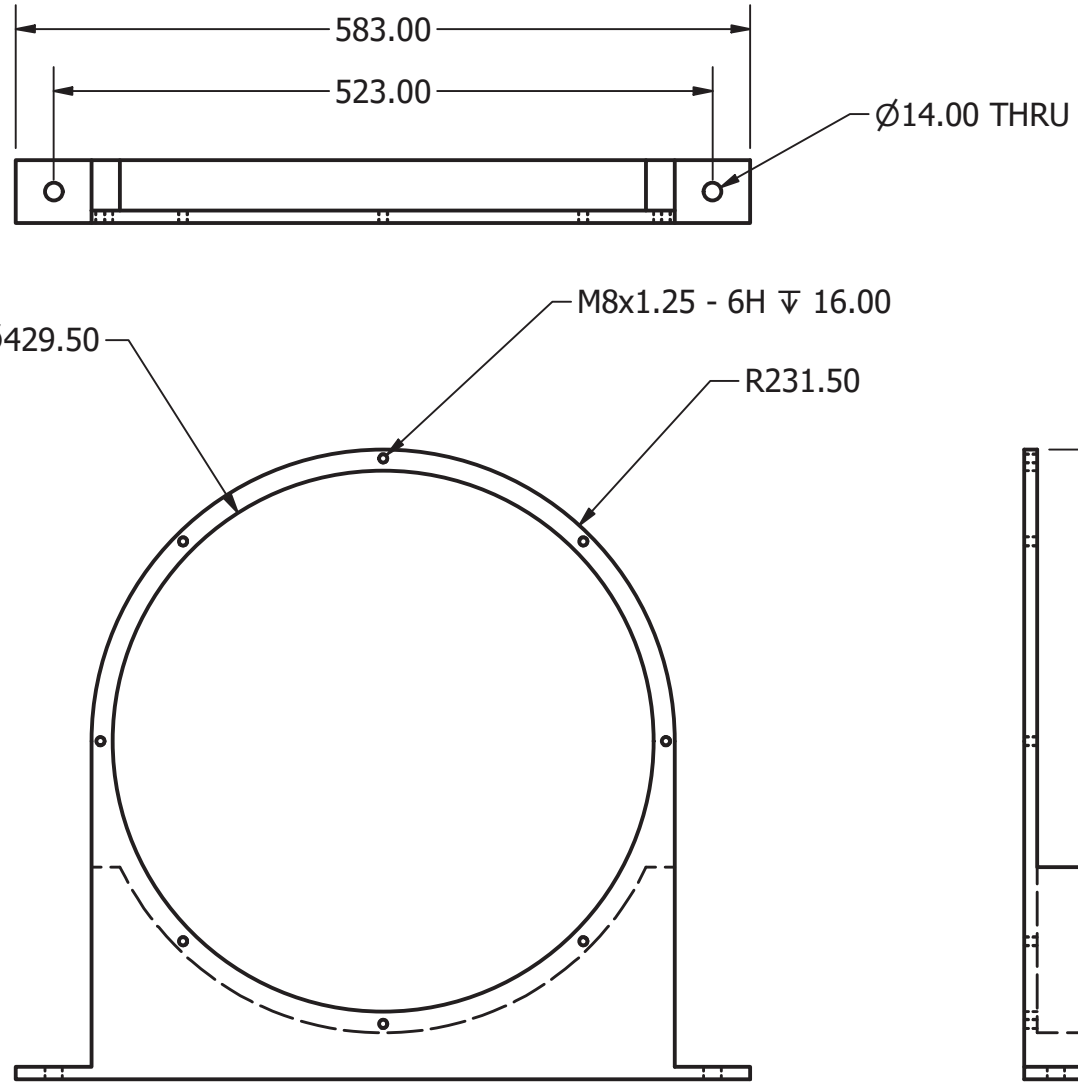

Date: 16-Nov-20	Durban University of Technology
Drawn: Sanjimba	
Approved:	Drawing Title: **Alternator Support**
Checked:	
Scale: 1/5	DWGNO: SWT-002-00-03A
Not to scale	Sheet No: 1 of 1 — A4

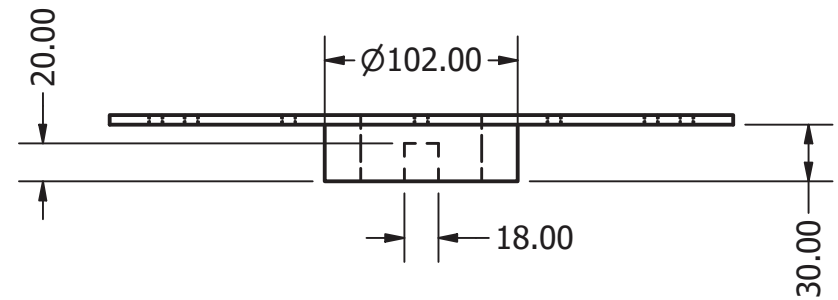

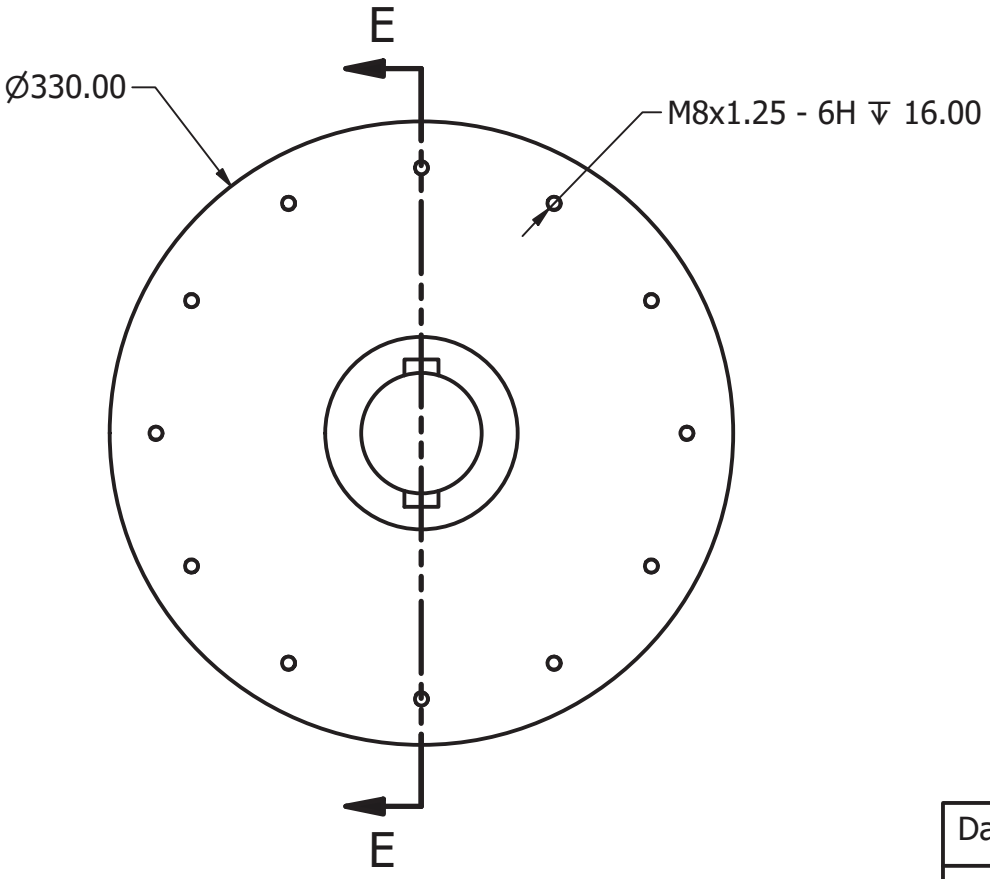

SECTION E-E
SCALE 1 / 4

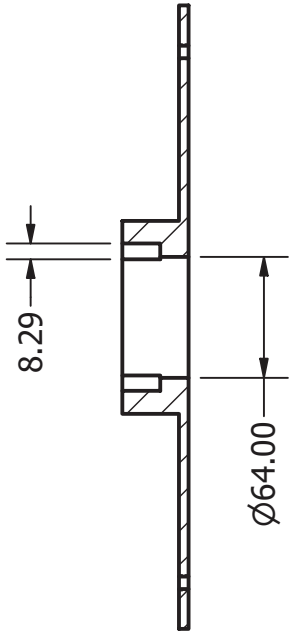

Date: 16-Nov-20	Durban University of Technology
Drawn: Sanjimba	
Approved:	Drawing Title: **Alternator Cover**
Checked:	
Scale: 1/4	DWGNO: SWT-002-00-03B
Not to scale	Sheet No: 1 of 1 — A4

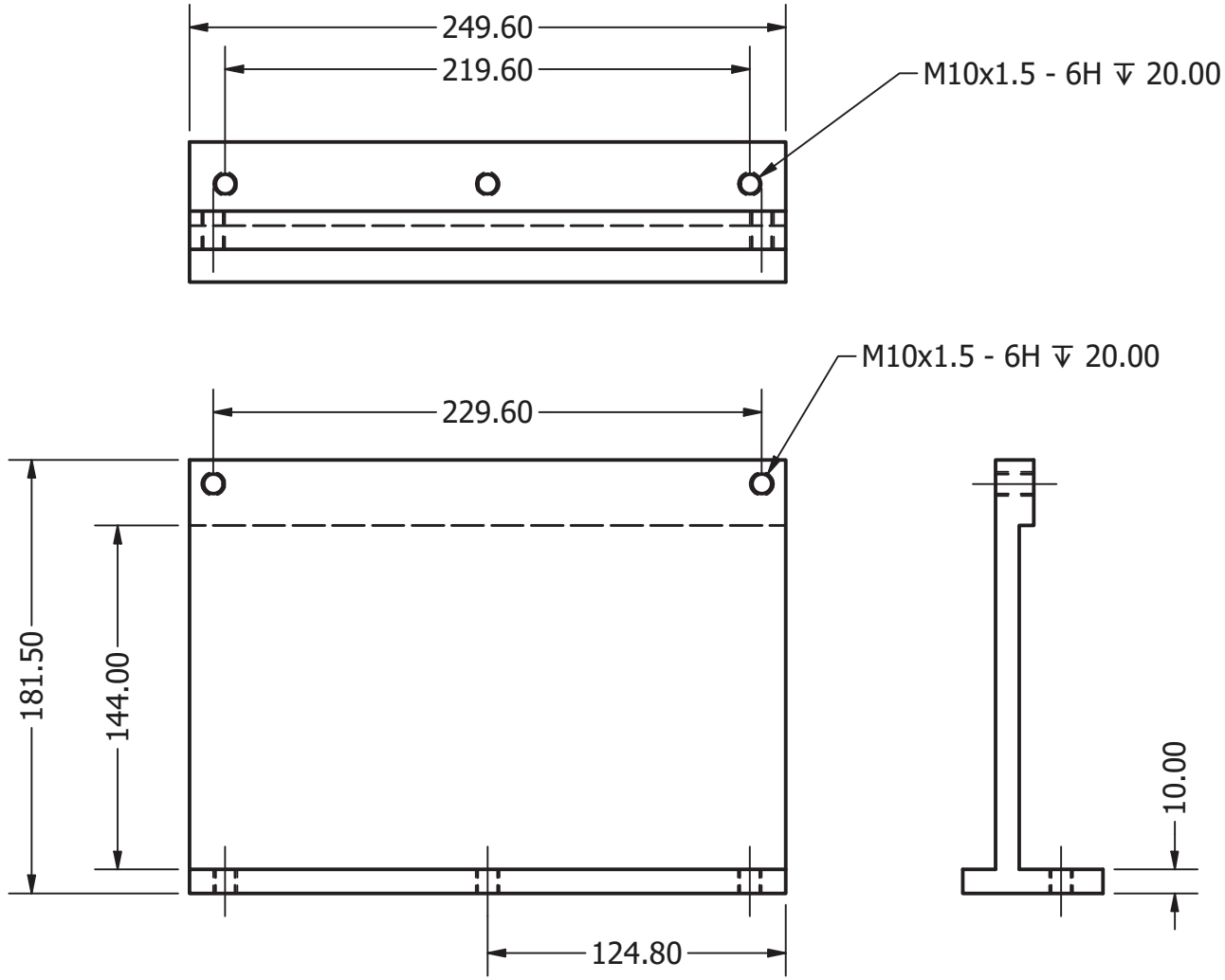

Date: 16-Nov-20	Durban University of Technology
Drawn: Sanjimba	
Approved:	Drawing Title: **Brakes Support**
Checked:	
Scale: 1/3	DWGNO: SWT-002-00-04
Not to scale	Sheet No: 1 of 1 — A4

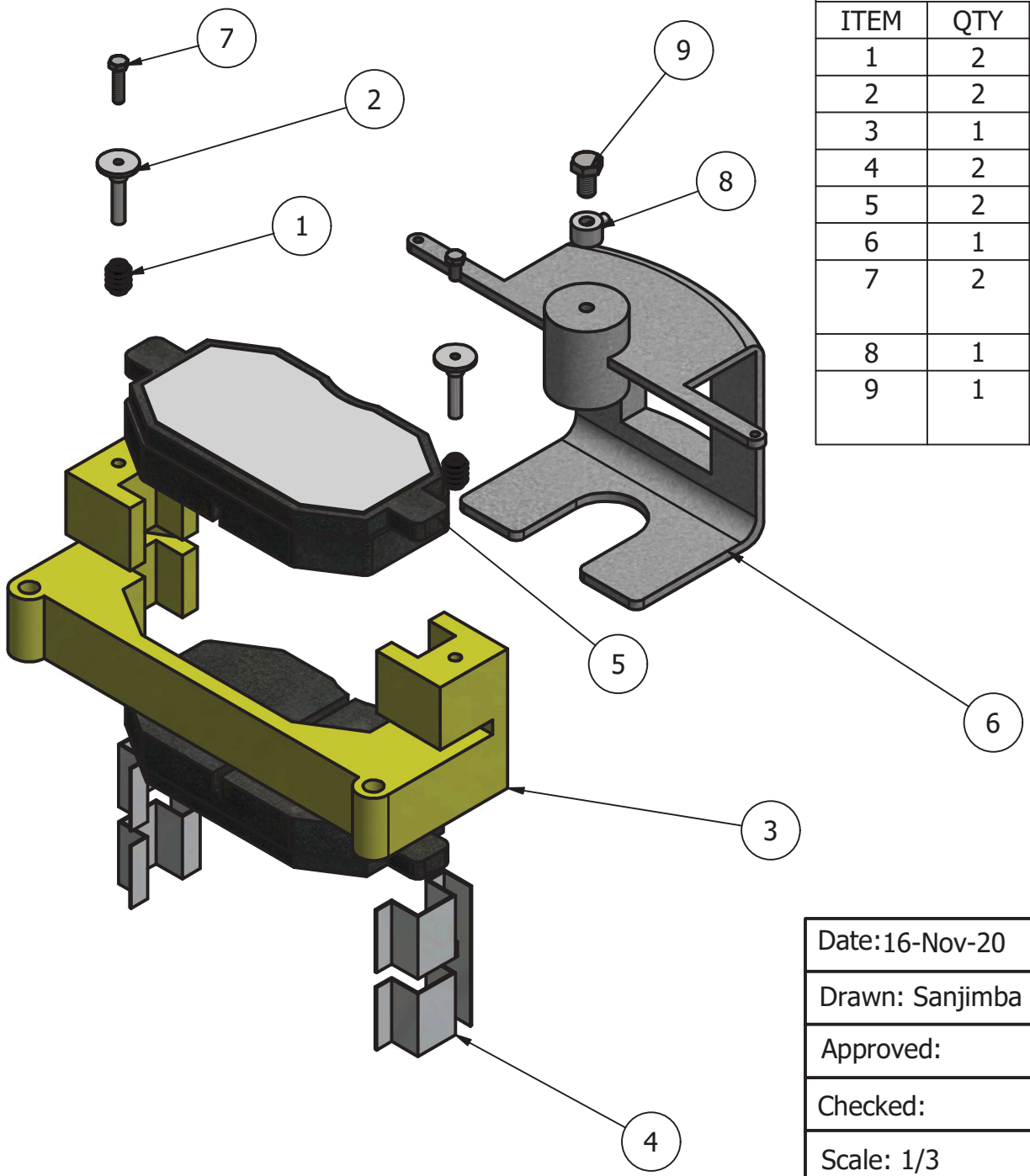

PARTS LIST			
ITEM	QTY	PART NUMBER	DESCRIPTION
1	2		Dust boot
2	2		Slinding Pin
3	1		Mounting Bracket
4	2		Brake mounting clip
5	2		Brake Pad
6	1		Caliper Frame
7	2	ANSI B18.2.3.2M - M5 x 0.8	Metric Formed Hex Screw - Formed Hex Screw - Metric (2)
8	1		Fluid connector
9	1	ANSI B18.2.3.2M - M8 x 1.25	Metric Formed Hex Screw - Formed Hex Screw - Metric (2)

Date: 16-Nov-20	Durban University of Technology	
Drawn: Sanjimba		
Approved:	Drawing Title:	
Checked:	**Brakes Pads Assembly**	DWGNO: SWT-002-00-05
Scale: 1/3		Sheet No: 1 of 1 | A4
Not to scale		

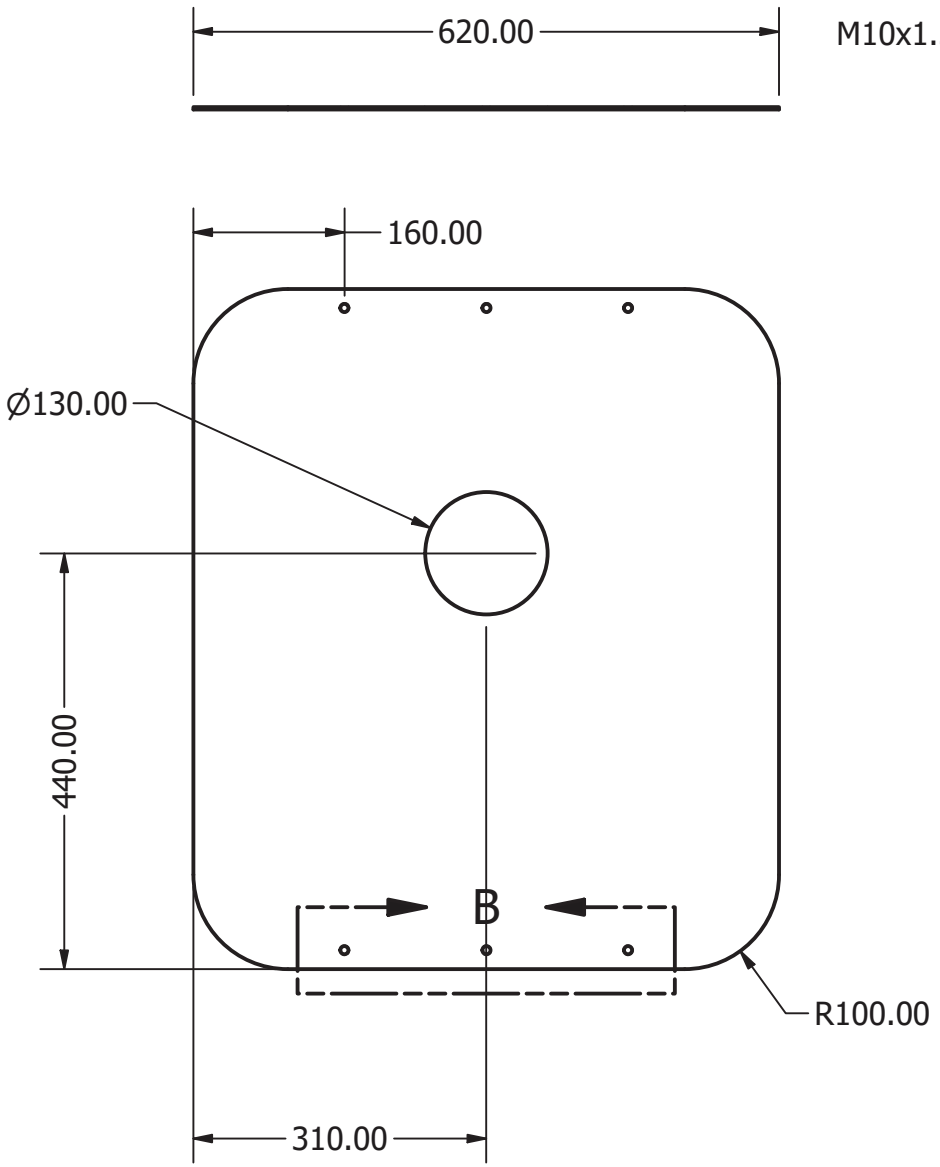

DETAIL B SCALE 1 / 4

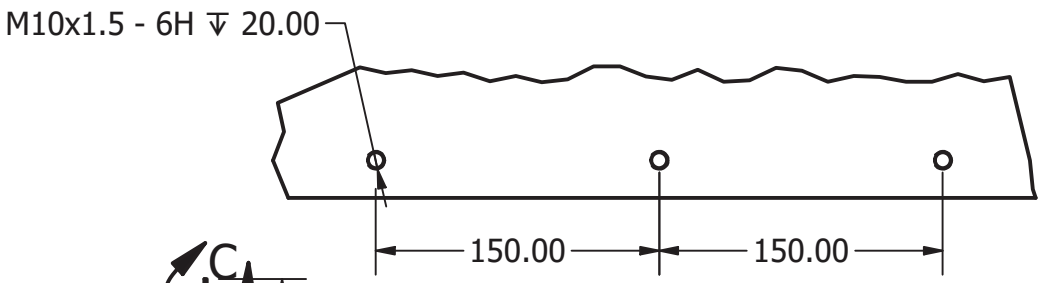

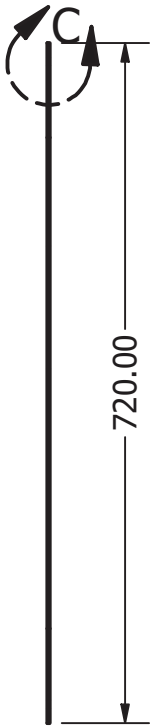

DETAIL C SCALE 1

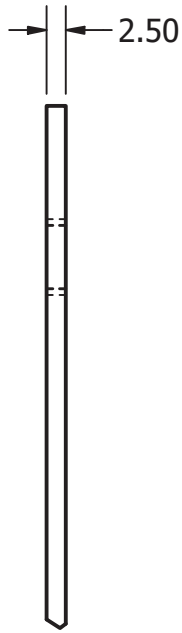

Date: 16-Nov-20	Durban University of Technology
Drawn: Sanjimba	
Approved:	
Checked:	Drawing Title: **Nacelle Front Cover**
Scale: 1/8	DWGNO: SWT-002-01
Not to Scale	Sheet No: 1 of 1 — A4

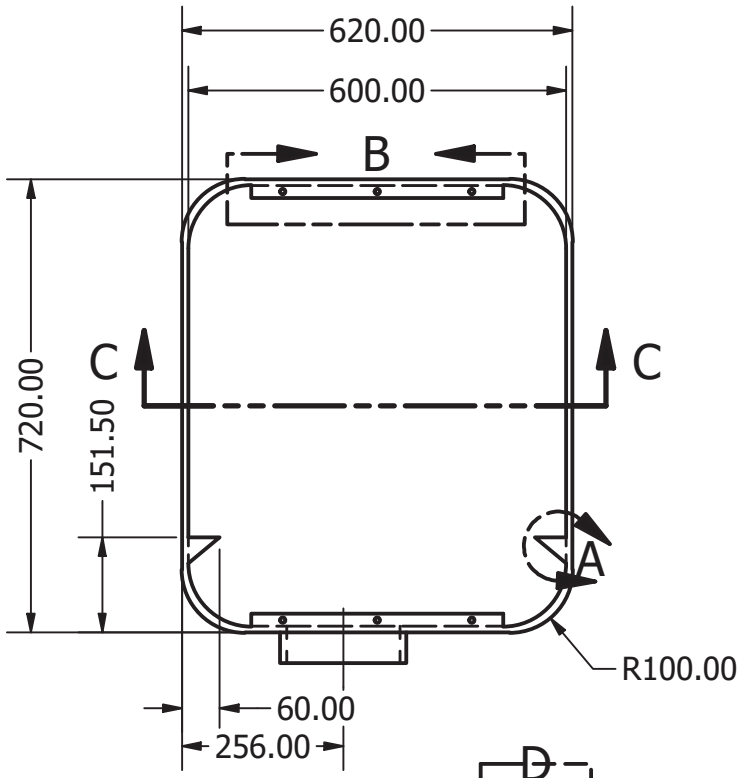

SECTION C-C SCALE 1:12

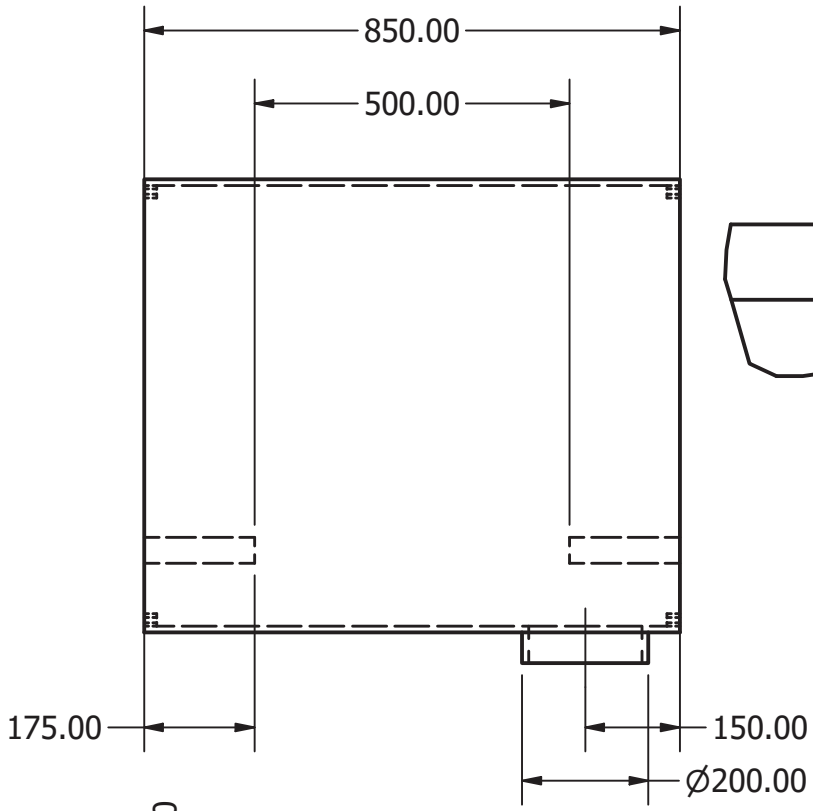

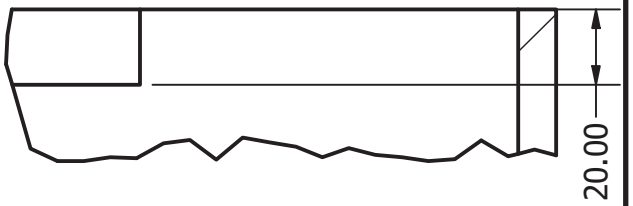

DETAIL D
SCALE 1 / 2

DETAIL B SCALE 1 / 4

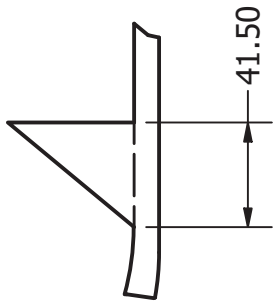

DETAIL A
SCALE 1/3

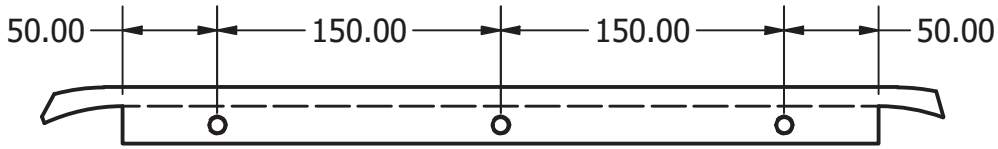

Date: 16-Nov-20	Durban University of Technology
Drawn: Sanjimba	
Approved:	
Checked:	Drawing Title: **Nacelle Cover**
Scale: 1/12	DWGNO: SWT-002-02
Not to Scale	Sheet No: 1 of 1 — A4

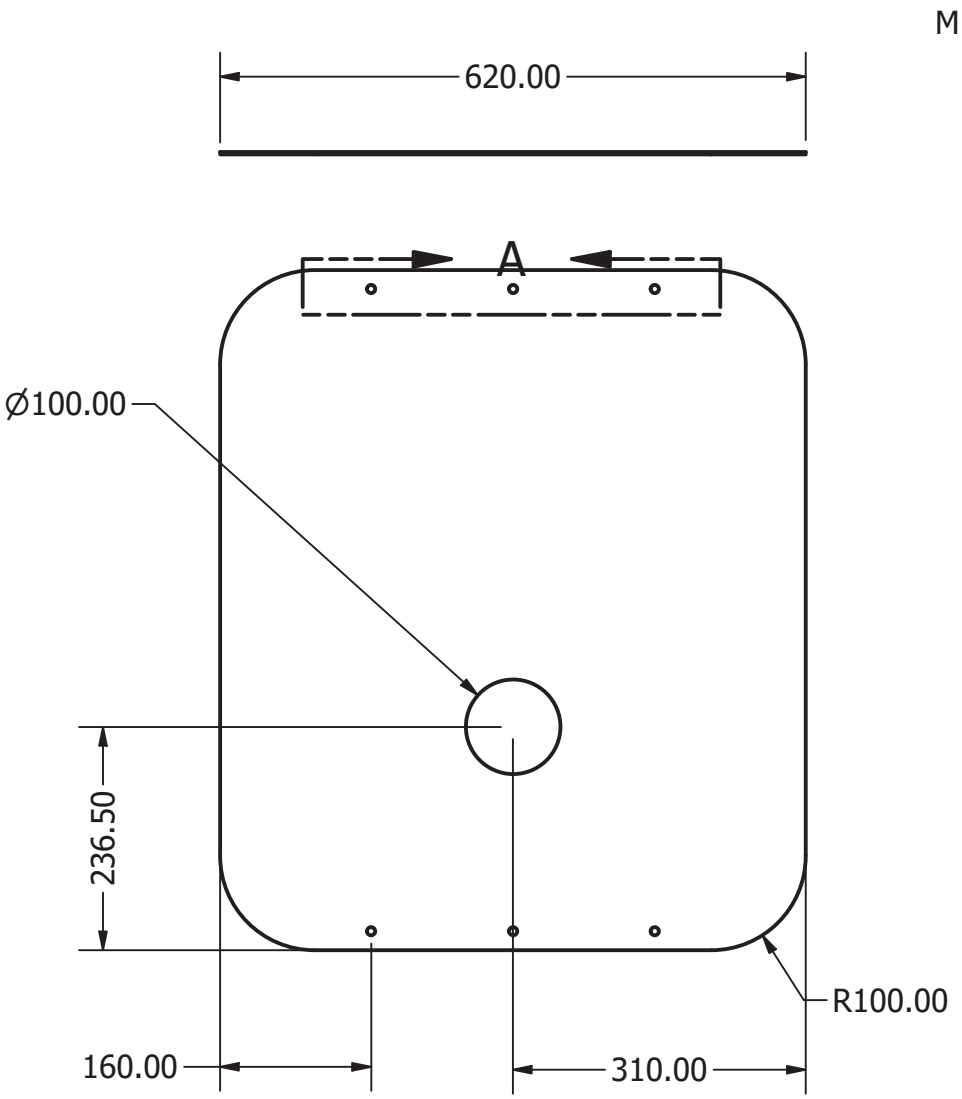

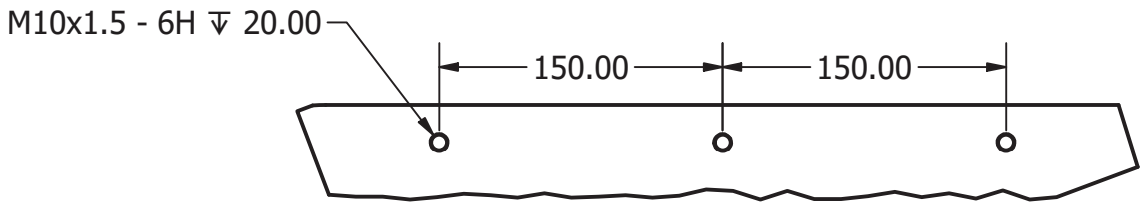

DETAIL A
SCALE 1 / 4

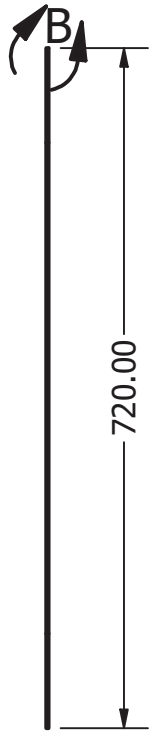

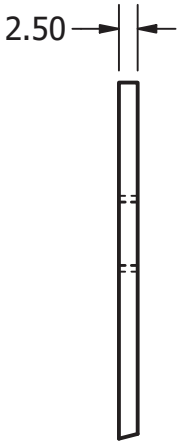

DETAIL B
SCALE 1

Date: 16-Nov-20	Durban University of Technology	
Drawn: Sanjimba		
Approved:		
Checked:	Drawing Title:	
Scale: 1/8	**Nacelle Rear Cover**	DWGNO: SWT-002-03
Not to Scale		Sheet No: 1 of 1 / A4

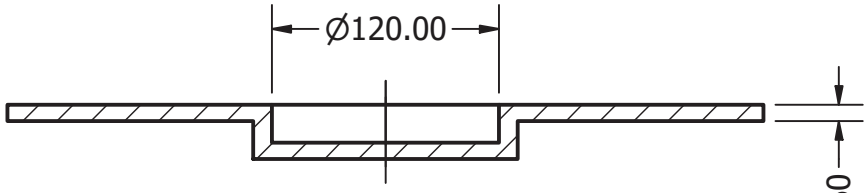

SECTION E-E
SCALE 1/4

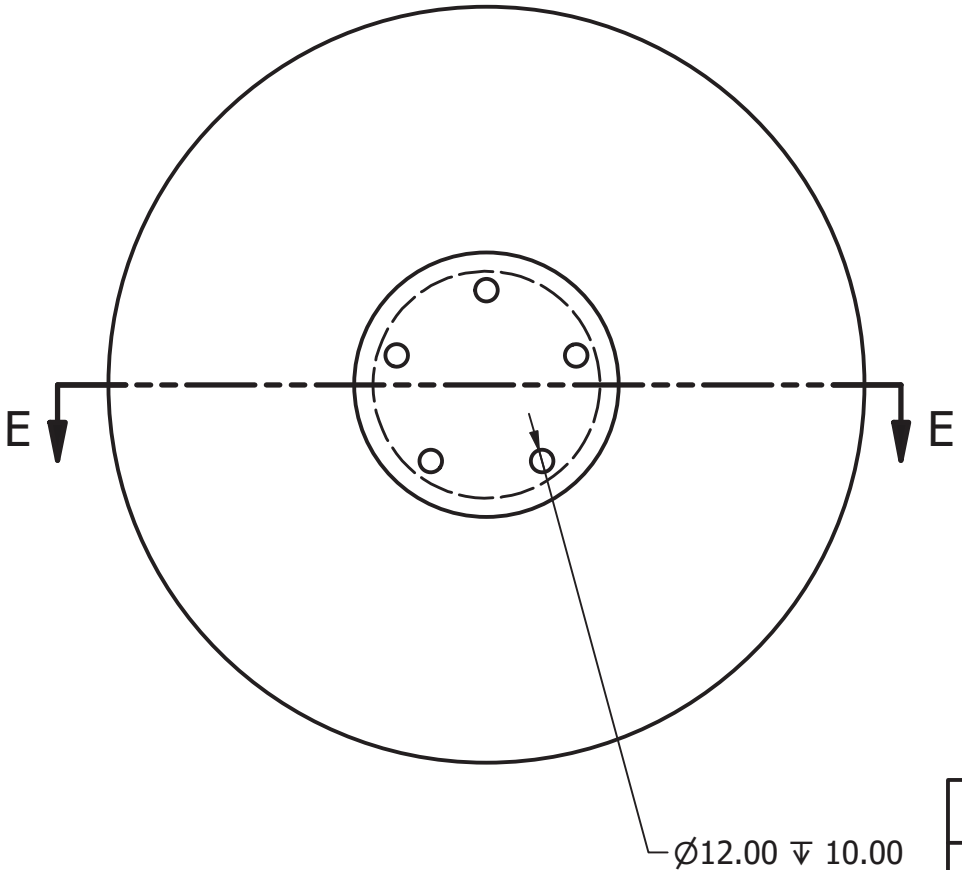

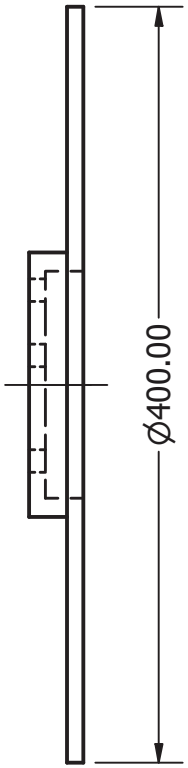

Date: 16-Nov-20	Durban University of Technology
Drawn: Sanjimba	
Approved:	Drawing Title: **Brakes Disc**
Checked:	
Scale: 1/4	DWGNO: SWT-002-06
Not to scale	Sheet No: 3 of 3 — A4

PARTS LIST			
ITEM	QTY	PART NUMBER	DESCRIPTION
1	1	SWT-003-01	Tail support
2	1	SWT-003-02	Nuckle
3	1	SWT-003-03	Tail
4	1	DIN 1850 - G - 65 x 80 x 80	Bush
5	1	SWT-003-04	Nuckle pin
6	1	ANSI B27.7 - 70, R(1)	General Purpose Tappered and Reduced Cross Section Retaining Rings Basic External Series 3AM1 Retaining Rings

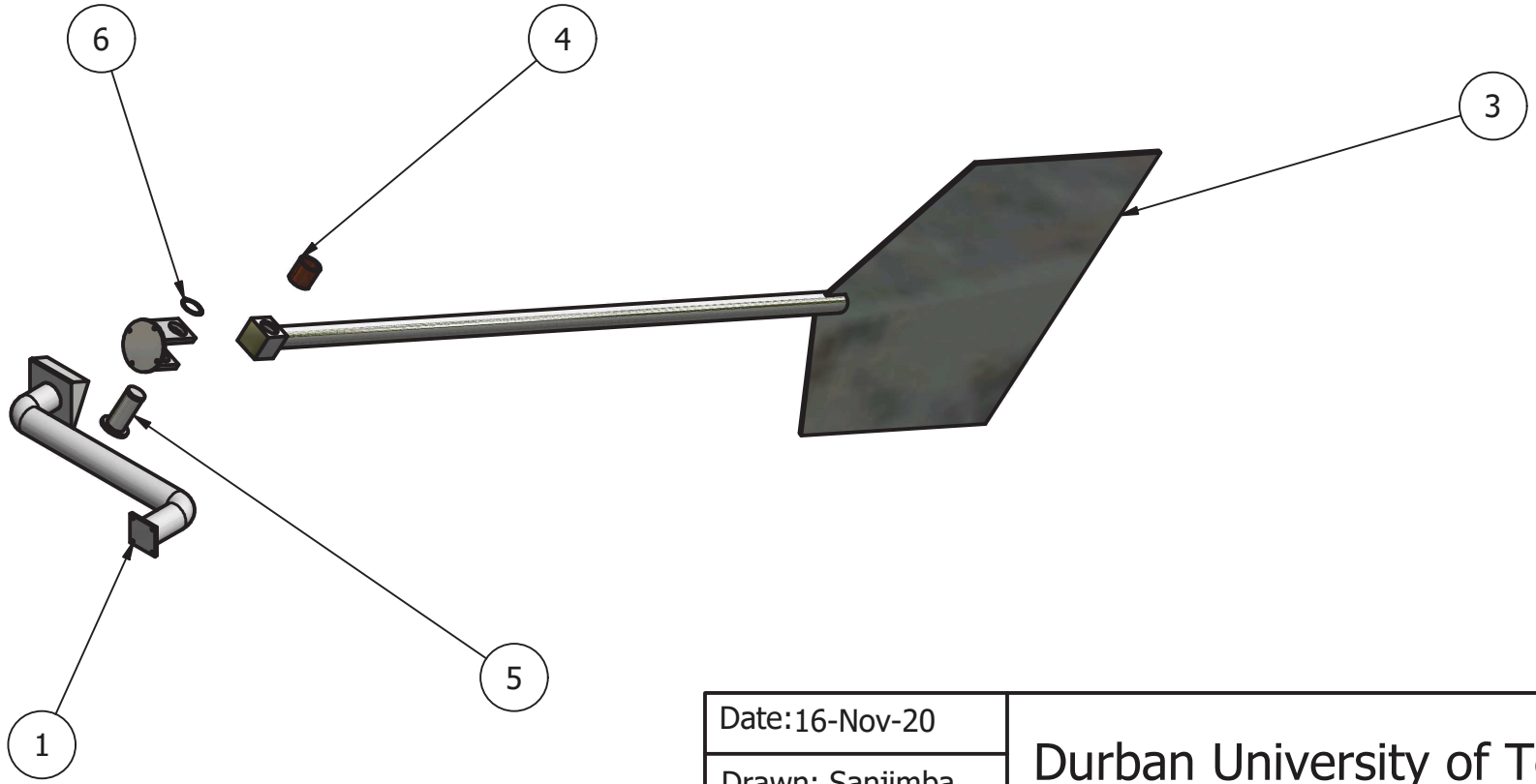

Date: 16-Nov-20	Durban University of Technology	
Drawn: Sanjimba		
Approved:	Drawing Title: **Tail Assembly**	
Checked:		DWGNO: SWT-003
Scale: 1/25		
Not to scale		Sheet No: 1 of 1 A4

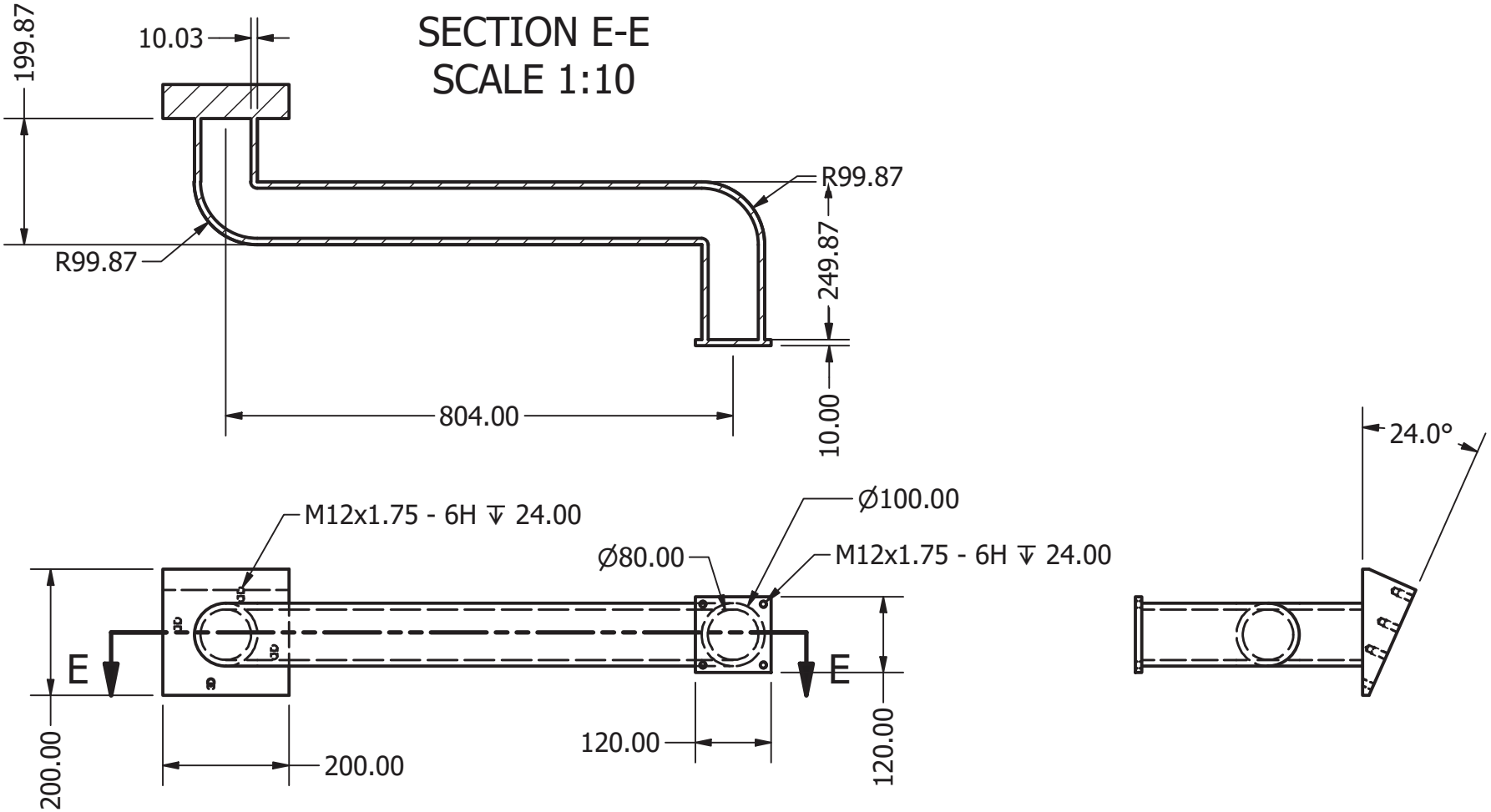

Date: 16-Nov-20	Durban University of Technology
Drawn: Sanjimba	
Approved:	Drawing Title: **Tail Support**
Checked:	
Scale: 1/10	DWGNO: SWT-003-01
Not to scale	Sheet No: 1 of 1 | A4

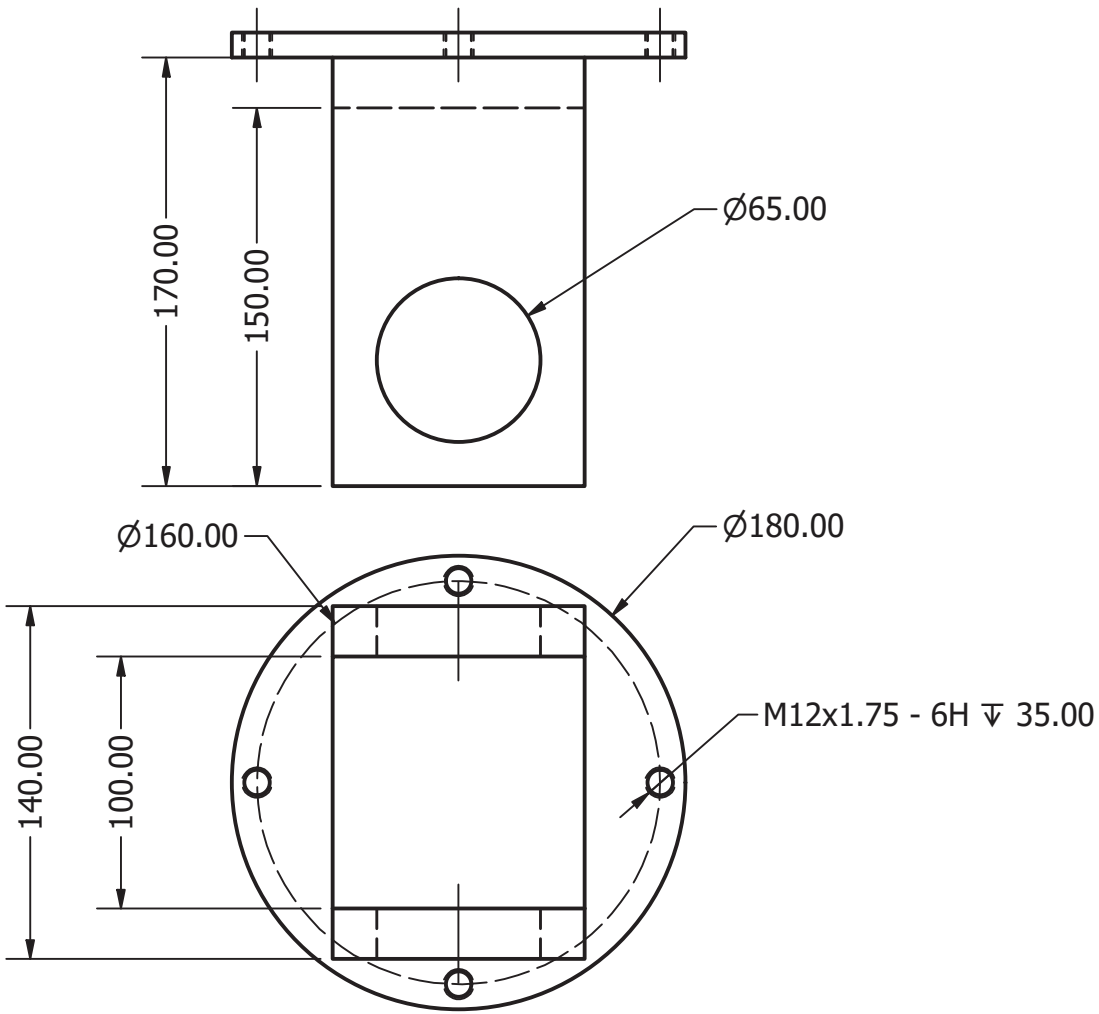

Date: 16-Nov-20	Durban University of Technology
Drawn: Sanjimba	
Approved:	Drawing Title: **Nuckle**
Checked:	
Scale: 1/3	DWGNO: SWT-003-02
Not to scale	Sheet No: 1 of 1 — A4

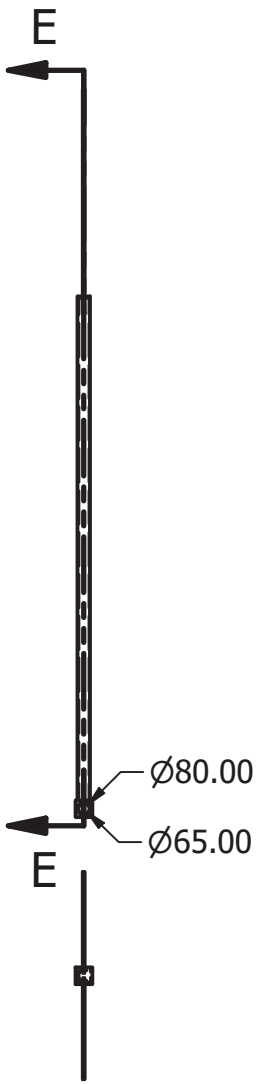

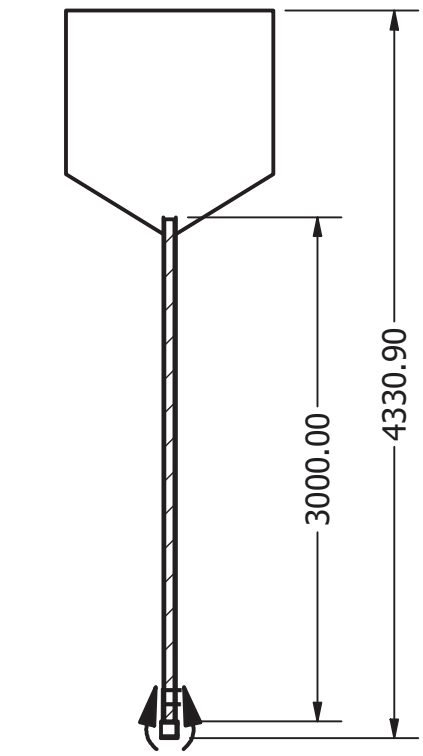

SECTION E-E
SCALE 1:45

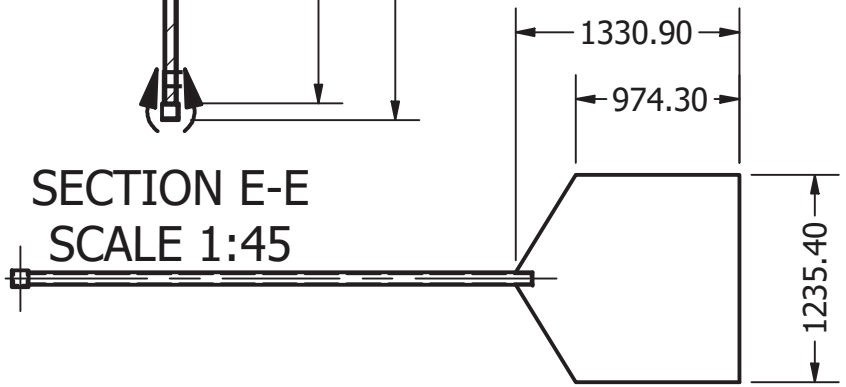

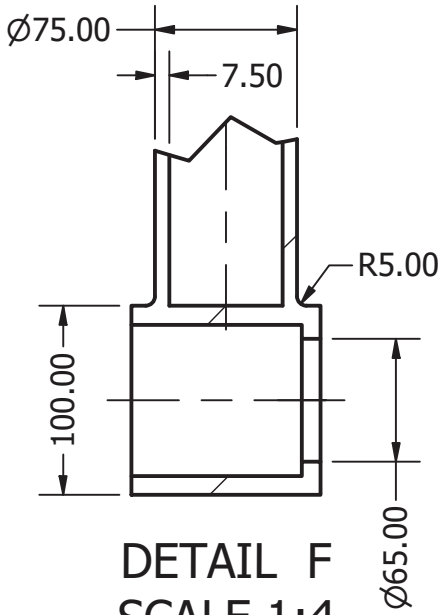

DETAIL F
SCALE 1:4

Date: 16-Nov-20	Durban University of Technology	
Drawn: Sanjimba		
Approved:	Drawing Title: **Tail**	
Checked:		DWGNO: SWT-003-03
Scale: 1/45		Sheet No: 1 of 1 | A4
Not to scale		

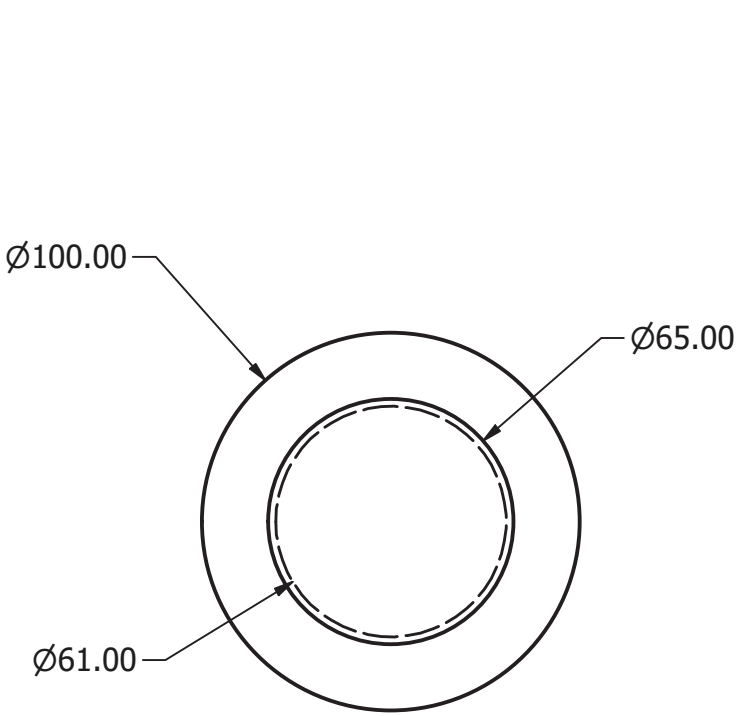

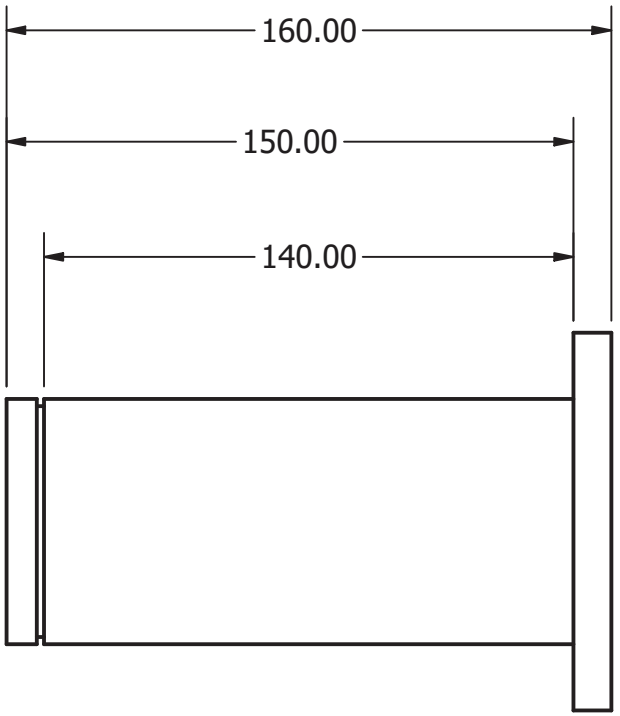

Date: 16-Nov-20	Durban University of Technology
Drawn: Sanjimba	
Approved:	Drawing Title: **Nuckle Pin**
Checked:	
Scale: 1/2	DWGNO: SWT-003-04
Not to scale	Sheet No: 1 of 1 | A4

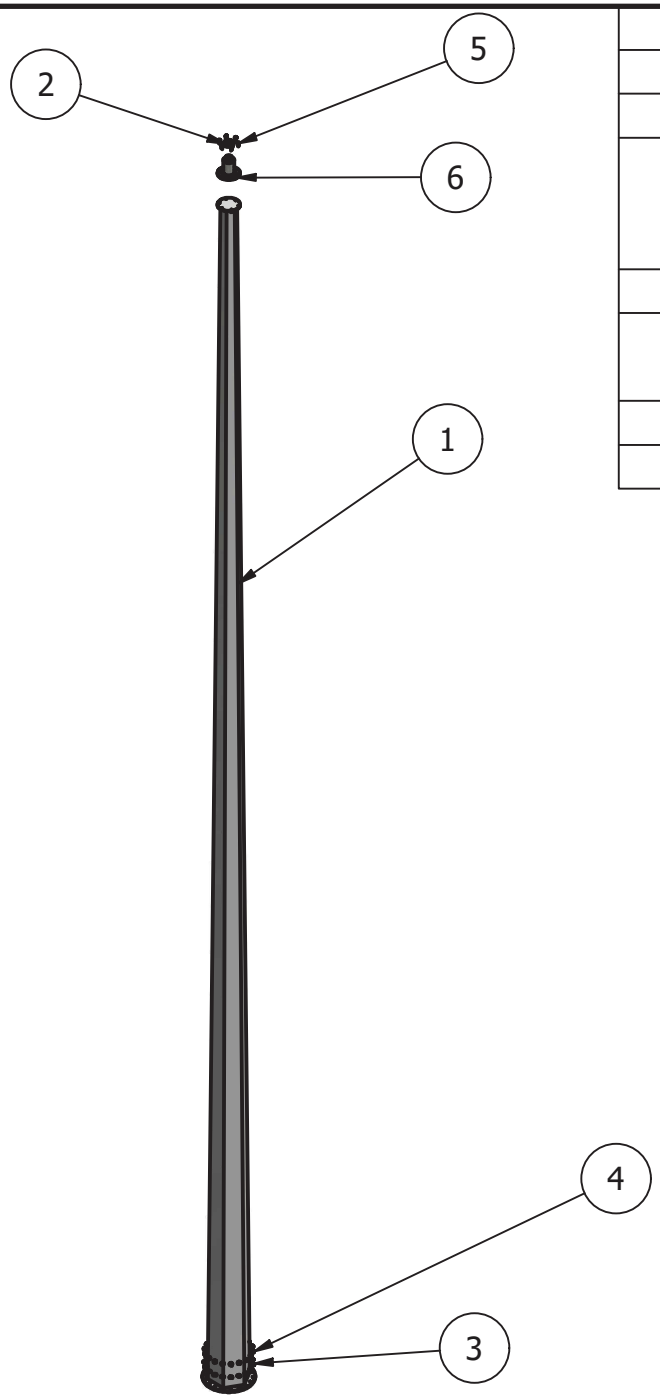

PARTS LIST			
ITEM	QTY	PART NUMBER	DESCRIPTION
1	1	SWT-004-01	Tower
2	1	DIN 635 SKF - SKF (22214 CC)	Spherical Roller Bearings Double Row with Cylindrical Bore SKF
3	18	IFI - 20, RTW	Round Test Washer
4	18	ANSI B 18.2.4.1 M - M20 x 2.5	Hex Nut
5	6	EN 14399-4 - M12 x 35	Hex-Head Bolt
6	1	SWT-004-02	Nacelle shaft

Date: 16-Nov-20	Durban University of Technology		
Drawn: Sanjimba			
Approved:	Drawing Title: **Brakes Support**		
Checked:		DWGNO: SWT-004	
Scale: 1/3			
Not to scale		Sheet No: 1 of 1	A4

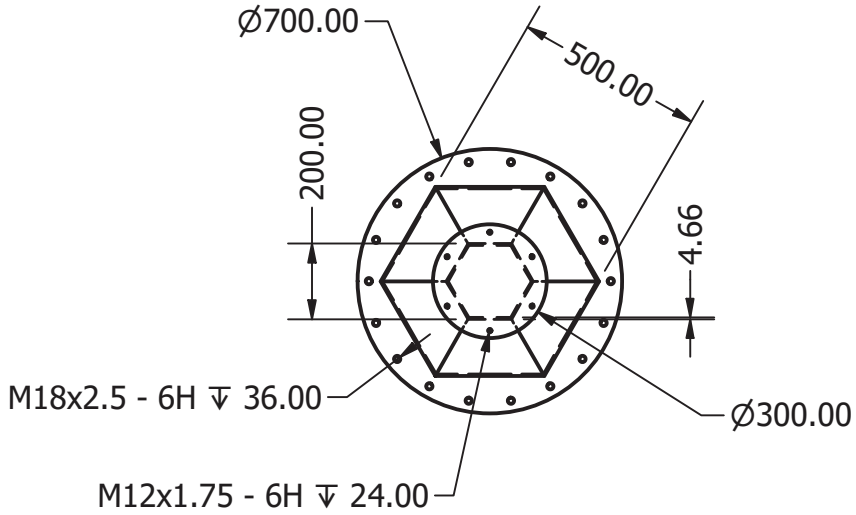

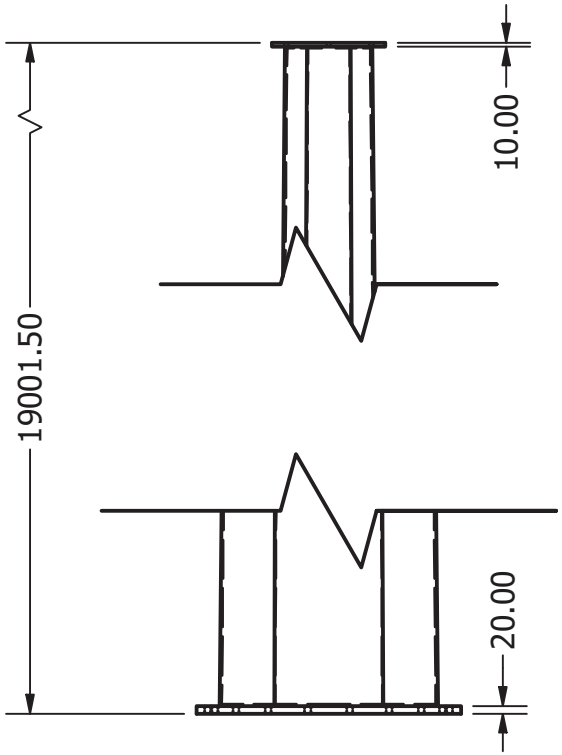

Date: 16-Nov-20	Durban University of Technology
Drawn: Sanjimba	
Approved:	Drawing Title: **Tower**
Checked:	
Scale: 1/20	DWGNO: SWT-004-01
Not to scale	Sheet No: 1 of 1 — A4

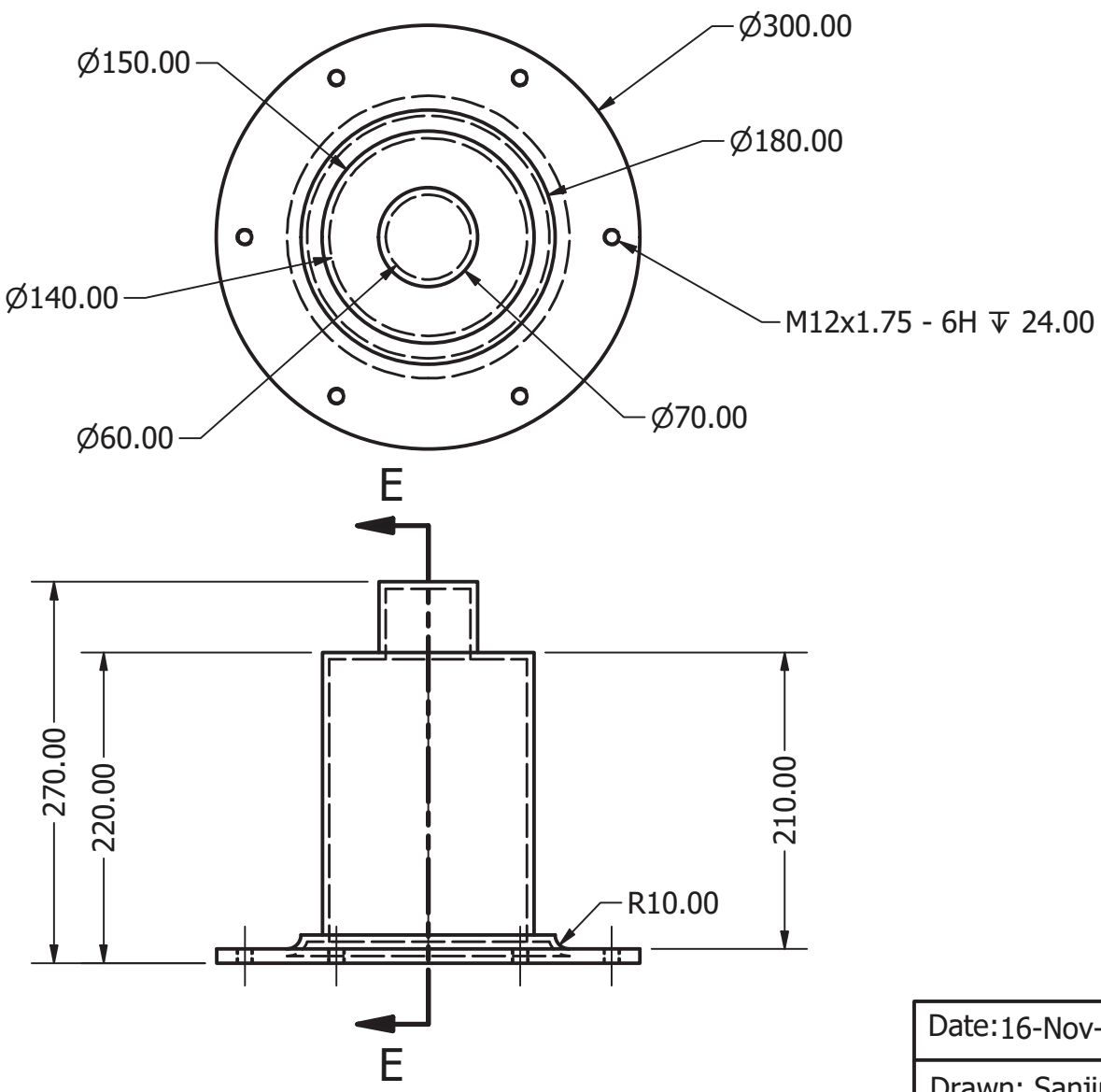

SECTION E-E
SCALE 1/5

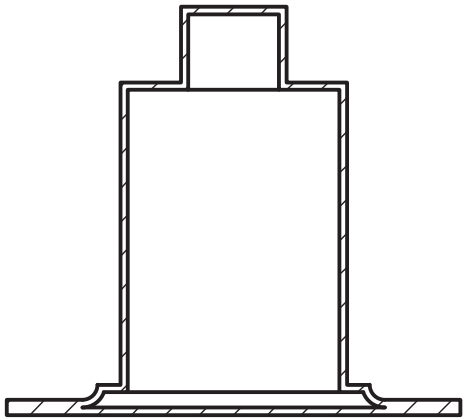

Date: 16-Nov-20	Durban University of Technology
Drawn: Sanjimba	
Approved:	Drawing Title: **Nacelle Shaft**
Checked:	
Scale: 1/5	DWGNO: SWT-004-02
Not to scale	Sheet No: 1 of 1 — A4

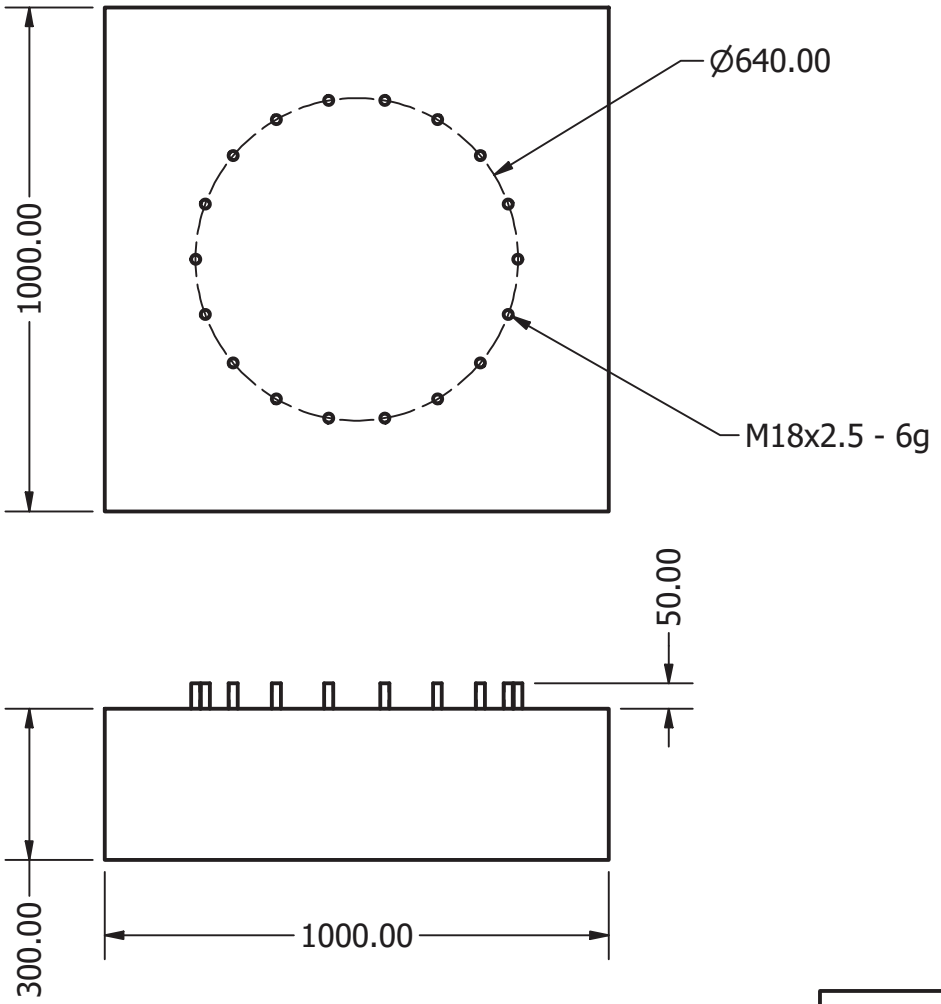

Date: 16-Nov-20	Durban University of Technology
Drawn: Sanjimba	
Approved:	Drawing Title: **Tower Base**
Checked:	
Scale: 1/15	DWGNO: SWT-005
Not to scale	Sheet No: 1 of 1 — A4